ULTRASONIC BATCH MODE MICROMACHINING AND ITS APPLICATION TO PIEZOELECTRIC SENSORS FOR FINE NEEDLE ASPIRATION BIOPSY

by

Tao Li

A dissertation submitted in partial fulfillment
of the requirements for the degree of
Doctor of Philosophy
(Electrical Engineering)
in The University of Michigan
2009

Doctoral Committee:

Professor Yogesh B. Gianchandani, Chair
Professor Khalil Najafi
Professor Noel C. Perkins
Professor Kensall D. Wise
Assistant Professor Roma Y. Gianchandani

To my wife Jing, who has always
encouraged me with unlimited love, and to
my dear daughter Annie, who has given me
the greatest happiness of life.

ACKNOWLEDGMENTS

I would like to express my sincere gratitude and appreciation to my research advisor Professor Yogesh B. Gianchandani for his support, encouragement and guidance throughout my doctoral study at the University of Michigan-Ann Arbor. I thank him for giving me such a great opportunity to explore the exciting field of MEMS. His patience and support helped me overcome many challenges in research. My dissertation and accomplishment would not have been possible without his methodical and effective mentoring and continuous encouragement and guidance. I am also indebted to my committee members, Professors Kensall D. Wise, Khalil Najafi, Roma Y. Gianchandani, and Noel C. Perkins for their valuable discussion and insightful suggestions on my research work.

Undergraduate students, Adam Barnett, Saira Shariff and Rachit Gupta worked on sub-projects of this research. I appreciate their excellent work. I also thank Naveen Gupta and Karthik Visvanathan for discussion and support on the μUSM related projects.

I would like to thank former and current members of Prof. Gianchandani's research group, Kenichi, Long, Shamus, Chester, Senol, Kabir, Weibin, Bhaskar, Amar, Jong, Mark, Christine, Scott W., Scott G., Naveen, Allan and Karthik, especially Dr. Kenichi Takahata for introducing me into the field of μEDM. I would also like to thank many students and colleagues from other groups, Ying Y., Jianbai, Yang L., Gayatri, Sang-Hyun, Sang-Won, Jae-Yoong, Neil, Jay, Burcu, Hanseup, Seow Yuen, Tzeno, Yuan

X., Sheng-Shian, Wen-Lung, Ruba, Meng-Ping, Linda, Jun Y., Dawen, Yuhai, Xiaoyang, and many others for their encouragement, discussion and friendship.

Special thanks to many former and current LNF technical staff, including Ning, Ed, Tony, Rob, Cedric, Zeying, Russ, Greg, Brian, Katherine, Pilar, Matt, and others for their help in the UM clean room. My CMOS process run would not have been possible without their dedicated work and help. Additional thanks to all the administrative staff at WIMS, SSEL, and LNF. My graduate study would not have been as smooth without their devoted service.

Finally, I sincerely thank my parents who have always cheered and encouraged me to reach every milestone in my life. And last but not least, I want to thank my wife Jing for her enormous capacity to love and support. Without her, I could never have reached this day.

TABLE OF CONTENTS

LIST OF FIGURES

LIST OF TABLES

LIST OF APPENDICES

ABSTRACT

The development of micro-electro-mechanical systems (MEMS) is constrained by the range of materials that can be processed lithographically. Bulk ceramics (including piezoceramics) are of particular interest due to unique properties for application to micromachined transducers and packages. This effort has two goals: the development of lithography-compatible batch-mode micro ultrasonic machining (μUSM) of bulk ceramics; and the demonstration of this technology by its application to piezoelectric sensors for guiding fine needle aspiration (FNA) biopsy.

The new micromachining process, LEEDUS, uses lithography, electroplating and batch micro-electro-discharge machining (μEDM) to define stainless-steel microtools, which are then used in batch μUSM of ceramic substrates. This die-scale pattern transfer provides high throughput and resolution. A related process (SEDUS) uses serial μEDM without lithography for rapid prototyping of simple patterns. A computer-controlled μUSM apparatus with force feedback is developed as part of this effort. Die-scale patterns with 25μm feature sizes can be transferred onto Macor™ ceramics at a machining rate of >18μm/min. Other process characteristics are also described. Spiral in-plane actuators are machined from bulk lead zirconate titanate (PZT) for demonstration purposes.

The process is applied to piezoelectric sensors integrated on biopsy needles to aid in real-time tissue differentiation during FNA biopsy, which is challenging because of the

precision required to obtain samples from small target tissue volumes. The 200μm-diameter and 50μm-thick sensors are batch-fabricated from bulk PZT and located on a steel diaphragm formed at the needle tip by μEDM. Tissue contrast detection is demonstrated, showing resonance-frequency shifts (≈13MHz) in sensor impedance when the needle is moved between tissue layers (porcine fat/muscle). *In vitro* characterization shows proportional relationship between the frequency shift and sample acoustic impedance, demonstrating its potential utility during FNA biopsy. For tissue depth >15mm, differential sensor configurations are designed with oscillating interface circuits, which include an analog CMOS circuit fabricated in the UM 3μm process. The circuit functionality is experimentally verified: an inverter amplifier provides a voltage gain of >390V/V; oscillating signals of ≤19.67MHz are generated with quartz crystals. For the piezoelectric sensor to be used with this interface a higher Q is necessary and various options have been defined.

CHAPTER 1

Introduction

The emergence and rapid development of micro-electro-mechanical systems (MEMS) have largely relied on established semiconductor manufacturing technologies for integrated circuits (IC). Since the first microsensors in the 1970's and microactuators in the 1980's, micromachining processes for silicon have been extensively used for MEMS fabrication, and silicon based device structures virtually play the dominant role for most MEMS devices. This brings significant advantages such as lithography-based batch manufacture of devices and monolithic integration with microelectronic circuits, and leads to today's device commercialization and development of integrated microsystems. Among these techniques, surface micromachining processes based on thin film deposition and etching have been used to build fairly complex microstructures, but their two-dimensional (2D) structural geometry seriously limits their mechanical functionalities which can be best realized with three dimensional (3D) components made from bulk materials. This limitation can be addressed by using bulk micromachining techniques. In this category anisotropic wet etching, deep dry etching like DRIE, and wafer bonding techniques have been widely used to effectively fabricate complex 3D microstructures; however, the applicable materials for these techniques are almost limited to silicon. Electroplating with molds fabricated by deep-UV or X-ray lithography enables the use of thick metal layers to form 3D microstructures, but the applicable

metals are usually confined to gold, copper, and nickel, and the structures formed are subject to stress and degradation of material properties. Lack of diversity in bulk material availability for device structures has limited the functionality and performance of many MEMS devices, and often impedes the development of new and potential MEMS applications. Compatibility with environments such as the human body for implanted devices and harsh conditions in most environmental monitoring applications is also challenging to achieve and demands a high standard from device packaging. This further calls for diversified materials suitable for various environmental situations and corresponding micromachining technologies to handle them.

One category of bulk materials of interest is high strength and refractory metals and alloys such as steel, titanium, and platinum-rhodium. Steel has played an important role in macroscale applications due to its various exceptional characteristics controlled by the amount and types of impurities added to iron, but they have not been substantially explored for use in MEMS. Several kinds of steel are also well characterized for use as machining tool materials. Titanium is well recognized for its biocompatibility and has been used as packaging material for implantation applications such as pacemakers or drug delivery, but in the MEMS field it has only been used as thin films. Platinum-rhodium has a proven history in the contact switch application, but due to the limitation of current MEMS processing capability, RF MEMS switches usually just use electroplated gold, which greatly reduces the longevity of the devices. These constraints have been addressed by batch mode micro-electro-discharge machining (μEDM), which is a lithography-based bulk-machining technology capable of handling any conductive or semi-conductive materials including all kinds of metals [Tak02, Tak05].

Another important category of bulk materials is ceramics, which in broad definition refer to any non-metallic and non-organic solid materials, and may be amorphous (such as glass), polycrystalline, or crystalline. Ceramics have been playing increasingly important roles in micromachined transducers and electronic devices because of their unique properties such as high electrical and thermal insulation, high melting temperatures, and high chemical stability [Buc86, How95, Kum96]. Several types of ceramics have found applications in electronic and MEMS packaging areas [Ots93, Pal99, Yan87]. In addition to conventional IC high-performance packaging, ceramics are also attractive for microsystem packaging, such as for hermetic packages made entirely of ceramic or a combination of ceramic and metals [Bro99, Cap03]. In many of these cases, holes, grooves, or complex patterns are often required on ceramic workpieces like substrates for packaging or microfluidic channels. As an important category of ceramics, piezoelectric ceramic materials, such as lead zirconate titanate (PZT) and related ferroelectric materials have been widely used in the fabrication of sensors and actuators [Buc86], and PZT is of particular interest for MEMS applications due to its high piezoelectric coefficients and good electro-mechanical coupling [Tro04]. However, in the MEMS area PZT has mostly been used as thin films with degraded material properties. Although there are already several approaches that can process ceramics for MEMS applications, lithography-based pattern transfer for ceramics still remains a challenge due to various limitations of the current techniques. Ultrasonic machining (USM), which is a highly effective technology for any hard and brittle material, can be a promising candidate, but at microscale, it has only been used in serial mode, which greatly limits its throughput and capability in handling complex patterns. In

this effort, a batch mode micro ultrasonic machining (μUSM) process is to be developed for lithographic pattern transfer on any hard and brittle materials such as ceramics and glasses. It will be shown that this process is facilitated in an important way by the μEDM process which provides hard-metal microtools with lithographically-defined patterns.

The expanded material choices enabled by the capabilities of μEDM and μUSM can be used to develop MEMS devices that can enhance the capability and performance of current medical instruments, and a piezoelectric sensor integrated on a steel needle for tissue contrast detection during fine needle aspiration (FNA) biopsy is one of the potential applications. FNA biopsy, such as thyroid biopsy, is challenging because of the precision required to obtain a sample from the small target tissue volumes. A biopsy needle that can detect different tissue planes and other complementary tissue properties can provide effective guidance to physicians during the procedure. In this effort, as a demonstration of application of the developed process, a piezoelectric tissue contrast sensor is to be integrated in a cavity formed in the wall of a biopsy needle at the tip. The sensor can be made from bulk PZT ceramic material with excellent piezoelectric properties by the developed batch mode μUSM process, and the cavity on the stainless steel needle for sensor integration can be prepared by the μEDM process. System level integration of the sensor with interface circuit in differential mode will also be explored to expand the capability of the device for deep tissue biopsy such as breast biopsy, and also to simplify the sensor readout scheme for potential device commercialization.

In summary, this research effort has two primary goals. The first one is to develop a new batch mode micromachining technology, *i.e.* batch μUSM, for hard and brittle materials, such as ceramics, to expand the choices of bulk materials available for

the development of MEMS devices. The second goal is to demonstrate the effectiveness and the capability of the developed technology with the implementation of a piezoelectric sensor for tissue differentiation during FNA biopsy, which provides a compelling test application.

Section 1.1 reviews the batch mode μEDM process for handling bulk hard metals which can be used as tool materials for the development of batch mode μUSM. Current micro processing techniques available for ceramic materials and their limitations are discussed in Section 1.2, including both additive and subtractive processes. The detailed mechanism of μUSM in serial mode is given in Section 1.3, as well as the need and scheme to convert it into a batch mode lithography-based technology. As a demonstration, the proposed process can be applied to fabricate a piezoelectric sensor for guidance of FNA biopsy, and Section 1.4 describes the background information and motivation of such a device as well as the research scheme. Finally, an outline of the research discussed in this dissertation is given in Section 1.5.

1.1 Batch Mode μEDM for Conductive Materials

This section reviews batch mode μEDM technology, which is an important base technology for the proposed research. In particular, this technology will be used to fabricate hard metal microtools for batch mode μUSM. In addition, for this effort, it will be used to customize the FNA biopsy needles for system integration of the piezoelectric sensors.

Bulk conductive materials like hard metals have attractive properties for MEMS applications. While the traditional silicon based technologies have difficulties in

processing these materials, μEDM is well suited for this purpose. It can micromachine into 3D microstructures any electrically conductive materials, including steel, graphite [Tak01], silicon [Rey00], and magnetic materials [Gri01, Hon98] such as permanent magnets [Fis01]. When combined with lithography technology, μEDM can be applied in batch mode, providing high spatial density, high uniformity, and more than 100× higher throughput compared with the serial mode μEDM [Tak02].

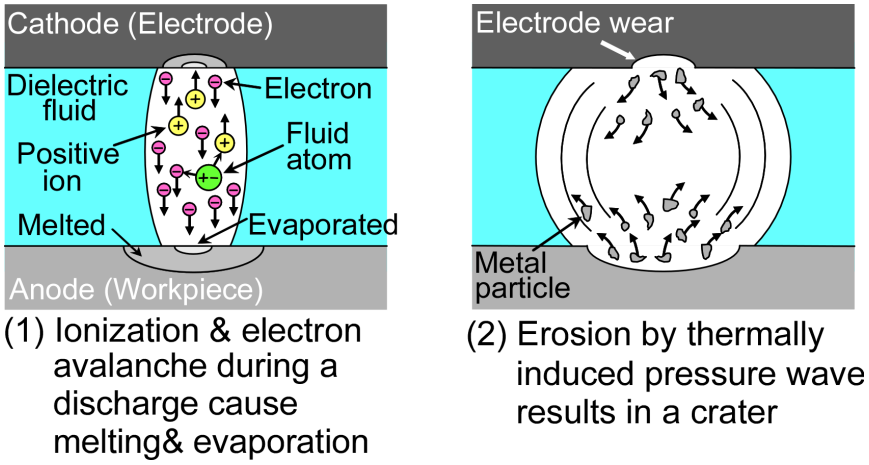

Figure 1.1: Mechanism of μEDM. The figure is modified from [Tak05].

1.1.1 Principle of the μEDM Process

The mechanism of the EDM process is shown in Figure 1.1. A voltage is applied between a cutting electrode (cathode) and the workpiece (anode) when they are both immersed in dielectric oil. Electrical discharge arc is fired when the gap is reduced to several microns, and ionization and electron avalanche in the oil fluid occurs. This raises the temperature on the workpiece, resulting in local melting and evaporation. The melted parts are eroded by a thermally generated pressure wave, forming a crater shape, and the EDM process proceeds as high-frequency repetition of this removal sequence. The same procedure occurs on the electrode and results in electrode wear. Due to a smaller

temperature rise on the cathode and the choice of electrode material with a higher melting point, this wear is much smaller than the machining on the workpiece.

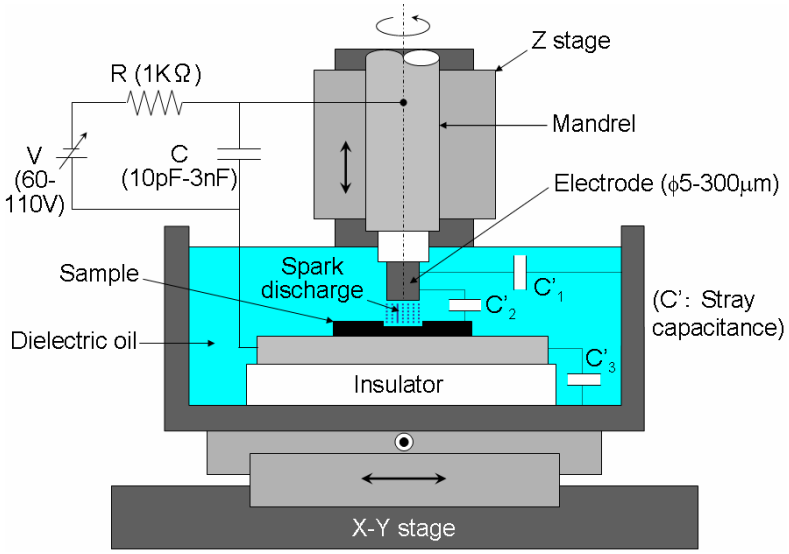

Figure 1.2: Basic configuration of a μEDM machine [Tak05].

In order to achieve the micron-scale precision in the EDM process, a μEDM machine has been developed by using an extremely small amount of discharge energy (10^{-7} J level) and a precise mechanism which provides submicron accuracy in spindle rotation, feeding, and positioning [Mas90]. The basic configuration of such a machine is shown in Figure 1.2. A relaxation RC circuit is used for discharge pulse timing. An extremely short width pulse discharge is produced by charging capacitor C through resistor R and then discharging it between the electrode and workpiece. Discharge energy E is determined by $E = \frac{1}{2}(C + C') \cdot V^2$, where $C' = C'_1 + C'_2 + C'_3$ is the stray capacitance. As lower discharge voltage can result in unstable discharge, the low discharge energy is obtained by minimizing C and stray capacitance C'. This is done by minimizing the use of metallic components around the discharge circuit and mainly using

ceramics. The electrode used is a cylindrical tungsten wire, and 5-300 μm diameter can be obtained by using a μEDM technique called wire electro-discharge grinding (WEDG) [Mas85, Pan00], during which the original Φ300 μm tungsten electrode is machined down to the desired diameter by a brass wire traveling through a wire guide (Figure 1.3). By moving the Z stage, which has the electrode mounted through a mandrel, relative to the XY stages, which hold the workpiece, micro holes, slots, and 3D microstructures can be produced by the "writing" movement of the electrode on the workpiece with submicron tolerance and fine surface finish of 0.1 μm R_{max} roughness. This technique is referred to as serial mode μEDM and gives low throughput especially for complex patterns such as gears, which require contour scanning along the edge of the patterns.

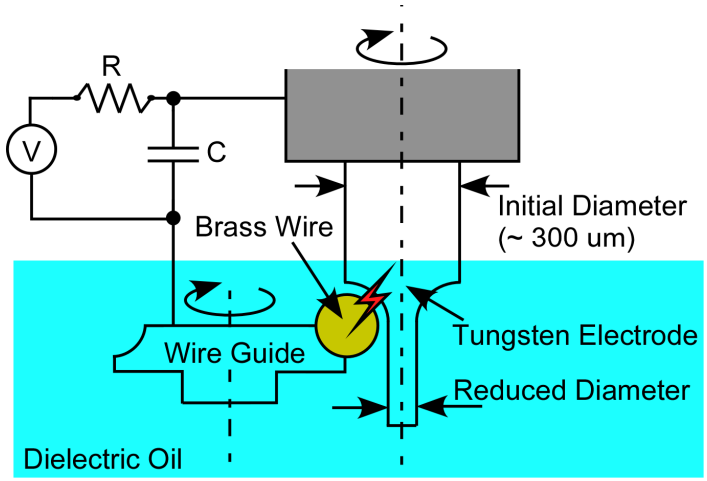

Figure 1.3: WEDG function of a μEDM machine for tool electrode shaping.

1.1.2 μEDM in Batch Mode

Although the serial mode μEDM has been widely used in research and industry applications such as ink-jet nozzles, it is inherently a low throughput process. Additionally, since the workpiece movement is realized with X and Y stages that cannot move concurrently, it is not possible to directly machine a slot or curve at any arbitrary

angle without using the approach of contour cutting with a series of holes to form the outline of the slot or curve. This further reduces its throughput. Another limitation with serial μEDM is the precision. Because the electrodes are individually shaped by the WEDG function, variation can occur in the electrode shape.

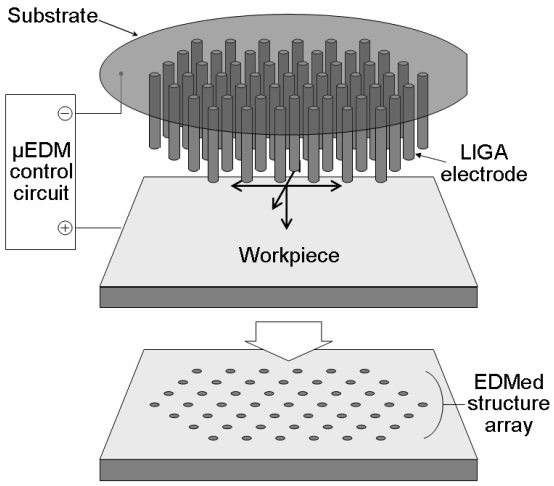

Figure 1.4: Concept of batch mode μEDM with single pulse generating circuit [Tak02].

To overcome these issues, batch mode μEDM has been developed [Tak99, Tak01, Tak02]. The concept is shown in Figure 1.4. By using precisely located high-aspect-ratio electrode arrays fabricated by lithography and electroplating processes, the batch mode μEDM process can provide not only high throughput but also high spatial density and uniformity over the whole machining area. Electroplated copper is used as the electrode material because it has high melting point and high thermal conductivity for minimized wear of the electrodes. The LIGA process, which is the German acronym for lithography, electroplating, and molding, is used to form high-aspect-ratio molds for electroplating by deep X-ray lithography processes. In serial μEDM, the electrode is rotated at 3000 rpm to increase uniformity and prevent local welding to the workpiece. This rotation is replaced by a dithering motion of the electrode array in the direction of

the cutting depth generated by a vibrator on which the electrode array is mounted. During machining, the whole electrode array (cathode) is fed into the workpiece (anode), discharge sparks are fired, and the pattern is transferred onto the workpiece, giving a throughput 20-30× higher than that by serial μEDM in the machining of a 20 by 20 hole array through a 50 μm thick stainless steel workpiece [Tak02].

In Figure 1.4, the electrode array has a common plating base, and the batch μEDM occurs with a single pulse timing circuit. With this configuration, no more than one discharge can be fired simultaneously between the whole electrode array and the workpiece, making this setup spatially parallel but temporally serial. By dividing the pulse timing circuit so that each electrode has separate timing capacitance and resistance, each electrode can fire discharge independently and its discharge frequency can be sustained at the value determined by the RC components in the circuit. Using this parallel discharge concept, a monolithic partitioned electrode array with multiple pulse generating circuits has been fabricated by a two-mask sacrificial LIGA process [Tak02]. This electrode array intended for gear cutting has 10 μm wall thickness and 300 μm height, and the gear clusters made from 70 μm-thick tungsten carbide cobalt (WC/Co) super hard alloy plate using the electrode array give a throughput more than 100 times higher than that of serial μEDM using a single electrode.

With the introduction of the batch mode concept, the shaping capability, feature density, throughput, and uniformity of μEDM technology has been greatly improved. Although it is not suitable for machining dielectric materials, the capability of EDM to handle hard metals such as tool steel and WC/Co makes it an attractive technique for preparing cutting tools which can be used to mechanically machine dielectrics.

1.2 Current Microfabrication Processes for Ceramics

Ceramics have their unique electrical, chemical, mechanical, and physical properties. Typically, they are hard and electrically and thermally insulating, with high melting temperatures and high chemical stability. They are also brittle, with low toughness and ductility [Bro99]. Although superb for packaging and device applications, these properties of ceramics also make them difficult to process with lithography-based technology, which is preferred in today's microfabrication industry for its high density and high throughput.

1.2.1 Additive Processes

At macroscale, ceramics are traditionally fabricated by molding from a powder form and then going through a high temperature step for sintering. The sintering temperature is usually ~1000°C or higher except for the sol-gel process which uses lower temperatures (200°C for initial firing and 800-900°C for crystallization). This high temperature can cause problems for other fabrication steps if the process sequence is not carefully designed. During sintering the volume of the molded powder body shrinks when the organic bonder is removed, bonding the grains together and producing a solid material. Depending on the method of forming the shape of the powder body, this category may include tape casting, dry pressing, fused deposition, sol-gel process, *etc.* Tape casting and dry pressing are commonly used in the electronic packaging industry. Injecting ceramic slurry into a mold is another common approach to form ceramic parts with various shapes, while at microscale the mold itself would be difficult to fabricate in the first place.

Tape casting, also called doctor blading or green tape technology for ceramics, is the best and most commonly used technique for forming large-area flat ceramic substrates with thicknesses ranging from 12 μm to over 3 mm [Mad02]. During this process, a ceramic slurry is continuously dispensed onto a moving substrate. The substrate and dispensed slurry then move under a doctor's blade which is an adjustable gate with a precisely controlled height to limit the slurry to a known thickness of material. Flat and thin ceramic plate is obtained after drying and removal of the organic content in the green ceramic part by a controlled high-temperature sintering process. This technology can not only provide substrate for packaging purposes, but has also been used for device fabrication. A ceramic pressure sensor has been demonstrated using ceramic tape technology and provides excellent high temperature performance [Eng99].

Another additive process is fast deposition of ceramics (FDC) in which a nozzle controlled by a CAD-based program dispenses melted green ceramic filaments onto a platform in a predefined path to form the desired shape layer by layer, and then a sintering step is performed [Ban98]. This technique has been used to fabricate PZT actuators in various shapes such as spirals, cones, tubes, and so on at macroscale. No microscale results have yet been reported.

The sol-gel process uses a colloidal suspension of solid particles and chemical precursors in a liquid solution (a sol) to form a gelatinous network (a gel). When used to fabricate thin films such as PZT in MEMS applications, the solution is spun on a substrate and initial firing is done at 200°C. A second firing at 800-900°C is used to crystallize the film. During the initial firing, large volume shrinkage occurs, which limits the thickness of the film to no more than several microns due to high stress developed

during shrinkage. Other thin-film deposition technologies such as molecular beam epitaxy (MBE) [Mur04] and pulsed-laser deposition are commonly used for thin-film ZnO and other semiconductor materials, and are limited by a slow deposition rate on the order of 0.1 μm/hour.

Although well developed at macroscale for making bulk ceramics, these additive processes, especially at microscale, can suffer from problems such as volume shrinkage, high temperature steps, non-uniform material properties, and difficulty in mold forming. Thus it is often desirable to directly pattern a bulk material without degrading the original material properties. This can be achieved by using subtractive processes.

1.2.2 Subtractive Processes

Subtractive processes usually use mechanical, thermal, or chemical approaches to achieve volume removal from bulk materials which are formed at macroscale and usually possess excellent material properties due to the maturity of macro manufacturing technology. This category includes serial mode and lithography-based processes.

1.2.2.1 Serial Mode Subtractive Processes

Serial subtractive processes for ceramics usually include laser drilling, diamond grinding, and serial mode μUSM.

Laser drilling, or laser beam machining, uses highly-focused high-density energy from a laser beam such as a UV excimer laser to melt and evaporate portions of the workpiece in a controlled manner [Kal03, Kan01]. This process is non-contact, clean and simple, does not require a vacuum, and can machine inside solid and transparent materials for some microfluidic applications. However, the surface produced is usually

rough and has a heat-affected zone. This zone is characterized by thermal shock and changes in morphology, and has to be removed or specially treated in critical applications because of the degradation in material properties.

Diamond grinding usually uses a wheel with bonded diamond abrasives to machine ceramics by chipping. Due to the brittleness of the workpiece material, this grinding process must be precisely controlled to prevent large cracks from forming, and the diamond wheel has to be regularly maintained by dressing [Mam02]. The minimum feature sizes are also limited by the size of the diamond wheel which is difficult to make in microscale.

Serial mode ultrasonic machining has been demonstrated in microscale and feature size as small as 5μm in glass and silicon has been achieved [Ega99], showing excellent potential for MEMS applications. The process details are described in Section 1.3.

These serial mode subtractive processes have been commonly used for conventional precision machining of ceramics and have their own advantages depending on the application situations, while they also have their own limitations. Moreover, as serial processes they are usually limited by the inherently low throughput. They are unfavorable for complex patterns which can be best defined by a lithographic mask and then transferred to the workpiece in batch mode.

1.2.2.2 Lithography-Based Subtractive Processes

The processes that use lithography to define a pattern and then transfer it onto the workpiece are most favorable for high-throughput, low-cost, and large-volume industry applications, and virtually the entire IC industry is based on this type of process. In this

category, dry and wet etching and powder blasting are processes that have been demonstrated for ceramics.

One type of dry etching that has been used for processing ceramics is reactive ion etching (RIE) which uses ions generated from certain gas species in a plasma formed by glow discharges [Mad02]. These ions, when reaching the sample surface, react chemically with the materials and also physically etch some material due to their high kinetic energy. By using a mask, a lithographic pattern can be delivered onto the sample selectively. RIE gives an anisotropic etch profile and submicron features can be achieved, but it is limited by a slow etch rate which is usually less than 0.5-1 μm/min. as in other dry etching processes [Wan99]. Different etching gases are also required for different ceramics. Phosphoric acid or other wet chemical etching methods for ceramics have also been studied to take advantage of lithography-based pattern transfer. As these are chemical processes, the etching profile is isotropic, which limits the achievable minimum feature size due to lateral undercutting. They also suffer from limited etching rates (~1 μm/min.) and varying etchant requirements for different ceramics [Mak99, Wan00]. For these reasons, RIE and wet etching are usually only used for patterning thin film ceramic materials such as PZT in surface micromachining.

In powder blasting, also called abrasive jet machining, workpiece material is removed by the mechanical impact of a high-velocity stream of gas mixed with fine powders. This process uses a thick special mask (such as electroplated copper) to achieve lithographic pattern transfer, and provides excellent machining rates (25 μm/min. on a 3" wafer) [Wak03, Wen00]. The machined sidewall is V-shaped and the process has a blast lag problem, which means a wider feature opening on the mask will produce a

larger cutting depth than smaller openings. These problems become rather severe when the feature size gets smaller and the cutting depth gets larger.

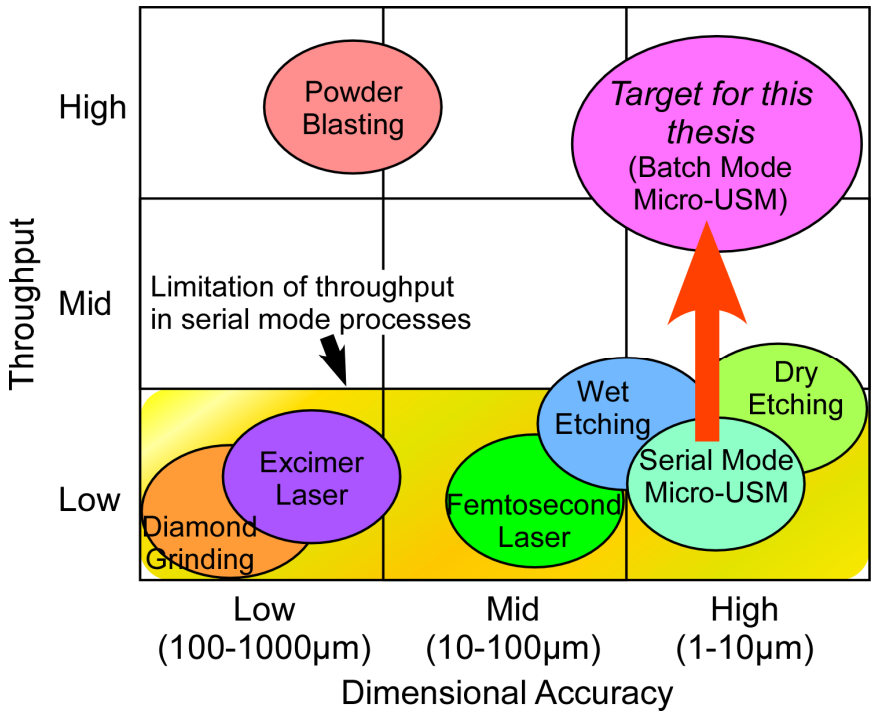

Figure 1.5: Performance comparison in terms of throughput and dimensional accuracy for current ceramic subtractive processes and target for this effort.

1.2.3 Summary

As discussed above, additive processes at the micro level can suffer from volume shrinkage, high temperature steps, non-uniform material properties, and difficulty in mold forming. Thus it is often desirable to directly pattern a bulk material without degrading the original material properties. However, subtractive processes have their own challenges. Serial subtractive processes like laser drilling and diamond grinding, which are most commonly used for conventional precision machining of ceramics, are unfavorable for complex patterns which can be best defined by a mask, with laser drilling also causing thermal shock and changes in morphology. As for lithography-based

processes, RIE is limited by a slow etching rate and varying gas requirements for different ceramics. Phosphoric acid or other wet chemical etching methods for ceramics typically have limited etching rates and minimum achievable feature sizes. Powder blasting provides good machining rates, but suffers from V-shaped sidewalls and blast lag. The performance comparison of these subtractive processes in terms of throughput and dimensional accuracy is summarized in Figure 1.5. The blank preferred region in the upper-right corner of the figure indicates that a bulk micromachining process with lithography-based pattern-transfer capability to provide high throughput without degrading the dimensional accuracy continues to be a challenge. The μUSM that can provide high dimensional accuracy in serial mode is a promising candidate if it is applied in batch mode.

1.3 Micro Ultrasonic Machining: Serial or Batch Mode

Conventional USM has been widely accepted as an effective machining process for hard and brittle materials like ceramics, glass, *etc.*, providing high-aspect-ratio features on these hard-to-machine materials. By using microtools made by WEDG function on the μEDM machine, USM has been used for micromachining in serial mode to obtain micron-scale precision, but its throughput and structural shapes are limited as in other serial processes.

1.3.1 Principle and Characteristics of Conventional USM

The conventional USM, also called ultrasonic impact grinding, uses high-frequency (20 to 100 KHz) ultrasonic vibrations with low amplitudes (0.05 to 0.125 mm)

delivered to a tool (Figure 1.6) [Mor92]. This vibration in the cutting-depth direction, in turn, transmits a high velocity to fine abrasive powders that are suspended in water slurry between the tool and the surface of the workpiece. The tool can be made from low-carbon steel or stainless steel, and undergoes wear. The powders are usually boron carbide, silicon carbide, or aluminum oxide with particle diameter ranging from 0.008 to 0.5 mm. Boron carbide is the hardest abrasive and lasts the longest. The slurry has a concentration of 20% to 60% by volume and also carries away the debris from the cutting area. When the tool is gradually fed into the workpiece, the workpiece material is removed by microchipping or erosion caused by bombardment of the high speed powders on the surface [Kal03, Mad02]. This mechanism is similar to that in the powder blasting process, while here the powder velocity obtained from the adjacent vibrating tool tip is better defined in terms of direction, thus accurate cavities can be formed corresponding to the shape of the tool, eliminating the V-shaped sidewall and blast lag problems observed in powder blasting.

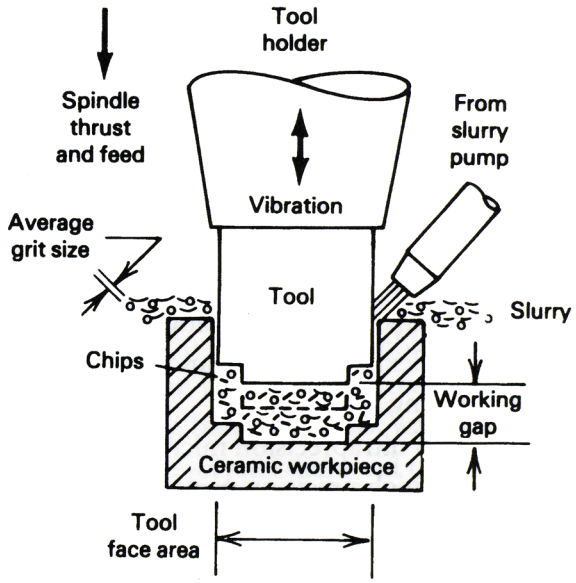

Figure 1.6: USM tool setup used to machine ceramics [Mor92].

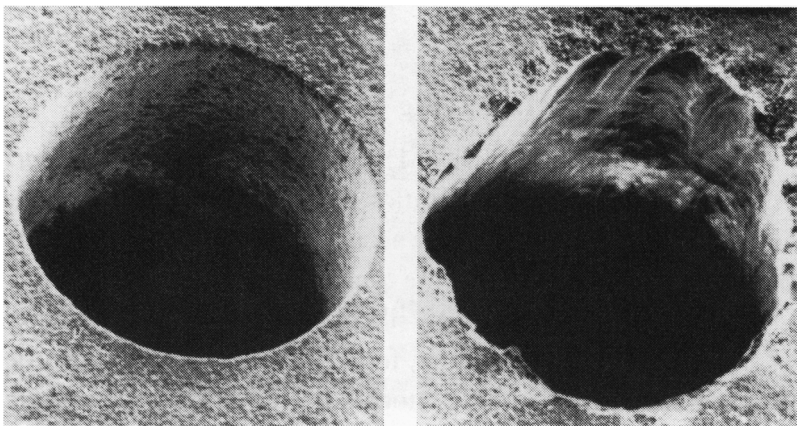

(a) (b)

Figure 1.7: SEM images of 640 μm-diameter holes drilled into alumina with: (a) ultrasonic machining; (b) laser-beam machining [Mor92].

USM is best suited for hard and brittle materials, and almost any hard materials can be ultrasonically machined, including ceramics, carbides, glass, silicon, hardened steels, quartz, alumina, piezoceramics, precious stones such as sapphire, ferrite, fiber optics, *etc.* For soft materials, too much sound energy is absorbed and the process becomes less efficient. The process is non-thermal, non-chemical, and non-electrical, and produces virtually stress-free shapes with high-quality surface finish. As the workpiece materials are brittle, it is easier to fracture them with a high local stress than to plastically deform them. The average force F_{ave} of a powder striking a surface can be defined as $F_{ave} = \frac{2mv}{t_0}$, where m is the mass of the powder, v is the velocity with which the powder strikes the surface, and t_0 is the time of contact between the powder and the workpiece. For hard materials t_0 is very short (10-100 μs), resulting in a significant force F_{ave}, and due to the small contact area determined by the powder size, very high local stress is produced and is sufficient to cause microchipping and surface erosion. Because of the brittleness of the workpiece material and this microchipping mechanism, USM

produces little or no damage or high-stress deformation at or below the surface. Nor is there any thermal or chemical alterations in the sub-surface characteristics of the machined material [Tho98]. As shown in Figure 1.7 which is sourced from [Mor92] and cited in [Mad02], the 640 μm-diameter hole drilled in alumina by USM provides much better defined edges than that by laser beam machining.

Figure 1.8: Sonic-Mill® AP-1000 ultrasonic machine [Son09].

1.3.2 Limitation of Conventional USM for Micromachining

Because of the difficulty and lack of enough precision in fabricating and mounting microscale tools, conventional USM was not used to micromachine features smaller than 100 μm, and most commercially available USM machines and service providers have a minimum feature size of 250 μm. For example, the AP-1000 stationary USM machine from Sonic-Mill® (NM, USA) shown in Figure 1.8 provides a minimum sample size of 250 μm, and can only reach 100-150 μm after special adjustment. Bullen Ultrasonics, Inc., one of the major service providers for USM, sets their minimum hole diameter on glass to 250 μm [Bul09]. On the other hand, features with sizes less than 100 μm have become popular and necessary for many MEMS devices as fabrication and integration technologies develop, while are beyond the capability of the conventional

USM. By using the μEDM WEDG function to fabricate a microtool for USM, μUSM has been developed and a feature size as small as 5 μm has been demonstrated and is discussed in the next section.

As a note, there are usually two operation modes for USM, the stationary and rotary modes. The difference between the two modes is that, in the rotary mode, the vibrating tool is also rotated to help reduce machining load and extend tool life. Because of the rotary motion, the rotary mode can only be used for circular-hole drilling in most situations, and is not applicable for batch mode pattern transfer.

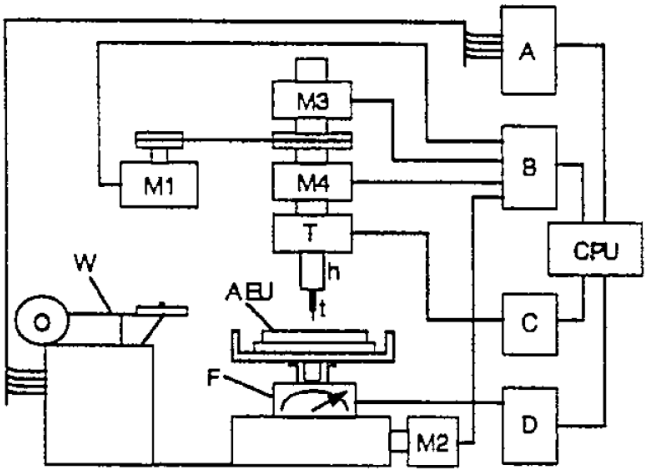

Figure 1.9: One configuration of the μUSM machines using tool vibration. A: WEDG and EDM control circuits; B: driving and positioning control; C: electronic oscillation circuits; D: electronic weight display; M1, M2, and M3: motors for X, Y, and Z axes movement; M4: motor for Z axes rotation; T: ultrasonic transducer; W: WEDG unit; AEU: EDM and USM worktable; F: force sensor; h: horn; t: microtool [Sun96].

1.3.3 USM in Microscale – Serial Mode

The conventional USM tool is attached to a horn on the ultrasound generator, usually by soldering or brazing after shaping with traditional metal machining techniques. When the tool size is reduced to the micron level (<100 μm), this mounting approach cannot provide sufficient tool accuracy, let alone overcome the difficulty of making the

microscale tool itself. To solve this problem, a combined machine that includes the functions of WEDG, μEDM, and μUSM has been developed [Ega99, Sun96]. This machine is similar to the configuration shown in Figure 1.2 and uses the WEDG function of the μEDM machine to shape a microtool tip as small as 5 μm.

Two methods to obtain ultrasonic vibration between the tool and the workpiece have been demonstrated. One method is to integrate an ultrasound generator into an assembly similar to the mandrel which holds a μEDM electrode in Figure 1.2. As shown in Figure 1.9, after the tool tip is shaped by the WEDG function, it is moved above the worktable where the ceramic workpiece is mounted, the ultrasound generator is turned on, and the tool is fed into the workpiece to carry out the process [Sun96]. In this approach, the mandrel and tool assembly are rotated when the ultrasonic vibration is delivered to the tool tip. This rotation enhances material removal rates and overall drilling efficiency, while large eccentricity of the tool rotation caused by the massive assembly of the ultrasound generator and related parts results in high out-of-roundness of the machined holes. Thus this technique cannot be applied to make microholes smaller than the demonstrated diameter of 20 μm. In the second approach, the ultrasound generator is moved to the worktable and the vibration is delivered directly to the workpiece [Ega99]. High precision rotation was obtained and rotation eccentricity was smaller than 0.5 μm. WC alloy was chosen as the tool material and used to make microholes of 5 μm diameter on quartz glass and silicon. An aspect ratio that is >4 has also been demonstrated with a hole diameter of 9 μm.

1.3.4 The Need for Batch Mode Process

Since the μUSM microtool discussed above is shaped by WEDG, this initial demonstration of μUSM is mainly used to drill microholes [Cho03], and any other patterns such as slots or more complex ones have to be realized using computerized numerical control (CNC) to program the movement of the worktable. The tool tip can then serially "write" on the workpiece to scan the contour and form the pattern. This approach not only largely reduces the throughput of the process, especially for complex patterns, but also limits the structural shapes the process can handle.

As discussed in Section 1.2.2, it is preferred to use lithography technology to define a complex pattern in the IC and semiconductor industry. If the μUSM process can be combined with lithography and have the pattern transferred in die-scale or even wafer-scale, not only is the machining throughput greatly improved, but the easy integration with other micromachining steps and familiar approach for pattern definition and customization will enhance its usability in many potential MEMS applications.

Toward this target, the batch mode μEDM process discussed in Section 1.1 is applied to make the microtool for batch mode μUSM, which can facilitate die-scale transfer of complex lithographic patterns to ceramics with potentially high resolution and throughput, while retaining the favored characteristics of conventional USM.

1.4 Application: Fine Needle Aspiration Biopsy Tool

Fine needle aspiration (FNA) biopsy is an extensively-used clinical procedure for diagnosis of cancers or diseases in thyroid, breast, lung, *etc.* However, the complexity involved in the procedure to obtain accurate sampling calls for a new approach of real-

time procedure guidance. This section describes the background and motivation of the proposed micromachined tissue contrast sensor for guidance of FNA biopsy, and potential approach for its implementation.

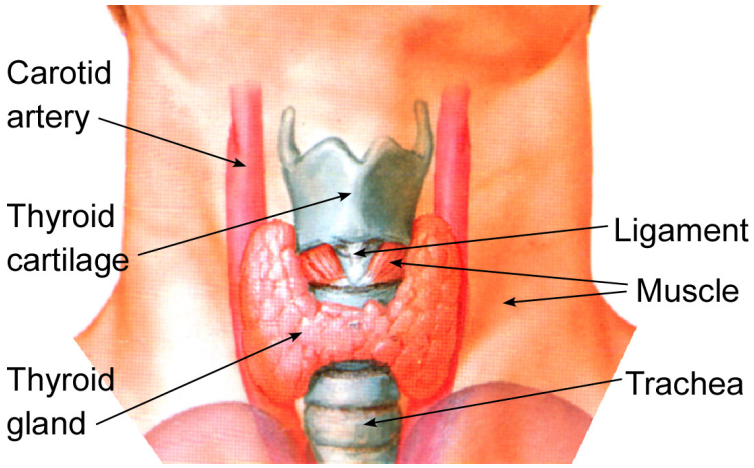

Figure 1.10: Illustration of the human thyroid and surrounding organs.

1.4.1 Background and Motivation

The human thyroid, a butterfly-shaped gland that lies in front of the trachea in the neck, is an important gland for making hormones (Figure 1.10) [Net03]. While thyroid cancer results in <1% of cancer deaths and can be easily cured with timely detection, its clinical diagnosis can be very challenging because malignant tumors must be differentiated from benign nodules that exist in more than 20% of the general US population [Pac96]. Since the ultrasound characteristics of benign and malignant nodules are similar, FNA biopsy is usually required to make a final diagnosis. This is typically performed by a trained physician with a fine needle attached to a syringe for extracting cells or other materials from the target nodule in the thyroid. These cell samples are then sent to a cytopathologist, who attempts to make a diagnosis by examining the samples under a microscope as shown in Figure 1.11.

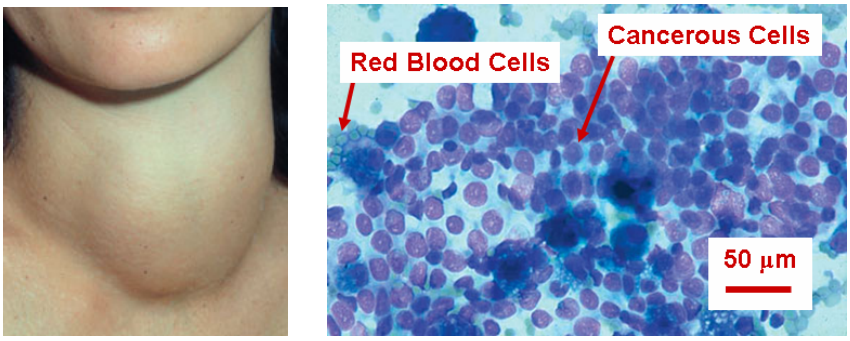

(a) (b)

Figure 1.11: Example of thyroid FNA biopsy. (a) A 38-year-old woman with a 48 mm solid nodule in the left thyroid lobe. (b) FNA cells sample from a papillary thyroid cancer (photos modified from [Mac04]).

Similar to the case of thyroid cancer, FNA biopsy has been applied in the diagnosis of other kinds of neck mass diseases such as lymphoma, salivary gland neoplasia, lipoma, *etc.* [Joh08]. As it is considered a minimally-invasive, cost-effective, and minor surgical procedure compared with other open surgical biopsy techniques, it has also been extensively used for diagnosis of breast, lung, bone, kidney, and liver diseases [Ang02].

However, the FNA biopsy procedure can be challenging for the healthcare professional that is performing it, because of the precision required in manually acquiring the desired sample from the target volumes with a thin needle, especially when the target is small and/or deeply buried under the skin. The needle used is usually 20-27 gauge, with an outer diameter <1mm. This is in order to obtain precise samples from the correct place, to minimize damage in the path of the needle, and to avoid collateral damage to surrounding features, such as the carotid artery in the case of a neck-mass biopsy (Figure 1.10). Using a thin needle is also critical to reduce the risk of tumor seeding along the needle tract [Ang02] that can change a potentially treatable localized disease into metastatic disease and directly reduce the effectiveness of locoregional therapies.

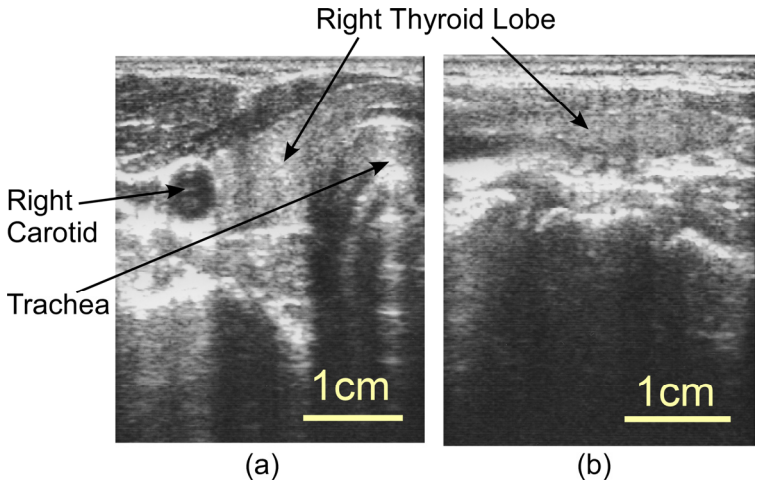

Figure 1.12: Medical ultrasound images of human thyroid used for guiding FNA biopsy. (a) Longitudinal view. (b) Transverse view. Note the scale bar for 1 cm length. The biopsy needle tip, the size of which is about 1 mm or less, will show up in the image as a small white dot, requiring abundant experience from a specially trained physician for operation.

To guide the positioning of the needle during FNA biopsy, conventional ultrasound imaging is performed in real time, especially for those targets that are difficult to palpate or contain complicated solid and cystic areas in the case of thyroid FNA. Physicians hold the ultrasound probe with one hand and insert the needle into the target region with the other hand, while observing the relative position of the needle tip and the thyroid nodule on the ultrasound screen. Sample ultrasound images for thyroid FNA guidance are shown in Figure 1.12, indicating the complexity of the operation. X-ray imaging or computerized tomography (CT) is also frequently required in FNA biopsies of other organs. These current guiding techniques add significant operational complexity (especially in overweight patients), requiring special training and equipment that is not widely available, yet are not always effective in providing the necessary precision. For example, at least 2-5% of thyroid FNA biopsies are read as non-diagnostic because of improper sampling [Gha93, Tak94]. A biopsy needle with integrated sensors that can

detect different tissue planes according to variations of characteristics such as density (*e.g.*, solid *vs.* cystic) and other complementary tissue properties can provide effective guidance to physicians, making this procedure not only more accurate, but more widely accessible.

1.4.2 Tissue Contrast Detection Approaches

The contrast of different tissue planes can be defined in terms of various properties of tissue. Mechanical properties can include density and elasticity, *etc.*; chemical properties include abnormal pH value and ionic composition in the diseased tissue or tumor region; electrical properties can be resistance, *etc.*; and thermal properties include temperature and thermal conductivity. While all of these are useful information about the target tissue, the mechanical properties, especially density related properties, are of particular interest to physicians for guidance of the procedure. This is not only because density changes occur in almost all abnormal tissue to be diagnosed, but also because they closely match those properties detected by medical ultrasound or X-ray imaging. By providing density related information in a way that is more current, local, precise, and immediate than these imaging techniques, a novel biopsy needle that has integrated tissue contrast detection capability can provide much clearer guidance to physicians.

In research or clinical applications, several measurement approaches for the mechanical properties of living tissue have been demonstrated. These approaches either measure density and elasticity separately, or measure them together in a form such as acoustic impedance. A most widely used approach to evaluating living tissue properties

is based on the processing of conventional medical imaging data. For example, computed tomography (CT) or other X-ray based imaging data that are related to sample density have been effectively used to detect tissue density deviation as low as 4 mg/cm^3 [Mom96], or absolute density with 0.1% precision [She02]. Another technique uses magnetic resonance imaging (MRI) phase contrast to measure tissue elasticity by propagating a transverse wave in the tissue [Gre97]. However, large and sophisticated equipment as well as complicated data processing are required for the application of these imaging techniques. This is because there is great complexity involved to generate and process radiation in the case of X-ray and CT, or in the case of MRI to maintain a strong magnetic field and obtain images as a function of proton spin density and relaxation times [Dow98]. This makes it obvious that they are not appropriate for *in vivo* local tissue property measurement.

Ultrasound based techniques have been extensively used for medical imaging or non-destructive testing (NDT). These techniques usually work in either pulse-echo mode or through-transmission mode. Both modes involve transmission of an ultrasound pulse which is generated with a piezoelectric transducer by converting electrical energy into acoustic vibrations. When this sound pulse travels through the target sample, part of the sound energy is reflected back at a sample interface and is detected by the original transducer in the pulse-echo mode, and the part of sound energy going through the sample interface can be detected by another transducer in the through-transmission mode. As the implementation of a second transducer is not always feasible, pulse-echo mode is exclusively used in some situations such as medical ultrasound imaging. The ratio of reflected sound intensity I_R and transmitted intensity I_T is determined by the different

acoustic impedance of the materials on the two sides of the interface. Acoustic impedance Z_a is given by $Z_a = \rho \cdot c$ where ρ is the density of the material, and c is the sound velocity in the material and is further related to density ρ and bulk elastic modulus K by $c = \frac{1}{\sqrt{\rho \cdot K}}$. By measuring I_R and comparing it with a known reference, the acoustic impedance of the sample can be obtained. However, this technique requires the existence of a tissue interface, and cannot be utilized to measure properties of tissue that is local and close to the source transducer, although this is the most wanted information that can be used to guide the positioning of the biopsy needle tip.

When the ultrasound pulse is generated by a piezoelectric transducer, a sound wave also exists inside the piezoelectric material and is then transmitted into the samples through the interface between the transducer and the sample. When different samples make contact with the interface, the amount of sound energy transmitted into the sample will change, resulting in a change of sound energy remaining in the transducer, or in other words, a change in the vibrating characteristics of the piezoelectric transducer. This change will accordingly be reflected in the electrical characteristics of the transducer due to piezoelectric coupling. By measuring these characteristics electrically, a measure of the local tissue properties can be obtained. The piezoelectric transducer has the potential to be miniaturized using MEMS technology, and this approach is of the most interest for the FNA biopsy guidance application.

Piezoelectric materials such as piezoceramics (PZT, *etc.*), polymers (PVDF, *etc.*), quartz, and ZnO, have been widely used for sensing and actuating [Gau02, Su01, Uch97]. As a category of piezoceramics, PZT series is of particular interest for many applications due to its high piezoelectric coefficients and good electro-mechanical coupling. For

example, a tactile biosensor has been developed using a resonating PZT element, which measures the firmness of tissue that is in contact with the element by detecting the resonance frequency shift through vibration pickup. This frequency shift is determined by the acoustic impedance of the tissue, and in this case directly correlated with its firmness [Axi08, Oma92]. An electrical impedance measurement that benefits from the piezoelectric coupling is also widely used [Ayr98, Cha03, Tse05]. In another example, when the mechanical boundary condition of a PZT-horn assembly in a geological probe changes by touching different types of rocks, the resonance frequency and the electrical impedance of the assembly change accordingly [Cha03].

Although extensively used in macroscale applications, the limitation of conventional micromachining techniques has allowed PZT material to be used for MEMS applications, mostly in the form of films with thicknesses of no more than several microns, which has resulted in degraded material properties and device performance [Pol96]. With the development of the batch mode μUSM process in this effort, bulk PZT materials with superior properties can be patterned lithographically on the microscale, and are used to fabricate bulk PZT piezoelectric transducers. With the bulk metal processing capability of μEDM, these micro transducers can be integrated onto biopsy needles, providing guidance for physicians.

1.5 Outline

As mentioned earlier, to further expand the material availability for MEMS applications, this research aims to develop the batch mode ultrasonic micromachining process which can achieve transfer of lithographic patterns onto hard, brittle, and non-

conductive materials such as ceramics (including piezoceramics like PZT) and glass. The batch or serial mode μEDM process will be used to prepare the hard metal microtools with desired lithographic or non-lithographic simple patterns.

As a demonstration of expanded material choices including bulk ceramics and hard steels, the capabilities of the developed process and the μEDM are then used to create and integrate piezoelectric tissue contrast sensors on biopsy needles to provide real-time guidance for FNA biopsy. The sensors will be tested and characterized for differentiation of shallow tissue with a depth less than ≈15 mm, which is adequate for thyroid biopsy. To explore the potential expansion of device application to deeper tissue detection, and to simplify sensor readout scheme, a differential implementation of the sensors with CMOS interface circuit will be proposed.

In this dissertation, Chapter 2 describes the development of the batch mode micromachining process called LEEDUS/SEDUS by combining lithography, electroplating, batch mode μEDM, and newly developed batch mode μUSM. The machining details and characteristics are discussed with results on Macor^{TM} ceramic plate, and bulk-PZT spiral-shaped actuators are fabricated as demonstrations. Chapter 3 presents the application of the μEDM and LEEDUS/SEDUS processes to fabricate a piezoelectric tissue contrast sensor for real time guidance of FNA biopsy. Device design, fabrication, and testing results are reported in details. The effort to develop the differential mode sensors with CMOS interface circuits for deep tissue detection is discussed in Chapter 4, and the conclusions and future work are described in Chapter 5.

CHAPTER 2

LEEDUS: Batch Mode Pattern Transfer Process for Ceramics

In this chapter, a fabrication process called LEEDUS [Li04, Li05, Li06] is described. This process utilizes μUSM in batch mode to transfer a mask-defined die-scale pattern from a batch μEDM'ed microtool into a ceramic (including PZT) plate with high resolution and throughput. Microtools made from steel and WC/Co super hard alloy were explored. A derivative process called SEDUS uses serial mode μEDM to make the microtool for rapid prototyping of simple patterns. Section 2.1 gives details of the process flow and the apparatus created for batch mode μUSM. Section 2.2 discusses the results of the process characterization experiments. Octagonal and circular spiral in-plane actuators were fabricated from bulk PZT-5H plate using this process as a demonstration, and are described in Section 2.3. Several operational issues were identified in the initial μUSM apparatus, and modifications in the apparatus were carried out and discussed in Section 2.4 for improvement of the functionality and controlling of the process. Finally, Section 2.5 is a discussion section on advantages and current scaling limit issues of the batch mode μUSM process.

2.1 Process Description and Implementation

The LEEDUS process flow is illustrated in Figure 2.1 as option 1. An electroplated metal structure with the desired, lithographically-defined pattern is used as

the electrode for batch mode µEDM to transfer the pattern onto a hard-metal microtool. The microtool is then mounted on a self-built batch mode µUSM setup to transfer the pattern onto the ceramic workpiece. The process is named LEEDUS as it combines Lithography, Electroplating, batch mode micro-Electro-Discharge machining, and batch mode micro UltraSonic machining. In a related process, the pattern on the hard-metal microtool is directly defined by using the Serial mode µEDM. This derivative process is called SEDUS (serial electro-discharge and ultrasonic machining), and can be used for non-lithographic rapid prototyping of simple patterns.

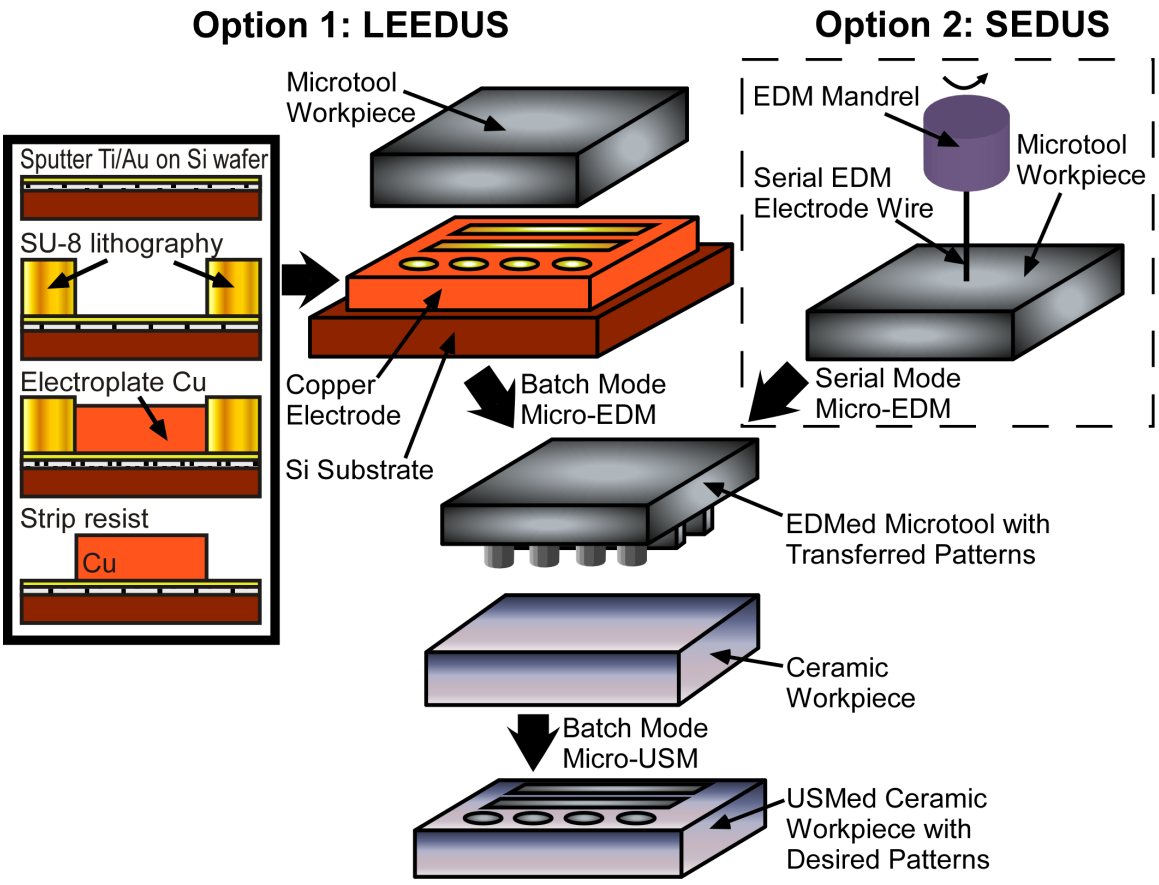

Figure 2.1: LEEDUS process utilizes lithography, electroplating, and batch mode µEDM to fabricate a microtool with a pattern which is defined by a mask, and then uses batch mode µUSM to transfer the pattern onto ceramic or other brittle materials. Non-lithographic rapid-prototyping can also be performed for simple patterns using option 2 (SEDUS).

2.1.1 Electrode Preparation for Batch Mode μEDM

In the LEEDUS process, the first step is to lithographically define the desired patterns to be transferred onto ceramics, and then the exposed and developed photoresist, which should carry a negative version of the desired patterns, is used as electroplating mold to form a metal structure with the desired pattern. Copper is used as the structural metal material because it can be easily electroplated and can provide good electrical and thermal conductivity, thus relatively low cutting electrode wear during batch mode μEDM. The copper structure is electroplated into an SU-8 mold on a silicon substrate using a lithographically defined image of the final desired pattern. The lithography process to make the high-aspect-ratio SU-8 mold is referred to as UV-LIGA process, and has been used to make copper structures with a feature size of 3 μm and height of 29 μm, giving an aspect ratio slightly less than 10:1 [Ude06]. An alternative for this step is the X-ray LIGA process, which has the capability of mass production of ultra-fine patterned high-aspect-ratio microstructures with very smooth side-wall surfaces [Guc98], and may be more appropriate to fabricate the copper pattern when an aspect ratio greater than 10:1 is required.

2.1.2 Fabrication of μUSM Microtool

The copper pattern on the silicon die is then used as an electrode to perform batch mode μEDM on a hard-metal microtool workpiece, transferring a corresponding negative pattern onto it at die scale. The setup used for batch mode μEDM, as shown in Figure 2.2, is based on the Panasonic μEDM machine MG-ED72W. A new workpiece mounting approach has been developed in order to hold die-scale workpieces on the Z-

axis stage of the machine. A metal tube with 5 mm diameter is used to replace the mandrel shown in Figure 1.2 and to hold the workpiece at one end. The metal tube is cut into the appropriate length and the end for workpiece attachment is flattened by the WEDG function. This WEDG step also ensures parallelism between the workpiece mounted at the tube end and the electrode substrate on the worktable. During the machining, electric discharges are fired between the electrode and the workpiece when they are both immersed in dielectric oil. This wears away both of them, but the workpiece is eroded much faster. By using lithographically-defined electrodes, the batch mode µEDM can provide high throughput, high density and high uniformity over the whole array on any conductive materials. More details on the batch mode µEDM process can be found in [Tak00, Tak02].

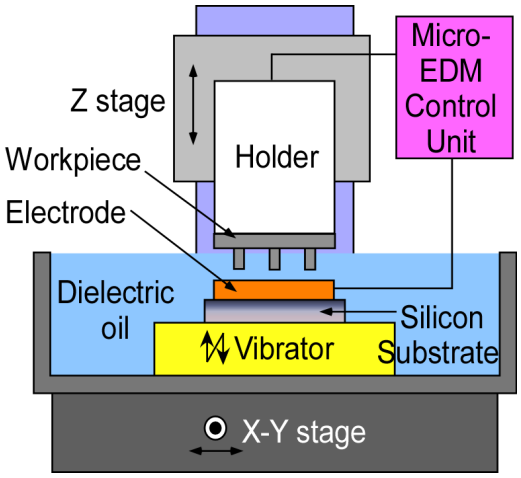

Figure 2.2: Modified µEDM setup used for batch mode fabrication of microtools.

Non-lithographic rapid-prototyping can also be performed for simple patterns by a similar process called SEDUS, in which the original serial µEDM function of the MG-ED72W machine is used to directly define the pattern on the microtool. This is done by running a QBASIC program on a computer to control the "writing" movement of the

rotating EDM electrode wire on the microtool workpiece. Due to the limitation of the μEDM machine, the patterns that can be fabricated by serial mode μEDM are usually restricted to holes and slots in X and Y directions. Slots in an angled direction from X or Y require special treatment, such as rotation of the workpiece before cutting the angled slots. Any other patterns with curved features require segmented cutting, using series of holes or short-slot cuttings to form the outline of the patterns. In this case, batch mode μEDM is clearly a more appropriate option using lithographically-defined and electroplated electrode, thus leading to the LEEDUS process.

2.1.3 Batch Mode μUSM of Ceramics Using Customized UM-Built Apparatus

In the last step of LEEDUS/SEDUS process, the microtool with negative patterns is mounted on an ultrasonic machining setup created for batch mode μUSM of a ceramic workpiece, thus having the desired positive pattern transferred onto it. As discussed in Section 1.3, a USM machine has several major components, including ultrasonic generator for controlled vibration generation, machining feeding mechanism such as a motorized stage, process monitoring mechanism such as a load/force sensor, and slurry supply subsystem. The implementation of each component in the UM-built machining apparatus is described in the following subsections, and then the characteristics of the complete machine system are summarized.

2.1.3.1 Ultrasonic Generator

The ultrasonic generator is the core component of a USM machine. It takes the 50/60 Hz electrical power and converts it into an ultrasonic electric energy at a certain frequency such as 20 or 40 kHz. This electric energy is then fed into a piezoelectric

transducer to transform the energy into ultrasonic mechanical vibrations. With the help from a horn or acoustic-lens assembly that is attached to the transducer, the ultrasonic vibrations can be focused to get maximum energy in the direction of the cutting depth at the tip of the cutting tool.

Several options for the ultrasonic generator were inspected. Conventional USM machines, such as Model AP-1000 from Sonic-Mill® (Figure 1.8), provide a complete solution for USM processing. However, as discussed in Section 1.3.2, they have limited capability for micromachining due to the difficulty in tool fabrication and mounting. The process control and stage feeding mechanism packaged with the generator are usually not compatible with the high-resolution and low-machining-load requirements of microscale USM. Moreover, the ultrasonic-vibration amplitude and thus the ultrasonic energy delivered to the tool tip are usually not easily adjustable to accommodate the need of different materials and microscale feature sizes.

Figure 2.3: Model 170 Ultrasonic Disk Cutter from Fischione Instruments, Inc [Fis09].

Another option was ultrasonic disk cutter used to cut transmission electron microscopy (TEM) specimens from hard, brittle materials without mechanical or thermal damage. This tool is basically a subcategory of USM machines, and usually operates at a

fixed frequency between 26 kHz and 36 kHz to cut TEM specimens in disk or rectangular shape with feature sizes ranging between 1 – 10 mm. Common suppliers include Gatan, South Bay Technology, SPI Supplies, and Fischione Instruments, *etc*. One of such tools from Fischione Instruments is shown in Figure 2.3. These tools also have fixed, and relatively large vibration amplitude that is not compatible with the need of microscale machining, and are difficult to customize and integrate with a motorized stage for machining feeding.

Figure 2.4: CV52/H520 ultrasonic handheld welder from Ultra Sonic Seal. The picture is modified from [Ult08].

The third option is an ultrasonic handheld welder that is used for ultrasonic assembly of plastics or plastic and metal. These tools apply ultrasonic vibrations to thermoplastics, and frictional heat is generated at the plastic/plastic or plastic/metal interface. This frictional heat melts the plastic, allowing the two surfaces to fuse together. Although developed for different applications, the ultrasonic welders, such as the one shown in Figure 2.4, use the same energy conversion and delivery approaches as those of an ultrasonic generator for USM. They also provide the additional benefit of

adjustable vibration amplitude, which enables the capability of using different ultrasonic energy for different materials and feature sizes during microscale USM. The ultrasonic handheld welder shown in Figure 2.4 was selected as the ultrasonic generator for the batch mode μUSM setup, and its specifications are listed in Table 2.1.

Table 2.1: Specifications of CV52/H520 Ultrasonic Handheld Welder used as the ultrasonic generator for the batch mode μUSM setup [Son00].

Hand Gun Model	CV52
Power Supply Model	H520
Ultrasonic Frequency	20 kHz
Full Scale Vibration Amplitude	≈80 μm, or 160 μm peak to peak
Minimum Adjustable Amplitude	20% of full scale, or ≈15 μm (digital control)
Maximum Power	500 W
Horn Tip Diameter	12.7 mm replaceable

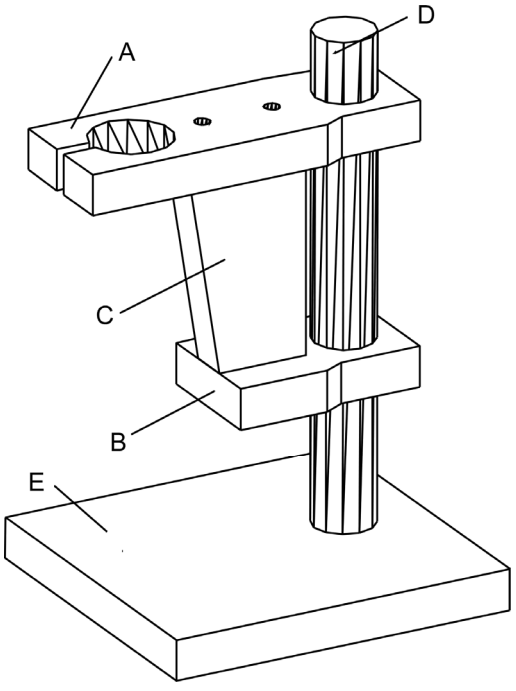

Figure 2.5: Scaled (proportional) drawing of the machining platform designed and machined for batch mode μUSM. Holder (A) is fitted for the selected ultrasonic generator. Brackets B and C are added for enhanced stability and strength of the setup. The highly-damped post (D) is mounted on an optical breadboard (E). The latter has threaded mounting holes for installation of motorized stages.

The replaceable horn tip has a diameter of 12.7 mm, and its flat tip surface can be used to attach the μEDM'ed microtools with epoxy such as the titanium filled Araldite 2044. Special treatment such as overnight baking at temperature around 60-80°C is used to enhance the adhesion strength of the epoxy so that it can sustain the strong ultrasonic vibration applied during machining.

A machining platform is designed and machined for the batch mode μUSM as shown in Figure 2.5. It has a holder *A* fitted for the selected ultrasonic generator. The extra brackets *B* and *C* are added to enhance the stability and strength of the setup. The post *D* is a highly damped post (Part Number DP14 from Thorlabs, Inc.) which can provides fast ring-down and damping of the dynamic vibrations generated during machining. The bench *E* is an optical breadboard with threaded mounting holes for installation of machine stages which are discussed in the next section.

2.1.3.2 Motorized Stage

The stages of the machining apparatus need to provide motorized feeding motion in Z direction, and also manual or motorized motion in X and Y directions for tool-workpiece alignment.

Figure 2.6: Thorlabs MT3/M 3-axis translation stage with micrometer controls.

The Thorlabs 3-axis translation stage (Figure 2.6) is selected to provide the 3-axis motion needed in the process [Tho03]. This stage uses hardened-steel linear bearings to get precision motion and long life, and can provide a travel range of 12.7 mm in each axis. The vertical loading capacity of the stage is 9 kg, well exceeding the requirement of the process. Using an L-shaped bracket mounted on the Z axis module of the stage, a horizontal platform can be formed to support the sensor and workpiece table.

Figure 2.7: KT-LA28 stepper-motor linear actuator from Zaber Technologies, Inc.

The selected stage comes with micrometers for manual motion control. The Z-axis micrometer is replaced by a stepper-motor linear actuator, model KT-LA28 from Zaber Technologies, Inc (Figure 2.7). This actuator has a compact size, a resolution of 0.1 μm, a backlash of 2 μm with anti-backlash and anti-sticktion features, RS-232 communication port as well as built-in manual control knob [Zab03]. The actuator can move at a speed in the range of 0.1 μm/sec - 4 mm/sec, has a maximum force of 22 N, and a continuous force of 15 N, all meeting the requirements of the target process.

2.1.3.3 Force Sensor for Zero-Position Calibration and Machining Load Measurement

A force/load sensor is required in the batch mode μUSM setup for two purposes. First, at the beginning of the process, a zero-position calibration procedure is necessary to obtain the relative distance between the tip of the microtool and the workpiece surface.

This is done by moving the workpiece towards the tooltip while monitoring the reading of the force sensor underneath the workpiece. Once the two touch each other, the force sensor detects the generated force. The process control program reads this force, and if it exceeds a certain threshold value which is well below the fracture force of the workpiece, the stage motion is immediately stopped and the current position of the stage is stored in memory as the zero position of the process. The second function of the force sensor is to monitor the machining load during cutting, and the readings can be used to analyze the process and/or used for feedback control of the stage feeding motion.

Figure 2.8: ICP® general purpose quartz dynamic force sensor from PCB Piezotronics, Inc.

The commonly-used load cell sensors based on strain gauges cannot detect the rapidly-changing forces generated during machining due to the dynamic nature of the ultrasonic vibrations. Piezoelectric load cells, such as quartz dynamic force sensors from PCB Piezotronics, Inc., are more appropriate in this regard. The selected sensor is ICP® Model 208C01 quartz force sensor. It has a force measurement range of 45 N, a sensitivity of 110 mV/N, a resolution of 0.45 mN rms, and a frequency range of 0.01 Hz – 36 kHz [Pcb03]. All sensor specifications satisfy the process requirements. A sensor signal conditioner ICP® Model 484B06 is used to power the sensor and condition the sensor output for readout. The voltage output from the signal conditioner is read into the

process control computer through the National Instrument® (NI) PCI-6251 data acquisition (DAQ) card for further processing and process control.

2.1.3.4 Process Control Software

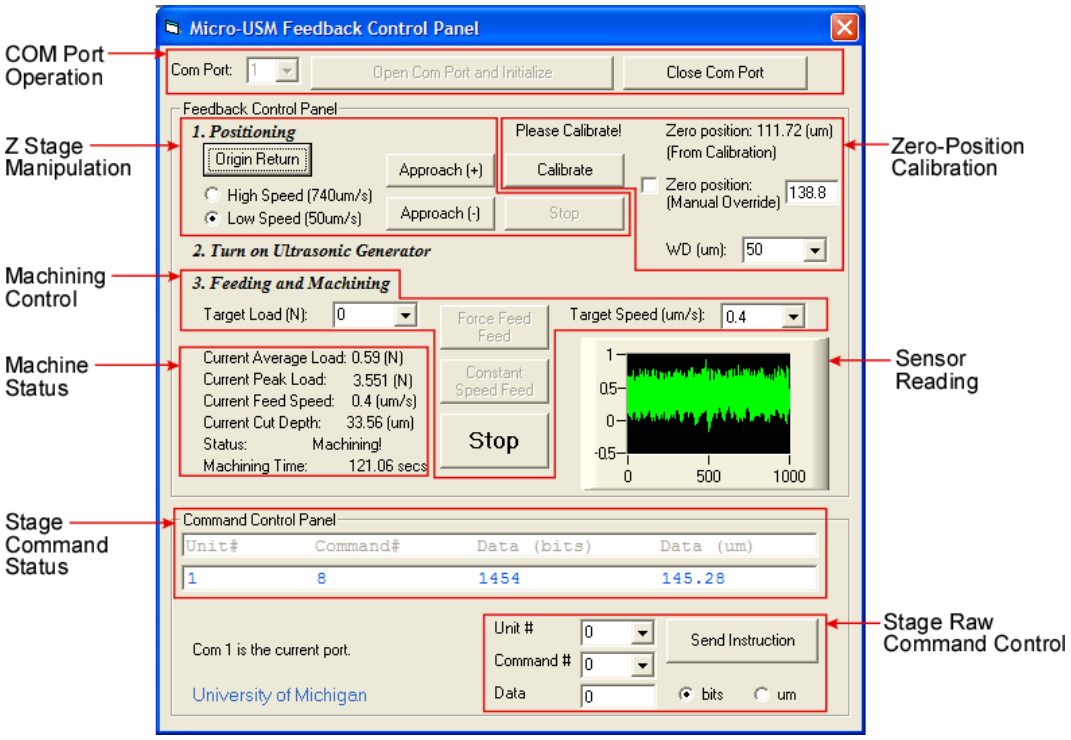

Figure 2.9: Process control software developed for batch mode µUSM, showing status of machining in the constant feeding speed mode.

The control of the motorized stage and the reading of the force sensor are conducted by the process control software, which also provides a user interface (Figure 2.9) for the operation of the machining setup and report of machining status and characteristics data. Codes for feedback control of the stage based on sensor data are also implemented. The software was developed for Microsoft® Windows XP or higher using Microsoft® Visual Basic 6.0 with Service Pack 6. The operation of the NI PCI-6251 DAQ card requires a software programming interface package, NI-DAQmx 8.3 or higher. To display the sensor-reading data using an ActiveX chart control, NI Measurement

Studio for Visual Studio 6 is required. The operational flow chart of the process control software is shown in Figure 2.10. The program scripts are listed in Appendix A.1.

As a side note, the process control program was initially developed using NI Labview programming language. However, Labview could not provide enough capability and speed for real-time processing of the large amount of sensor data for feedback control. Therefore, the program was ported to Visual Basic 6.0.

2.1.3.5 Apparatus Integration

As a summary, the schematic diagram for the integrated apparatus built for batch mode μUSM is shown in Figure 2.11. A photo of the actual setup is shown in Figure 2.12. This apparatus has a manually-controlled X-Y stage for relative positioning of the microtool and the ceramic workpiece. The Z stage is motorized and computer-controllable. A quartz dynamic force sensor is implemented on the Z stage to monitor the machining load and to provide a feedback signal when necessary, so that the apparatus can work in either a constant-machining-load mode or a constant-feeding-speed mode. The vibration amplitude of the ultrasonic transducer is adjustable down to 20% of the full scale output. The μEDM'ed microtool is mounted by epoxy at the tip of the horn where the vibration energy generated by the ultrasonic transducer is maximized in the vertical direction. Abrasive slurry which consists of water and fine abrasive powders is supplied between the tip of the microtool and a ceramic workpiece. The vibrating tip of the microtool is fed into the ceramic workpiece. On its downward stroke the ultrasonic motion of the microtool imparts velocity to the abrasive particles. These particles, in turn, are responsible for the erosion of the workpiece, thus creating the desired cavities in the shape of the microtool.

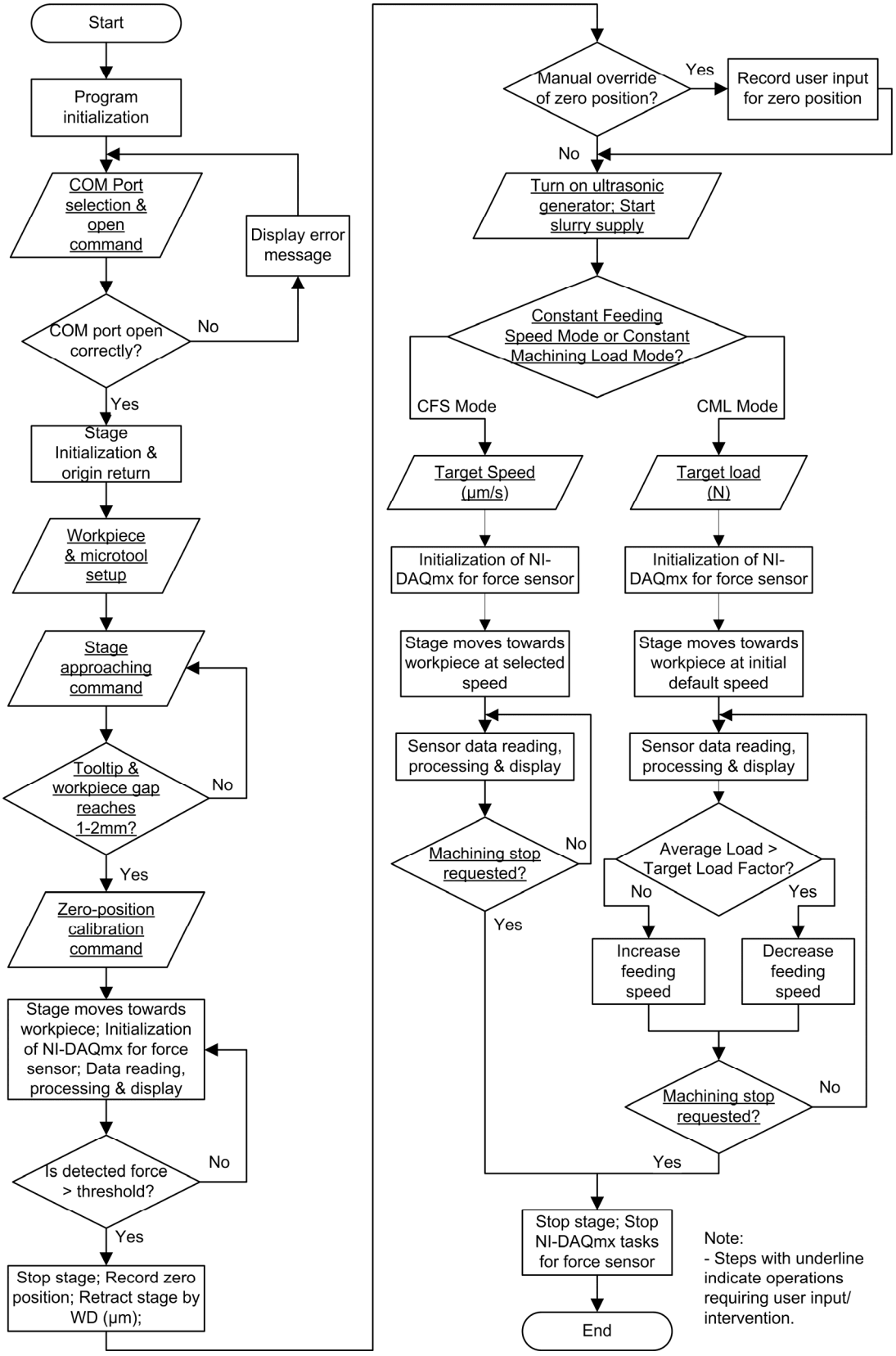

Figure 2.10: Operational flow chart of the control program for the batch μUSM setup.

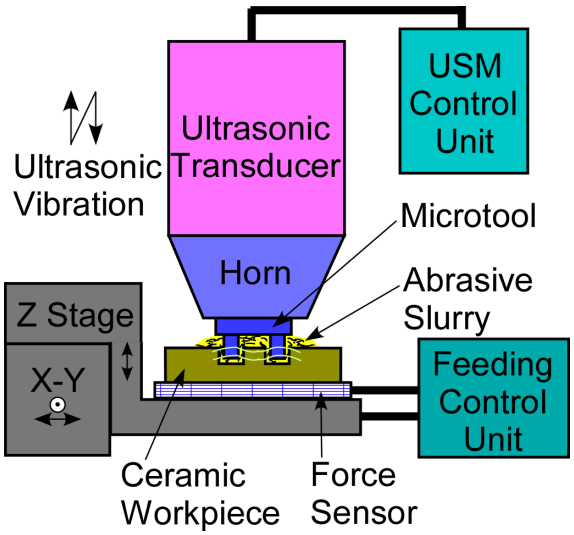

Figure 2.11: Schematic of the basic µUSM setup created for batch mode pattern transfer on ceramic workpiece.

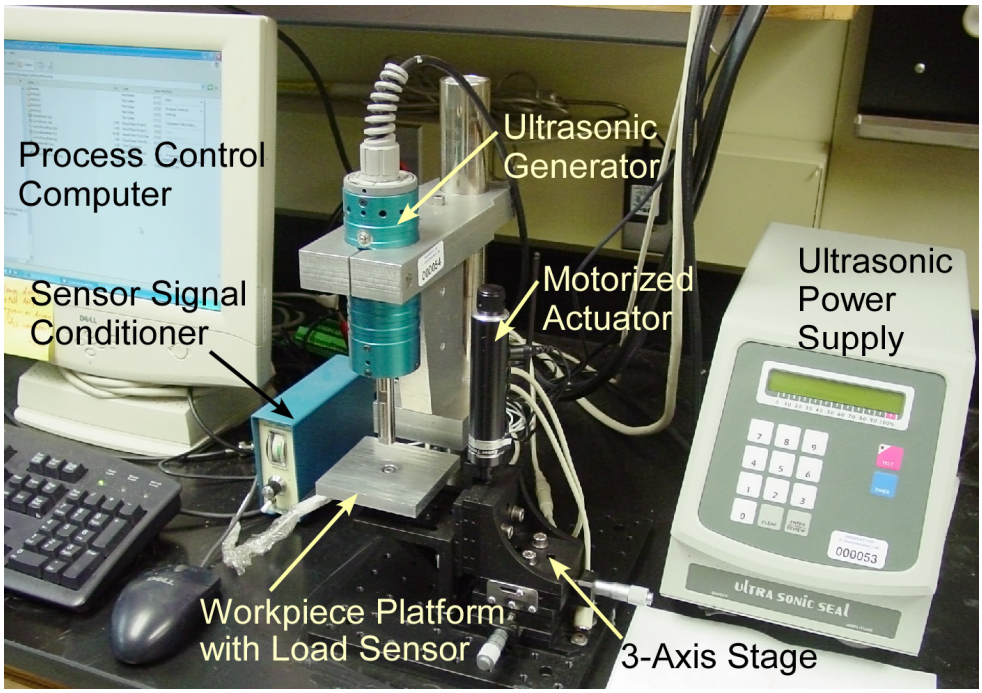

Figure 2.12: Customized UM-built machining apparatus for batch mode µUSM with computer-based process control.

2.2 Process Characterization

2.2.1 Electroplated Electrode and Batch Mode µEDM Results

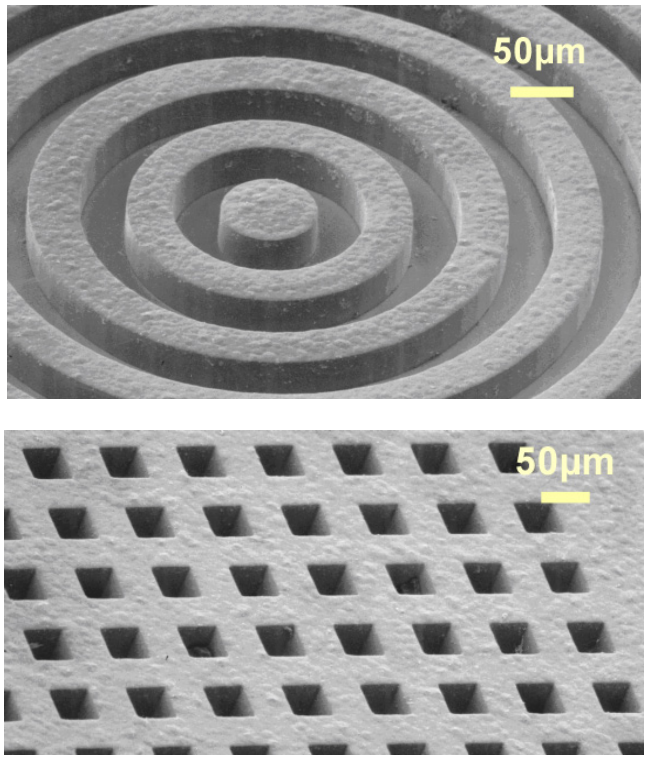

Figure 2.13: SEM images of two of the patterns on electroplated copper die (both with 40 µm lateral feature size).

A set of experiments were performed to characterize the process. A 4.5 mm × 4.5 mm silicon die with 50 µm-high electroplated copper structures on top of a Ti/Au adhesion layer was used as the electrode for batch mode µEDM of stainless steel or WC/Co microtools. The EDM discharge voltage was 80 V and the discharge control capacitance was 100 pF. Figure 2.13 shows SEM images of two of the demonstrative copper patterns, both of which have features with lateral dimension of 40 µm. Figure 2.14 shows µEDM'ed microtools made with stainless steel and WC/Co. The grainy nature of WC/Co led to a rougher finish. The 40 µm features in the copper pattern were

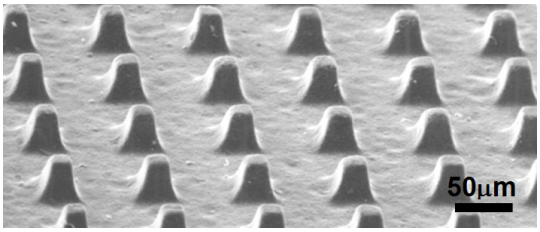

(a)

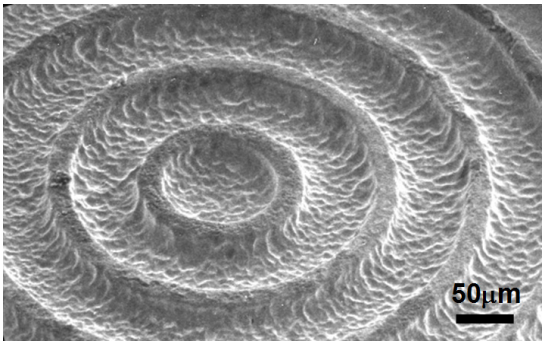

(b)

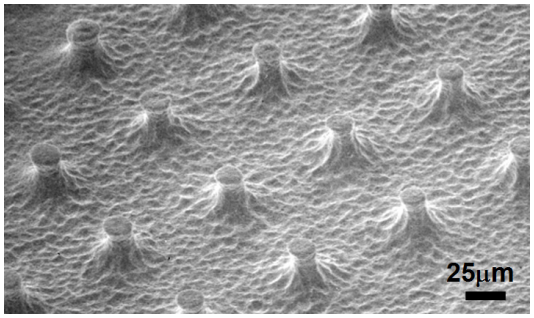

(c)

Figure 2.14: SEM images of batch mode μEDM'ed microtools: (a) stainless steel microtool pattern of 35 μm height; (b) and (c) WC/Co microtool pattern of 32 μm height.

Table 2.2: Material properties for ultra-high temperature glass-mica (Macor^{TM}) ceramic plate used in experiments (quoted from McMaster Carr. Item no. 8489K231).

Temperature Range	-185˚C to 800˚C
Flexural Strength	94 MPa
Compressive Strength	345 MPa
Dielectric Strength	3.94×10^{7} volt/m
Thermal Conductivity	1.46 W/m·K
Density	2.5×10^{3} Kg/m^{3}
Others	Nonporous, opaque white

reduced to 24 μm on the microtool due to the μEDM discharge gap which was measured as about 8 μm. This gap is generally determined by the discharge energy and is stable under fixed discharge conditions when the secondary EDM discharge caused by machining debris is minimized. The dimension of the electrode patterns should be designed while keeping this gap in mind.

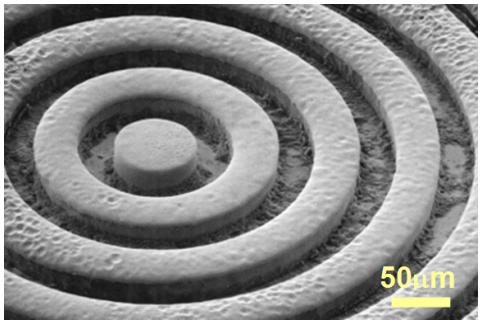

Figure 2.15: SEM image of a copper electrode used after μEDM of the steel microtool, tool wear ratio ≈29%.

Figure 2.15 shows the copper electrode after μEDM of the stainless steel microtool. A tool wear ratio of ≈29% was measured, which corresponds to ≈10 μm loss of copper tool height for making a 35 μm-high microtool. This tool wear can be compensated by increasing the SU-8 mold height or using the LIGA process to get a higher copper electrode, or can be reduced using parallel-discharge mode μEDM with a partitioned die area as described in [Tak02]. The machining debris, which is prone to get clogged in the array when the die area is large, also contributes to the heavy tool wear. An approach that facilitates debris removal during machining would be much more desirable to minimize this tool wear.

2.2.2 Batch Mode μUSM Results

Both the stainless steel and the WC/Co microtools were then used for batch mode μUSM on a glass-mica (Macor^{TM}) ceramic plate whose properties are listed in Table 2.2. The ultrasonic vibration utilized for the demonstration had a frequency of 20 KHz and amplitude of 15 μm. The abrasive was WC powder in water with particle size of 0.5 - 1 μm and volume ratio of 1:3 to 1:4 (WC:H_2O). Results are shown in Figure 2.16 and Figure 2.17. A minimum feature size of 25 μm on the ceramic plate was achieved using a stainless steel microtool with a machining depth of 34 μm. The overall process performance achieved so far is summarized in Table 2.3.

The average machining rate observed in this demonstration with a stainless steel microtool was 18 μm/min, with ≈5 mm^2 cutting surface area and ≈0.5 N machining load. For USM, the machining rate usually increases with any of the following: the brittle fracture hardness of the workpiece material, mean radius of abrasive grains, working load applied in the cutting zone, amplitude of vibration, and frequency of oscillation [Kom93]. Figure 2.18 shows the change of machining rate with increasing amplitude of ultrasonic vibration. A linear relationship was assumed for the dashed trend line. Although larger amplitude results in faster machining speed, the surface finish becomes rougher and chips can occur at feature edges.

The wear ratio of μUSM microtools usually varies with different tool materials, or changes with machining parameters such as machining load, abrasive powder size, *etc*. In order to compare microtool materials, the stainless steel and WC/Co microtools were tested for μUSM under the same machining parameters. Figure 2.19(a) and (b) show post-use stainless steel and WC/Co microtools, respectively. The stainless steel

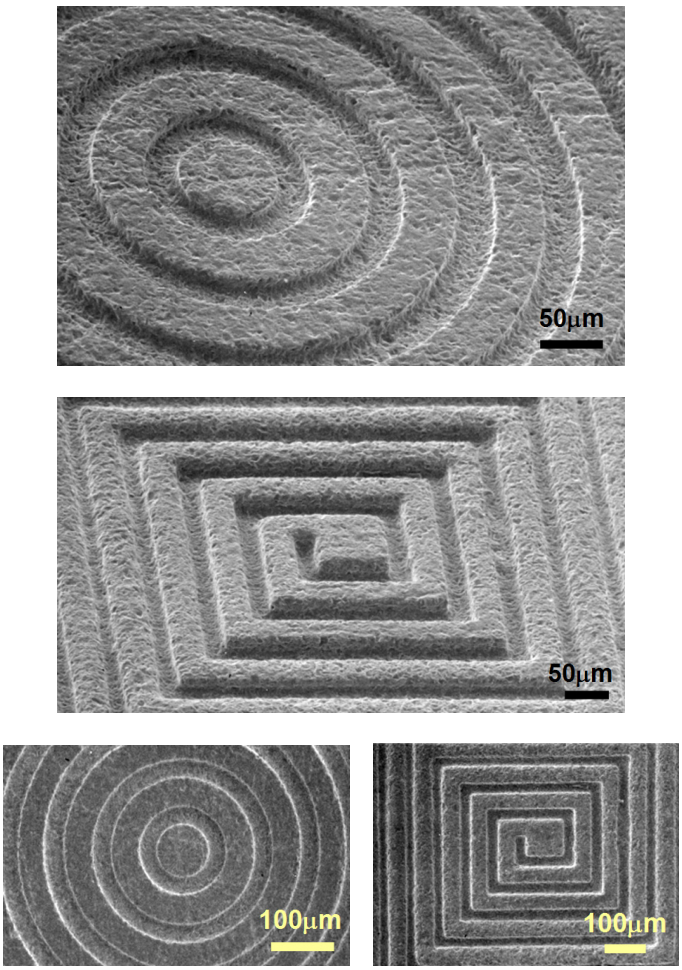

Figure 2.16: SEM images of two of the patterns transferred onto ceramic surface in perspective view showing depth, and corresponding top-down view showing fidelity of the features.

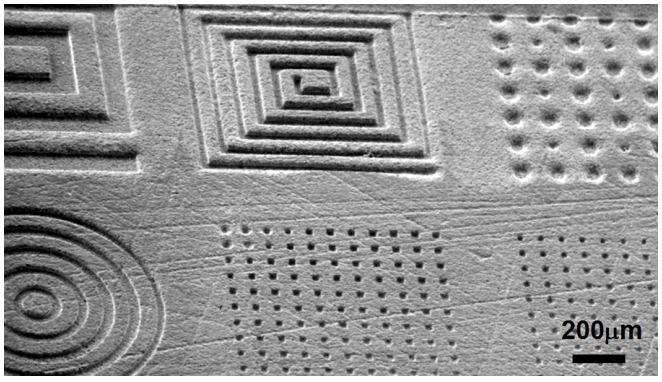

Figure 2.17: SEM image of patterns on the Macor ceramic plate transferred from the die-scale stainless steel microtool. The scouring on the surface was present in the unprocessed workpiece. It is notable that the pattern transfer does not remove it.

Table 2.3: Machining parameters for batch mode μUSM of Macor ceramic plate.

Transducer frequency	20 KHz
Vibration amplitude	15 μm
Abrasive powders	WC (0.5 to 1 μm average diameter)
Batch machining die area	4.5 mm × 4.5 mm
Avg. machining rate	>18 μm/min.
Machining load	≈0.5 N
Minimum feature size	25 μm
Cutting depth	34 μm
Surface roughness (R_a)	≈0.4 μm (0.55 μm for the raw material)
Tool wear ratio (height)	< 6% (Stainless steel)

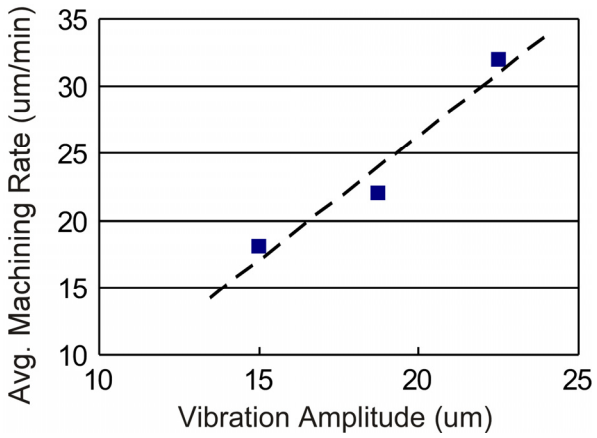

Figure 2.18: Variation of machining rate as the amplitude of ultrasonic vibration is increased. Other machining parameters remain the same as those in the characterizing test.

microtool showed a wear ratio of <6%, taking as the ratio of tool height worn (≈2 μm) *vs.* cutting depth (34 μm), while the WC/Co microtool showed a wear ratio that was ≈4× higher, likely due to its brittleness, which is a preferred characteristic for USM. This suggests that stainless steel is a better choice for this application, opposing the usual preference for WC/Co as a machining tool material. The 6% wear ratio of the stainless steel microtool was the worst case measurement obtained from the structures with 25 μm feature size. For larger feature sizes and smaller die area, the wear ratio reduced accordingly. The lateral feature dimensions of the structures on the microtool did not

have noticeable change after machining, while the top edges of the structures became slightly rounded as shown in Figure 2.19(a).

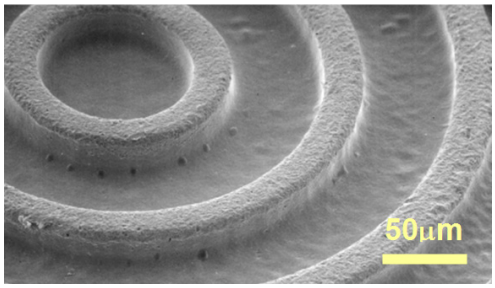

(a)

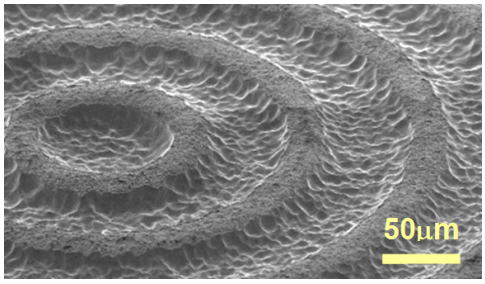

(b)

Figure 2.19: Post-use SEM images of: (a) stainless steel microtool, after µUSM of the ceramic part, tool wear ratio <6%; (b) WC/Co microtool, after µUSM of the ceramic part, tool wear ratio >25%.

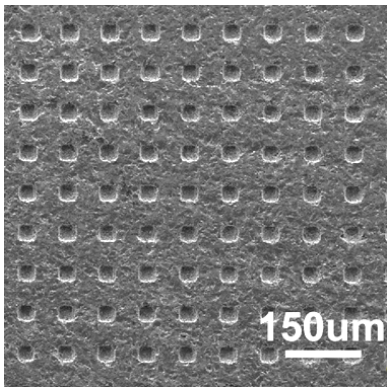

(a)

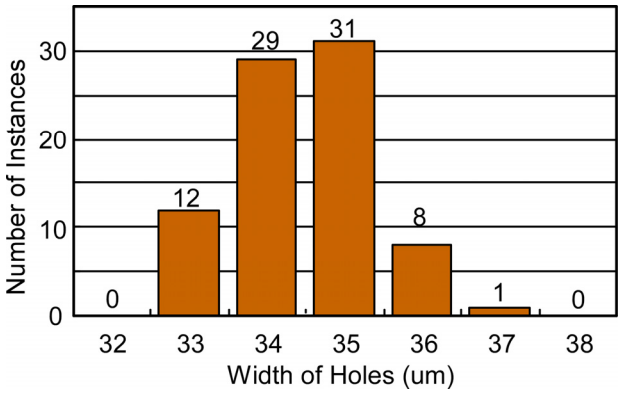

(b)

Figure 2.20: (a) SEM image of an 81-hole array of 35 µm-width holes transferred from WC/Co microtool. (b) Size variation in the array. Mean hole width: 34.8 µm. Standard deviation: 0.88 µm.

Figure 2.20(b) shows the hole-width distribution for the 9×9 array of 35 μm features in Figure 2.20(a). The average hole width is 34.8 μm. The standard deviation of holes size is 0.88 μm, providing acceptable size uniformity for many applications. Note that the width was measured at the top surface of the machined holes, and defects in the microtool resulted in a few shallower holes and holes with reduced bottom dimensions.

2.3 Demonstrative Device Fabrication and Testing

2.3.1 Device Concept

Piezoelectric ceramics such as lead zirconate titanate (PZT) are nowadays widely used for sensing or actuating applications. For PZT materials, both the piezoelectric longitudinal d_{33} and transverse d_{31} coefficients are often used. When the longitudinal coefficient d_{33} is applied directly for actuating ($\Delta h = d_{33} \cdot V$), a high voltage (>1 KV) is required to generate a reasonable displacement (*e.g.* 1 μm) due to the relatively low d_{33} value of the materials. Although d_{31} is even less than 50% of d_{33}, the transverse displacement ($\Delta h = L/W \cdot d_{31} \cdot V$) can be much higher by a factor of length-to-width (L/W) aspect ratio than the longitudinal displacement of a sufficiently long PZT beam actuator, where V is the actuating voltage, and Δh is the resulting displacement. For example, with a normal d_{31} value of -300 pm/V, a 1 μm displacement can be generated under 50 V actuating voltage if the straight beam actuator has an aspect ratio of >67.

By transforming the straight beam with large aspect ratio into a plane coil with spiral geometry, the total size of the actuator can be significantly reduced. It has been shown in macro-scale that a spiral-shaped PZT actuator of 3 cm diameter with metalized sidewall electrodes can provide in-plane displacement at the tip of the spiral which is 5 -

12× larger than that of an equivalent straight beam actuator with the same effective length of 26 cm [Moh99, Moh00]. Some other spiral PZT actuators are described in [Kol84, Lav74]. All these results were achieved exclusively using additive fabrication processes, because unlike ultrasonic machining, the traditional machine cutting process would result in microcracks and structural damage on the brittle PZT material. Neither has micromachining result ever been reported on the spiral PZT actuators.

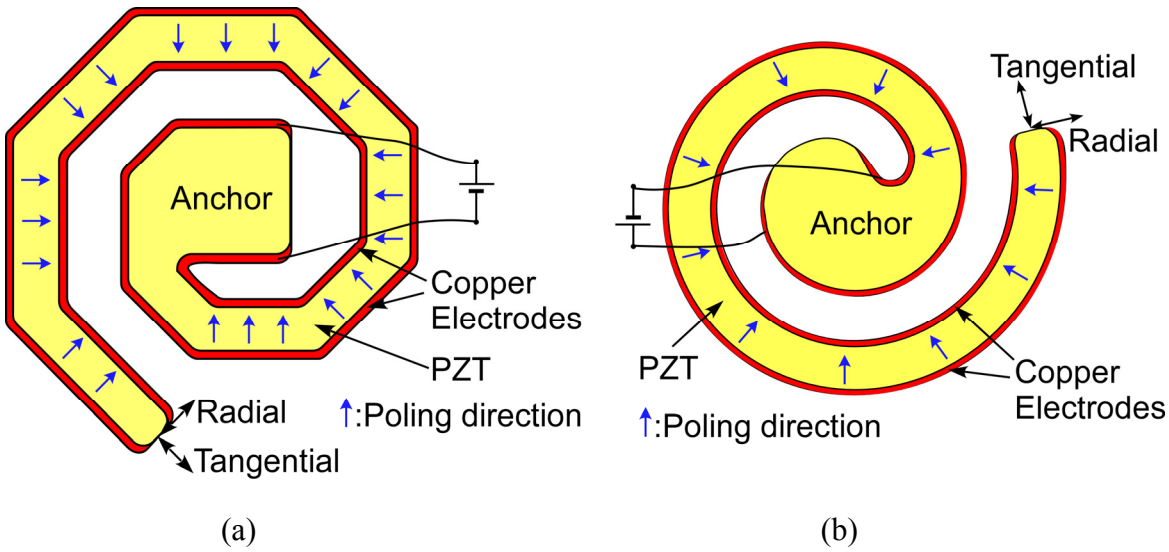

Figure 2.21: Schematics of: (a) octagonal spiral actuator; (b) circular spiral actuator. The short arrows indicate poling direction along the spiral.

2.3.2 Device Fabrication and Description

The spiral-shaped actuators were chosen to demonstrate the practical use of the LEEDUS/SEDUS process. Both octagonal and circular spiral geometries were designed as shown in Figure 2.21. Note that the circular version is only feasible with the LEEDUS process due to the machining limitation of serial mode μEDM in the SEDUS process. As shown in Figure 2.22, the fabrication starts with a bulk PZT-5H plate with excellent material properties for actuating. The PZT plate is bonded to a glass substrate. Either

LEEDUS or SEDUS process is carried out to get the desired pattern on the PZT plate with a target depth, and then Cu/Ti film is sputtered. The copper film on the top surface is removed by lapping, and then the PZT plate is flipped by releasing in acetone and bonding again to a second glass substrate. Lapping is carried out again to remove the extra thickness of the PZT plate, and epoxy is applied at the center anchor area to bond the structure to a third glass substrate. Finally the device is released and *in-situ* poling is carried out.

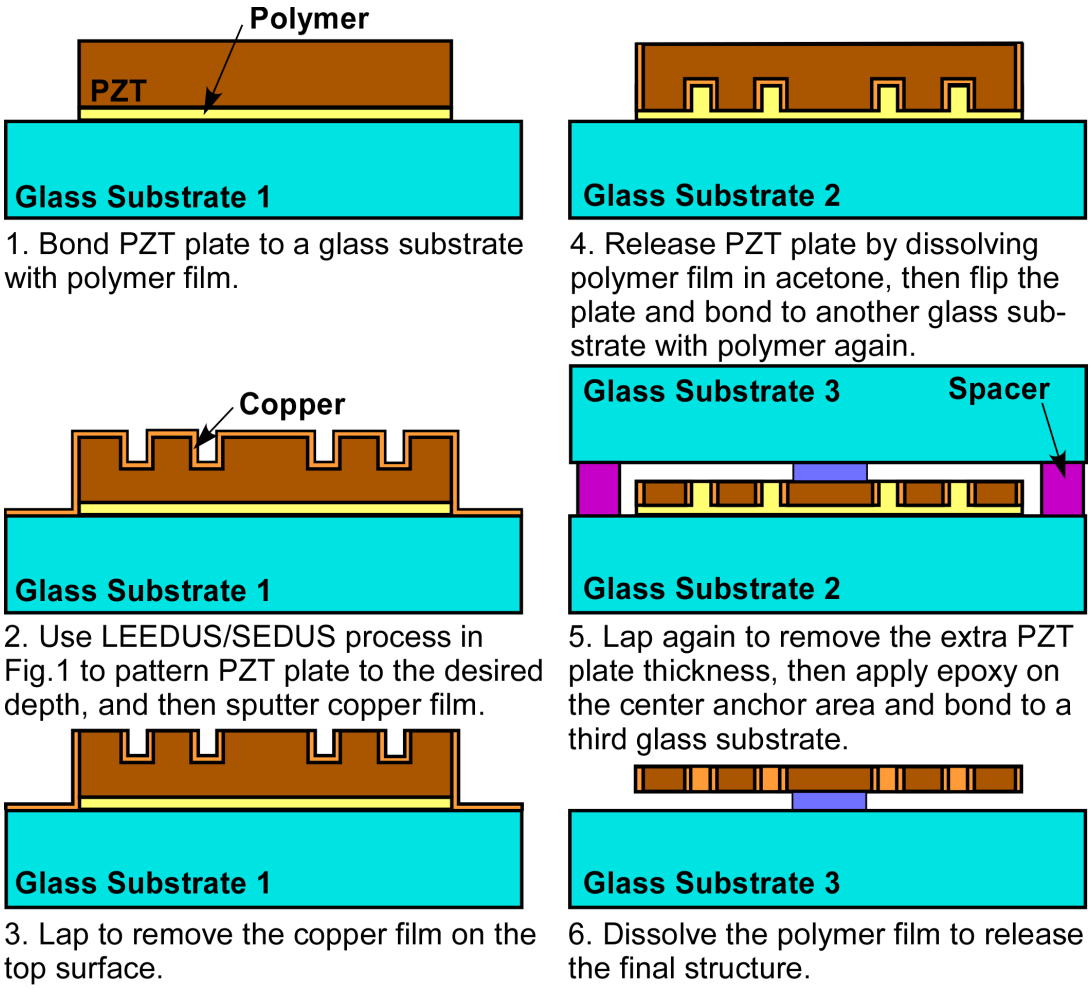

Figure 2.22: In-plane PZT actuator fabrication process flow.

The μEDM'ed microtools for both the octagonal and the circular spiral actuators were machined using stainless steel and are shown in Figure 2.23. The octagonal spiral microtool made by serial μEDM had a cutting depth of 100 μm and can be easily adjusted by modifying the controlling program. The circular spiral made by batch μEDM had a cutting depth of 48 μm. The final released device supported at the center anchor by epoxy is shown in Figure 2.24 for the octagonal version and in Figure 2.25 for the circular version. The octagonal spiral actuator has a footprint of 450 μm × 420 μm, beam width of 50 μm, and height of 20 μm, and the circular one has an outer diameter of 500 μm, beam width of 80 μm, and height of 28 μm. These devices were poled *in-situ* by a bias to the copper electrodes on their sidewalls using a probe station.

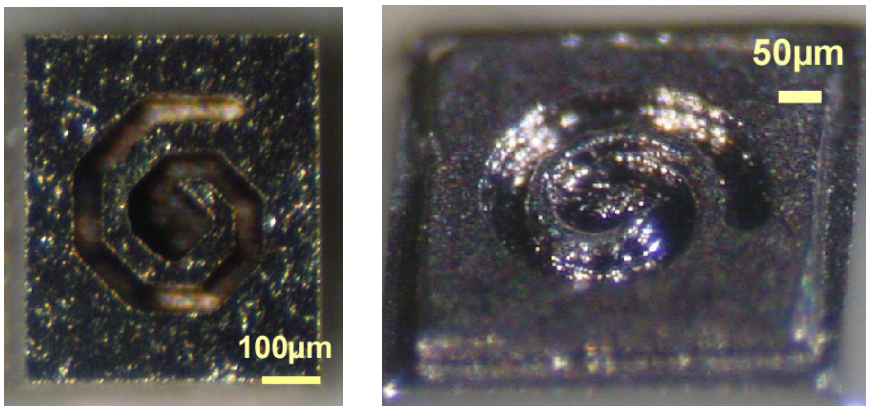

(a) (b)

Figure 2.23: (a) Photos of the microtool fabricated by serial μEDM. (b) A circular spiral-shaped microtool is also possible using batch mode μEDM.

2.3.3 Devices Testing Results

The testing results of the actuators displacement are shown in Figure 2.26. For the octagonal spiral actuator, a displacement of ≈2 μm was achieved at an actuating voltage of 40 V. This measured displacement is 6 - 7× larger than the calculated d_{31}

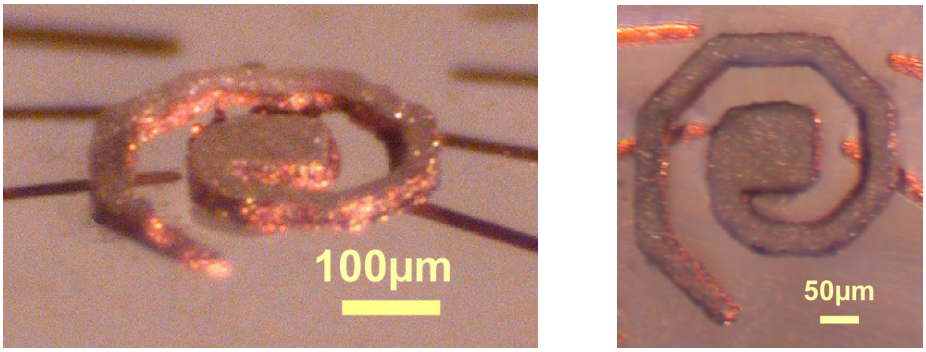

(a) (b)

Figure 2.24: Photos with perspective and top-down view of the final released actuator supported on its center anchor with epoxy. This device was fabricated by SEDUS, using the design and microtool shown in Figure 2.21(a) and Figure 2.23(a), respectively.

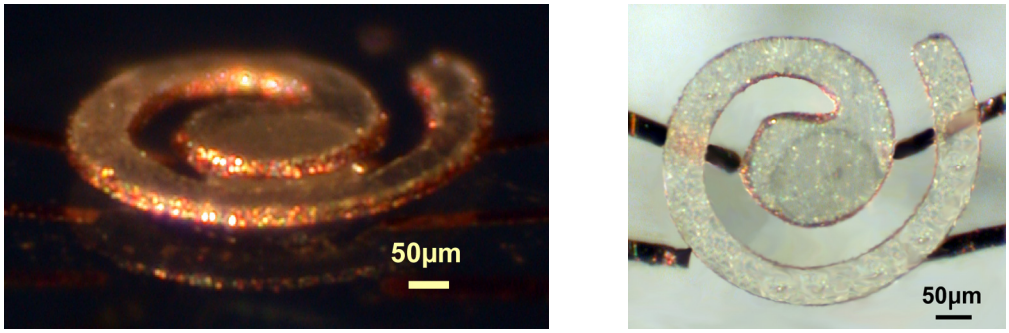

(a) (b)

Figure 2.25: Photos with perspective and top-down view of the final released circular spiral actuator supported on its center anchor with epoxy. This device was fabricated by LEEDUS using the design and microtool shown in Figure 2.21(b) and Figure 2.23(b), respectively.

transverse displacement from an equivalent straight beam actuator. For the circular version, the multiple is 7 - 8×, giving similar results as those shown in [Moh99]. It is obvious that the transverse d_{31} effect is not the sole cause for the measured displacement. One explanation given in [Moh99] is that the non-uniform stress developed under applied voltage creates a bending moment, which changes the curvature of the spiral and results in the magnified displacement at the tip. This magnification multiple is related to the effective length and wall width of the actuator, as discussed in [Moh99]. In both cases,

the displacement started dropping at higher actuating voltage. This is likely due to a degradation of polarization when the applied electric field is too strong, reaching the initial depolarization field of ≈500-1000 V/mm.

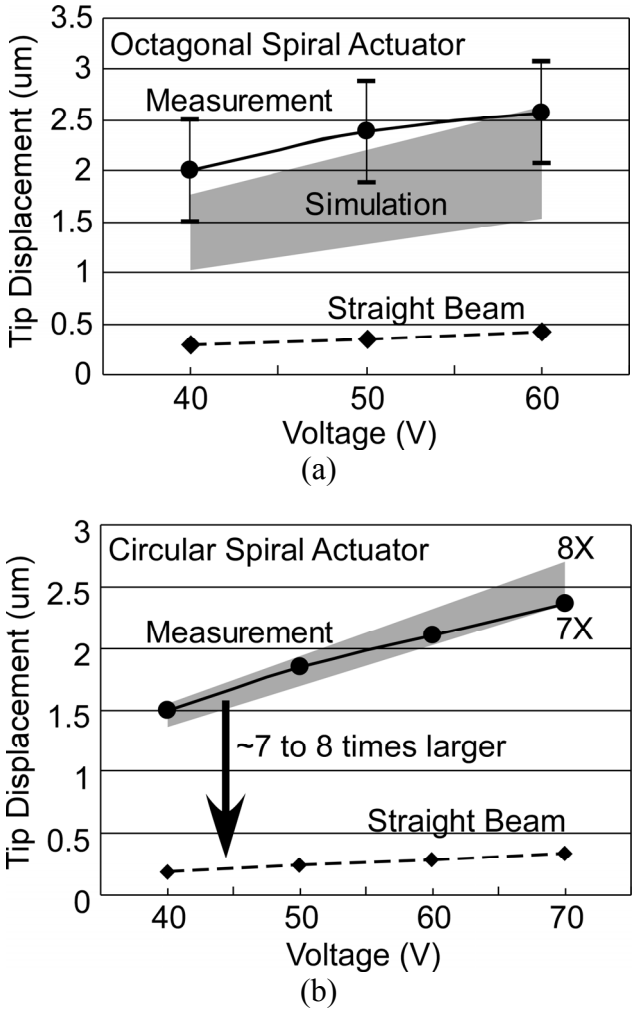

Figure 2.26: Measured displacement at the tip of the spirals as a function of actuating voltages, compared with the calculated d_{31} transverse displacement of corresponding PZT-5H straight beam actuators with the same effective length. (a) Octagonal spiral results (Effective length = 1101 μm, Width = 49.7 μm, d_{31} = -320 pm/V). FEMLAB simulation result (shaded area) is shown as a range, caused by uncertainty in the material properties and device geometry non-ideality. An estimated measurement error of ±0.5 μm is indicated by error bar for the measurement results. (b) Circular spiral results (Effective length = 1205 μm, Width = 79.5 μm, d_{31} = -320 pm/V). Shaded area indicates the corresponding multiples (7× to 8×) of displacement of an equivalent straight beam actuator.

2.3.4 FEM Simulation

An FEM analysis was performed for the octagonal spiral actuator using FEMLAB Multiphysics (now COMSOL Multiphysics) simulation software. In the simulation, Piezo Solid application mode was used for modeling. Because poling was performed by applying voltage on the sidewall of the spiral beam, in order to model the varying polarization direction along the spiral beam as shown in Figure 2.21(a), a local coordinate system was created for each segment of the octagonal spiral geometry. The geometry parameters and the manufacture's material properties for the PZT-5H bulk plate are summarized in Table 2.4. To accommodate the device geometry non-ideality and uncertainty in the PZT material properties caused by poling and estimation of some parameters, estimated variation of up to 15% in these parameters was included during simulation. The simulation results, which are shown in Figure 2.26(a) as shaded area, approximately match the measurement result although the variation of the simulation parameters caused a range of simulation results.

Table 2.4: Geometry parameter and material properties for FEM analysis. Error or uncertainty estimation of up to ±15% was added to parameters during simulation.

Spiral beam width	50 μm
Spiral beam thickness	20 μm
PZT density	7800 Kg/m^3
Piezoelectric coefficient d_{31}	-320 pm/V
Piezoelectric coefficient d_{33}	650 pm/V
PZT relative permittivity K^T_3	3800
Elastic modulus Y^E_3	50 GPa
Elastic modulus Y^E_1	62 GPa

2.4 Improvement of the Basic Batch μUSM Apparatus

Although the basic apparatus built for batch mode μUSM described in Section 2.1.3 has been successfully utilized for characterization on Macor ceramic plate and demonstration on bulk PZT, several issues were identified during the testing, which could affect the functionality and performance of the apparatus, including tilting error in the Z axis stage, inefficient force detection for feedback control during machining, and lack of slurry flush mechanism. Efforts have been made to improve the functionality and controlling of the process with regards to these issues.

2.4.1 3-Axis Stage with Improved Precision

The XYZ stages used in the basic apparatus are linear-bearing translation stages. This type of stage can provide large travel range and good loading capacity, but in order to obtain 3-axis movement, two L-shaped brackets have to be used. One is for mounting the Z axis stage onto the top of XY stages, and the other one is mounted on the Z axis stage to convert its vertical platform surface to a horizontal worktable surface. The error in the bearings causes flexibility in the stages, and the brackets in this kind of structure result in side loading to the stages. All these factors lead to a deflection in the worktable surface when the ultrasonic vibration is applied. This deflection, though very tiny, can affect the uniformity of the actual machining depth especially when the cutting area becomes large, and can also result in a reduced actual cutting depth from the feeding distance.

The solution to this issue is using a 3-axis flexure stage which has a built-in top-loading platform. This kind of stage relies on the elastic deformation (flexing) of a lever

and eliminates the use of bearings. The resolution of such stages is limited only by the actuator driving them, and loading capacity is also very high. The travel range for these stages is limited to several millimeters, but is still acceptable for this application. The selected stage type is Thorlabs® MAX303 NanoMax 3-axis flexure stage. It has a load capacity of 10 N and travel range of 4 mm in each axis [Tho03]. The Thorlabs DRV001 stepper motor is used as the driver for the Z axis of this stage, and the BMS001 Mini apt™ stepper motor controller is used to control the stepper motor and provide the connectivity to the process control computer through a USB interface. The X and Y axes of the stage are driven by a manually operated differential micrometer as shown in Figure 2.27(c). Instead of the COM port communication interface in the basic setup, this new stage with stepper motor requires USB drivers from Thorlabs as well as a new process control program, which is discussed in Section 2.4.4.

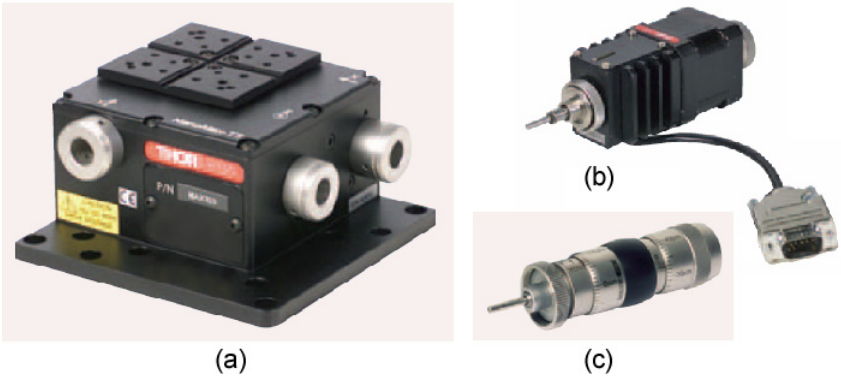

Figure 2.27: (a) Thorlabs® MAX303 NanoMax 3-axis flexure stage; (b) DRV001 stepper motor drive used for Z axis; (c) differential micrometer drive used for X and Y axes.

2.4.2 Acoustic Emission Sensor for Feedback Detection

The feedback detection in the original setup is achieved by using the piezoelectric quartz force sensor embedded between the worktable and the stage platform. This sensor

detects the Z-axis position of the workpiece surface in the zero-position calibration mode, and senses the ultrasonic vibration transmitted through the workpiece and the worktable to evaluate the machining load for use in the feedback controlled machining mode. However, because of the large surface area of the microtool substrate, the relatively short tool tips, and the presence of the slurry, the measured machining load is an averaged value over the whole tool substrate area, and is less sensitive to the working distance between the tool tip and the cutting front than to the distance between the tool substrate and the workpiece surface.

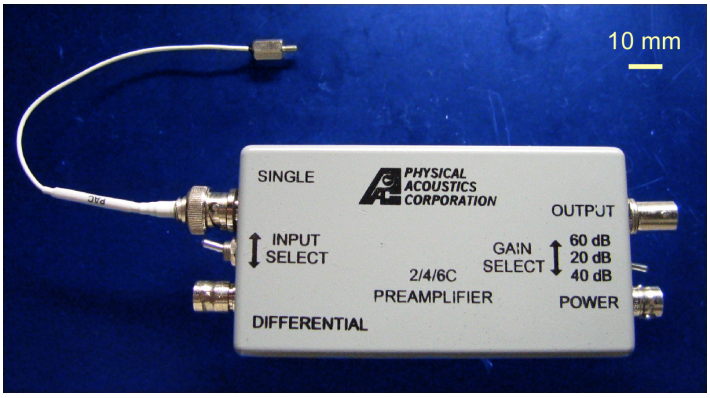

Figure 2.28: HD15 acoustic emission sensor with 2/4/6C preamp from Physical Acoustics Corporation.

To explore the possible solutions of this issue, an acoustic emission detection scheme has been implemented. Acoustic emission (AE) usually refers to the transient elastic waves generated by the rapid release of energy from localized sources within a material, or in this case, generated by the microchipping that occurs in the workpiece during USM. By using a commercial AE sensor to detect this transient elastic wave instead of the vibration transmitted from the USM ultrasound generator, the actual cutting front can potentially be accurately detected and used to control the feeding speed of the Z

stage. This approach has been proved effective in a serial mode μUSM setup to achieve tool wear compensation [Mor02].

There are a limited number of vendors for AE sensors. Solutions from Digital Wave Corporation (CO, USA) and Physical Acoustic Corporation (PAC, NJ, USA) have been considered, and PAC HD15 miniature sensor (Figure 2.28) was selected due to its small size (8 mm diameter × 9.5 mm length) and operating frequency range (130-530 kHz). A preamplifier 2/4/6C is connected to the sensor to provide a selectable gain of 20, 40 and 60 dB and a band pass filter of 100-400 kHz. The band pass filter is necessary to remove the main frequency component in the machining vibrations from the ultrasonic generator working at 20 kHz, so that only the higher frequency acoustic emission signals are detected. The upper limit of the filter frequency range is relatively high, and the sampling rate of the DAQ card for A/D conversion on the process control computer should be at least twice of it. The NI PCI-6251 DAQ card has a maximum sampling rate of 1.25 Ms/sec, well above the minimum rate requirement.

2.4.3 Slurry Flushing Setup

In the original setup, slurry is supplied into a reservoir formed by moldable paste surrounding the workpiece before the machining starts. During machining there is no slurry flushing to carry away the debris generated in conventional USM. The powders in the slurry also tend to be pushed away from the machining region so that manual slurry refreshment in the region usually has to be done with a syringe. To solve this problem, a continuous slurry flow has been obtained by implementing a nozzle connected to a slurry reservoir through a pump (Figure 2.29). A magnetic stirrer in the slurry reservoir can

keep the slurry well mixed. The used slurry in the custom-machined workpiece table is recirculated back to the reservoir and reused. The slurry pump used for the setup is SP100 peristaltic pump from APT Instruments (IL, USA), and a rotational rate of ≈20-30 rpm is used to drive the slurry flow.

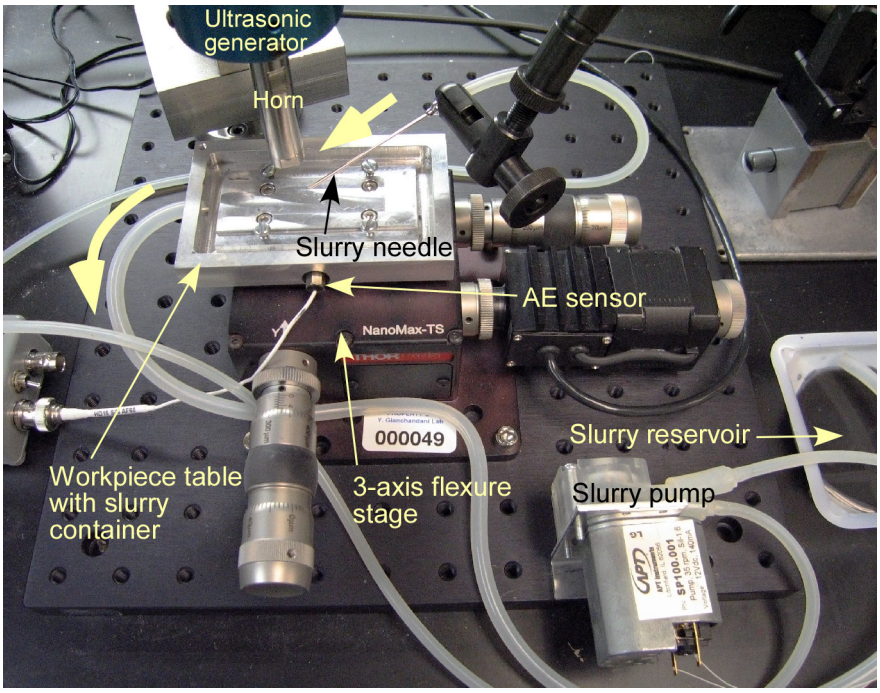

Figure 2.29: Slurry flushing setup for the batch mode μUSM setup.

2.4.4 Process Control Software

A modified version of the process control software has been developed for the Thorlabs apt stepper motor controller and the AE sensor reading. The user interface is shown in Figure 2.30. The operational flow chart of the modified process control software is shown in Figure 2.31. The program scripts are listed in Appendix A.2. The software was developed in the same environment as that for the original setup. The Thorlabs apt® driver version 1.1.8 or higher is required to establish the USB connection to the motor controller and provide an ActiveX-based programming interface for Visual

Basic 6. The NI PCI-6251 DAQ card needs to work at a sampling rate higher than 800 kHz to prevent signal aliasing.

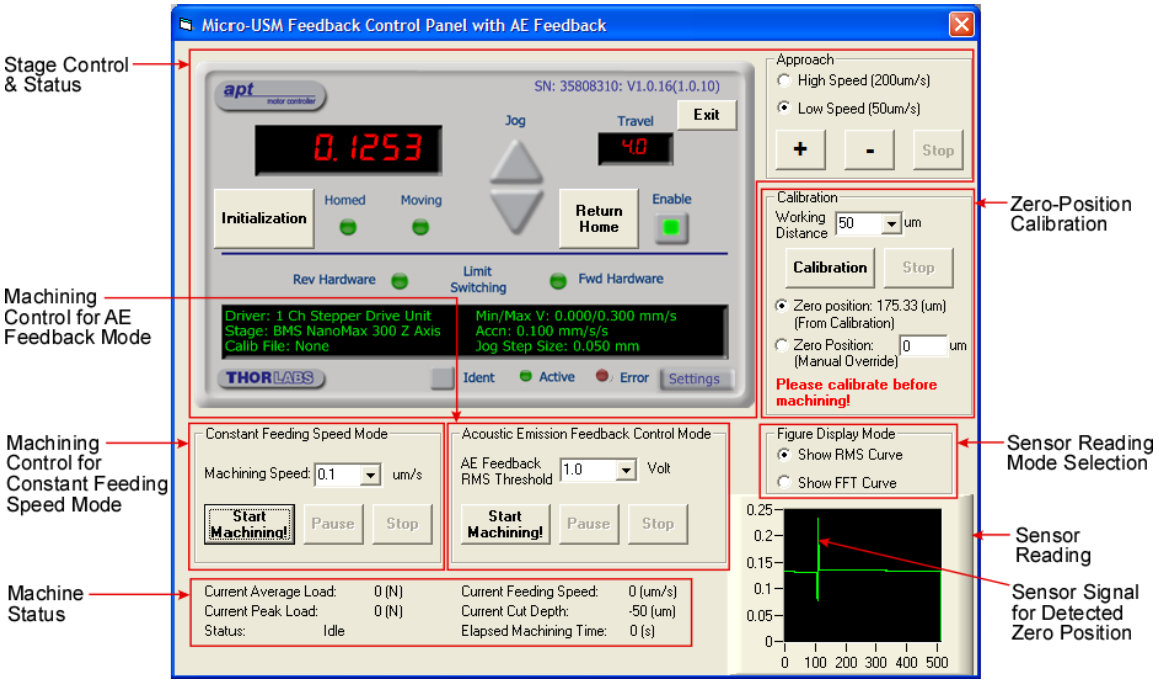

Figure 2.30: Process control software developed for the advanced batch mode µUSM apparatus, showing status after zero-position calibration and ready for machining.

2.4.5 Integration and Testing of the Advanced Apparatus

A schematic of the integrated advanced apparatus including the three improvements discussed in previous sections is shown in Figure 2.32. The finished advanced machining apparatus without the slurry flushing subsystem is shown in Figure 2.33. The slurry flushing subsystem is preferably used only for a large number of cuttings in series. Test machinings have been successfully carried out on PZT-5H and 5A materials using this apparatus and confirmed its functionality.

Table 2.5 lists the measured cutting depth and the stage feeding depth for the basic apparatus using the side-loading bearing stage and for the advanced apparatus with

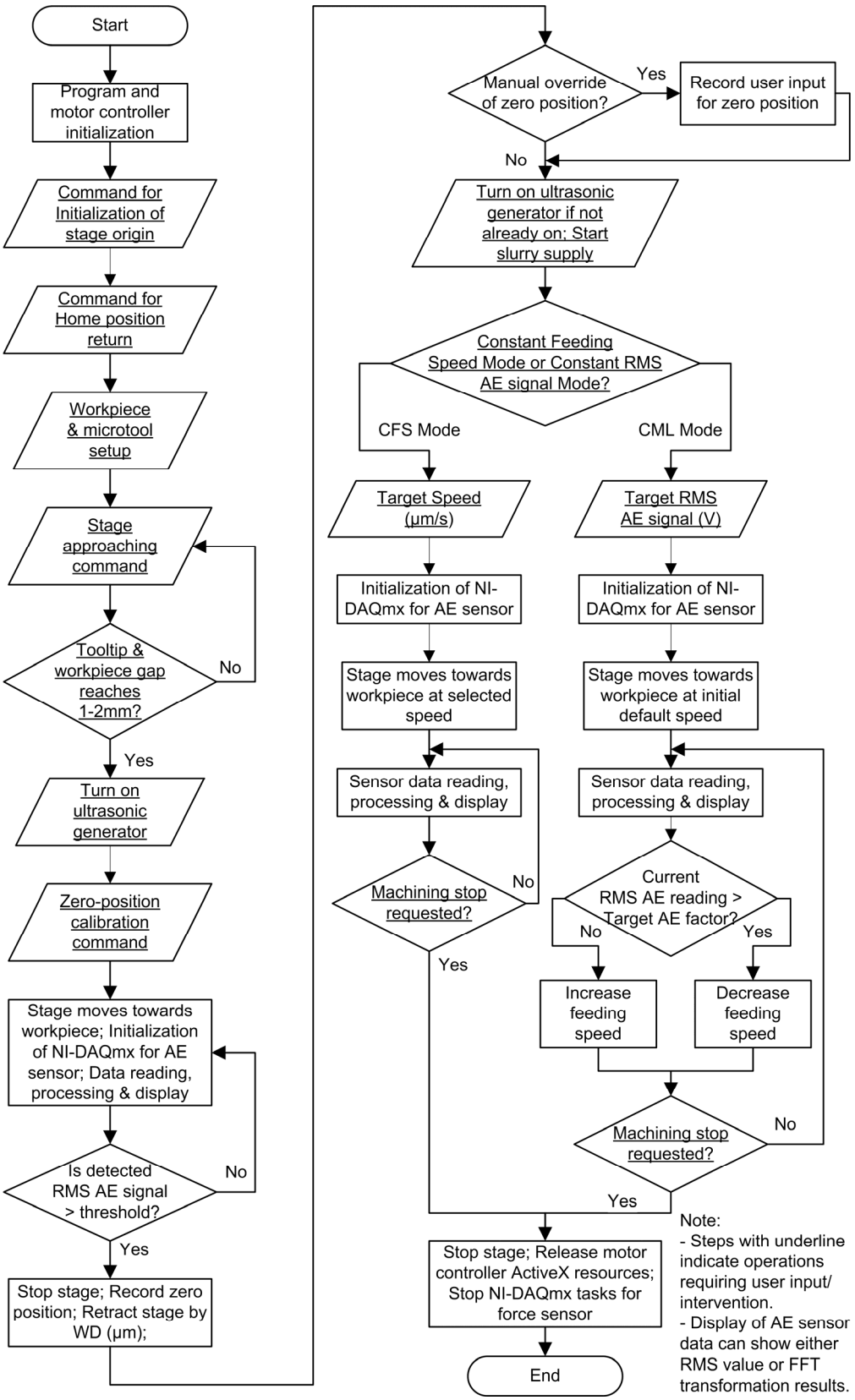

Figure 2.31: Operational flow chart of the modified control program.

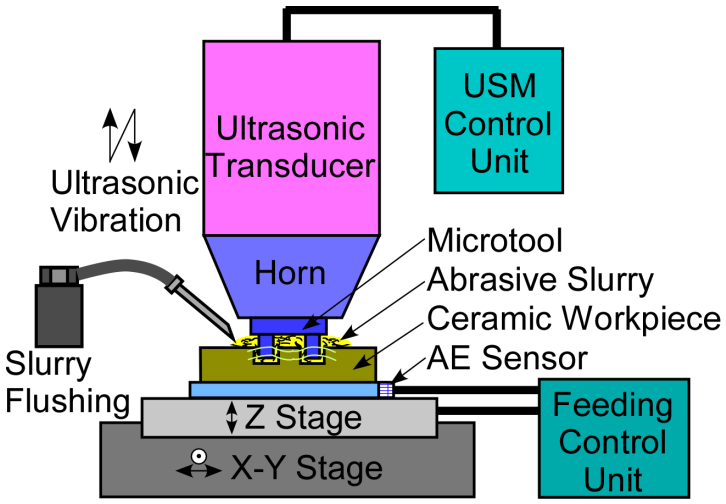

Figure 2.32: Schematic of the advanced μUSM apparatus created for batch mode pattern transfer on ceramic workpiece.

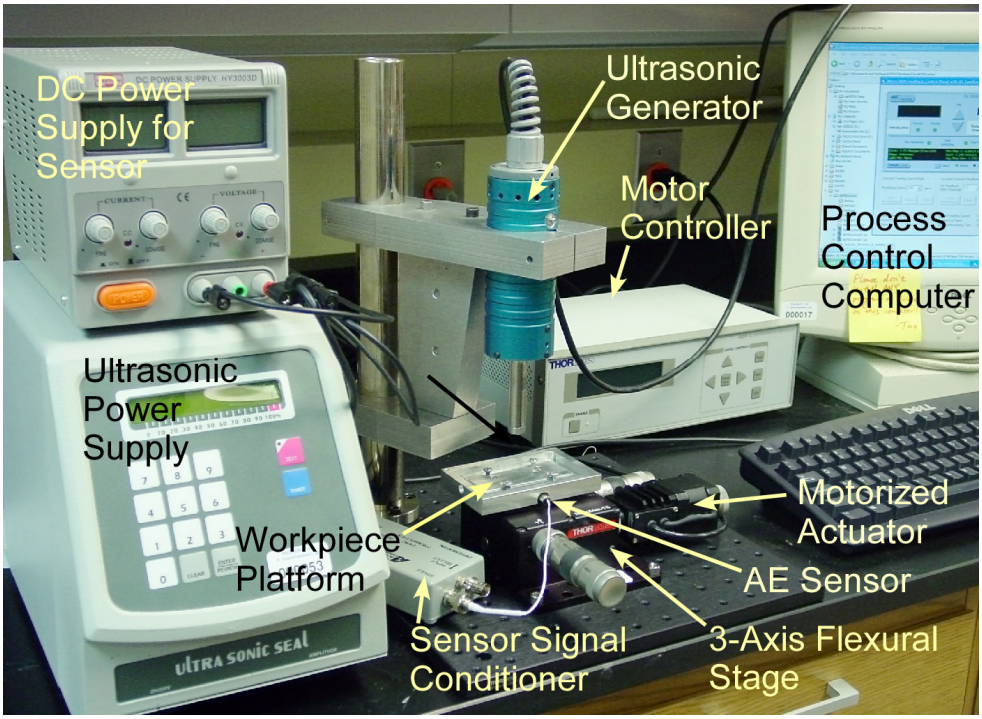

Figure 2.33: Advanced apparatus for batch mode μUSM with top-loading flexural stage and AE sensor feedback scheme. The slurry flushing subsystem is not shown.

the top-loading flexure stage. In the basic apparatus, the measured cutting depth is only 61.3% of the stage feeding depth, suggesting a large amount of stage deflection. The advanced apparatus has a larger cutting depth than the feeding depth (129.6%), likely due

to the presence and bombardment of the slurry powders, indicating a much smaller stage deflection than that in the basic apparatus.

The AE sensor has been successfully used for zero-position calibration and AE signal detection during machining. A basic feedback scheme implemented in the control software based on the detected AE signals has been proved to be more effective than that based on the force sensor detection. The AE sensor can provide up to ≈20% trackable signal variation during machining according to the size of the gap between the tip of the microtool and the workpiece, compared to <1% signal variation from the dynamic force sensor under the same machining conditions. Development of advanced control algorithm and signal analysis can be carried out to further improve the effectiveness and efficiency of the feedback operation.

Table 2.5: Comparison of measured cutting depth and stage feeding depth for the basic and advanced apparatuses. The advanced apparatus has a larger cutting depth than the feeding depth, likely due to the presence and bombardment of the slurry powders, indicating a much smaller stage deflection than that in the basic apparatus.

	Basic apparatus	Advanced apparatus
Stage feeding depth (μm)	150	50
Measured cutting depth (μm)	92	64.8
Ratio	61.3%	129.6%

The slurry flushing subsystem has also been tested for machining. It is especially helpful when a large number of cuttings are carried out, saving the effort to prepare the paste reservoir for each cutting. It is less beneficial for prototype machining that requires just a few cuttings due to the large amount of slurry needed in the reservoir and to flush the pipes.

2.5 Discussion

The μUSM technology included in the LEEDUS/SEDUS process has some advantages over traditional methods when applied to hard, brittle materials, in that it does not degrade the workpiece material in terms of damage, stress regimes, and thermal or chemical alterations. It can achieve precision surface finish of Ra 0.4 - 0.76 μm [Tho98]. In traditional machining, the mechanism for removing material causes plastic deformation at the microscale, resulting in microcracks and other damage in brittle materials. Another option for making microstructures is to use an additive process, *i.e.* one in which the structural material is selectively deposited onto a substrate. However, with these processes it is difficult to get the desired uniformity in terms of material properties as discussed in Section 1.2.1.

The μUSM cutting rate demonstrated in this work is >18 μm/min. for both Macor and PZT, while RIE etching of PZT is at 0.3 μm/min. [Wan99], and wet etching of PZT is at 0.13 μm/min. [Wan00]. Powder blasting can reach an etching rate of 25 μm/min. for glass [Wen00] and a minimum feature size of 30 μm [Wen02], but it has the problems of V-shaped sidewalls and blast lag, which become rather severe when the feature size gets smaller and the cutting depth gets larger. For μUSM, the machined cavities follow the shape of the microtool, eliminating V-shaped sidewalls or blast lag problems. It can be seen that complex lithographic patterns, such as the circles and spirals in Figure 2.16 and Figure 2.21, present significant challenges for previously established methods. RIE and wet etching are too slow to be efficiently used for bulk micromachining of PZT, while the V-shaped sidewalls made by powder blasting will make it difficult to form electrodes on the sidewalls of these shapes.

The LEEDUS and SEDUS processes have been demonstrated at die-scale. An eventual target of wafer-scale pattern transfer would be beneficial to a number of applications in terms of throughput. However, there are still some limitations that prevent the process from going to wafer level. The batch mode μEDM used to make microtools presents the first major barrier. Although parallel discharge mode can be used to improve the scaling limit, the debris generated at the center of the wafer can cause secondary discharge and damage to the electrodes. (This may also ultimately limit the aspect ratio achievable in LEEDUS.) New techniques for flushing debris are under investigation to solve the debris problem [Ric05, Ric06]. Another limitation would come from the microtool mounting error, *i.e.* the error of the parallelism between the surfaces of the microtool and the workpiece during μUSM. If the machining area is increased to wafer level, this problem becomes much more significant than it is for die-scale machining. New mounting techniques or a compensation mechanism on the Z-stage would be necessary to reduce this error.

CHAPTER 3

Micromachined Piezoelectric Tissue Contrast Sensor for FNA Biopsy

In this chapter, a bulk PZT-based *in-situ* sensor intended for tissue contrast detection during FNA biopsy of tissue, *e.g.* thyroid nodules, is described [Li06a, Li06b, Li07]. The device is created as a demonstration of the expanded material choices for MEMS applications enabled by μEDM and μUSM, including bulk piezoceramics and hard steel. Intended to complement traditional ultrasound imaging, the device uses a micromachined piezoelectric sensor embedded near the tip of a biopsy needle to distinguish tissue planes. The sensor responds only to tissue in close proximity to the needle tip in order to provide local information about samples that are collected through the needle tip. The design details are given in Section 3.1. The sensor is fabricated from bulk PZT using a customized process involving SEDUS discussed in Chapter 2, and details of the fabrication process are described in Section 3.2. The devices were tested in materials that mimic the ultrasound characteristics of human tissue in the training of physicians, and were separately tested with porcine fat and muscle tissue. The results are presented in Section 3.3, followed by analysis and discussion in Section 3.4. This device clearly indicates tissue differentiation in shallow tissue regions of about 15 mm insertion depth with a needle length of 25 mm. Modifications of sensor design are needed for application to deeper tissue biopsy and are described in Chapter 4.

3.1 Device Design

3.1.1 Theory

A PZT disc that is actuated in longitudinal mode for free vibration in the direction of its thickness has both the piezoelectric polarization and the applied electrical field parallel to its thickness. Mechanical resonance for such a disc occurs when its thickness t_0 equals the odd multiples of half of the vibration wavelength, $\lambda/2$, or equivalently when

$$f_{(n)} = \frac{n \cdot v_0}{2t_0}, \qquad n = 1,3,5... \tag{3.1}$$

where $f_{(n)}$ is the n^{th} resonance frequency, $v_0 = \lambda \cdot f_{(n)}$ is the vibration velocity in the material, and n is a positive odd integer that represents the harmonic number. Due to the piezoelectric effect of the disc, these mechanical resonances correspond to a series of electrical impedance peaks of the PZT disc, and the mechanical resonance frequency $f_{(n)}$ is equal to the anti-resonance frequency, $f_{a(n)}$, of the electrical impedance for the disc in this thickness longitudinal driving mode (also referred to as maximum impedance frequency f_m) [IEE88, Ike90]. The thickness of the PZT disc, t_0, will thus determine the location of the impedance peaks on the spectra, and the diameter of the disc, R, should be several times larger than t_0, in order to reduce the cross-coupling from the lateral wave resonance mode by reducing the lateral resonance frequency. When the mechanical boundary conditions, such as mass and elastic loading, are change by contact with the materials to be tested, the mechanical resonance of the PZT disc will change accordingly. This is transduced into changes in the electrical impedance peaks of the PZT disc, and can be monitored by measuring the electrical impedance spectra.

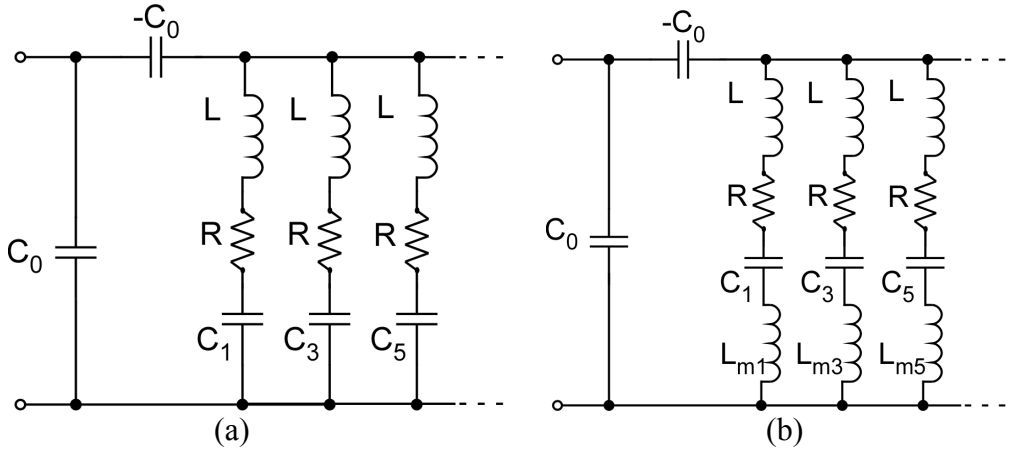

Figure 3.1: Lumped-element BVD equivalent circuits of a piezoelectric resonator in longitudinal vibration mode. (a) Free resonance; (b) with equivalent loading.

The lumped-element Butterworth-Van Dyke (BVD) equivalent circuit shown in Figure 3.1(a) can be used to model the electrical characteristics of the PZT disc in the absence of loading [IEC76, Ike90, Pan06]. The clamped capacitance between the two electrodes of the disc is denoted C_0, and an infinite number of series RLC_n (n=1,3,5…) motional branches are connected in parallel. The first branch of R, L, and C_1 corresponds to the fundamental resonance mode, and the n^{th} branch of R, L, and C_n represents the n^{th} mode defined by Equation 3.1. The n^{th} anti-resonance frequency, $f_{a(n)}$, and resonance frequency, $f_{r(n)}$, of the measured electrical impedance are:

$$f_{a(n)} = f_{(n)} = \frac{1}{2\pi\sqrt{LC_n}}, \qquad n = 1,3,5... \tag{3.2}$$

$$f_{r(n)} = \frac{1}{2\pi\sqrt{LC_n \dfrac{C_0}{C_0 - C_n}}}, \qquad n = 1,3,5... \tag{3.3}$$

The circuit elements are related to the physical parameters of the PZT disc by:

$$C_0 = \frac{\varepsilon \cdot A}{t_0} \tag{3.4}$$

$$C_n = \frac{8k_t^2}{n^2\pi^2} C_0, \qquad n = 1,3,5... \tag{3.5}$$

$$L = \frac{1}{4\pi^2 f_{a1}^2 C_1} \tag{3.6}$$

$$R = \frac{\eta_0}{\rho_0 v_0^2 C_1}\left(\frac{f}{f_{a1}}\right), \qquad n = 1,3,5... \tag{3.7}$$

where ε is the permittivity of the piezoelectric layer; A and t_0 are the area and thickness of the PZT disc, respectively; k_t^2 is the electromechanical coupling constant determined by material properties including piezoelectric constant, stiffness, and permittivity of the piezoelectric material; v_0 and η_0 are the acoustic velocity and viscosity of the piezoelectric layer, respectively; and ρ_0 is the density of the piezoelectric layer. As shown in Equations 3.2 and 3.3, both $f_{a(n)}$ and $f_{r(n)}$ are related to motional parameters L and C_n, which are coupled with mechanical boundary conditions, so either one can be used to monitor the resonance change. However, the anti-resonance modes, $f_{a(n)}$, are preferred for this longitudinal piezoelectric coupling because it is fundamentally related only to the thickness of the disc, and less affected by circuit parameters such as variation of C_0 due to parasitic capacitances [Mck98].

A modification to the original BVD circuit is necessary to accommodate the piezoelectric loading effect by using an inductor to model the mass loading, such as a diaphragm attached to a piezoelectric sensor [Mar91, Zha05]. This is shown in Figure 3.1(b) as the mass loading inductances, $L_{m(n)}$. The inductance is related to the physical parameters of the PZT disc and the added mass by

$$L_{m(n)} = \frac{4 f_{a1} L \rho_m t_m}{n \rho_0 v_0}, \qquad n = 1,3,5... \tag{3.8}$$

where ρ_m and t_m are the density and thickness of the added mass layer, respectively. The thickness, t_m, should be as small as possible, since it is inversely proportional to the sensitivity of the sensor to any additional mass loading on the diaphragm [Zha05]. This modified BVD circuit model will also be used in Section 3.4.1 to describe the equivalent loading provided by tissue.

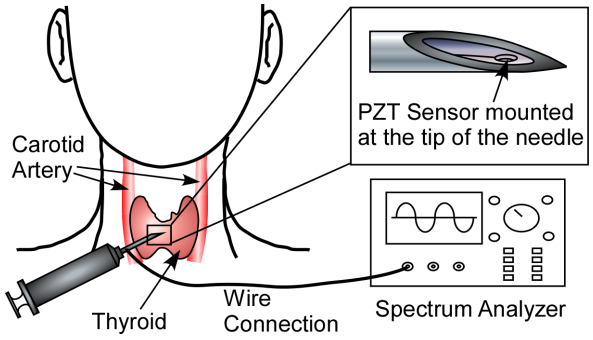

Figure 3.2: System diagram of the *in-situ* tissue contrast sensor intended for thyroid FNA biopsy.

3.1.2 Device Description

The scheme for the *in-situ* detection of tissue contrast using the piezoelectric sensor during thyroid biopsy is illustrated in Figure 3.2. A PZT sensor is integrated at the tip of the needle and is connected to a spectrum analyzer for real-time impedance measurement, thus providing information of the tissue contrast during thyroid biopsy. Figure 3.3 shows the schematics of the proposed device. The PZT disc is located within a cavity micromachined into the wall of the needle near the tip, and against a diaphragm which is retained at the bottom of the cavity. The thickness of the diaphragm is non-uniform because of the cylindrical shape of the needle. The metal needle serves as a ground plane for one electrode of the PZT sensor. The second lead, which is to the top of

the PZT disc, is a flexible, insulated copper wire that extends along the inside of the needle. Epoxy is used to provide electrical insulation and to seal the device.

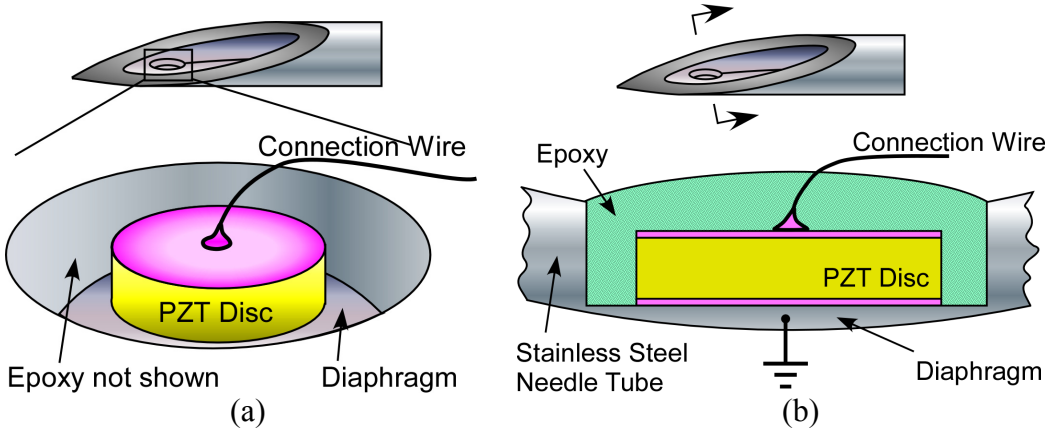

Figure 3.3: Schematics of the tissue contrast sensor. (a) Perspective view with sealing epoxy removed; (b) cross sectional view.

The sensor is designed to respond to tissue that is in contact with the diaphragm and in close proximity to the probe as it is inserted during a biopsy procedure. Different tissue types have different density and elastic properties. The mass loading and elastic loading to the diaphragm, and thereby the vibration characteristics of the diaphragm, change accordingly. This changes the mechanical boundary condition of the PZT disc, which is transduced into a change of electrical impedance by the piezoelectric effect, and subsequently detected by the impedance analyzer, providing a measure of tissue contrast.

3.2 Device Fabrication

3.2.1 PZT Disc Batch Fabrication

The fabrication process for the PZT disc is shown in Figure 3.4(a). A bulk PZT-5H plate (Piezo Systems, Inc., USA), which has attractive material properties for sensor

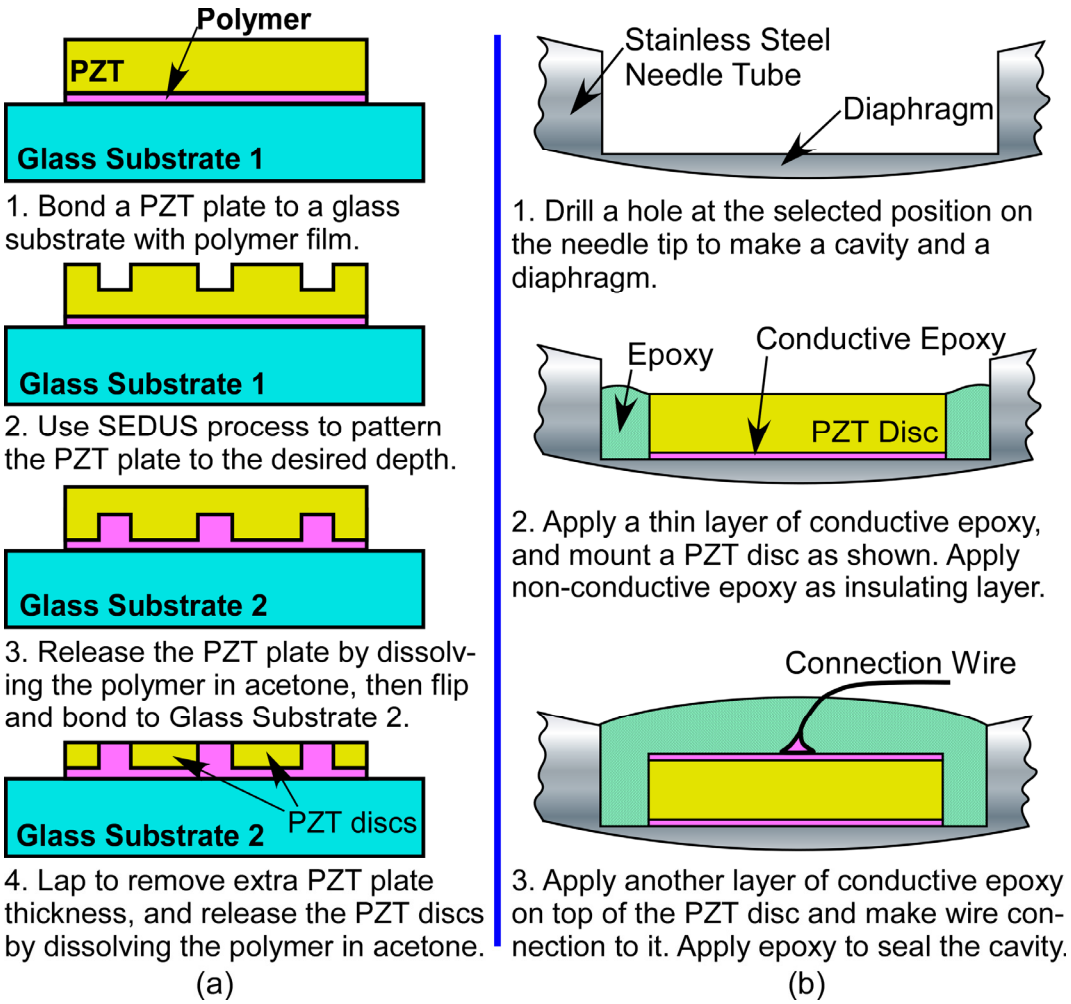

Figure 3.4: Diagram of fabrication process flow for: (a) PZT discs; (b) the *in-situ* tissue contrast sensor at the tip of a biopsy needle.

applications, is bonded to a glass substrate by a polymer. The SEDUS process is performed to fabricate disc-shaped structures with desired depth on the PZT plate. As described in Chapter 2, this is a batch mode micromachining process that uses serial mode μEDM to define patterns on a steel microtool, which is then used in batch mode μUSM to transfer patterns onto ceramic substrates with the help of abrasive slurry. The PZT plate is then released by dissolving the polymer, flipped over and bonded again to a second glass substrate. The discs are released by lapping away the extra thickness of the plate and dissolving the bonding polymer. Figure 3.5 shows a released PZT disc with a

diameter of 200 µm and a thickness of 50 µm. PZT discs with other thicknesses are shown in Figure 3.6. Discs with more than 100 µm thickness have been fabricated from the 127 µm-thick PZT substrate before the bottom of the cutting cavity becomes too thin and breaks. Thicker PZT discs are possible using a PZT substrate with a larger thickness.

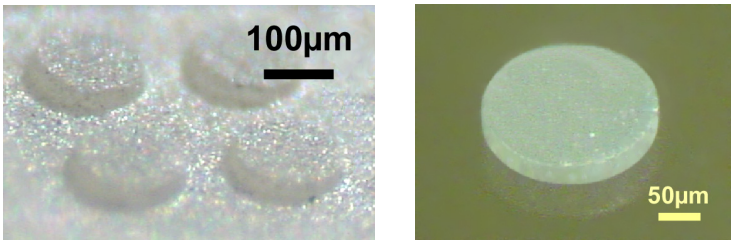

(a) (b)

Figure 3.5: Photos of: (a) PZT disc array fabricated by SEDUS process using batch µUSM to transfer a pattern defined by serial µEDM. (b) Released batch-fabricated PZT disc. Diameter: 200 µm. Thickness: 50 µm.

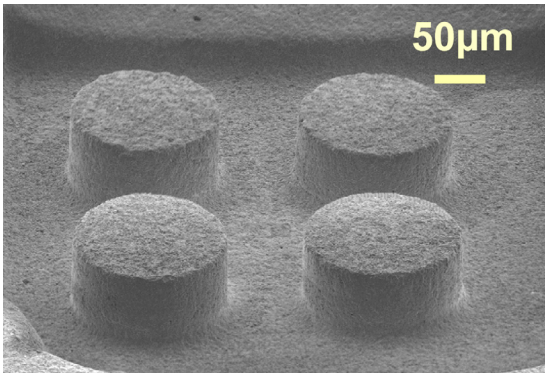

(a)

(b)

Figure 3.6: (a) SEM image of a disc array pattern transferred onto the PZT substrate using the SEDUS process. The cutting depth is ≈100 µm. (b) Photo of released PZT discs with various thickness. The discs with a light color do not have metal electrodes.

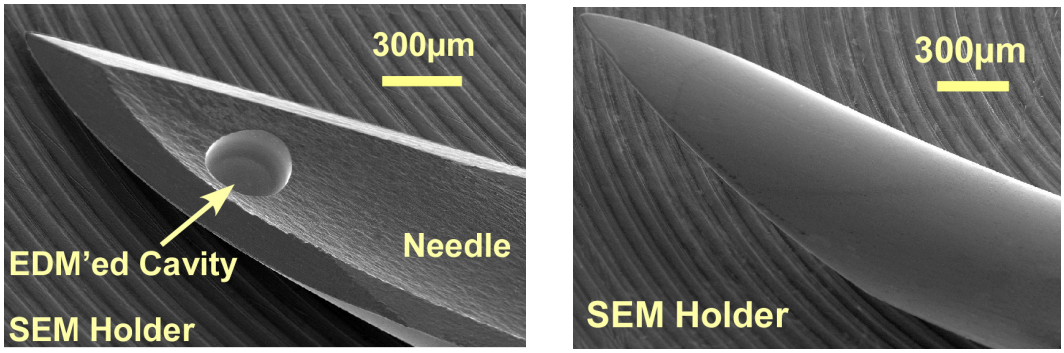

(a) (b)

Figure 3.7: SEM images of µEDM'ed biopsy needle tip with a cavity for mounting PZT sensor: (a) inner side view; (b) outer side view. Cavity diameter: 300 µm, depth: 150 µm. Corresponding diaphragm thickness: 10 - 36 µm.

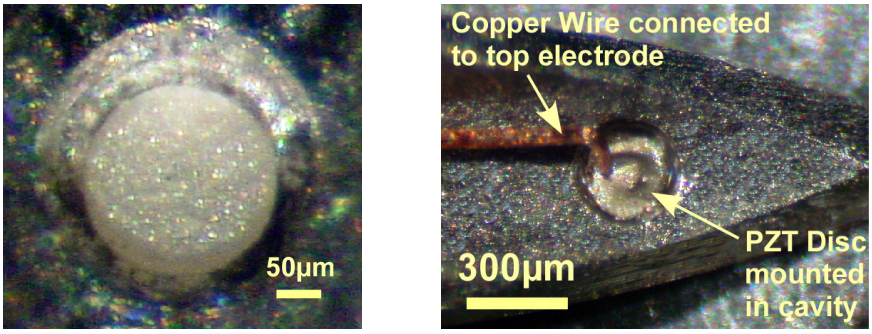

(a) (b)

Figure 3.8: Photos of: (a) the PZT disc mounted in the cavity at the tip of a biopsy needle; (b) a finished device, before sealing epoxy is applied. A coated copper wire is used to make connection to the top electrode of the PZT disc. The stainless steel needle body is used as a ground.

3.2.2 Sensor Integration on Biopsy Needle

To integrate the sensor onto a biopsy needle, the interior apex of the needle is machined by µEDM to form the cavity and the diaphragm (Figure 3.7), and the PZT element is inserted as illustrated in Figure 3.4(b). The cavity diameter and depth are 300 µm and 150 µm, respectively. This results in a diaphragm, with a thickness varying from 10 to 36 µm, on the 20-gauge needle. A thin layer of conductive epoxy is used to attach the PZT disc to the bottom of the cavity, as well as to attach the lead wire to the top

surface of the disc. Non-conductive epoxy is then applied as an insulating layer and sealing material. Figure 3.8 shows a photo of the PZT disc mounted in the cavity, and a photo of the final device with a lead connection to the top electrode, immediately before applying the sealing epoxy.

3.3 Experimental Results

The fabricated devices were tested by penetrating the biopsy needle into: (*A*) a physician training arrangement for a thyroid FNA biopsy; (*B*) porcine tissue consisting of fat and muscle layers; and (*C*) oils samples and saline solutions of various concentrations, which provided a method for calibrating the device. An HP 4195 spectrum analyzer was used to obtain impedance spectra and monitor the change in its resonance peaks.

3.3.1 Biopsy Training Setup

Figure 3.9(a) illustrates a procedure that is sometimes used for training healthcare professionals in thyroid FNA biopsy: a pickled olive simulates the thyroid nodule, while an Aquaflex® ultrasound gel pad (Model 04-02 from Parker Labs, Inc., USA) and a dampened sponge simulate the surrounding tissue. A trainee holds the ultrasound probe with one hand and inserts the needle into the target region (Figure 3.9b) while observing its position using a real-time 2D ultrasound image (Figure 3.9c).

This training setup with tissue model is used in test *A* (Figure 3.10a), and a typical sensor response as the biopsy needle advances into the sample is shown in Figure 3.10(b). A resonance mode with a relatively high frequency and large quality factor Q was selected for testing. When the needle was inserted from free space into the ultrasound gel

pad, the resonance frequency dropped from the 176 MHz to 154 MHz. Both the resonance frequency and the peak impedance decrease gradually with the advancement of the needle into the gel pad. After the needle tip reaches the olive, the resonance frequency stays almost constant while the impedance peak magnitude increases with advancement into the olive. From the gel pad surface to the olive, the total frequency decrease is ≈4 MHz from the initial 154 MHz, and the magnitude decreases by ≈800 Ω from the initial 2 KΩ. This kind of shift does not occur if the olive is missing, and these electrical characteristics are thereby indicative of a tissue contrast between the olive and the gel pad, which emulate a thyroid nodule and the surrounding tissue, respectively.

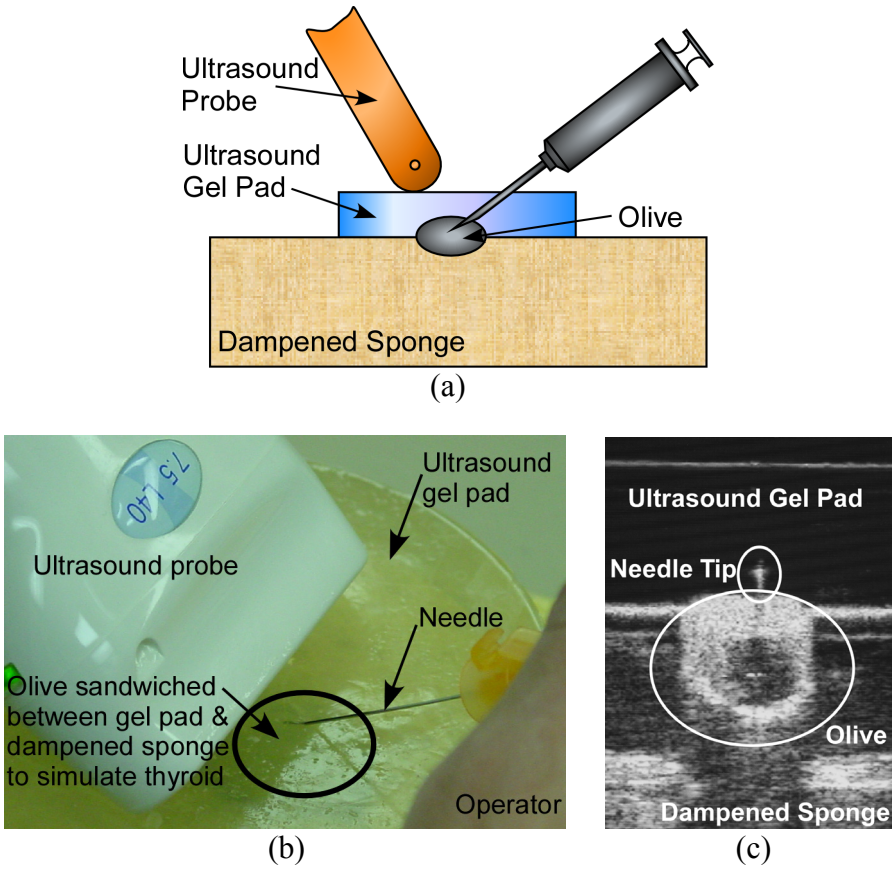

Figure 3.9: Physician training for thyroid biopsy. (a) Schematic diagram showing the training setup and tissue model. (b) Photo of operation. Medical ultrasound probe is used to guide the process. A sample ultrasound image is shown in (c).

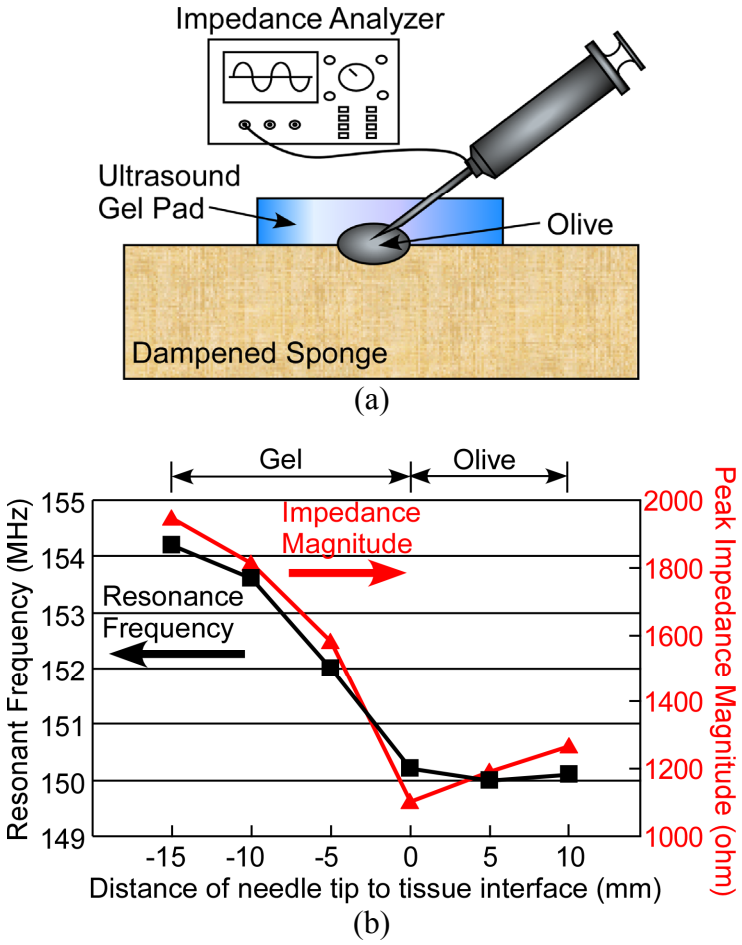

Figure 3.10: (a) Schematic diagram of the biopsy training setup used for test *A*. (b) Measured impedance resonance frequency and peak magnitude of the PZT sensor *vs.* proximity to tissue interface when the needle tip is inserted from the gel pad into the olive. Once the tip moved into the olive, the resonance frequency remained almost constant while the peak magnitude started increasing.

3.3.2 Porcine Tissue

For Test *B* involving samples of porcine fat and muscle tissue, the needle was first inserted, from free space, directly into either fat or muscle tissue to separately study the sensor response to each kind of tissue. The results are shown in Figure 3.11. While the resonance frequency drops as the needle is inserted into either tissue, the slope is smaller in muscle tissue. The impedance peak magnitude drops with increasing insertion depth in the fat, but increases in the muscle. These frequency and magnitude changes in the same

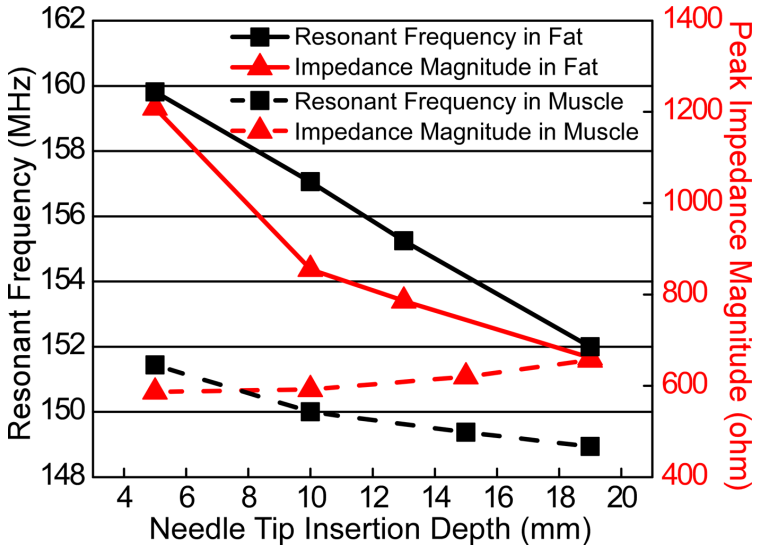

Figure 3.11: Measured resonance frequency and peak magnitude of the PZT electrical impedance *vs.* needle tip insertion depth from free space directly into fat or muscle.

type of tissue are likely due to signal attenuation or stray capacitance caused by the surrounding tissue, and constrain the sampling depth at which the sensor can be effective. However, as can be seen in Figure 3.11, this device shows clear contrast between fat and muscle up to a depth of >15 mm, which is adequate for thyroid and other superficial biopsies.

The device was also tested with layered samples of porcine fat and muscle tissue, and the results are shown in Figure 3.12. Both the resonance frequency and the impedance peak magnitude decrease gradually as the needle is inserted into the fat tissue. Then, at the insertion depth of about 9 mm, where the needle passes into a muscle layer, the impedance peak magnitude stops dropping, while the resonance frequency further drops with a much smaller slope (≈1/5 of that in fat). From the fat surface to the muscle, the total frequency change is ≈13 MHz from the initial 163 MHz, and magnitude changes about 1600 Ω from the initial 2100 Ω. When the results in Figure 3.11(b) and Figure 3.12 are compared, similar impedance characteristics can be observed for each kind of

tissue. This confirms that the characteristics shown in Figure 3.11 demonstrate the tissue contrast between porcine fat and muscle.

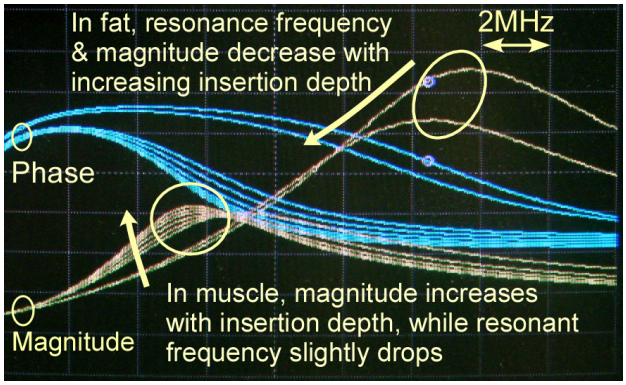

(a)

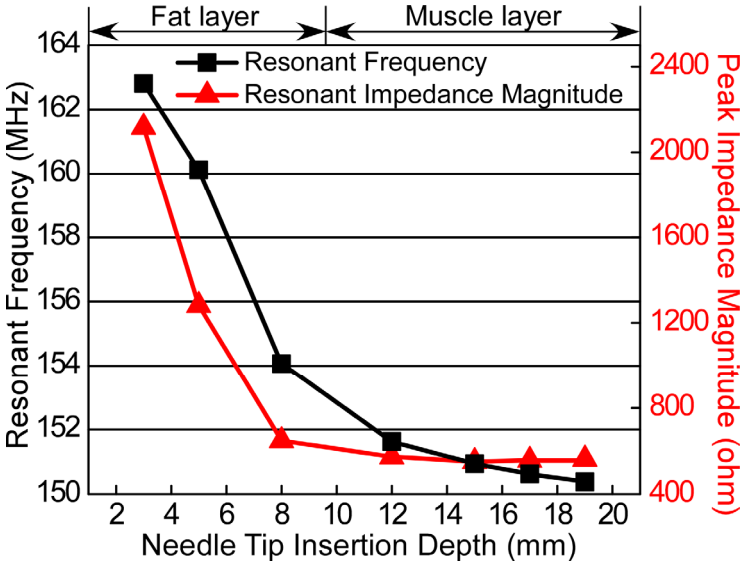

(b)

Figure 3.12: (a) Screen image of HP 4195 spectrum analyzer showing impedance resonance change when needle tip went from porcine fat layer to muscle layer. (b) Measured resonance frequency and peak magnitude of the PZT impedance *vs.* needle insertion depth into the porcine tissue consisting of fat and muscle layers.

3.3.3 Saline Solution and Oils

For the purpose of device calibration and modeling, the sensor was tested with samples that have known and controlled acoustic impedance (Z_a). These are oil samples

and saline solutions of varying concentrations. The sensor response was measured at a needle insertion depth of 5 mm for all cases. The Z_a of these samples ranged over 1.1-1.6×10^6 kg/m^2s, with Z_a of common tissue types toward the upper end of this range. The sample properties and experimental results of measured shift of resonance frequency are summarized in Table 3.1. These results are used in an empirical tissue contrast model described in Section 3.4.1.

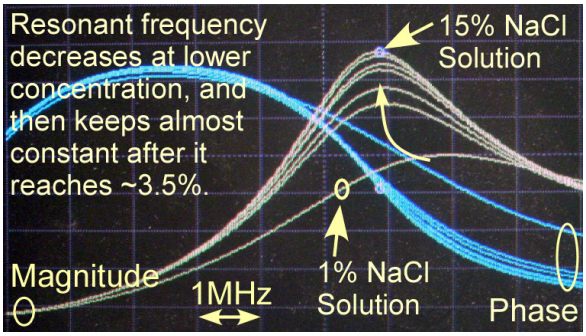

(a)

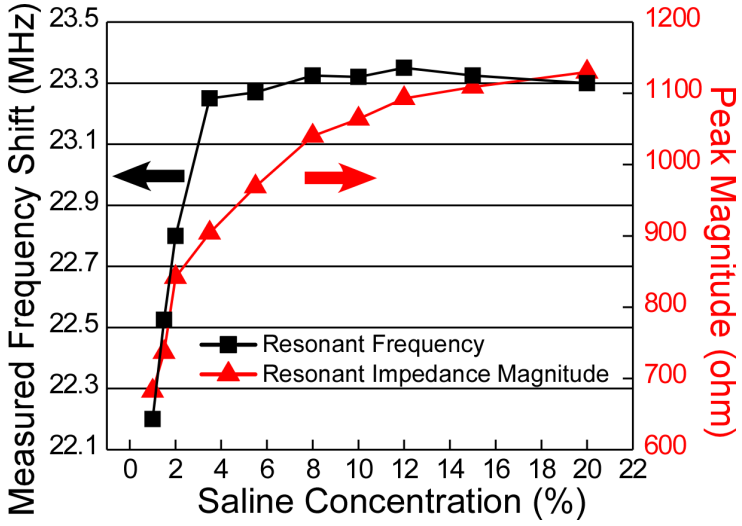

(b)

Figure 3.13: Measurement results of saline samples with concentration between 1% and 20%. (a) Screen shot of HP 4195 spectrum analyzer. (b) Measurement results shown as measured frequency shift and peak magnitude of impedance *vs.* saline concentration. Above ≈3.5%, the frequency shift remained approximately constant, similar to that in the reference [Zha04].

In the experiment with saline samples, solution concentrations from 1% to 20% were tested; the measurement results are shown in Figure 3.13. The measured shift of resonant frequency increased with greater saline concentration when the concentration was smaller than ≈3.5%, and remained approximately constant when the concentration became greater than ≈3.5%. This phenomenon is similar to that discussed in [Zha04], and is possibly due to saturation of available cation binding cites on the sensor diaphragm.

3.4 Analysis and Discussion

3.4.1 The Tissue Contrast Model

The resonance frequency shift (Δf) of the piezoelectric sensor is dependent on both the mass loading effect and elastic properties of the samples. The Z_a of a sample is the product of its density and acoustic velocity, the latter being further related to the elastic bulk modulus of the material. Thus an empirical tissue contrast model can be built for the biopsy device by plotting the measured Δf *vs.* Z_a, as shown in Figure 3.14(a). The data used in this plot are from Table 3.1. The relationship is approximately proportional, as shown in the shaded area, considering the uncertainty in the acoustic properties of the samples.

In Section 3.1.1, a modified BVD equivalent circuit is described using inductance $L_{m(n)}$ to model the effect of the mass loading of the diaphragm to the PZT disc. To include the tissue loading effect in the model, $L_{m(n)}$ can be extended by adding in series another equivalent loading inductance $L_{eq(n)}$. This additional inductance is an equivalence

that includes the effect of both mass and elastic loading. The new anti-resonance frequency for the impedance is therefore:

$$f_{a(n)} = \frac{1}{2\pi\sqrt{(L + L_{m(n)} + L_{eq(n)})C_n}}, \qquad n = 1,3,5... \tag{3.9}$$

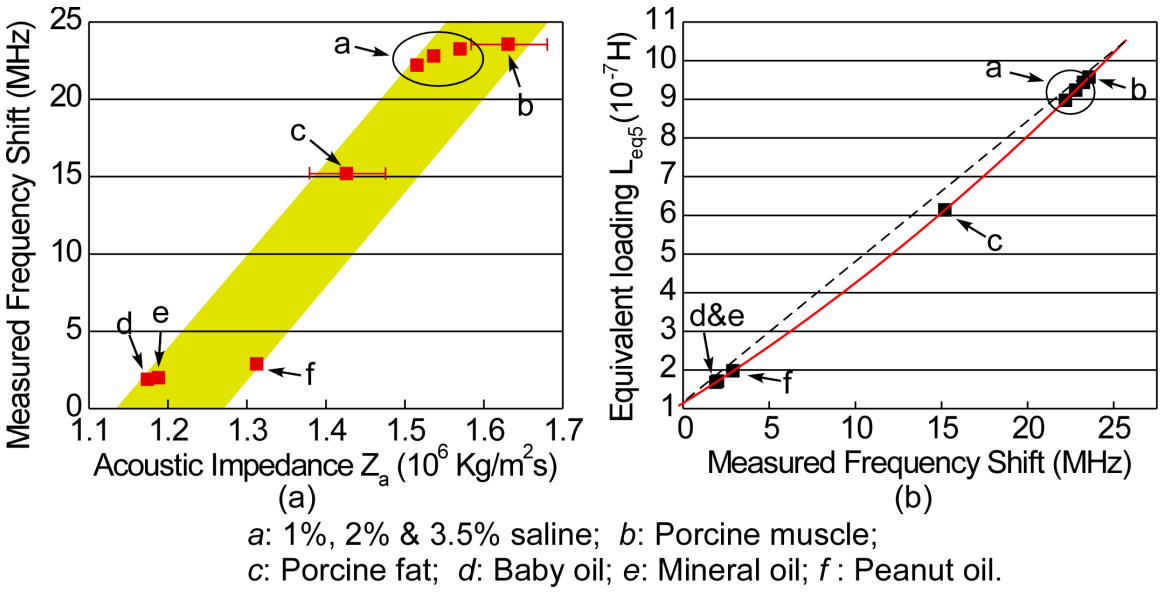

Figure 3.14: (a) Measured resonance frequency shift *vs.* acoustic impedance of the samples. The error bars on the data for porcine samples indicate the lack of certainty in calculated values of acoustic impedance Z_a. (b) Calculated equivalent loading L_{eq5} as a function of frequency shift for the samples. The dotted line provides a linear comparison. Data are listed in Table 3.1.

In the experiments, the 5th harmonic mode (at 176MHz in air) was found to have a higher Q than the fundamental and 3rd harmonic mode, and was consequently selected for measurement. This is similar to the situation discussed in [Zha05], and is possibly due to less acoustic energy loss in the 5th harmonic mode than in the 1st and 3rd modes, but the underlying physical reason remains unclear. Therefore, the 3rd RLC_n branch (for the 5th harmonic mode) of the modified BVD circuit is of the most interest. The calculated equivalent loading L_{eq5} for each of the samples, used to build the empirical tissue contrast model, is listed in Table 3.1 and plotted as a function of the measured frequency shift Δf_{a5}

in Figure 3.14(b). The two plots in Figure 3.14 provide the empirical tissue contrast model (*i.e.*, the relationship of Z_a to Δf_{a5}) and the relationship of L_{eq5} to Δf_{a5}. These relationships can be used with the modified BVD circuit model to relate the physical parameters of the device and samples to Δf for design and optimization of the sensor.

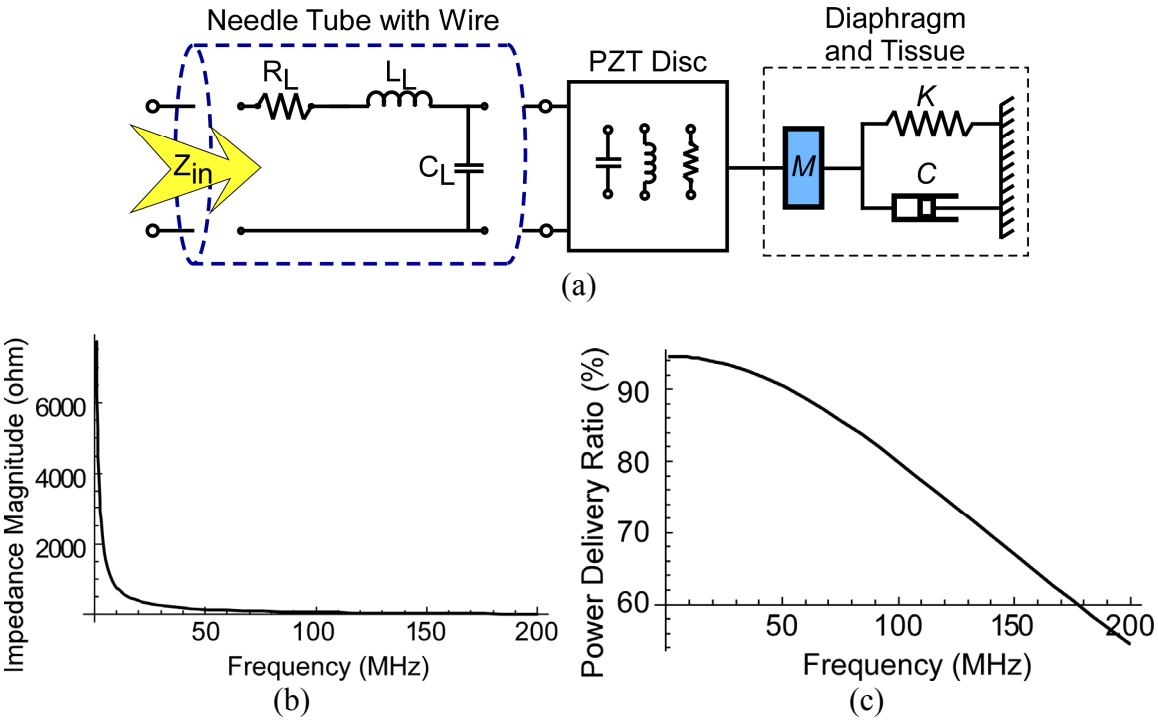

Figure 3.15: A transmission line analysis carried out to evaluate the effect of the needle tube and the copper wire on the measured impedance characteristics. A coaxial-line model was used and the PZT disc was replaced by an equivalent static capacitor. (a) The transmission line circuit model. (b) Input impedance Z_{in} *vs.* frequency. (c) Ratio of power delivered to the PZT disc through the needle tube *vs.* frequency.

3.4.2 Transmission Line Assessment

The transmission line characteristics of the stainless steel needle tube, along with the inside copper wire, are not related to tissue properties and are thus not required to detect a contrast in the tissue. However, they are worth considering because they can affect the measured electrical impedance. In the absence of a liquid within the biopsy

Table 3.1: Test results and acoustic properties of samples.

Samples	Δf (MHz)	Density (kg/m^3)	Sound Velocity (m/s)	Acoustic Impedance Z_a (10^6 kg/m^2s)	Equivalent Loading Inductance L_{eq5} (10^{-7} H)
a. Saline-1%*	22.2	1005	1507	1.515	8.98
Saline-2%*	22.8	1012	1518	1.537	9.24
Saline-3.5%*	23.3	1023	1534	1.570	9.44
b. Porcine muscle[#]	23.6	1040	1568	1.630	9.57
c. Porcine fat[#]	15.2	970	1470	1.426	6.14
d. Body oil[$]	1.9	821	1430	1.174	1.68
e. Mineral oil[$]	2.0	825	1440	1.188	1.71
f. Peanut oil[$]	2.9	914	1436	1.313	1.98

Sources for density and sound velocity data:

* Gucker et al., *Chemistry*, vol. 55, pp. 12-19, 1966.

[#] Dowsett et al., *The Physics of Diagnostic Imaging*, Thomson Science, 1998

[$] A.R. Selfridge, *IEEE Transactions on Sonics and Ultrasonics*, vol.SU-32, pp. 381-94, no.3, 1985

needle, *i.e.* while the needle is approaching the target, the connection wire to the sensor and the surrounding needle structure can be approximately modeled as a coaxial line. An equivalent circuit model is shown in Figure 3.15(a). In this model, the PZT disc can be replaced with an equivalent static capacitor for the transmission line analysis, so the piezoelectric effect is not considered. The extension wire that connects the needle tube to the impedance analyzer is neglected because it can be compensated for during the measurement. According to the classic transmission line theory for a terminated lossy coaxial line [Poz05], the input impedance Z_{in} is:

$$Z_{in} = Z_0 \frac{Z_P + Z_0 \cdot \tanh \gamma l}{Z_0 + Z_P \cdot \tanh \gamma l} \tag{3.10}$$

where Z_P is the impedance of the equivalent static capacitor replacing the PZT disc, and the capacitance value is 20 pF for this analysis; l is the length of the coaxial line and is equal to 25 mm; Z_0 and γ are the transmission line characteristic impedance and the complex propagation constant, respectively, and are both related to the transmission line parameters R_L, C_L, and L_L by equations found in the classic transmission line theory. These parameters R_L, C_L, and L_L are further related to the physical parameters of the coaxial line, including the radius of the copper wire r_a which is 25 μm, and the inner radius of the needle tube r_b which is 292 μm. Since air is used as the dielectric material for this coaxial line model, its permittivity and permeability properties are used in the analysis.

According to this approximate analysis, the calculated input impedance Z_{in} of this model drops smoothly within the frequency range of interest (Figure 3.15b), and the length of the equivalent coaxial cable can be considered much shorter than the calculated transmission line characteristic wavelength. Thus, the effect of the needle tube can be

basically ignored for our purpose. The calculated ratio of the power delivered to the PZT disc through the needle tube and copper wire varies almost linearly with frequency from ≈95% at 1 MHz to ≈65% at 160 MHz (Figure 3.15c).

3.4.3 Other Issues

The working depth of the device is limited by the length of the needle to 25 mm, and as discussed in the porcine tissue tests in Section 3.3.2, is also limited by the degradation of sensor performance due to possible signal attenuation or stray capacitance. The working depth of the current device is enough for the anticipated use in shallow FNA procedures such as thyroid biopsy, the working depth of which is usually <15 mm. In order to be used in deep tissue biopsies such as those for breast or celiac organs, longer needles are required. This increased needle length and thus greater insertion depth into tissues can cause further degradation of sensor performance, and will be investigated in Chapter 4.

In this effort, a Φ 200 μm PZT disc was embedded in a Φ 300 μm cavity in a 20-gauge biopsy needle. For needles of smaller gauge that are sometimes needed in biopsy procedures, the wall thickness of the needle tube reduces, while the curvature of the wall increases, requiring the size of the PZT disc to be scaled down accordingly. For example, a 27-gauge needle has an outer diameter of only 406 μm and wall thickness of 102 μm. As discussed in Chapter 2, the LEEDUS/SEDUS process that has been used to fabricate the discs has the capability of handling feature size as small as 25 μm [Li04, Li05, Li06] and can provide PZT elements much smaller than the current 200 μm diameter. However, the integration of these discs onto the biopsy needle can be a problem when the

size is too small to handle manually or by a pick-and-place machine. A new approach for this integration is needed in this case.

During FNA biopsy, it is sometimes desirable to have the capability of keeping the needle tip precisely in place after aspiration starts, so that a subsequent percutaneous alcohol injection can be performed to reduce the risk of some side effects such as seeding [Ger09] and pseudoaneurysm [Baz02]. However, after a target site of the needle tip is located with the developed sensor, the sensor reading may change when sample aspiration is performed. This would be caused by the change in the boundary condition of the diaphragm as adjacent tissue is being removed by aspiration. To provide an approach to monitor any unwanted needle movement after aspiration starts, a potential solution is to integrate additional sensors on the needle tube at a distance away from the needle tip where tissue is removed. These additional sensors can also be used for differential operation of the sensors as discussed in the next chapter.

CHAPTER 4

The Development of a Differential Mode Piezoelectric Tissue Contrast Sensor with Integrated Interface Circuit

The piezoelectric tissue contrast sensor described in Chapter 3 cannot effectively differentiate tissue contrast when the penetration depth is greater than ≈15 mm. For example, in a test using breast phantom that has built-in artificial nodules, although resonance frequency shifts can still be observed in the impedance characteristics when the needle tip approaches the artificial nodules, these shifts are much less obvious compared with the results obtained in the previous gel-pad/olive or porcine tissue experiments, and the difference between the results of frequency shift with and without artificial nodules in the needle insertion path is relatively small. Signal attenuation and stray capacitances caused by the needle tube and surrounding tissue can become substantial in certain tissue environments or at large insertion depth. Sensitivity may not be high enough to differentiate these testing materials. This could make it difficult to clearly indicate the tissue contrast during an actual biopsy procedure, particularly for deep tissue biopsy.

To address this issue, and to eliminate the requirement of the expensive impedance analyzer so that this technology can be low-cost and widely accessible, a proposed solution is described in this chapter. This approach implements the differential mode piezoelectric tissue contrast sensors with locally integrated interface circuits to eliminate any common mode changes caused by attenuation and parasitic capacitances,

thus potentially enabling application of the device to deep tissue detection. Section 4.1 discusses the design of the differential sensor and design and simulation of the interface circuit. Section 4.2 describes the details of the device fabrication process involving the UM 3 μm CMOS process. The fabricated device and interface circuit are tested and the preliminary results are discussed in Section 4.3.

4.1 Design of Differential Tissue Contrast Sensor with Interface Circuit

Differential mode operation of sensors is usually used to eliminate any common mode interference and noise which are present in both an active sensor subject to the measurand and a reference sensor screened from the measurand. These interference and noise can become significant and bury the desired measurand signal in a single-sensor operation mode. In the differential mode, the difference between the outputs of the two sensors is extracted and is free of these interference and noise, revealing the buried measurand signal. For the piezoelectric tissue contrast sensor, an interface circuit is necessary to locally convert the measurand into a signal that is not easily affected by the increased tissue depth and other parasitics. The differential mode is also enbabled by simply subtracting the circuit outputs of the active and reference sensors. Two schemes to implement the differential tissue contrast sensor are discussed in Section 4.1.1, and the design and simulation details of the interface circuit are given in Section 4.1.2.

4.1.1 Piezoelectric Tissue Contrast Sensor in Differential Mode

Two schemes are proposed to configure differential mode sensors for tissue differentiation during FNA biopsy. In the first scheme, a set of two sensors, shown as

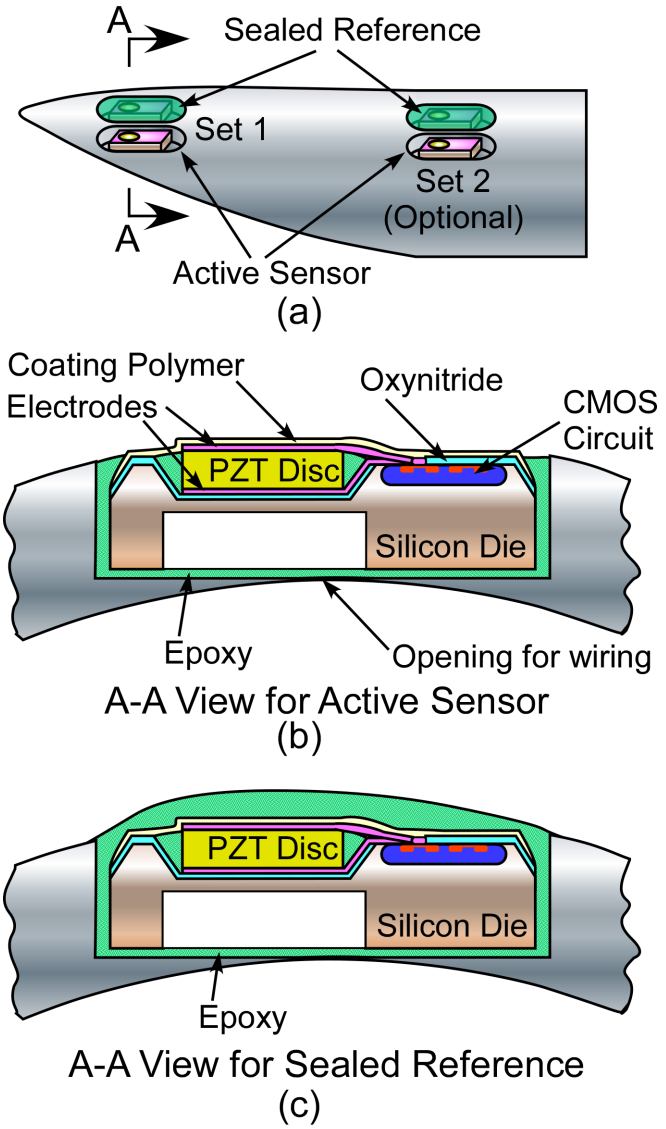

Figure 4.1: Proposed differential mode piezoelectric tissue contrast sensor.

Set 1 in Figure 4.1(a), are integrated on the biopsy needle. One sensor actively measures the tissue characteristics, while the other is sealed in acoustic insulating material such as epoxy or polystyrene. This scheme is used to eliminate any common mode changes in the sensor response caused by parasitic capacitance and other interference from the human body, *etc*. In the second scheme, another set of two sensors (Set 2) with the same configuration as Set 1 are integrated on the needle tube at a distance from Set 1. This

scheme is proposed so that at the tissue interface one set of sensors can be inside the target tissue and the other outside, providing tissue contrast by the differential readout between the two sets. As shown in the cross sectional view A-A for an active sensor in Figure 4.1(b), a PZT disc is mounted in an etched cavity on a silicon die, and the interface circuit is located beside the cavity on the same die. A thin polymer coating such as parylene is applied to insulate the whole device. Due to the curvature of the needle sidewall, an opening at the center of the bottom of the cavity is formed when the cavity is deep enough, and is used to route connecting wires into the lumen of the needle. A reference sensor sealed by acoustic insulating material such as epoxy or polystyrene is shown in Figure 4.1(c). A perspective view of an active or reference sensor without epoxy is shown in Figure 4.2. The dimensions of the sensor die are limited by the size of the cavity that can be made on the needle sidewall, and a die size of 900 μm (L) × 300 μm (W) × 100 μm (H) is selected for a 20-gauge needle.

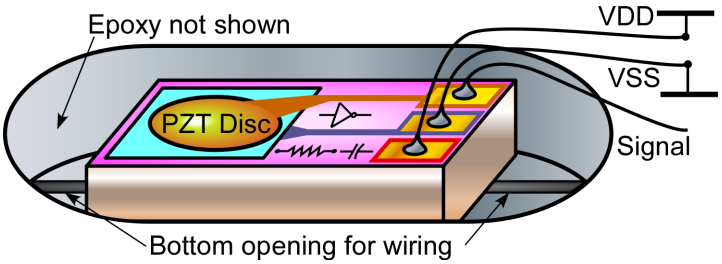

Figure 4.2: Perspective view of an active or reference sensor module placed in a cavity etched on the wall of a biopsy needle. Insulating epoxy is not shown.

The active and reference sensors can be placed in two separate slots as shown in Figure 4.1(a), or alternatively they can be arranged in one slot and stacked together with each other as shown in Figure 4.3. Two possible arrangements are shown in Figure 4.3(a) and (b), respectively. The one in Figure 4.3(b) is preferred to allow wire bonding

to the metal pads on the top surface of the sensor die, and also to increase the gap between the active and reference sensors to minimize any possible crosstalk. Since the maximum possible depth of the cavity on the sidewall of a 20-gauge needle is ≈170 μm, which is smaller than the stacked height of two sensors (≈200 μm), the top of the active sensor is slightly protruding above the needle outer surface. In the design shown in Figure 4.3(b), an optional steel sealing plate can be used to cover the cavity opening to the inner side of the needle underneath the reference sensor, providing extra support during sensor integration into the cavity.

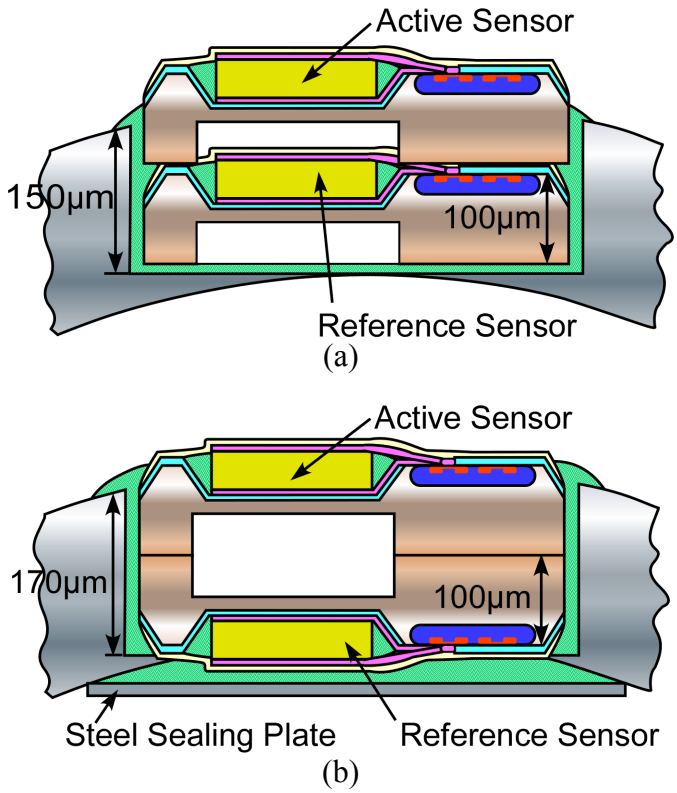

Figure 4.3: Alternative arrangements of the active and reference sensors in one cavity on a biopsy needle. The design shown in (b) is preferred.

4.1.2 Interface Circuit Design and Simulation

The differential design of the biopsy sensor for deep tissue applications requires interface circuits that can simplify the tissue contrast signal readout and enable signal differentiation. The original measurement scheme used an impedance analyzer to obtain the impedance spectra of a PZT disc, and thus indicating tissue contrast by a change in the frequency of an impedance resonance peak. However, the relatively large acquisition time and limited number of channels of the analyzer limit its usefulness for differential tissue contrast sensors.

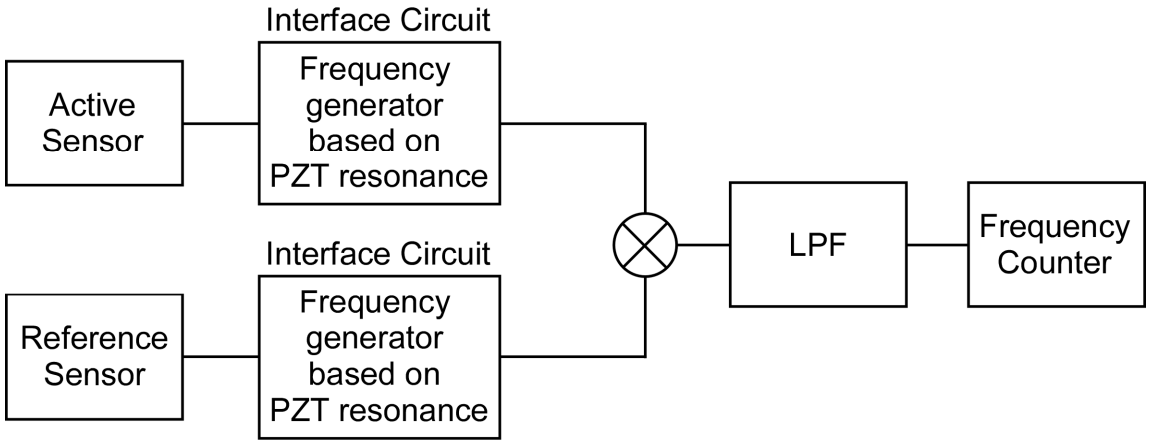

Figure 4.4: Functional block diagram of the sensors and their interface circuits in the differential configuration.

An interface circuit is thus needed to dynamically convert the resonance-shifting characteristic of the PZT disc into a form that can then be easily processed to provide a differential signal. In addition, the interface circuit should be located beside the sensor, minimizing the length of the signal path and any parasitics. This on-chip integration also requires the interface circuit to be simple considering the limited die area available for the whole device. The most important shift of the resonance characteristics is in frequency. Therefore, the interface circuit should be capable of tracking the resonance frequency

shift of the piezoelectric sensor and accordingly generate a clock signal at the tracked frequency for later processing. The output signals from the interface circuits of the sensors in a differential configuration can then be simply fed into an external frequency mixer followed by a low pass filter (LPF) to obtain the frequency difference, which can be read out by a frequency counter. The functional block diagram of such a sensor-circuit configuration is shown in Figure 4.4. The cost of a frequency mixer and counter is much lower than that of an impedance/network analyzer, and can be easily integrated with other signal processing circuits if needed. This can potentially benefit future commercialization of the device.

Alternatively, the clock signal at a tracked frequency can be converted into a voltage signal using a frequency-to-voltage converter circuit and read into computer for further processing. The frequency-to-voltage converter has to be operated at a high frequency with a low converting time period, so that the sensor readout can be pseudo-realtime.

4.1.2.1 Overall Design of the Oscillating Interface Circuit

Similar to a quartz crystal which can be used as a frequency reference for electronic oscillating circuits, the piezoelectric PZT sensor can work based on piezoelectric resonance. The interface circuit that can convert the resonance into frequency is basically an oscillating circuit working at a frequency set by the PZT sensor. The quality factor Q of a PZT sensor is much lower than that of a quartz crystal resonator, and SPICE simulation is necessary for the oscillating circuit design to verify oscillation can be started at the designed Q of the sensor.

Figure 4.5 shows the Pierce oscillating circuit, which is the most commonly used crystal oscillating circuit. As in other active oscillating circuits, this circuit consists of an amplifier and a feedback network. A CMOS inverter in the circuit is used as a high-gain and high-bandwidth amplifier when the feedback resistor R_f is present. The inverter amplifier provides a phase shift φ of approximately 180° from its input to output, and the feedback network formed by the crystal X_1, R_1, C_1, and C_2 provides another 180° phase shift θ at its resonance frequency, making the total phase shift around the loop to be 360°. This satisfies one of the Barkhausen criteria required to sustain oscillation. The other condition requires a closed loop gain $A \cdot \beta \geq 1$ for startup and sustaining oscillation, and can be satisfied with appropriate design of the element values. The inverter-based Pierce oscillating circuit can provide the required interfacing function with a simple structure, which is preferred given the limited device size.

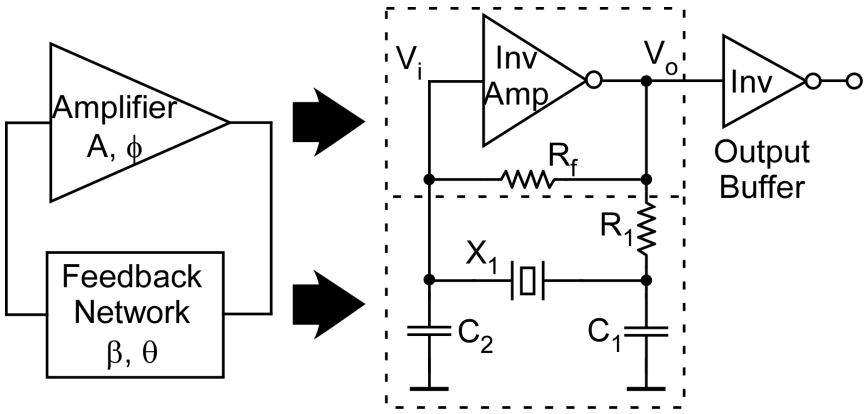

Figure 4.5: Overall structure of the Pierce oscillating circuit.

The Pierce oscillating circuit is selected as the primary candidate for this application, while other types of simple CMOS amplifier or variations of the inverter circuits are considered as well. A crystal oscillator circuit can also be built using BJT transistors, although the configuration of such a circuit would be more complex. Some of

the commonly used active oscillating circuits use the phase-locked loop (PLL) to track the resonance frequency of a quartz crystal or other sensing resonators [Fer97], but these circuits require components such as a voltage-controlled oscillator (VCO) and phase comparator, and are too complex for integration in this application.

4.1.2.2 Circuit Design and Analysis

In this section, the electrical characteristics of the PZT resonator, the analysis of the feedback network in the Pierce oscillator circuit, and the design and analysis of several inverter amplifier configurations are discussed in details.

A. Electrical Characteristics of the PZT Resonator

The piezoelectric characteristics of the PZT disc are similar to those of a quartz crystal which is commonly used as a frequency reference in clock generation circuits. As shown in Figure 4.6(a), the electrical characteristics of the piezoelectric resonator around its fundamental mode frequency are commonly modeled by the equivalent circuit consisting of motional elements L_S, C_S and R_S, and a static capacitance C_P. The reactance of this equivalent model *vs.* frequency is shown in Figure 4.6(b).

As indicated in Figure 4.6(b), there are two resonance frequencies in the electrical characteristics of the resonator: series resonance frequency ω_S, and anti-resonance or parallel resonance frequency ω_P. At ω_S, the resonator is in series resonance mode, its impedance $Z(\omega)$ is at a minimum and purely resistive, and current flow will be at a maximum. At frequencies between ω_S and ω_P, the resonator is in parallel resonance mode, the reactance of the resonator becomes inductive, its $Z(\omega)$ is at its maximum, and current flow will be at its minimum. The frequencies are defined as

$$\omega_S = \frac{1}{\sqrt{L_S C_S}} \tag{4.1}$$

$$\omega_P = \omega_S \sqrt{1 + \frac{C_S}{C_P}} \tag{4.2}$$

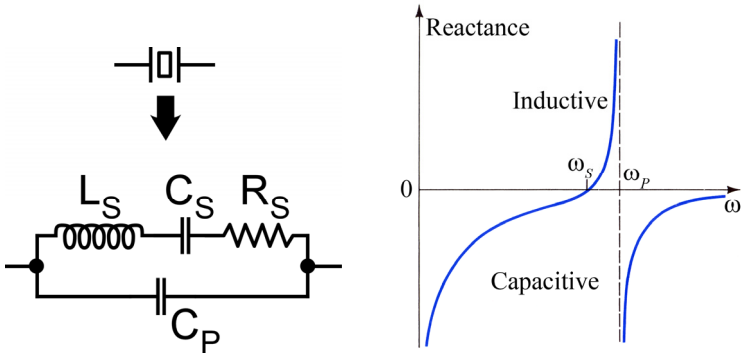

(a) (b)

Figure 4.6: (a) Equivalent circuit for a piezoelectric resonator. (b) Reactance *vs.* frequency of the resonator [Sed04].

Table 4.1: Element parameters for the equivalent circuit of the PZT disc (based on 200 μm diameter PZT-5H disc).

Thickness (μm)	Diameter (μm)	Mode	ω_S (MHz)	C_P (pF)	L_S (μH)	C_S (pF)	R_S (Ω) (est.)
50	200	Longitudinal	38.46	18.91	7.247	2.363	50
100	200	Longitudinal	19.23	9.45	57.95	1.182	200
50	200	Transverse	9.615	18.91	463.6	0.591	500

The equivalent circuit in Figure 4.6(a) is usually for transverse shear mode, and is exclusively used for crystal oscillator design in industry because most of the commonly-used quartz crystal for clock generation is in AT- or BT-cut thickness shear mode. For the biopsy tool application, the PZT disc can work in either longitudinal or transverse mode. From Equation 3.2, as usually $C_S << C_P$, we have $\omega_S \approx \omega_P$ for transverse mode. In longitudinal mode, ω_P is defined by Equation 3.1, and Equation 3.2 still holds. Therefore

we still have $\omega_S \approx \omega_P$. The resonance frequencies for both modes are close to each other, and the circuit in Figure 4.6(a) will be used as the equivalent model in all the following designs regardless of the actual sensor mode in order to simplify the process. The element parameters listed in Table 4.1 are estimated from the same PZT material properties as those in Chapter 3, and are used for the circuit design and simulation.

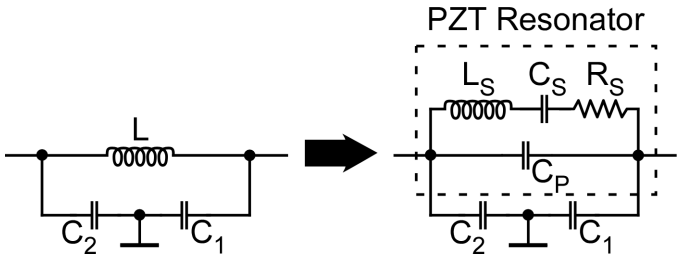

Figure 4.7: Colpitts feedback configuration with the inductor substituted with a PZT resonator.

B. Oscillator Feedback Network

As discussed in Section 4.1.2.1, the feedback network should provide a phase shift θ=180° and a feedback ratio β so that $A\beta \geq 1$. In series mode resonance, the resonator operates at maximum currents and has large power consumption. The single-frequency resonance also raises difficulty in feedback network matching. Since the PZT resonator becomes inductive in parallel resonance, it can be simply used to substitute the inductor in LC-tuned oscillator circuits. There are two commonly used configurations of LC-tuned oscillators: Colpitts oscillator and Hartley oscillator [Sed04]. It is easier to use Colpitts configuration with PZT resonator because in this configuration two capacitors are connected in parallel to an inductor to form a capacitive divider for the feedback path, and the inductor can be simply substituted by a PZT resonator (Figure 4.7). In contrast, the Hartley oscillator uses two inductors and one capacitor to form the feedback path, and

is harder to implement using PZT resonator. The Pierce oscillator circuit in Figure 4.5 is based on the Colpitts feedback configuration.

As shown in Figure 4.5, the resonator X_1 appears as a large inductor when it is in parallel resonance, and together with C_1 and C_2, it forms a π network that provides a 180° phase shift, thus satisfying the phase requirement for oscillation. When the resistor R_1, which is used to limit the resonator driving level is ignored, feedback in this configuration is obtained by a capacitive divider formed by C_1 and C_2 when X_1 is at resonance. The feedback ratio β is thus given as:

$$\beta = \frac{C_1}{C_2} \tag{4.3}$$

When choosing C_1 and C_2, their ratio β should satisfy the requirement $A\beta \geq 1$. Larger β can increase the loop gain and thus help in oscillation start-up. However, if β becomes too large, the circuit becomes unstable and the oscillation will not be determined by the resonator alone. The series combination of C_1 and C_2 (denoted as C_O) is in parallel with X_1. The value of the parallel combination of C_O, C_P and any parasitic capacitances should be much larger than C_S so that the resonance frequency is less affected by stray capacitance and is primarily determined by L_S and C_S. From Figure 4.7, the resonance frequency ω determined by this feedback configuration is defined in Equation 4.4. When $C_P + C_O >> C_S$, ω is only determined by the motional parameters L_S and C_S.

$$\omega = \frac{1}{\sqrt{L_S C_S}} \sqrt{1 + \frac{C_S}{C_P + C_O}}, \quad \text{where } C_O = \frac{C_1 C_2}{C_1 + C_2} \tag{4.4}$$

The resistor R_1 isolates the output of the amplifier from the resonator so that the resonator is not overdriven and a clean waveform can be obtained from the output of the amplifier. It also prevents spurious high-frequency oscillation by forming a low pass

filter with C_1, giving a cutoff frequency $(2\pi R_1 C_1)^{-1}$. The value of R_1 is usually chosen to be roughly equal to the capacitive reactance of C_1 at the frequency of operation, or the value of combined impedance of the X_1, C_1, and C_2. However, R_1 can reduce the loop gain due to voltage divider effect with C_1, and can also shift the resonance frequency and introduce additional phase delay. Therefore, for high frequency, using this series feedback resistor is not always feasible as the additional phase shift makes it impossible to satisfy the 180° phase requirement. In this case, R_1 can be simply skipped, or replaced by a capacitor C_{R1} with a value approximately equal to C_1 or the input impedance of the resonator.

C. Amplifier Design

In this section, several amplifier designs will be discussed. The design results will be verified with HSPICE simulation which is discussed in the next section.

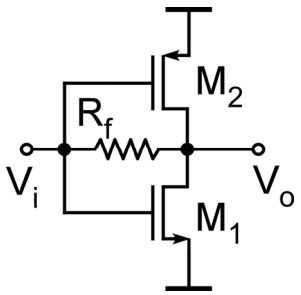

Figure 4.8: CMOS inverter biased in linear region used as a compact high-gain wideband amplifier.

(a) CMOS inverter amplifier with passive feedback resistor

While there are various types of CMOS amplifiers that can be used in the oscillating circuits, the most commonly used type is a CMOS inverter that is biased in the linear region as a compact high-gain wideband amplifier. The CMOS inverter amplifier

will be used as the primary type in the design due to its simple structure that allows small die size, as well as its proven feasibility for oscillating circuits.

Table 4.2: UM 3 μm CMOS process characteristics used for circuit design and analysis.

k_n' (A/V^2)	k_p' (A/V^2)	V_{tn} (V)	V_{tp} (V)	λ_n (V^{-1})	λ_p (V^{-1})
35.6×10^{-6}	17.5×10^{-6}	0.95	-0.55	1.900757×10^{-2}	4.495901×10^{-2}

As shown in Figure 4.8, a resistor R_f is connected between the input and output of a CMOS inverter, setting the circuit operating point at V_i=V_o. In order to get a symmetrical transfer characteristic between V_i and V_o so that the amplifier gain is maximized in the linear region, the NMOS and PMOS devices should be matched. This can be achieved when

$$k_n^{'}(\frac{W}{L})_n = k_p^{'}(\frac{W}{L})_p \tag{4.5}$$

or equivalently, $\frac{(W/L)_n}{(W/L)_p} = \frac{k_p^{'}}{k_n^{'}} = \frac{1}{2.034}$. When L_n and L_P are both at the minimum value of 3 μm, $\frac{W_n}{W_p} = \frac{1}{2.034}$. The inverter threshold voltage or the targeted operating point V_{TH} at V_i=V_o is given by

$$V_{TH} = \frac{r(V_{DD} - |V_{tp}|) + V_{tn}}{1+r}, \qquad r = \sqrt{\frac{k_p^{'}(W/L)_p}{k_n^{'}(W/L)_n}}, r = 1 \text{ for matched inverter.} \tag{4.6}$$

In the UM CMOS process, a source of ±5 V is used. This is equivalent to V_{DD}=10 V with respect to GND, and thus V_{TH}= 5.2 V, or 0.2 V in terms of a ±5 V source.

The current flowing through the inverter is

$$I_D = \frac{1}{2}(\frac{W}{L})_{n/p} k_{n/p}^{'}(V_{GS} - V_{tn/p})^2 \tag{4.7}$$

To calculate the open-loop gain A of the inverter, the conductance g_m and output resistance r_o are given by

$$g_m = \sqrt{2(\frac{W}{L})k^{'}I_D}, \quad r_o = \frac{1}{\lambda I_D} \tag{4.8}$$

Plug in the process values, we have

$$g_{mn} = 0.1513\times10^{-3}(\frac{W}{L})_n, \quad g_{mp} = 0.0744\times10^{-3}(\frac{W}{L})_p$$
$$r_{on} = 163.64\times10^{3}\cdot(\frac{L}{W})_n, \quad r_{op} = 140.73\times10^{3}\cdot(\frac{L}{W})_p$$

The intrinsic open-loop gain of the inverter is

$$A_i = -(g_{mn} + g_{mp})(r_{on} \parallel r_{op}) \tag{4.9}$$

and for the UM process, it is calculated that A_i = -14.77 regardless of the W/L ratio. The actual open-loop gain A_v is smaller than A_i due to the load presented by the oscillation feedback network.

The propagation delay t_p of the amplifier can be estimated using the following equations [Sed04]:

$$t_p = \frac{1}{2}(t_{PHL} + t_{PLH}) \tag{4.10}$$

$$t_{PHL} = \frac{2C}{k_n^{'}(W/L)_n(V_{DD} - V_{tn})}\left[\frac{V_{tn}}{V_{DD} - V_{tn}} + \frac{1}{2}\ln\left(\frac{3V_{DD} - 4V_{tn}}{V_{DD}}\right)\right] \tag{4.11}$$

As shown in Equation 4.11, in order to increase the bandwidth and operate at high frequency especially for the longitudinal mode of the resonator, the load capacitance C should be kept at minimum, and W/L ratio should be increased. Larger process transconductance factor k' and higher supply voltage also help reduce the delay and increase the bandwidth.

The feedback resistor R_f approximately determines the input impedance Z_{in} of the CMOS inverter amplifier by the Miller reflection effect:

$$Z_{in} = \frac{R_f}{A} \tag{4.12}$$

and Z_{in} is usually matched to the load impedance Z_L of the oscillation feedback network. The feedback resistance R_f should be as large as possible for the CMOS inverter amplifier to obtain a large input impedance and sufficient isolation between the input and output nodes of the amplifier. However, it is usually difficult to make resistors more than 100 KΩ using CMOS process. Remedies are discussed in the following sections.

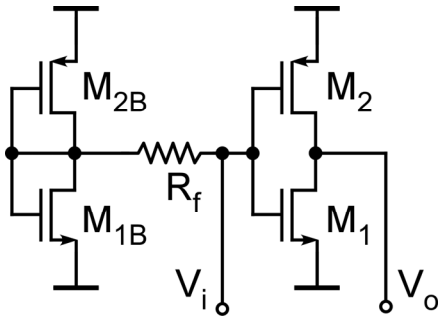

Figure 4.9: CMOS inverter amplifier using reference inverter for biasing.

(b) CMOS inverter amplifier with reference inverter

An alternative implementation of the inverter amplifier is shown in Figure 4.9. A biasing voltage that sets the inverters in the high-gain linear region is generated using a reference inverter consisting of two diode-connected transistors M_{1B} and M_{2B} that have the same dimensions as M_1 and M_2. This biasing voltage is then transferred to the amplifying inverter through R_f. The input impedance of this amplifier is $Z_{in} \approx R_f$, reducing the required value of the resistor R_f by a ratio of A. As R_f is only connected to the input node of the amplifying inverter, it is not subject to the large signal variations

that exist at the output node of the amplifier, making it easier to implement this resistor with special techniques such as active resistors which are discussed in the next section.

(c) CMOS inverter amplifier with active feedback resistor

As mentioned in the previous sections, a large feedback resistor is desirable for both Design (*a*) and (*b*), while it is usually difficult to make resistors more than 100 KΩ in the CMOS process. These resistors can alternatively be implemented using active resistors.

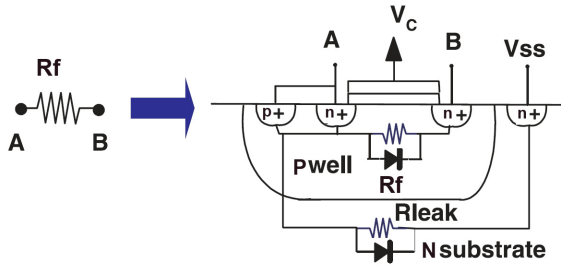

Figure 4.10: Large resistor implemented using reverse-biased PN junction in NMOS transistor.

The simplest active resistor is a floating PN junction available within a transistor's well (basically a diode). As shown in Figure 4.10, it can be implemented with the reverse-biased drain/source-well junction of an NMOS transistor in cutoff by setting V_C=V_{SS}. However, these resistors have relatively limited voltage swing (<0.3 V) to prevent the junction from becoming forward biased. This makes it difficult to be used with amplifier Design (*a*) due to the large swing at the output node of the amplifier, although it should work well with Design (*b*). According to HSPICE simulations, the resistance from this implementation is 187.5 MΩ when V_{BA} = -0.3 V, 6.25 MΩ when V_{BA} = -0.4 V, and can reach GΩs in the reverse bias region.

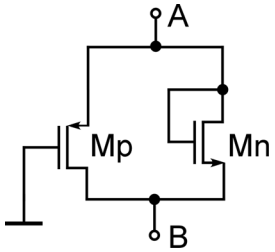

Figure 4.11: Active resistor implemented using MOS transistors.

Figure 4.11 shows an alternative implementation of an active resistor using a diode connected NMOS transistor in parallel with a saturated PMOS transistor. It is also possible to implement an active resistor using just a PMOS transistor biased in triode region. However, in order to get large resistance with these schemes, a very small *W/L* ratio of the transistors is needed in order to reduce the current I_D, thus requiring large *L* and a large device area.

Another scheme to get large active resistor uses two transistors in sub-threshold region so as to get large resistance with small device area; however, it requires dedicated reference voltages for biasing which is not favorable in this application.

4.1.2.3 Design Simulation and Discussion

The oscillator circuits with different amplifier and feedback network designs discussed in the previous section have been simulated in HSPICE. This section discusses the simulation results. Considering the uncertainty in the values of the elements in the PZT equivalent circuit model, several sets of element parameters for the feedback network are selected as listed in Table 4.3, following the design guideline discussed in Section 4.1.2.2.B with consideration of the UM 3 μm CMOS processing capability (Table 4.4).

Table 4.3: Sets of element parameters of the feedback network used for simulation.

β	C_1 (pF)	C_2 (pF)	R_1 (kΩ)	C_{R1} (pF)
1	5	5	-	-
			2.4	-
			9.6	-
			19.2	-
			-	5
1	10	10	-	-
			2.4	-
			9.6	-
			19.2	-
			-	10
1	15	15	-	-
			2.4	-
			9.6	-
			19.2	-
			-	15
1.5	7.5	5	-	-
			2.4	-
			9.6	-
			19.2	-
			-	7.5
1.5	15	10	-	-
			2.4	-
			9.6	-
			19.2	-
			-	15
2	10	5	-	-
			2.4	-
			9.6	-
			19.2	-
			-	10

Table 4.4: Typical UM 3μm CMOS process parameters for resistor and capacitor.

Sheet Resistance (Ω/□)				Capacitance (fF/μm^2)
Poly1	Poly2	Pwell without field implant	Pwell with field implant	Poly1 to Poly2
11	22	2200	1200	0.691

Table 4.5: HSPICE simulation results for the amplifier with passive feedback resistor.

β	C_1 (pF)	C_2 (pF)	R_1 (kΩ)	C_{R1} (pF)	W_n, W_p (μm)	R_{f_Min} (kΩ)	Output Voltage Swing at R_{f_Min} (mV)
1	5	5	-	-	20, 40	35	94
			2.4	-	20, 40	100	48
			9.6	-			
			19.2	-			
			-	5	20, 40	60	58
1	10	10	-	-	40, 80	20	93
			2.4	-			
			9.6	-			
			19.2	-			
			-	10	20, 40	18	48
1	15	15	-	-	30, 60	15	69
			2.4	-			
			9.6	-			
			19.2	-			
			-	15	30, 60	18	77
1.5	7.5	5	-	-	15, 30	18	81
			2.4	-	20, 40	130	43
			9.6	-			
			19.2	-			
			-	7.5	20, 40	50	97
1.5	15	10	-	-	35, 70	15	103
			2.4	-			
			9.6	-			
			19.2	-			
			-	15	35, 70	20	95
2	10	5	-	-	20, 40	20	82
			2.4	-			
			9.6	-			
			19.2	-			
			-	10	20, 40	30	95

A. Design using CMOS inverter amplifier with passive feedback resistor

This is the fundamental design of the amplifier (Figure 4.8) which also serves as the basis for design variations with active feedback resistor. During the simulation,

optimal *W/L* ratios of the NMOS and PMOS transistors are found for each set of feedback network elements by using HSPICE iterations to get the best output voltage swing at a preset value of R_f, and then the minimum R_f that is necessary to generate oscillation at the optimal value of *W/L* is found by another set of HSPICE iterations. The output oscillating voltage swing at the minimum R_f is also recorded. The simulation results are listed in Table 4.5. The test sets with a slash in the table means oscillation cannot start at all regardless the value of R_f and *W/L* ratio. Figure 4.12 shows a typical output oscillation voltage from the simulation. L_n=L_p=3 μm for all transistors.

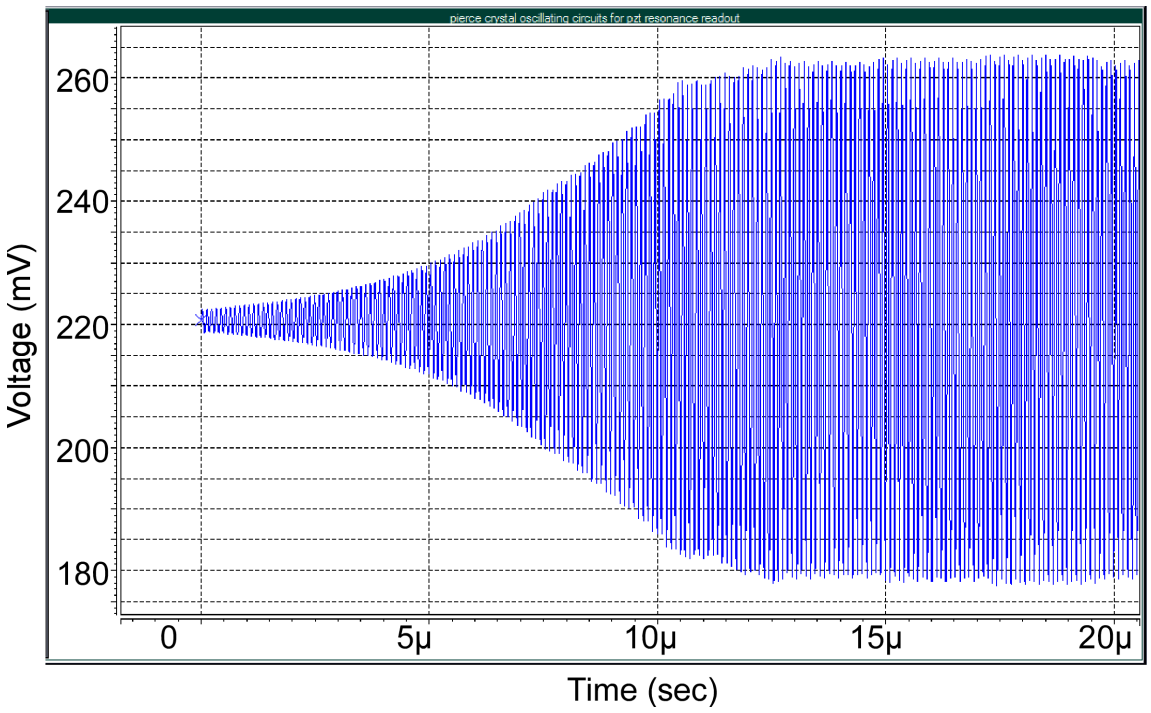

Figure 4.12: HSPICE simulation plot showing a typical oscillation output signal.

The simulation results in Table 4.5 were generated using the 9.615 MHz mode. According to these results, the inclusion of R_1 generally prevents the oscillation from starting at this frequency due to the reduction of open-loop gain as discussed before. Removing or replacing R_1 with a capacitor C_{R1} solves the problem, and use of C_{R1} also

retains the benefits of R_1 such as limiting the driving level of the PZT resonator, while an extra capacitor would result in a substantial increase in required die area. In the following designs, R_1 will not be considered any more. Due to limitation of the inverter amplifier bandwidth which is restricted by CMOS process parameters, the oscillation in the higher-frequency longitudinal modes (19.23 MHz and 38.46 MHz as listed in Table 4.1) of the PZT resonator cannot start during simulation. For longitudinal operation, a PZT resonator with a larger thickness (≥100 μm) is necessary to lower its longitudinal resonance frequency for the oscillation to start.

In order to test the stability of circuit when the electrical characteristics of the PZT resonator changes, different C_S and L_S values (multiplied by 2×, 5× and 10×) were used for additional tests. For all these tests, the different C_S and L_S values change the oscillating frequency as expected. According to the test results, the value of L_S only changes the oscillating frequency of the output signal, and does not affect the capability of oscillation generation or the output voltage swing. However, C_S affects the operation a lot. In most of the tests, oscillation cannot be generated at all when the R_f value remains at the minimum in Table 4.5. It was shown by the simulations that in order to maintain stable oscillation with larger C_S, R_f needs to be increased by at least 10×. The minimum value of R_f shown in Table 4.5 is ≈20 KΩ or more, making it difficult to get 10× more resistance due to the limited CMOS process parameters and available die area. This circuit design is therefore not a favorable design for implementation, but is still included in the mask design for testing purposes.

B. Design using CMOS inverter amplifier with reference inverter

The second design uses a separate reference inverter with transistors of the same dimension as those in the amplifying inverter (Figure 4.9). This reference inverter biases the amplifying inverter in the linear region. Similar sets of simulations were performed for this design, with R_1 not considered any more, and the simulation results are listed in Table 4.6. By using a separate reference inverter to set the operating point for the amplifying inverter, the circuit is much more stable and requires a much smaller isolating resistor R_f to generate the oscillation. When C_S and L_S were varied (again, multiplied by 2×, 5× and 10×) to test the stability of the circuit, the results were similar to those observed for Design (*a*), and R_f needs to be increased by 10×. With the low R_f in Table 4.6, this would not be a problem, and this design is included in the layout.

Table 4.6: HSPICE simulation results for the amplifier with a reference inverter.

β	C_1 (pF)	C_2 (pF)	C_{R1} (pF)	W_n, W_p (μm)	R_{f_Min} (kΩ)	Output Voltage Swing at $R_{f\ Min}$ (mV)
1	5	5	-	20, 40	8	102
			5	20, 40	8	62
1	10	10	-	20, 40	5	82
			10	20, 40	5	90
1	15	15	-	40, 80	1	82
			15	40, 80	1	89
1.5	7.5	5	-	20, 40	5	87
			7.5	20, 40	5	50
1.5	15	10	-	40, 80	5	103
			15	40, 80	5	95
2	10	5	-	40, 80	5	93
			10	40, 80	5	57

C. Design using CMOS inverter amplifier with reference inverter and active resistor

As discussed before, R_f value needs to be as large as possible to make the circuit more robust to element variations. The passive resistors available in CMOS process are usually no more than a couple of 100 KΩ and occupy a large area. As shown in Figure 4.13, an active resistor using MOS transistor M_{Rf} shown in Figure 4.10 is used to replace R_f. As the voltage swing across M_{Rf} is usually smaller than 50 mV, the simulated resistance varies from several hundred MΩ to GΩ.

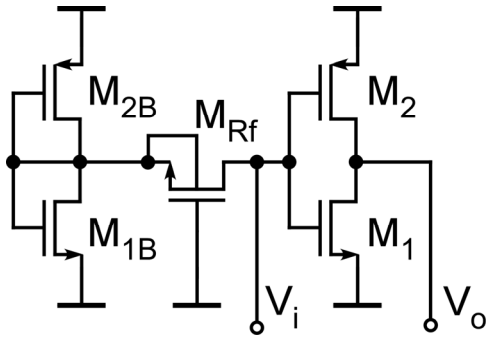

Figure 4.13: Amplifier design using reference inverter and NMOS active resistor.

Table 4.7: HSPICE simulation results for amplifier with reference inverter and active MOS resistor.

β	C_1 (pF)	C_2 (pF)	C_{R1} (pF)	W_n, W_p (μm)	W/L for M_{Rf} (μm)	Output Voltage Swing (mV)
1	5	5	-	20, 40	3/3	108
			5	20, 40	3/3	102
1	10	10	-	20, 40	3/3	106
			10	20, 40	3/3	45
1	15	15	-	40, 80	3/3	56
			15	40, 80	3/3	35
1.5	7.5	5	-	20, 40	3/3	183
			7.5	20, 40	3/3	98
1.5	15	10	-	40, 80	3/3	78
			15	40, 80	3/3	62
2	10	5	-	40, 80	3/3	139
			10	40, 80	3/3	97

Table 4.7 lists the simulation results of this design for each set of feedback network parameters. All parameter sets work as expected. Larger capacitances result in lower output voltage swing. This might be because higher capacitance load to the amplifier increases its propagation delay and thus reduces the gain at the resonating frequency, though this reduced gain still works to generate the oscillation. This design is also included in the layout.

C_S and L_S were also varied (multiplied by 2×, 5×, 10× and 100×) to test the stability of the circuit. For all the tests, this variation in C_S and L_S changes the oscillating frequency as expected. L_S does not affect the oscillation generation or output voltage swing. For C_S, the circuit still functions with a 100× larger value of C_S, and the output voltage swing reaches 8 V at 100× C_S because of the 10× lower operating frequency of the amplifier and thus higher gain.

The amplifier closed-loop gain is also evaluated in the simulation and was around 3.2 at the nominal frequency of the resonator testing mode. To check the impact of CMOS process variation, the transconductance factor k' of the NMOS and PMOS transistors is reduced by 20%, and for all the test sets, this variation only slightly changes the output voltage swing by <10 mV.

4.1.2.4 Discussion

1) Active feedback resistors turned out to be unnecessary especially in the case of the CMOS inverter amplifier biased with a reference inverter. The p-well resistors, which have sheet resistance of 2200/□, can easily provide sufficient resistance within a reasonable area. Although p-well resistors are not as accurate as polysilicon resistors, it will not cause any problem for this feedback scheme.

2) The values of the elements (C_1, C_2 and C_{R1}) in the oscillation feedback network have to be matched to the characteristics of the PZT resonator. The resonator equivalent model parameters C_S, L_S, and R_S can change a lot when the mechanical boundary condition of the resonator changes. The parameters may be affected by the resonator bonding approach (glue or epoxy properties), substrate properties (thickness, stiffness, *etc*.) and other variables. Several different sets of feedback network elements have been proposed, as shown in the simulation sets listed in the previous sections, and more can be included in the layout to provide additional options as needed.

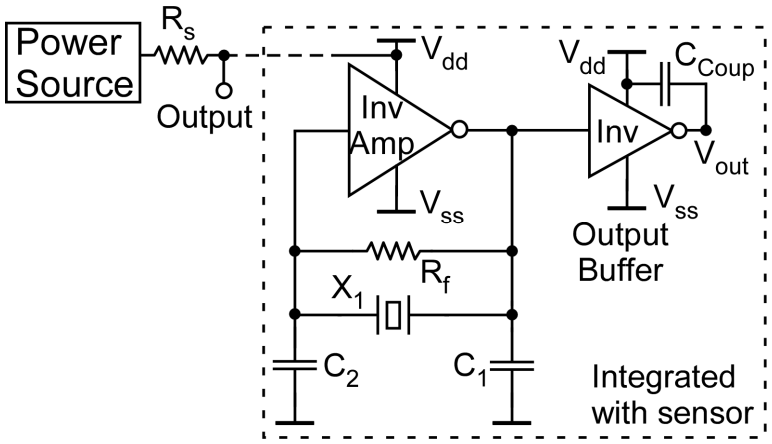

Figure 4.14: A variation of the oscillating circuit design with a coupling capacitor at the output node to potentially reduce the count of lead wires of the interface circuit.

3) The oscillating interface circuit requires three lead wires connected to external devices: V_{dd}, V_{ss} and signal-out. To explore ways to reduce the count of lead wires, an output coupling capacitor can be included in some design variations in the layout. This capacitor is used to couple the generated clock signal to the V_{dd} power line to potentially reduce another lead wire (Figure 4.14). SPICE simulation indicates that the output voltage signal V_{out} can be coupled to the V_{dd} line when an external resistor R_s is used to separate a regulated power source and the V_{dd} node of the circuit, although the amplitude

of the oscillating signal coupled on the V_{dd} line is reduced to <30% of the signal on the V_{out} node.

4.1.3 Device Layouts

The mask layout designs of the piezoelectric tissue contrast sensors with interface circuit for differential mode operation are shown in Figure 4.15. Two different layout designs are shown. Figure 4.15(a) is for the design using CMOS inverter amplifier with reference inverter and passive feedback resistor; Figure 4.15(b) is for the design using CMOS inverter amplifier with reference inverter and active MOS feedback resistor. An additional output inverter is connected to the output node of the oscillating circuit as a buffer stage. Other designs are included on the mask layout as well, and are modified from these two layout designs, such as the designs using the basic CMOS inverter amplifier without the reference inverter, with a passive or active feedback resistor.

In the layouts of design variations shown in Figure 4.15, output coupling capacitors discussed in Section 4.1.2.4 are included to couple the output clock signal to the V_{dd} power source line to possibly reduce another lead wire. Diodes for ESD protection are also included beside the two metals pads connected to the PZT sensor in the cavity. This is to prevent any electrostatic charges that might exist during PZT sensor integration from damaging the gates of the MOS transistors. As shown in Figure 4.15, each of the two large feedback capacitors present in all designs is made up of three smaller capacitors to form a pseudo-variable capacitor. The capacitors are formed during CMOS process by using two polysilicon films with an oxide layer sandwiched in between. The bottom polysilicon electrodes of these small capacitors are connected

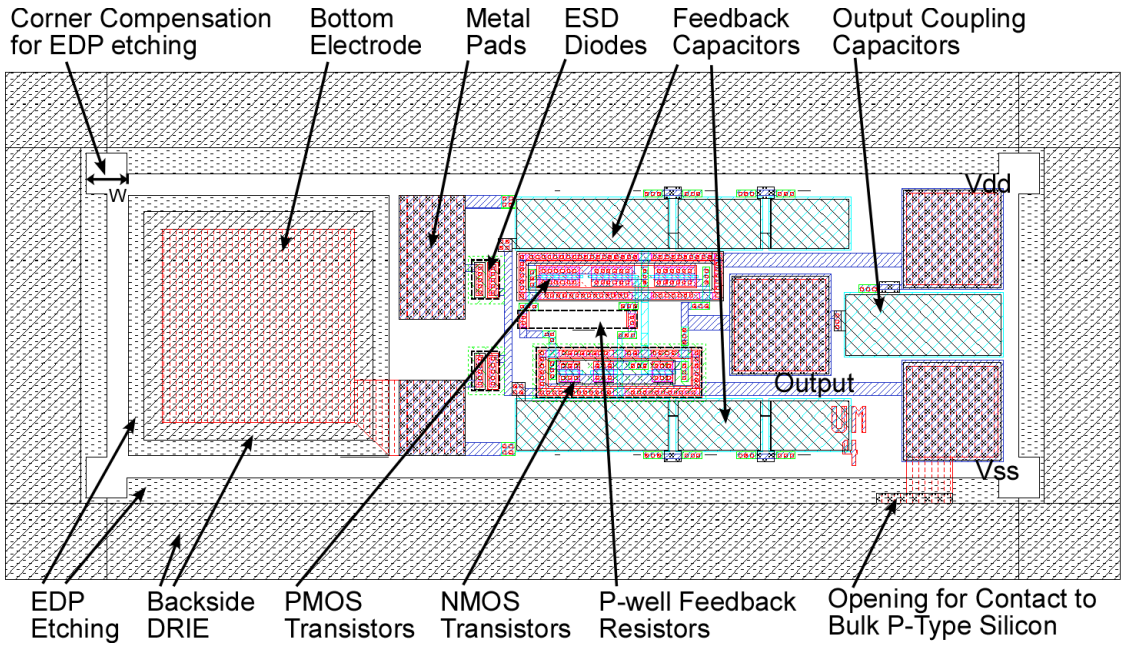

(a)

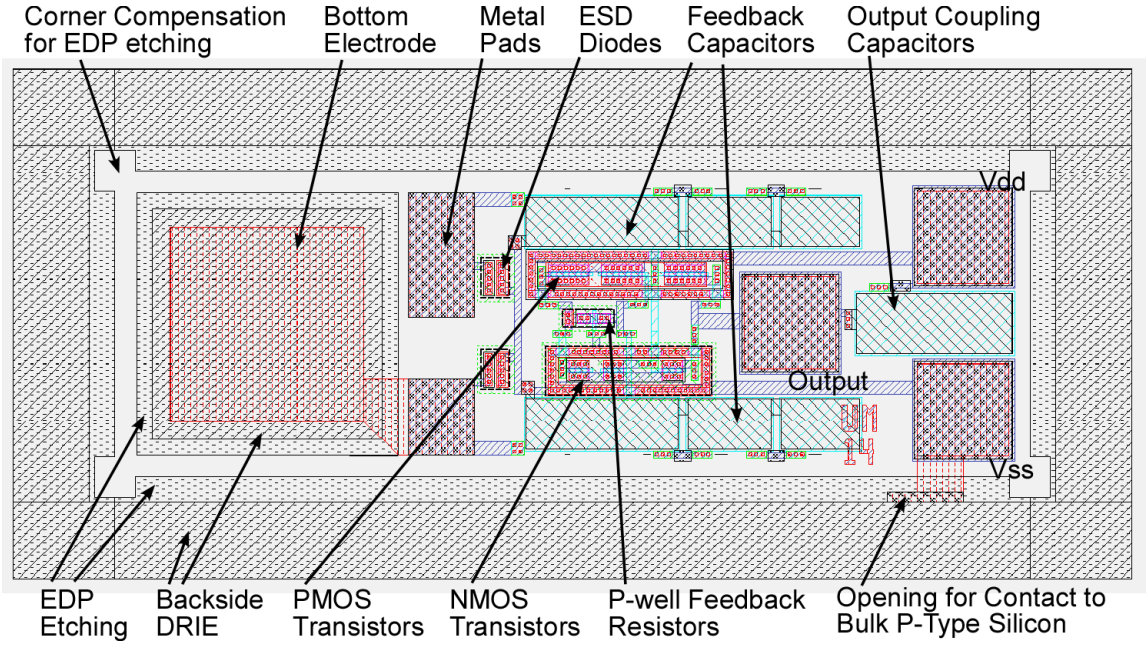

(b)

Figure 4.15: Two of the mask layout designs of the piezoelectric tissue contrast sensors with interface circuit for differential mode operation: (a) design using CMOS inverter amplifier with reference inverter and passive feedback resistor; (b) design using CMOS inverter amplifier with reference inverter and active MOS feedback resistor. Other designs are modified from these two layout designs.

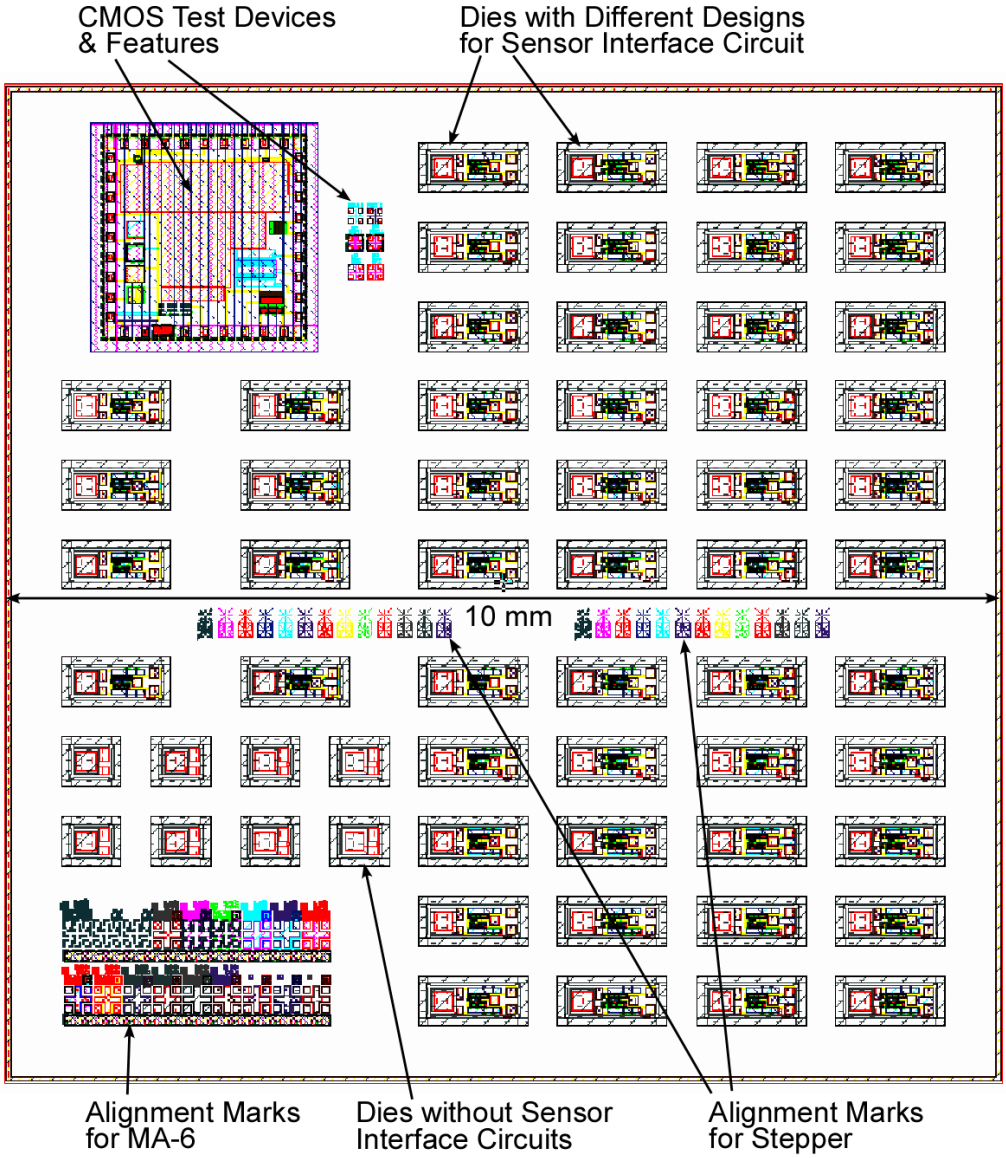

Figure 4.16: The 10 mm × 10 mm die layout designed for stepper consisting of all different interface circuit designs and CMOS test devices and features, as well as alignment marks for stepper and MA-6 aligner.

together, while the top polysilicon electrodes are connected with metal lines. The insulating silicon oxynitride layers on top of the metal lines are removed to allow laser trimmer to cut these lines if necessary, so that the feedback capacitances C_1 and C_2 can be varied independently to change the feedback ratio.

Since there are four convex corners on the silicon die that are exposed during EDP etching, corner compensation features are added to the layout to prevent damage to the die corners. The side width W of the compensation square shown in Figure 4.15(a) is equal to the target EDP etching depth.

Figure 4.16 shows the 10 mm × 10 mm die layout designed for GCA AutoStep 200 stepper. The die consists of all different interface circuit designs and CMOS test devices and features, as well as alignment marks for both stepper and MA-6 aligner. The alignment mark for MA-6 aligner is necessary for the backside DRIE, as AutoStep 200 stepper in UM cleanroom does not provide the capability of backside alignment. A few smaller dies without interface circuits are also included and can be used as silicon holders for PZT discs for other applications.

4.2 Device Fabrication

The fabrication process used for the PZT discs is the same as that discussed in Chapter 3. This section focuses on the process flow used to fabricate the silicon die with interface circuit and cavity, as well as its integration with the PZT disc.

4.2.1 Fabrication Process

The fabrication process flow for the piezoelectric sensor with interface circuit is shown in Figure 4.17. A detailed process run sheet is attached as Appendix B. This is a 12-mask, 85-step process, out of which 8 masks and 65 steps are used for CMOS interface circuit fabrication.

Step 1&2: CMOS process run and EDP etching. The process starts with a p-type silicon wafer, (100) orientation with a 15 µm-thick n-type epitaxial layer at the top. The epitaxial structure is used to suppress optically induced noise in circuits and to prevent on-chip potentials from coming in contact with the steel biopsy needle, similar to the purposes discussed in [Gin02]. The p-type substrate is held at circuit ground, forming a reserve biased p-n junction with the n-epitaxial layer which is at the V_{dd} potential during circuit operation.

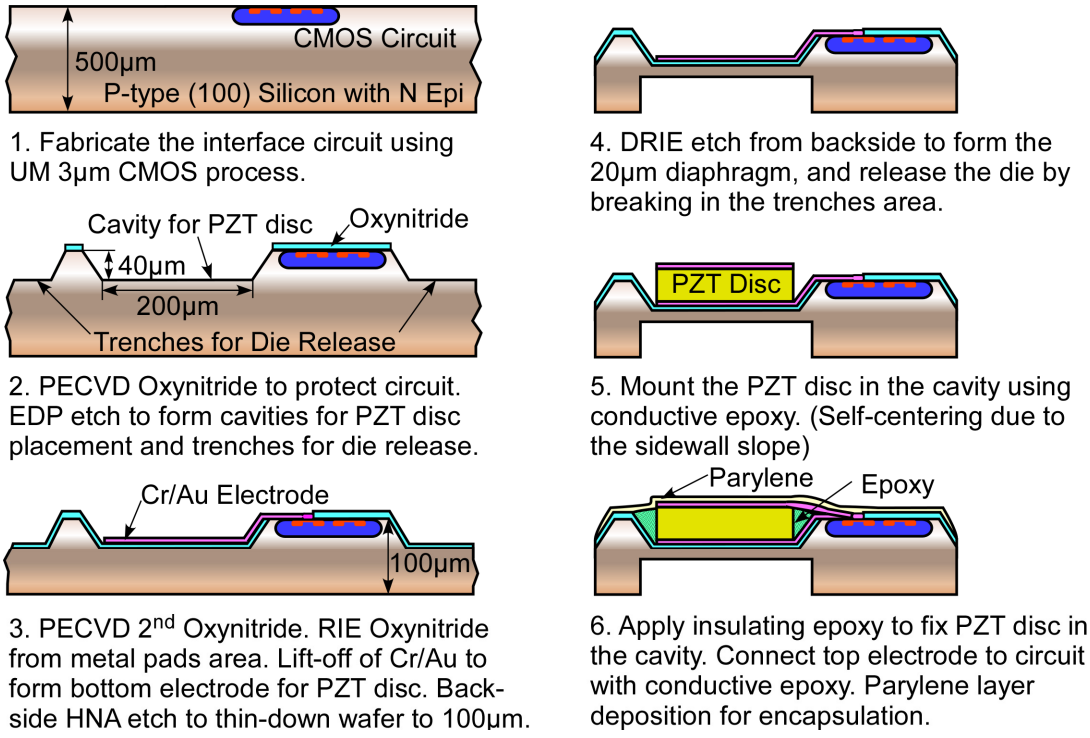

Figure 4.17: Fabrication process flow for the piezoelectric sensor with interface circuit.

The University of Michigan 3 µm, p-well CMOS process is carried out on the n-epi layer for the interface circuit. The details of this fairly standard CMOS process with some minor updates and changes are discussed in Section 4.2.2.1. After the CMOS circuit is formed, a 1 µm thick low-stress oxynitride layer is deposited using PECVD

with parameters presented in [Aga05] to cover and protect the circuit area, and is then patterned by RIE plasma etching. The PECVD deposition is carried out in two steps, with 0.5 μm-thick oxynitride deposited in each step. The use of the second step is to re-seal any randomly located pin holes possibly formed during the first deposition, so that the oxynitride can be used as a good mask layer for the following EDP etching. The 110°C EDP etching is then performed to make the cavity for PZT disc integration and trenches for sensor-die release. The target EDP etching depth is 40 μm, therefore the side width W of the square for corner compensation is equal to 40 μm.

Step 3: Post EDP insulation and metallization, as well as wafer thin-down. After EDP etching to form the 40 μm deep cavity and trenches, the wafer is cleaned with overnight hot-water soak followed by acetone, IPA and DI water rinse to remove any EDP residue and organic contaminants. Piranha clean is not performed to prevent damage to the CMOS aluminum metallization as the oxynitride layer may not withstand the harsh etching conditions during Piranha clean. A second layer of 1 μm-thick low-stress PECVD oxynitride is then deposited on the wafer to insulate the exposed surface of the bulk silicon due to EDP etching. To reveal the buried CMOS aluminum metal pads for power and signal connections, the oxynitride layer is patterned again using RIE plasma etching. As shown in Figure 4.15, an opening in the oxynitride layer on the sloped sidewall formed during EDP etching is designed to allow electrical contact to the p-type bulk silicon and set its potential to the ground. This opening is also formed in the RIE step. The lift-off process of Cr/Au metals is then performed to make the bottom electrode at the bottom of the etched cavity for connection of the PZT disc to the circuit, and also to add extra metal layers on top of the exposed CMOS metal pads for easier

probing and wire bonding. The lithography steps for the RIE patterning and lift-off require special attention due to the existence of patterns on both the top surface and the etched 40 μm-deep bottom surface of the silicon wafer. More details on this are provided in Section 4.2.2.2. After removing the oxide layers on the back of the wafer by RIE etching, it is thinned down from backside to ≈100 μm thickness using HNA etching (HNO_3:HF:CH_3COOH = 900:95:5). The wafer is diced into quarters before the HNA etching to allow easier handling of the resulting thin wafer and to obtain better etching uniformity.

Step 4: Backside DRIE and die release. The thin quarter wafer is patterned from backside using DRIE to form a 20 μm-thick diaphragm in the cavity area, and also to further thin down the EDP etched trenches for die release, which are then manually broken to release the 900 μm × 300 μm silicon dies. Before the lithography for this step, all the mask alignment and exposure are done using GCA AutoStep 200 stepper. This final lithography step is performed using the MA-6 aligner so that backside alignment can be achieved.

Step 5&6: PZT disc integration and encapsulation. After releasing the silicon dies with interface circuit, a PZT disc that has been fabricated using the process discussed in Chapter 3 is then mounted using silver conductive epoxy in the cavity on the bottom electrode, which connects the bottom surface of the PZT disc to the interface circuit. The PZT disc has at least one surface coated with metals (Cr/Au), and the side with metals is facing up in this mounting step, to be used as the top electrode of the PZT disc. Due to the sloped sidewall formed by EDP etching, the mounted PZT disc is self-aligned to the center of the cavity. Non-conductive epoxy is applied around the PZT disc to form an

insulating layer, and the top electrode of the PZT disc is connected to the larger metal pad beside the cavity using silver epoxy. In the final step, after wire bonding for lead connection, a layer of parylene is deposited to encapsulate at least the front side of the finished device to insulate the sensor and circuit from tissue during operation.

4.2.2 Related Fabrication Techniques

In this section, several topics related to the fabrication techniques used in the process flow are discussed, including the process integration with the UM 3 μm CMOS process, and the techniques and considerations used to form the deep cavity and its metallization for PZT disc integration.

4.2.2.1 Process Integration with UM 3 μm CMOS Process

The UM 3 μm, p-well CMOS process was initially developed at the University of Michigan in late 1980s [Cho92], and has been adapted for fabricating active neural probes in 1990s and early 2000s [Gin02]. The CMOS flow integrated with the process in this effort retains the standard CMOS run characteristics of the active probe flow (Revision 09/2002), while removing the steps related to neural probe formation such as deep and shallow boron diffusion, and adding minor modifications to address equipment and process changes such as lithography with stepper, new or different furnace tubes and RIE machine, modified lift-off process, *etc*.

The CMOS flow uses 8 masks and has 65 steps. It is carried out on the 500 μm-thick p-type (100) silicon wafers with 15 μm n-type epitaxial layer, and the n-epi layer has a resistivity of 1.0-1.5 Ω·cm. The process starts with the thermal oxidation of a 7000 Å masking oxide, which is patterned for the p-well implantation. The p-well boron

implantation is carried out by an external vendor for a dose of $1.5\times10^{13}/cm^2$ with implantation energy of 100 KeV. The p-well implant is driven in at 1100 °C for 16.67 hours. As no deep boron diffusion is performed, the drive-in process is done in the thermal oxidation furnace instead of the usual drive-in furnace to prevent contamination of the wafer surface. To prevent too much oxide from forming during the long drive-in, 6 hours of the time is spent in dry oxidation ambient, while the rest of the time is used for annealing in N_2 ambient. The oxide grown during drive-in and the masking oxide for implantation are then stripped, leaving a clean wafer with p-well region defined.

After p-well formation, the LOCOS (LOCal Oxidation of Silicon) steps are performed to define the active areas which decide the transistor width, and to grow the field oxide which provides isolation between devices. A 500 Å-thick pad oxide is grown, followed by LPCVD deposition of Si_3N_4, which is then patterned by RIE using the active mask to define the active region. After this RIE patterning is done, it is important to keep the photoresist (PR) in place with a long hardbake to mask the subsequent boron field implantation because the stopping power of the dielectric layers alone is not sufficient to protect the active regions from getting implanted with boron ions. Next, the p-field implant mask is used for lithography on top of the hard-baked active layer PR, followed by the p-field implant for a boron dose of $5\times10^{13}/cm^2$ at 55 KeV. It is important to do a few test runs of these lithography steps to ensure the active PR layer stays after developing the field-implant PR layer. The process using a combination of the stepper and SPR220-3 PR is characterized and the parameters are provided in Appendix B. An n-type field implant is not necessary and was not performed in this CMOS run.

After p-field implant, the hard PR is stripped using a combination of oxygen plasma and Piranha clean, and then field oxide is grown for a thickness of 11,000 Å outside the active region. The nitride is then stripped using hot phosphoric acid, followed by buffered hydrofluoric acid (BHF) etching of the pad oxide. A thin (500 Å) sacrificial oxide is grown to clean up the transistor active regions, and then a threshold implant for PMOS transistors is done for a boron dose of $6\times10^{11}/cm^2$ at 35 KeV. When the wafers are out for the threshold implant, test runs should be done with the gate oxidation furnace, and TCA clean of the furnace tube should be carried out. After threshold implant, the sacrificial oxide is stripped with fresh BHF solution, and gate oxidation is done, followed by LPCVD deposition of amorphous polysilicon for a thickness of 6600 Å. The deposition is done at a lower temperature of 570 °C rather than the usual LPCVD condition to get a smoother polysilicon surface, as this polysilicon layer is also used as the bottom electrode for on-chip capacitors. The polysilicon is then degenerately doped for phosphorus (n-type) in the doping furnace tube. The three furnace runs are done in an uninterrupted sequence after a single pre-furnace clean, and the total run time can be more than 12 hours. Good process planning is especially important here to get a smooth run.

The first layer polysilicon is patterned by RIE. This is one of the most critical steps as it defines the gate length of the transistors. It is important to do test runs, especially when a new RIE machine is to be used and process recipe development is still in progress, as what happened when the process run for this effort was performed. The capacitor oxide is then thermally grown, and a second layer of amorphous polysilicon is

deposited and again doped with phosphorus. These three furnace runs are again done in an uninterrupted sequence, so planning ahead is necessary.

The second polysilicon layer and the source/drain regions are then re-oxidized for an oxide thickness of 1200 Å. The polysilicon re-oxidation helps smooth out the edges for better step coverage during later metallization. This oxide is important for the source/drain region as well because it helps to keep the peak of the following source/drain implants near the surface. The PMOS source/drain regions are patterned and heavily implanted n-type with boron ($7\times10^{15}/cm^2$ at 40 KeV), and the NMOS source/drain regions are then patterned and heavily implanted p-type with phosphorus ($8\times10^{15}/cm^2$ at 70 KeV). After each of these implantation steps, the hard PR formed due to the high energy and high temperature caused by long implant time should be removed by a combination of oxygen plasma etching and Piranha clean. The oxygen plasma etching should be done first followed by the Piranha clean; otherwise the PR can become impossible to remove when Piranha clean is used alone. Careful inspection is essential to ensure all PRs have been stripped.

After source/drain implantation, the wafer is LPCVD deposited with 5000 Å of high temperature oxide (HTO). The HTO is then doped with phosphorus and deglazed to planarize the film surface. The circuit contacts are then patterned and etched with RIE. Special attention is necessary during the lithography step for contact to make sure the contact regions are open and no residue PR is in the contact holes. An oxygen descum step after lithography and before RIE is also helpful to remove any PR scum in the patterned areas. All the dielectric layers are etched by RIE, and any leftover oxide in the contact holes is etched by BHF.

The circuit metallization is then performed by a lift-off process soon after contact opening. The PR used for the lift-off is 1827 spun at 4 Krpm, and a 5-minute chlorobenzene soak after exposure in stepper and before developing is done to harden the top surface of the PR, so that a negative-sloped sidewall can be formed in the developed PR patterns. This is to make the PR dissolving step in the lift-off process easier, and also to have rounded edges on the metal structures that have no spikes, which can cause coverage problems during the oxynitride deposition in the post-CMOS process. The metal layers for lift-off are sputtered, and consist of sandwiches of Ti/TiN/Al(1% Si) to prevent junction spiking [Gin02]. After lift-off, the metallization in the contacts is then sintered in forming gas (N2/H2: 90%/10%) at 450 °C for 30 mins, which concludes the CMOS process portion of the process flow, and wafers are ready for circuit testing.

4.2.2.2 Deep Cavity Formation and Metallization for PZT Disc Integration

As discussed earlier, a 40 μm deep cavity on the silicon die is needed to hold a 50 μm-thick PZT disc, and to reduce the gap between the top electrode on the disc and the metal pad on the surface of the silicon die so that electrical connection between them can be made by silver epoxy. EDP etching is selected to form the cavity as it does not attack oxide as much as alternatives like KOH, and has a fairly good etching profile and rate. However, a good protection layer is necessary to cover the CMOS circuit region and prevent the aluminum lines and contacts from being attacked. Initially, low temperature oxide (LTO) is used as the protection layer. However, during LTO deposition at 420 °C, some scars or fractures occur on the otherwise good and clean metal surfaces as shown in Figure 4.18(a). This degraded the LTO coverage on the metal surface, and resulted in etched metals during EDP etching as shown in Figure 4.18(b).

The process was then changed by using PECVD to deposit a 1 μm-thick low-stress silicon oxynitride (SiON) layer at 400 °C. As mentioned in the previous section, this deposition is divided into two serial steps with 0.5 μm deposition in each step, so that any pin holes formed during the first step can be re-sealed in the second step. The 1 μm-thick PECVD oxynitride layer was good enough to mask the EDP etching without attacking the underneath metals.

(a)

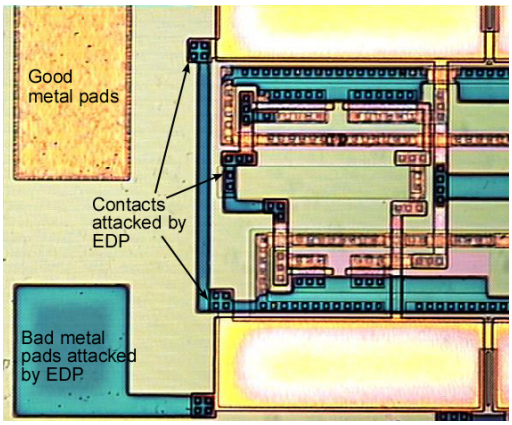

(b)

Figure 4.18: Microscopic photos of: (a) a scar formed during LTO deposition on a metal pad; (b) aluminum metals attacked by EDP etchant.

A metal electrode is necessary on the bottom surface of the cavity to make connection between the lower surface of a PZT disc mounted in the cavity and the circuit

on the top layer of the silicon die. The metal lead that goes to the electrode has to go over the sidewall of the 40 µm-deep cavity, making it difficult to do the lithography for the lift-off process. The 9260 PR was characterized for this step with a reflow time of 6-8 min. after spin-on and before a 30 min. softbake. An overexposure on the stepper is mandatory to ensure the PR in the cavity is patterned, and the correct exposure time was found by doing matrix exposure on the stepper. A good metallization for the cavity is shown in Figure 4.19.

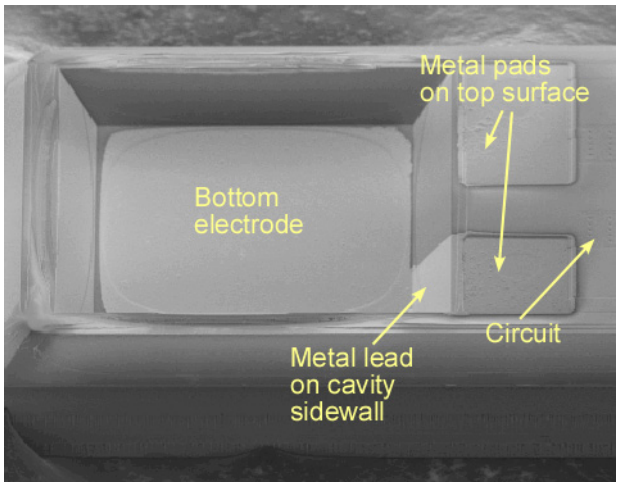

Figure 4.19: SEM image of a good metallization for the cavity.

4.2.3 Fabricated Devices

The microscopic and SEM images of the fabricated CMOS interface circuit and the released silicon sensor die are shown in Figure 4.20 to Figure 4.22. The SEM image of a biopsy needle tip prepared by µEDM for integration of differential sensors is shown in Figure 4.23.

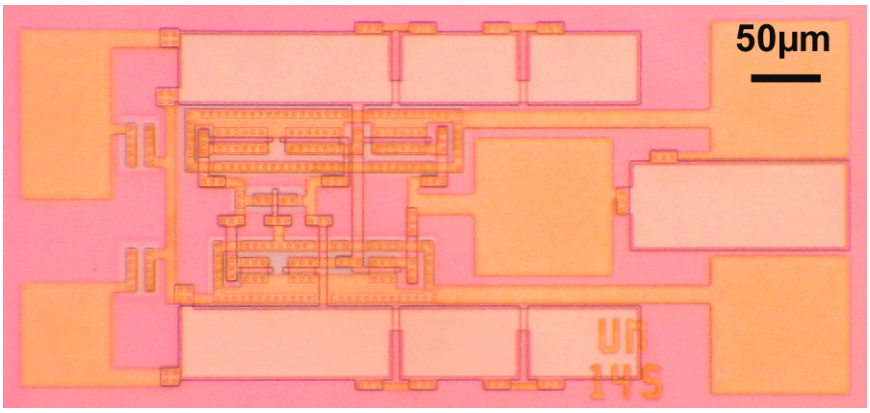

Figure 4.20: A microscopic die shot of one of the fabricated circuit die with reference inverter and active feedback resistor, before post-CMOS process is carried out.

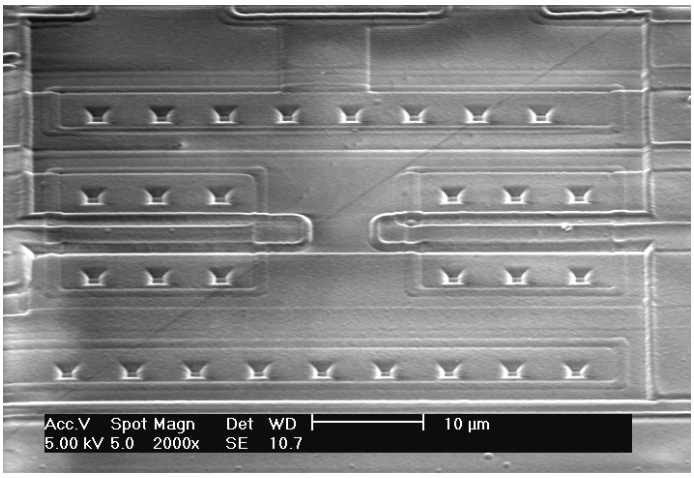

Figure 4.21: A close-up SEM view of the fabricated MOS transistors with 3 µm contact holes and metal interconnection.

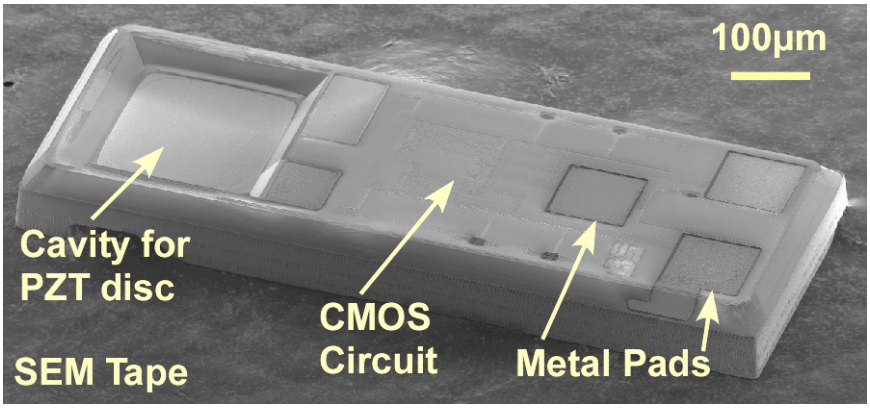

Figure 4.22: SEM image of the fabricated and released sensor die with CMOS interface circuit and a cavity for PZT disc integration.

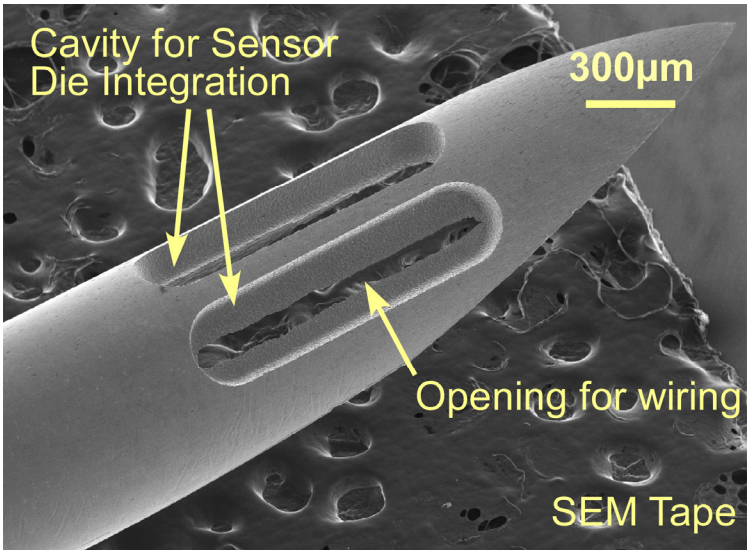

Figure 4.23: SEM image of cavities µEDM'ed onto the tip of a biopsy needle for integration of active and reference sensors. The cavities are located in the middle of the bevel region of the needle, and have a dimension of 1.3 mm (L) × 0.3 mm (W) × 0.170 mm (D). An opening for wiring is formed in each cavity due to the curvature of the needle sidewall.

4.3 Experimental Results

The design and fabrication of the piezoelectric sensors with interface circuits have been discussed in the previous sections. This section presents the experimental results of the CMOS process run and the interface circuit, and the preliminary test results of a piezoelectric sensor integrated with the interface circuit.

4.3.1 CMOS Characterization Results

The CMOS and post-CMOS fabrication processes were successfully completed using the 12-mask set. The measured CMOS process parameters are summarized in Table 4.8. The measurement was done using methods described in [Cho92] and [All87]. The measured threshold voltages for both NMOS and PMOS transistors have shifted from the previous values, which were 0.765 V (NMOS) and -0.700 V (PMOS) as

Table 4.8: Summary of measured CMOS process parameters.

Process Parameters	PMOS	NMOS
V_{th} (V_{bb}=0V) [V]	-0.934	0.967
KP [$\mu A/V^2$]	17.22	47.51
t_{ox} [Å]	490.5*	478.6#
μ_0 [cm^2/Vs]	253.01	676.78
Body effect (γ)	-0.478	1.319
λ (L=3μm) [V^{-1}]	0.04372	0.01480
λ (L=7μm) [V^{-1}]	0.01560	0.00750
Polysilicon [$\Omega/\square$]	35.7	
P-well w/ field implant [$\Omega/\square$]	1794.1	
Poly1/Poly2 [$fF/\mu m^2$]	0.470	

* Determined from NanoSpec reflectometry
# Determined from capacitance measurement

Table 4.9: Measured CMOS process parameters for NMOS transistors. (Wafer ID#: A5)

Process Parameters	Avg	Min	Max	Std. Dev.	% Variation
V_{th} (All W/L ratios) [V]	0.967	0.897	1.027	0.034	3.55
Body effect (γ)	1.319	1.259	1.352	0.024	1.816
KP [$\mu A/V^2$]	47.51	44.40	54.53	2.24	4.709
μ_0 [cm^2/Vs]	676.78	618.91	771.29	37.01	5.468
Gate Capacitance# [$pF/\mu m^2$]	7.104 E-04	7.066 E-04	7.174 E-04	4.186 E-06	0.59
t_{ox}# [Å]	478.62	473.96	481.18	2.80	0.59
N_{sub} [$10^6 cm^{-3}$]	6.35	5.78	6.67	0.37	5.85
lambda (λ) (L=3μm) [V^{-1}]	0.01480	0.01335	0.01554	0.00068	4.569
lambda (λ) (L=7μm) [V^{-1}]	0.00750	0.00687	0.00894	0.00063	8.338
lambda (λ) (L=13μm) [V^{-1}]	0.00432	0.00390	0.00492	0.00029	6.617
ΔL [μm]	0.38	0.15	0.83	0.21	54.500
ΔW [μm]	-1.60	-1.68	-1.52	0.05	-2.970
Subthreshold Slope [mV/dec]	43	31	49	5	12.357

Determined from capacitance measurement

Table 4.10: Measured CMOS process parameters for PMOS transistors. (Wafer ID#: A5)

Process Parameters	Avg	Min	Max	Std. Dev.	% Variation
V_{th} (All W/L ratios) [V]	-0.934	-0.993	-0.864	0.048	-5.17
Body effect (γ)	-0.478	-0.558	-0.392	0.063	-13.272
KP [$\mu A/V^2$]	17.22	15.25	18.34	0.77	4.478
μ_0 [cm^2/Vs]	253.01	222.44	271.93	10.50	4.150
Gate Capacitance* [$pF/\mu m^2$]	6.857 E-04	6.852 E-04	6.882 E-04	9.979 E-07	0.15
t_{ox}* [Å]	490.45	488.70	490.80	0.71	0.15
N_{sub} [$10^6 cm^{-3}$]	-	-	-	-	-
lambda (λ) (L=3μm) [V^{-1}]	0.04372	0.03734	0.04788	0.00325	7.425
lambda (λ) (L=7μm) [V^{-1}]	0.01560	0.01428	0.01628	0.00060	3.834
lambda (λ) (L=13μm) [V^{-1}]	0.00787	0.00697	0.00827	0.00039	4.927
ΔL [μm]	-0.17	-0.39	0.10	0.16	-92.326
ΔW [μm]	-1.77	-1.88	-1.70	0.06	-3.595
Subthreshold Slope [mV/dec]	41	36	50	4	9.451

* Determined from NanoSpec reflectometry

Table 4.11: Measured CMOS process parameters for threshold voltages of p-well to n-source/drain diodes. (Wafer ID#: A5)

Process Parameters	Avg	Min	Max	Std. Dev.	% Variation
P-Well/N+ Diode Forward [V]	0.672	0.660	0.683	0.007	1.02
P-Well/N+ Diode Reverse [V]	19.311	18.900	19.600	0.257	1.33
P-Well/N-Sub Forward [V]	0.638	0.625	0.648	0.008	1.21
P-Well/N-Sub Reverse [V]	>20	>20	>20	-	-

Table 4.12: Measured CMOS process parameters for sheet resistances. (Wafer ID#: A5)

Process Parameters	Avg	Min	Max	Std. Dev.	% Variation
P-Well (w/o Field Implant) [Ω/□]	5526.32	5363.39	5611.19	77.86	1.41
P-Well (w/ Field Implant) [Ω/□]	1794.10	1684.37	1877.38	81.53	4.54
Poly1 [Ω/□]	35.74	34.03	37.80	1.58	4.41
Poly2 [Ω/□]	38.90	37.37	42.10	1.64	4.22

Table 4.13: Measured CMOS process parameters for capacitances. (Wafer ID#: A5)

Process Parameters	Avg	Min	Max	Std. Dev.	% Variation
Poly1/p+ (P-Well) [fF/μm^2]	0.711	0.707	0.717	4.21E-06	0.59
Poly1/Poly2 [fF/μm^2]	0.470	0.457	0.483	9.73E-06	2.07

reported in [Cho92], and 1.12 V (NMOS) and -1.08 V (PMOS) for the active probe flow as reported in [Gin02]. This is mainly due to the difference in the thermal budget after threshold implantation; the process presented in [Gin02] also used a different threshold implantation dosage. The high-temperature thermal-budget change was caused by the use of different furnace tubes and changes in the furnace status and condition over time. For example, during the gate oxidation step, the oxidation time has to be doubled from previous values in the active probe flow in order to get a 500 Å thick gate oxide. Across a whole wafer, the measured threshold voltages for transistors of the same size and type vary 1-2%, taken as the standard deviation of the measurement divided by the average. Other parameters such as the values of KP and λ also vary from previously reported values. However, all these changes should not significantly affect the circuit operation because of the high robustness of the Pierce oscillating circuit as demonstrated in the simulation results discussed in Section 4.1.2.3. Additional detailed measurement results of CMOS parameters are listed in Table 4.9 to Table 4.13.

4.3.2 Oscillating Interface Circuit Testing Results

The shifted CMOS process parameters had no significant effect on the operation of the inverter amplifier and the oscillating circuit. According to measurement results, the gain of the amplifiers varies depending on the type of the designs. The inverter amplifier with a reference inverter and a passive feedback resistance provides the highest

gain, mostly in the range of 300-380 V/V. The inverter amplifier with a reference inverter and an active feedback resistance comes next in line, providing a gain in the range of 180-270 V/V. The basic inverter amplifier without reference inverter or output buffer inverter provides the lowest gain, in the range of 15-30 V/V.

The 3dB bandwidth of these amplifiers has been measured as in the range of 1.0-2.5 MHz. The measured bandwidth has been reduced by the loading effect of the capacitor C_1 (≥5 pF) at the output node of the inverter amplifier and C_2 (≥5 pF) at the input node as shown in Figure 4.24. This circuit configuration is modified from the Pierce oscillating circuit in Figure 4.5 by removing the resonator X_1, and shows the connectivity of the inverter amplifier during the characterization. The bandwidth is lower than the target resonance frequency of the PZT sensor, which is 9.6 MHz in the transverse mode. However, it should not cause significant problems for oscillation to start considering the very high voltage gain of the amplifiers and the minimum loop gain requirement (≥1) of an oscillating circuit.

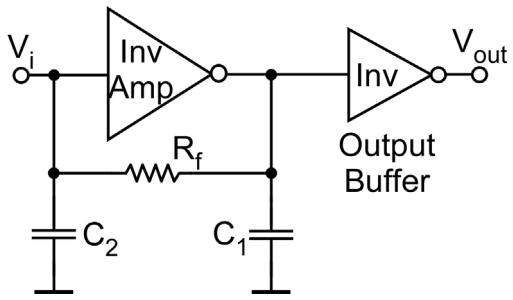

Figure 4.24: The amplifier circuit configuration used for characterization. The resonator X_1 in the Pierce oscillating circuit in Figure 4.5 is not connected in this test and removed in this circuit. The detail of the inverter amplifier circuit varies between designs.

Shown as the best case in Figure 4.25 and Figure 4.26, one of the inverter amplifiers with a reference inverter and a passive feedback resistor provides a voltage gain of ≈392 V/V at 1 kHz, and the gain is reduced to ≈278 V/V at 1.56 MHz, which

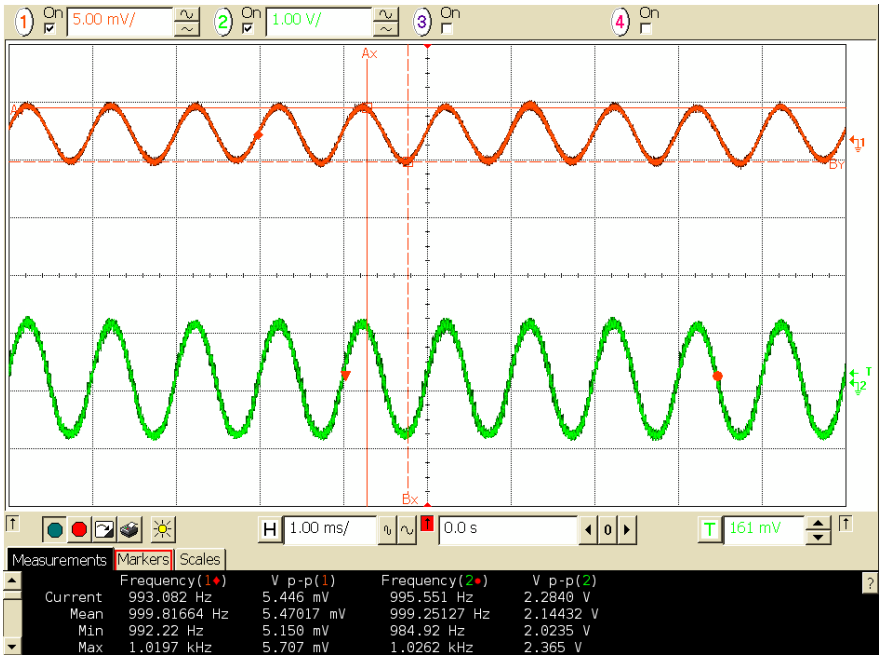

Figure 4.25: An oscilloscope screen shot showing a 1 kHz 5.47 mV_{p-p} signal at the input of an inverter amplifier with a reference inverter and a passive feedback resistor, and the corresponding output signal of 2.144 V, giving a circuit gain of ≈392 V/V.

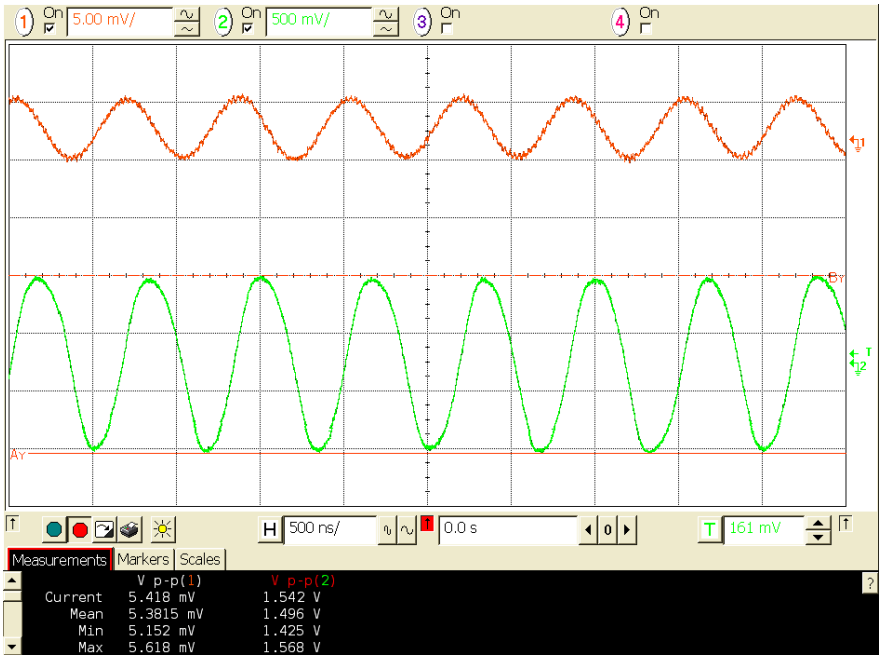

Figure 4.26: An oscilloscope screen shot showing a 1.56 MHz 5.38 mV_{p-p} signal at the input of an inverter amplifier with reference inverter and passive feedback resistance, and the corresponding output signal of 1.496 V, giving a circuit gain of ≈278 V/V. This indicates that the 3 dB bandwidth of the amplifier is ≈1.56 MHz.

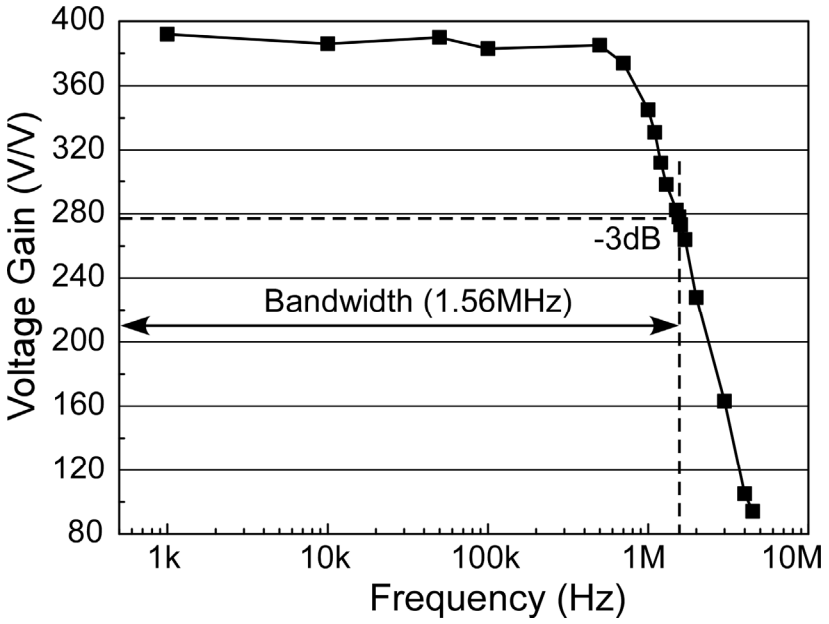

Figure 4.27: Measured voltage gain *vs.* signal frequency of an inverter amplifier with reference inverter and passive feedback resistance. The 3 dB bandwidth of the circuit is ≈1.56 MHz.

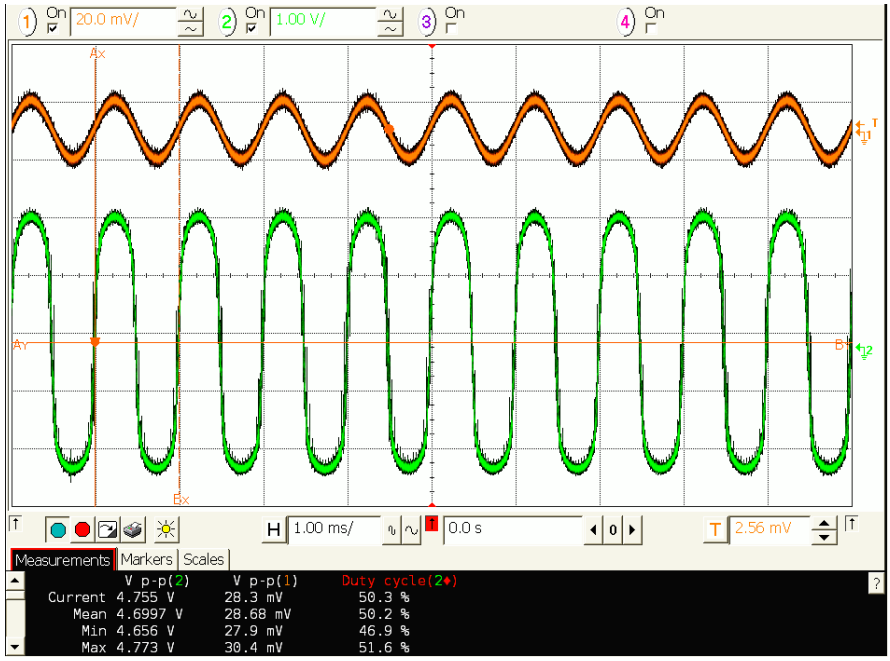

Figure 4.28: An oscilloscope screen shot showing a 1 kHz 28.6 $mV_{p\text{-}p}$ signal at the input of an inverter amplifier with reference inverter and passive feedback resistance. The corresponding output signal is 4.70 $V_{p\text{-}p}$, and is distorted from a sine wave due to satuation. The reduced circuit gain is ≈164 V/V.

gives the 3 dB bandwidth of the amplifier. In this circuit the C_1 and C_2 are both trimmed to ≈5 pF. The measured voltage gain *vs.* signal frequency is plotted in Figure 4.27.

When the peak-to-peak amplitude of the input sine signal used for testing is increased to more than merely 10 mV, the output signal of an inverter amplifier with reference inverter and passive feedback resistance becomes distorted from a sine wave due to saturation. Figure 4.28 shows a 28.6 $mV_{p\text{-}p}$ input signal and its distorted output signal, giving a reduced gain of ≈164 V/V. This saturation distortion is caused by the high voltage gain and the limited power supply voltage (10 V) of the circuit.

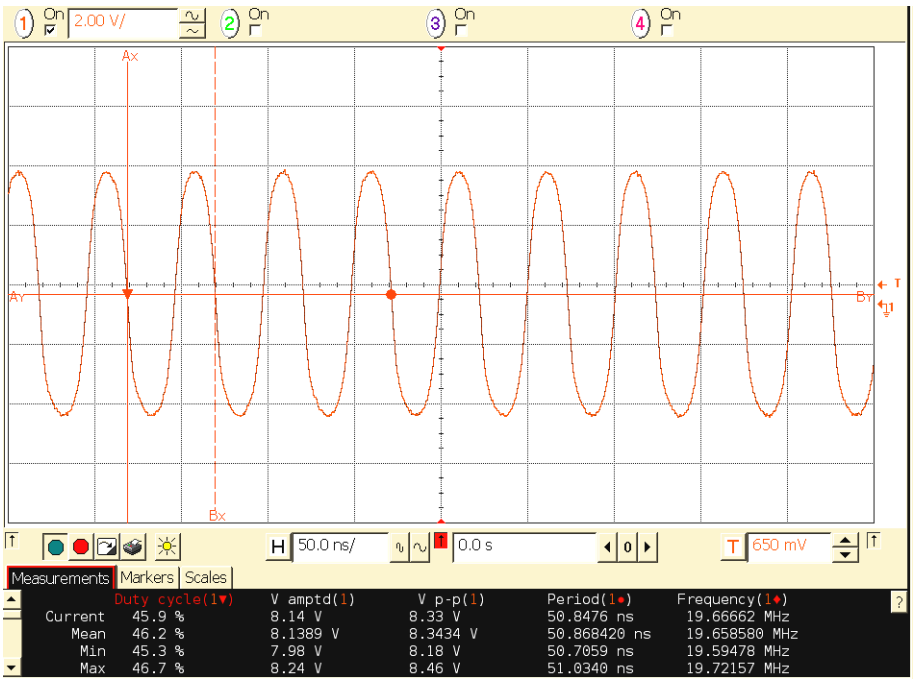

Figure 4.29: An oscilloscope screen shot showing an oscillating signal at 19.667 MHz and 8.34 $V_{p\text{-}p}$ generated by one of the interface circuit designs with reference inverter and passive feedback resistor. A quartz crystal is connected to the circuit for oscillation functional test.

Before integrating with PZT sensors, the oscillating circuits have been tested with quartz crystals to verify their capability to start oscillation. As shown in Figure 4.29, an oscillating signal at 19.667 MHz and 8.34 $V_{p\text{-}p}$ is generated with a 10 V power supply by

an oscillating circuit design that uses the inverter amplifier with a reference inverter and a passive feedback resistor. The measured peak-to-peak voltage (V_{p-p}) of the generated oscillating signal increases when the circuit operates at a lower oscillating frequency set by a different quartz crystal. This suggests that at a lower frequency a higher loop gain is in effect in the oscillating circuit. The V_{p-p} of the generated oscillating signals in this design remains above the power supply voltage (10 V) in the tested frequency range (1.8 MHz – 15.35 MHz), and can shoot to over 15 V at low frequencies. The majority of the other circuit designs can start oscillation at up to 15.35 MHz with a lower V_{p-p}, with some designs working at up to 13.5 MHz. This suggests that the design using the inverter amplifier with a reference inverter and a passive feedback resistor provides the best loop gain and highest possible oscillation frequency, making it the most favorable design.

4.3.3 Testing Results of Integrated PZT Sensor and Interface Circuit

The PZT discs have been integrated into the cavity on the silicon die, but oscillation signal could not be obtained. Further examination of the PZT discs has been carried out. Typical variation of PZT impedance *vs.* frequency sweep was plotted using an HP 4194 impedance analyzer with four-terminal measurement capability as shown in Figure 4.30. A stable resonant sweep with a parallel resonant frequency of 12.34 MHz is shown in Figure 4.31. However, the quality factor was only ≈7 at this mode. Additional HSPICE simulations were performed by using the measured CMOS process parameters listed in Table 4.8 to Table 4.13 and varying the values of PZT equivalent circuit elements in Table 4.1 for different Q. The simulations indicated that with the actual CMOS process parameters a minimum Q of ≈58 is necessary for the circuit design with a

reference inverter and a passive feedback resistor to start the oscillation. In order to obtain an output oscillating signal of >50mV$_{p-p}$ in the simulation, a Q of >60-75 is preferred.

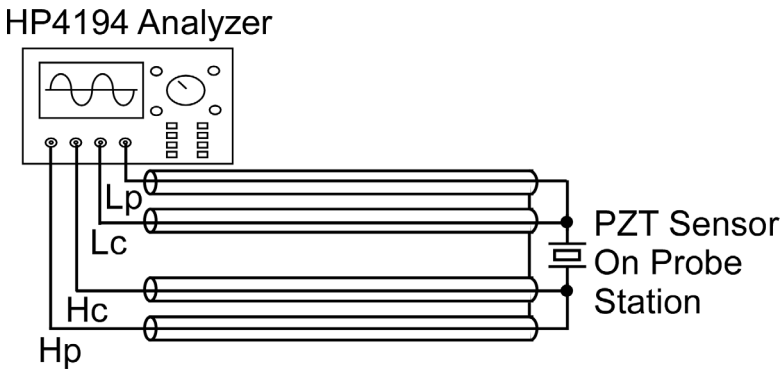

Figure 4.30: HP 4194 precision impedance analyzer is used for characterization of the PZT sensor. The sensor is integrated on a silicon die with the interface circuit disconnected by laser trimming of the CMOS metal lines. Four-terminal connection is used to minimize parasitics from the long connection cables from the analyzer to the sensor die on the probe station.

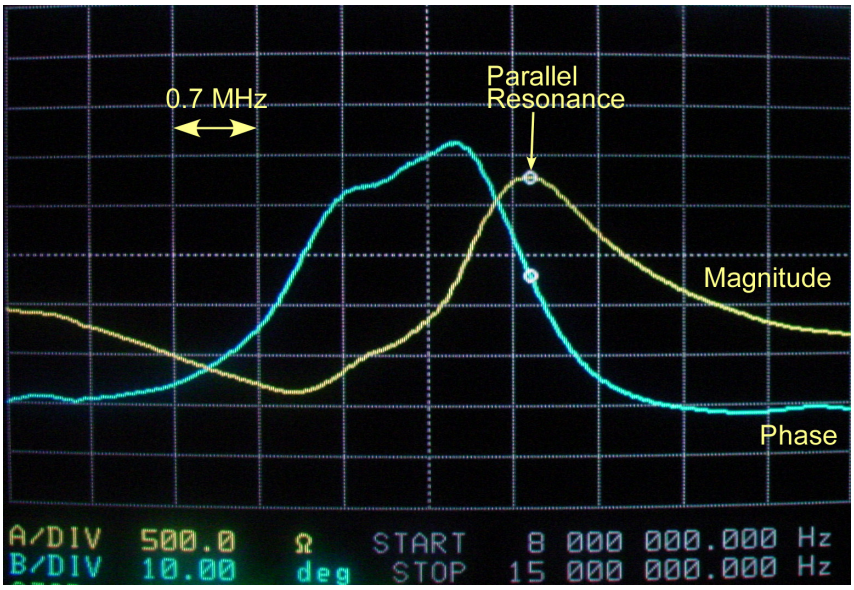

Figure 4.31: Screen shot of HP 4194 impedance analyzer showing the impedance sweep of a mounted PZT disc.

The low measured Q of the PZT disc, which prevented the circuit oscillation from starting, could be due to the attenuation caused by the transverse mode resonance and the

fact that the disc was mounted in the cavity with epoxy surrounding its sidewall. The series resistance of the mounted PZT disc, measured as ≈2 KΩ using the equivalent circuit analysis function of HP 4194, was also too high possibly because of the silver epoxy used for electrical connection. To get a better *Q*, the thickness (longitudinal) mode resonance can be used with a thicker disc to lower the resonance frequency. A better bonding approach for electrical connection between the circuit and the PZT disc is also desirable. An electrically conductive resin has been found, which can provide a resistivity 10× smaller than that of the silver epoxy. It will also be helpful to use a different PZT or piezoceramic material that has a higher mechanical *Q*. These improvements will be pursued as future work, and are further discussed in Chapter 5.

CHAPTER 5

Conclusions and Future Work

This chapter provides the summary and conclusions of the research results presented in previous chapters, as well as the outlines of future work of this research effort.

5.1 Conclusions

This research aimed to address the issue of limited material choices for current MEMS applications which largely rely on semiconductor manufacturing processes. Two primary goals were explored in this effort. The first one was to develop a batch mode micromachining technology for hard and brittle materials such as ceramics to expand the choices of bulk materials available for the development of MEMS devices. The fabrication technology was intended to be complementary to the batch mode μEDM process which is effective for conductive materials such as hard metals, and to be compatible with photolithography-based processes. The second goal was to demonstrate the effectiveness and the capability of the developed technology with applications. This was to be achieved by applying the technology to the fabrication and integration of MEMS devices onto medical instruments to enhance their capability and performance.

For the first goal, a new fabrication process, LEEDUS, which combines lithography, electroplating, batch mode μEDM, and batch mode μUSM, was developed

to provide the die-scale pattern transfer capability with high throughput and high resolution from a lithographic mask onto ceramics, including piezoceramics like PZT, PMN-PT, *etc*. A related process (SEDUS) uses serial μEDM and omits lithography for fast prototyping of simple patterns. The machining apparatus for batch mode μUSM was built with commercial and UM-fabricated components. A quartz force sensor was integrated with the apparatus for stage zero-position calibration and machining load monitoring. The process mechanism and the machining apparatus were successfully verified by the process characterization tests. In these tests, a die-scale pattern with 25 μm minimum feature sizes was defined by lithography and transferred onto Macor ceramic workpieces using stainless steel and WC/Co microtools at a machining rate of >18 μm/min. The machining rate increased with the amplitude of the ultrasonic vibration. The stainless steel microtool provided a much smaller wear ratio than that of the WC/Co, making stainless steel the preferable choice for tool material.

Octagonal and circular spiral-shaped in-plane actuators were machined from bulk PZT-5H plate as a process demonstration on piezoceramics. The fabricated octagonal spirals had a footprint of 450 μm × 420 μm and beam width of 50 μm, while the circular version had an outer diameter of 500 μm and beam width of 80 μm. Measurements showed that the displacement of these actuators is 6 - 8× larger than the calculated d_{31} transverse displacement from a straight beam actuator with the same equivalent length. This demonstration verified that the process is effective on piezoceramics, and suggested that practical devices can be made with this process.

During process characterization, several equipment issues were identified on the original, basic apparatus for batch mode μUSM, including the tilting error in the Z axis

stage, inefficient force feedback detection during machining, and lack of slurry flushing mechanism. An advanced machining apparatus was built with these issues addressed, and its functionality was verified with machining.

Toward the second goal of process application, a bulk PZT sensor micromachined using the batch mode μUSM process was integrated into a cavity at the tip of a biopsy needle to aid in real-time tissue differentiation during FNA biopsy, providing information that is complementary to any imaging method which may be used concurrently to guide the procedure. The batch-fabricated PZT disc had a 200 μm diameter and 50 μm thickness, and was located on a diaphragm formed with the cavity by using μEDM to customize the needle. PZT discs with >100 μm or <10 μm thickness were also made using the same process. Devices were tested in a simulated scheme for physician training, as well as in porcine tissue consisting of fat and muscle layers. In both types of tests, the frequency and magnitude of an impedance resonance peak showed tissue-specific characteristics as the needle was inserted into the tissue. For example, in the porcine tissue sample, the frequency shifted ≈13 MHz as the needle moved from fat to muscle tissue. Additional measurements with saline solutions and oil samples were carried out to build an empirical tissue contrast model, which showed a proportional relationship between the frequency shift and sample acoustic impedance. These results and subsequent analyses successfully proved the device concept and indicated that the proposed device is promising in providing effective guidance to physicians during FNA biopsy of shallow tissue up to ≈15 mm deep, while for deeper tissue applications the performance of the original device was degraded possibly due to signal attenuation, stray capacitances and insufficient sensitivity.

To explore potential solutions of the issue with deeper tissue biopsy, a differential mode piezoelectric sensor was proposed and fabricated. A CMOS interface circuit was also proposed to enable the differential operation of the sensor and to simplify the sensor readout scheme. The interface circuit was successfully fabricated using the UM 8-mask 3 μm CMOS process, and its functionality was experimentally tested and verified. The inverter amplifier in the circuit provided a voltage gain of ≈392 V/V, and oscillating signals of up to 19.67 MHz was generated by using quartz crystals for testing purposes. The piezoelectric sensor has a quality factor requiring further improvement for the differential mode operation with the circuit, which will be pursued in future efforts.

Overall, the application of both μUSM and μEDM to the development of the tissue contrast sensors provides a demonstration of broadened MEMS material choices and application experience of these technologies. As examples of broader material choices, bulk PZT and other piezoceramics have superior material properties over their thin-film form, but are usually difficult to process at microscale. The developed batch μUSM process provides an enabling technology for patterning bulk PZT in a lot of potential MEMS applications, and its application to both sensors and actuators has been demonstrated in this effort.

5.2 Future Work

There are several remaining improvements to be addressed in the piezoelectric tissue contrast sensor for FNA biopsy.

The piezoelectric sensor integrated on the silicon die for differential operation provided a quality factor that was lower than expected. This could be caused by the

transverse resonance mode and a high series resistance as discussed in Chapter 4. Potential solutions to improve the quality factor include longitudinal operation mode with a thicker PZT disc, new PZT bonding material with better electrical connection, and a different PZT or piezoceramic material with a higher mechanical Q, such as quartz which has been demonstrated to work with the interface circuit and can also be micromachined by the developed process. It is also possible to implement a structural design of the PZT sensor to isolate the resonating part from the anchor region for epoxy bonding, for example, through an integrated suspension that is formed from the same material as the sensor. With an improved quality factor Q, the PZT disc can be tested with the interface circuit, and the differential mode operation of the sensor system can then be implemented and tested.

Besides tissue contrast information, there are other tissue parameters that are of interest to physicians during a FNA biopsy and other medical procedures, such as pH value, ionic composition, electrical and thermal resistivity, *etc*. These characteristics can be helpful for both tool guidance and diagnosis purposes. Using a scheme that is similar to the piezoelectric tissue contrast sensor developed in this effort, sensors for various tissue characteristics can be integrated on commercial biopsy and surgical tools, providing additional information that can be of interest to physicians. For example, an electrode array for voltammetry or potentiometry to monitor the ionic concentration in the diseased tissue can be included on a silicon substrate and integrated on the biopsy needle to provide complementary tissue characteristics.

The developed piezoelectric sensors can also be potentially used for other applications, such as mass or density detection in medicine applications.

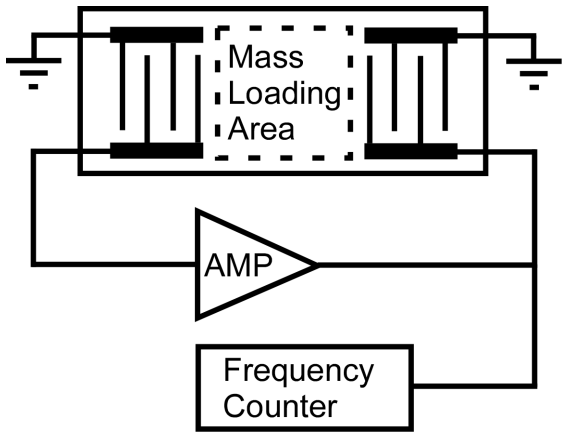

Figure 5.1: Testing of a delay line SAW sensor with frequency counter.

Another example of sensors that can be potentially integrated on biopsy and surgical tools are SAW (surface acoustic wave) sensor shown in Figure 5.1. SAW devices have found wide applications as sensors in different areas, and are also used as filters or other electronic components in telecommunications [Fen03]. SAW uses an elastic wave propagating near a stress-free surface of a piezoelectric plate. The finite propagation time from the moment the wave is generated until it reaches a detector is called its time delay. Small changes in the surface composition, such as added mass by surface adsorption, cause changes in the wave propagation speed, which can be detected as changes in the time delay. As this change is very small for SAW sensors, a delay line oscillation can be formed as shown in Figure 5.1 [Göp92]. The electrode array on the right, which is called interdigital transducer (IDT), is used as a generator and converts an electric signal into SAW which is detected and converted back to an electric signal by the IDT on the left (receiver). This detected signal is amplified and applied to the generator, and thus a delay line closed loop is formed. Using an amplifier with appropriate gain, this delay line oscillates at a frequency which depends on physical parameters such as the electrode spacings of the IDTs, thus converting the variations in time delay to variations

in oscillation frequency. This device has a high sensitivity and can tolerate a thin coating which can be a protection layer. It can also be configured in differential mode in a way similar to that described in Section 4.1.1. The SAW device can be fabricated by using μUSM to make a PZT plate. The IDT arrays can then be added by sputtering and etching with a mask, and the amplifier on a silicon die can be bonded underneath the PZT plate.

In addition to sensors, actuators can be integrated at the needle tip to assist in the insertion and sampling process. For example, the needle tip can be ultrasonically vibrated with an actuator to help minimize tissue damage during insertion, and to help dislodge cells for sample collection.

APPENDICES

APPENDIX A

Program Script of Process Control Software for the Batch µUSM Apparatus

A.1 Basic Apparatus

A.1.1 ControlPanel.frm

```
' Micro-USM Process Control Program - Visual Basic 6.0 - written by Tao Li
' The code for actuator operation is adapted from a template provided by Zaber Technologies
' Updated August 15, 2006: change to NI-DAQmx 8.30 library to operate with the NI PCI-6251 DAQ card

' Global variables for NI-DAQmx
Const MinVoltage = -10#
Const MaxVoltage = 10#
Const SamplingRate = 50000#
Const SamplesPerChanlToAcquire = 1000
Const bufferSize = 100000
Const Channel As String = "Dev1/ai0"
' Variables for system settings to be restored before closing com port
Dim OldHandShake As Integer
Dim OldSettings As String
Dim OldMode As Integer
Dim OldInputLen As Integer

Private Sub Form_Load()
   ' Initialize program settings
   With comboPortNum
      .AddItem 1
      .AddItem 2
   End With
   With comboUnitNum
      For i = 0 To 254
      .AddItem i
      Next i
   End With
   With comboCommandNum
      For i = 0 To 63
      .AddItem i
      Next i
   End With
   With comboWD
      For i = 25 To 300 Step 25
```

```
        .AddItem i
        Next i
    End With
    With comboTargetLoad
        For i = 0 To 8 Step 0.2
        .AddItem i
        Next i
    End With
    With comboTargetSpd
        .AddItem 0.4
        .AddItem 0.8
        .AddItem 1.1
        .AddItem 1.6
        .AddItem 2#
    End With
    comboTargetSpd.ListIndex = 0
    ' disable "Close COM port" button
    cmdCloseCom.Enabled = False
    cmdOpenCom.Enabled = True
    comboPortNum.Enabled = True
    ' initialize values of program status flags
    taskIsRunning = False
    flag_cal = True
    flag_pos_cal = False
    flag_feedback = False
    ' display com port status message
    lblStatus.Caption = "All com ports are currently closed."
    ' clear the text display area and add headings
    lstDisplay.Clear
    txtHeadings.Text = "Unit#       Command#       Data (bits)      Data (um)"
End Sub

Private Sub Form_Unload(Cancel As Integer)
    ' quit the program.
    If taskIsRunning = True Then
    ' call the NIDAQStopTask module to stop the DAQmx task.
        NIDAQStopTask
    End If
    End
End Sub

Private Sub cmdOpenCom_Click()
    ' the "open com port and initialize" button was clicked
    With objCommPort
        ' Set com port number based on user selection
        .CommPort = Val(comboPortNum.Text)
        ' try to open the port
        .PortOpen = True
        ' Save current port settings
        OldHandShake = .Handshaking
        OldSettings = .Settings
        OldMode = .InputMode
        OldInputLen = .InputLen
        ' Set the new settings for Zaber stage communications
        .Handshaking = comNone
        .Settings = "9600,N,8,1"
```

```
        .InputMode = comInputModeText
        .InputLen = 1
        .RThreshold = 1
    End With
    ' Disable port select button so different com port cannot be opened while the current one is in use
    cmdOpenCom.Enabled = False
    comboPortNum.Enabled = False
    ' enable the close com port button
    cmdCloseCom.Enabled = True
    ' display a com port status message
    lblStatus.Caption = "Com " & comboPortNum.Text & " is the current port."
    ' Stage initialization
    Call Renumber_All    ' Renumber all units
    Call Return_Pos_All    ' Return default data (position for LA28 devices)
    Call SetMaxLimit    ' Set maximum feeding limit
    Call SetMode    ' Initiate mode parameters for all units
    objCommPort.Output = Chr$(0) + Chr$(1) + Chr$(0) + Chr$(0) + Chr$(0) + Chr$(0)    ' origin return
    lblCalStatus.Caption = "Please Calibrate!"
End Sub

Sub Renumber_All()
    ' renumber all units
    objCommPort.Output = Chr$(0) + Chr$(2) + Chr$(0) + Chr$(0) + Chr$(0) + Chr$(0)
    Call Delay(0.3)    ' wait while renumbering
End Sub

Sub Return_Pos_All()
    ' tell all units to return their positions
    objCommPort.Output = Chr$(0) + Chr$(10) + Chr$(0) + Chr$(0) + Chr$(0) + Chr$(0)
    Call Delay(0.3)
End Sub

Sub SetMaxLimit()
    'set maximum feeding limit to 10000um / 100787 micro steps
    Call Position_to_bytes(100787)
    databytes = Chr$(iCommand(3)) + Chr$(iCommand(4)) + Chr$(iCommand(5)) + Chr$(iCommand(6))
    objCommPort.Output = Chr$(0) + Chr$(44) + databytes
    Call Delay(0.3)
End Sub

Sub SetMode()
    ' set mode parameters: Disable Potentiometer ('8') & Enable Constant Speed Position Tracking ('16')
    objCommPort.Output = Chr$(0) + Chr$(40) + Chr$(24) + Chr$(0) + Chr$(0) + Chr$(0)
End Sub

Private Sub cmdReturnOrigin_Click()
    ' the "Origin Return" button was clicked
    If (objCommPort.PortOpen = True) Then
        ' if the com port has already been opened, send the instruction
        objCommPort.Output = Chr$(0) + Chr$(1) + Chr$(0) + Chr$(0) + Chr$(0) + Chr$(0)
        lblCalStatus.Caption = "Please Calibrate!"
    Else
        ' the button was pressed before the com port was open
        MsgBox "You must open the com port before sending instructions."
    End If
End Sub
```

```
Private Sub cmdPApproachStart_Click()
   ' the "Approach (+)" button was clicked
   If (objCommPort.PortOpen = True) Then
      ' if the com port has already been opened, send the instruction
      If (optHighSpdApproach.Value = True) Then
         '750um/s
         objCommPort.Output = Chr$(0) + Chr$(22) + Chr$(64) + Chr$(0) + Chr$(0) + Chr$(0)
      Else
         '50um/s
         objCommPort.Output = Chr$(0) + Chr$(22) + Chr$(40) + Chr$(0) + Chr$(0) + Chr$(0)
      End If
      cmdApproachStop.Enabled = True
   Else
      ' the button was pressed before the com port was open
      MsgBox "You must open the com port before sending instructions."
   End If
End Sub

Private Sub cmdNApproachStart_Click()
   ' the "Approach (-)" button was clicked
   If (objCommPort.PortOpen = True) Then
      ' if the com port has already been opened, send the instruction
      If (optHighSpdApproach.Value = True) Then
         '750um/s
         ApproachSpd = -65
      Else
         '50um/s
         ApproachSpd = -41
      End If
      Call Position_to_bytes(ApproachSpd)
      databytes = Chr$(iCommand(3)) + Chr$(iCommand(4)) + Chr$(iCommand(5)) + Chr$(iCommand(6))
      objCommPort.Output = Chr$(0) + Chr$(22) + databytes
      cmdApproachStop.Enabled = True
   Else
      ' the button was pressed before the com port was open
      MsgBox "You must open the com port before sending instructions."
   End If
End Sub

Private Sub cmdApproachStop_Click()
   ' the "Approach Stop" button was clicked
   If (objCommPort.PortOpen = True) Then
      ' if the com port has already been opened, send the instruction
      objCommPort.Output = Chr$(0) + Chr$(23) + Chr$(0) + Chr$(0) + Chr$(0) + Chr$(0)
      cmdApproachStop.Enabled = False
   Else
      ' the button was pressed before the com port was open
      MsgBox "You must open the com port before sending instructions."
   End If
End Sub

Private Sub cmdCalibrate_Click()
   ' the "Calibrate" button was clicked
   On Error GoTo ErrorHandler
   If (objCommPort.PortOpen = True) Then
```

```
      ' if the com port has already been opened, send the instruction
      CalSpeed = 11
      flag_cal = True
      """"
      'DAQmx Configure Code'
      DAQmxErrChk DAQmxCreateTask("", taskhandle)
      taskIsRunning = True
      DAQmxErrChk DAQmxCreateAIVoltageChan(taskhandle, Channel, "", DAQmx_Val_Cfg_Default,
MinVoltage, MaxVoltage, DAQmx_Val_VoltageUnits2_Volts, "")
      DAQmxErrChk DAQmxCfgSampClkTiming(taskhandle, "", SamplingRate, DAQmx_Val_Rising,
DAQmx_Val_AcquisitionType_ContSamps, bufferSize)
      DAQmxErrChk DAQmxRegisterEveryNSamplesEvent(taskhandle, 1, SamplesPerChanlToAcquire, 0,
AddressOf EveryNSamplesEventHandler, Nothing)
      DAQmxErrChk DAQmxRegisterDoneEvent(taskhandle, 0, AddressOf TaskDoneEventHandler,_
Nothing)
      ReDim ScaledData(SamplesPerChanlToAcquire)
      """"
      'DAQmx Start Code'
      DAQmxErrChk DAQmxStartTask(taskhandle)
      """"
      objCommPort.Output = Chr$(0) + Chr$(22) + Chr$(CalSpeed) + Chr$(0) + Chr$(0) + Chr$(0)
      cmdCalibrate.Enabled = False
      cmdPApproachStart.Enabled = False
      cmdNApproachStart.Enabled = False
      cmdApproachStop.Enabled = False
   Else
      ' the button was pressed before the com port was open
      MsgBox "You must open the com port before sending instructions."
   End If
   Exit Sub
ErrorHandler:
   If taskIsRunning = True Then
      DAQmxStopTask taskhandle
      DAQmxClearTask taskhandle
      taskIsRunning = False
   End If
   MsgBox "Error:" & Err.Number & " " & Err.Description, , "Error"
End Sub

Private Sub cmdFBFeedStart_Click()
   ' the "Force Feedback Feed" button was clicked
   On Error GoTo ErrorHandler
   If (objCommPort.PortOpen = True) Then
      t_elapse = 0
      t_buffer = 0
      en_counttime = False
      CurrentSpeed = 1
      flag_cal = False
      flag_feedback = True
      """"
      'DAQmx Configure Code'
      DAQmxErrChk DAQmxCreateTask("", taskhandle)
      taskIsRunning = True
      DAQmxErrChk DAQmxCreateAIVoltageChan(taskhandle, Channel, "", DAQmx_Val_Cfg_Default,
MinVoltage, MaxVoltage, DAQmx_Val_VoltageUnits2_Volts, "")
```

```
      DAQmxErrChk DAQmxCfgSampClkTiming(taskhandle, "", SamplingRate, DAQmx_Val_Rising,
DAQmx_Val_AcquisitionType_ContSamps, bufferSize)
      DAQmxErrChk DAQmxRegisterEveryNSamplesEvent(taskhandle, 1, SamplesPerChanlToAcquire, 0,
AddressOf EveryNSamplesEventHandler, Nothing)
      DAQmxErrChk DAQmxRegisterDoneEvent(taskhandle, 0, AddressOf TaskDoneEventHandler,_
Nothing)
      ReDim ScaledData(SamplesPerChanlToAcquire)
      """
      'DAQmx Start Code'
      DAQmxErrChk DAQmxStartTask(taskhandle)
      """
      objCommPort.Output = Chr$(0) + Chr$(22) + Chr$(CurrentSpeed) + Chr$(0) + Chr$(0) + Chr$(0)
      cmdFBFeedStart.Enabled = False
      cmdCSpdFeedStart.Enabled = False
      cmdFeedStop.Enabled = True
   Else
      ' the button was pressed before the com port was open
      MsgBox "You must open the com port before sending instructions."
   End If
   Exit Sub
ErrorHandler:
   If taskIsRunning = True Then
      DAQmxStopTask taskhandle
      DAQmxClearTask taskhandle
      taskIsRunning = False
   End If
   MsgBox "Error:" & Err.Number & " " & Err.Description, , "Error"
End Sub

Private Sub cmdCSpdFeedStart_Click()
   ' the "Constant Speed Feed" button was clicked
   On Error GoTo ErrorHandler
   If (objCommPort.PortOpen = True) Then
      t_elapse = 0
      t_buffer = 0
      en_counttime = False
      CurrentSpeed = comboTargetSpd.ListIndex + 1
      flag_cal = False
      flag_feedback = False
      """
      'DAQmx Configure Code'
      DAQmxErrChk DAQmxCreateTask("", taskhandle)
      taskIsRunning = True
      DAQmxErrChk DAQmxCreateAIVoltageChan(taskhandle, Channel, "", DAQmx_Val_Cfg_Default,
MinVoltage, MaxVoltage, DAQmx_Val_VoltageUnits2_Volts, "")
      DAQmxErrChk DAQmxCfgSampClkTiming(taskhandle, "", SamplingRate, DAQmx_Val_Rising,
DAQmx_Val_AcquisitionType_ContSamps, bufferSize)
      DAQmxErrChk DAQmxRegisterEveryNSamplesEvent(taskhandle, 1, SamplesPerChanlToAcquire, 0,
AddressOf EveryNSamplesEventHandler, Nothing)
      DAQmxErrChk DAQmxRegisterDoneEvent(taskhandle, 0, AddressOf TaskDoneEventHandler,_
Nothing)
      ReDim ScaledData(SamplesPerChanlToAcquire)
      """
      'DAQmx Start Code'
      DAQmxErrChk DAQmxStartTask(taskhandle)
      """
```

```
      objCommPort.Output = Chr$(0) + Chr$(22) + Chr$(CurrentSpeed) + Chr$(0) + Chr$(0) + Chr$(0)
      cmdFBFeedStart.Enabled = False
      cmdCSpdFeedStart.Enabled = False
      cmdFeedStop.Enabled = True
   Else
      ' the button was pressed before the com port was open
      MsgBox "You must open the com port before sending instructions."
   End If
   Exit Sub
ErrorHandler:
   If taskIsRunning = True Then
      DAQmxStopTask taskhandle
      DAQmxClearTask taskhandle
      taskIsRunning = False
   End If
   MsgBox "Error:" & Err.Number & " " & Err.Description, , "Error"
End Sub

Private Sub cmdFeedStop_Click()
   ' the "Stop" button for feeding was clicked
   If (objCommPort.PortOpen = True) Then
      ' if the com port has already been opened, send the instruction
      Call Delay(0.3)
      objCommPort.Output = Chr$(0) + Chr$(23) + Chr$(0) + Chr$(0) + Chr$(0) + Chr$(0)
      lblCutStatus.Caption = "Status:               Idle"
      lblCurrentSpeed.Caption = "Current Feed Speed:    0 (um/s)"
      cmdFBFeedStart.Enabled = True
      cmdCSpdFeedStart.Enabled = True
      cmdFeedStop.Enabled = False
      flag_cal = True
      ' Call the NIDAQStopTask module to stop the DAQmx task.
      NIDAQStopTask
   Else
      ' the button was pressed before the com port was open
      MsgBox "You must open the com port before sending instructions."
   End If
End Sub

"""Stage Raw Command Control"""
Private Sub cmdSend_Click()
   ' the "send instruction" button was clicked
   If (objCommPort.PortOpen = True) Then
      ' if the com port has already been openned convert the user data and send the instruction
      If (optMicrons.Value = True) Then
         ' convert data from microns to microsteps before sending it
         Position = Round(Val(txtData.Text) * 64 / 6.35, 0)
      Else
         Position = Val(txtData.Text)
      End If
      Call Position_to_bytes(Position)
      ' put all entered values in format to send to com port
      unit = Chr(comboUnitNum.Text)
      inst = Chr(comboCommandNum.Text)
      databytes = Chr$(iCommand(3)) + Chr$(iCommand(4)) + Chr$(iCommand(5)) + Chr$(iCommand(6))
      objCommPort.Output = unit + inst + databytes
   Else
```

```
      ' the send button was pressed before the com port was open
      MsgBox "You must open the com port before sending instructions."
   End If
End Sub

Private Sub cmdCloseCom_Click()
   ' "close com port" button clicked, return com port settings to previous system values, then close the port
   With objCommPort
      .Handshaking = OldHandShake
      .Settings = OldSettings
      .InputMode = OldInputMode
      .InputLen = OldInputLen
      .PortOpen = False
   End With
   ' disable close com port button
   cmdCloseCom.Enabled = False
   ' enable open com port button
   cmdOpenCom.Enabled = True
   comboPortNum.Enabled = True
   ' change the status message
   lblStatus.Caption = "All com ports are currently closed."
End Sub

Private Sub objCommPort_OnComm()
   ' COM communication event handler
   If objCommPort.CommEvent = comEvReceive Then
      ' The com event was triggered because there is a byte in the receive buffer.
      ' Determine elapsed time since the last byte was received
      t_last = t_now
      t_now = Timer
      If (t_now - t_last) > 0.1 Then
         While bytecount > 0
         ' remove the questionable bytes from the receive buffer
         temp = objCommPort.Input
         ' adjust the bytecount accordingly
         bytecount = bytecount - 1
         Wend
      End If
      ' count the byte that was just received
      bytecount = bytecount + 1
      ' read the byte into the reply array
      bReply(bytecount) = Asc(objCommPort.Input)
      ' if this byte is the sixth then display the reply
      If bytecount = 6 Then
         ' calculate the value of the 4 byte data in the reply
         Call Bytes_to_position
         ' make sure there are enough lines in the display list to display the reply on appropriate line number
         If flag_pos_cal = True Then
            lblZero.Caption = "Zero position: " & dReplyDataUm & " (um)"
            lblCalStatus.Caption = "Ready!"
            lblCutDepth.Caption = "Current Cut Depth:    " & -Val(comboWD.Text) & " (um)"
            zeropos = dReplyDataUm
            bytecount = 0
            flag_pos_cal = False
         ElseIf flag_cal = False Then
            If chkManualZero.Value = 1 Then
```

```
            currentCutDepth = dReplyDataUm - Val(txtManualZero.Text)
          Else
            currentCutDepth = dReplyDataUm - zeropos
          End If
          lblCutDepth.Caption = "Current Cut Depth:       " & Round(currentCutDepth, 2) & " (um)"
        End If
        ' display text with appropriate column spacing
        ' determine text lengths
        L1 = Len(Str(bReply(1)))
        L2 = Len(Str(bReply(2)))
        L3 = Len(Str(dReplyData))
        ' determine needed spacing
        S1 = Left$("                ", 13 - L1)
        S2 = Left$("                ", 16 - L2)
        S3 = Left$("                ", 18 - L3)
        ' determine the complete line of display text
        DisplayString = bReply(1) & S1 & bReply(2) & S2 & dReplyData & S3 & dReplyDataUm
        ' display the text on the appropriate line number
        lstDisplay.List(0) = DisplayString
        ' reset the bytecount to zero
        bytecount = 0
      End If
    End If
End Sub
```

A.1.2 EventHandler.bas

```
Public Declare Function GetCurrentThreadId Lib "kernel32" () As Long

'NI-DAQmx variables
Public taskhandle As Long             ' NI DAQ Task Handler
Public taskIsRunning As Boolean       ' NI DAQ Task running flag
Public ScaledData() As Double         ' Scaled Data Array from NI DAQ
' Process control variables
Public AvgForce As Double             ' sensor reading statistics
Public MaxForce As Double
Public SumData As Double
Public MaxData As Double
Public Const InitSpeed = 5            ' initial feeding speed
Public CurrentSpeed As Integer        ' current feeding speed
Public Const CuttingThreshold = 0.5   ' threshold value for machining starting point
Public t_start As Double              ' machining starting timer value
Public t_end As Double                ' machining ending timer value
Public t_elapse As Double             ' machining time
Public t_buffer As Double             ' machining time buffer
Public en_counttime                   ' Time counter state control flag
Public flag_cal As Boolean            ' Flag to choose calibration or machining feeding
Public flag_pos_cal As Boolean        ' Flag to choose position return to calibrate or to display
Public flag_feedback As Boolean       ' Flag to choose force feedback feeding or constant speed feeding
Public zeropos As Double              ' zero position of tool head
Public currentCutDepth As Double      ' Current cutting depth
' Others
Public iCommand(1 To 6) As Integer    ' 6 byte instruction
Public t_now As Double                ' current timer value
```

```
Public t_last As Double              ' timer value when last byte was received
Public bytecount As Integer          ' number of bytes in receive buffer
Public bReply(1 To 6) As Byte        ' 6 byte reply from Zaber stage
Public dReplyData As Double          ' value of 4 data bytes in reply
Public dReplyDataUm As Double        ' as above but in units of um

Public Function TaskDoneEventHandler(ByVal LocalTaskhandle As Long, ByVal status As Long, ByVal
callbackData As Long) As Long
   MsgBox "Task ended in error! In task done event handler."
   TaskDoneEventHandler = 0
End Function

Public Function EveryNSamplesEventHandler(ByVal LocalTaskhandle As Long, ByVal eventType As
Long, ByVal numSamples As Long, ByVal callbackData As Long) As Long
   On Error GoTo ErrorHandler
   Dim i
   Dim numRead As Long
   MaxData = 0
   SumData = 0
   ' Read data
  DAQmxErrChk DAQmxReadAnalogF64(LocalTaskhandle, numSamples, 10,_
DAQmx_Val_GroupByScanNumber, ScaledData(0), numSamples, numRead, ByVal 0)
   If flag_cal = True Then
      Call CalibrateFeeding(ScaledData)
   Else
      Call MachiningFeeding(ScaledData)
   End If
   ControlPanel.CWGraph1.PlotY ScaledData
   EveryNSamplesEventHandler = 0
   Exit Function
ErrorHandler:
   If taskIsRunning = True Then
      DAQmxStopTask LocalTaskhandle
      DAQmxClearTask LocalTaskhandle
      taskIsRunning = False
   End If
   MsgBox "Error:" & Err.Number & " " & Err.Description, , "Error"
End Function

Public Sub CalibrateFeeding(CalData As Variant)
   For i = 0 To 999
      SumData = SumData + Abs(CalData(i))
      If Abs(CalData(i)) > MaxData Then
         MaxData = Abs(CalData(i))
      End If
   Next
   AvgForce = SumData / 1000 / 0.114
   MaxForce = MaxData / 0.114
   If AvgForce > 0.2 Then
      ControlPanel.objCommPort.Output = Chr$(0) + Chr$(23) + Chr$(0) + Chr$(0) + Chr$(0) + Chr$(0)
      Call Delay(0.3)
      flag_pos_cal = True
      ' return its current position to record as zero position
      ControlPanel.objCommPort.Output = Chr$(0) + Chr$(60) + Chr$(0) + Chr$(0) + Chr$(0) + Chr$(0)
      Call Delay(0.3)
      ' move relatively -WD um (or -WD*64/6.35 micro steps)
```

```
      Call Position_to_bytes(-Val(ControlPanel.comboWD.Text) * 64 / 6.35)
      databytes = Chr$(iCommand(3)) + Chr$(iCommand(4)) + Chr$(iCommand(5)) + Chr$(iCommand(6))
      ControlPanel.objCommPort.Output = Chr$(0) + Chr$(21) + databytes
      ControlPanel.cmdCalibrate.Enabled = True
      ControlPanel.cmdPApproachStart.Enabled = True
      ControlPanel.cmdNApproachStart.Enabled = True
      ControlPanel.cmdApproachStop.Enabled = False
      ' Call the NIDAQStopTask module to stop the DAQmx task.
      NIDAQStopTask
    End If
End Sub

Public Sub MachiningFeeding(FBData As Variant)
    For i = 0 To 999
      SumData = SumData + Abs(FBData(i))
      If Abs(FBData(i)) > MaxData Then
        MaxData = Abs(FBData(i))
      End If
    Next
    AvgForce = SumData / 1000 / 0.114     'Convert voltage signal (V) to force value(N) by divided by 0.114
    MaxForce = MaxData / 0.114
    AvgF = Round(AvgForce, 3)                    'Round to 3 digits for display
    MaxF = Round(MaxForce, 3)                    'Round to 3 digits for display
    ControlPanel.lblAvgLoad.Caption = "Current Average Load: " & AvgF & " (N)"
    ControlPanel.lblMaxLoad.Caption = "Current Peak Load:      " & MaxF & " (N)"
    If AvgForce >= CuttingThreshold Then
      ControlPanel.lblCutStatus.Caption = "Status:               Machining!"
      If en_counttime = False Then
        t_start = Timer
      End If
      en_counttime = True
      t_end = Timer
      t_elapse = t_buffer + t_end - t_start
      t_display = Round(t_elapse, 2)             'Round to 2 digits for display
      ControlPanel.lblCutTime.Caption = "Machining Time:         " & t_display & " secs"
      If flag_feedback = True Then
        If AvgForce > (Val(ControlPanel.comboTargetLoad.Text) * 1.10) Then
          If CurrentSpeed >= 1 Then
            CurrentSpeed = CurrentSpeed - 1
          End If
        ElseIf AvgForce < (Val(ControlPanel.comboTargetLoad.Text) * 0.90) Then
          If CurrentSpeed <= 4 Then
          CurrentSpeed = CurrentSpeed + 1
          End If
        Else
          CurrentSpeed = CurrentSpeed
        End If
      End If
      ' send speed change command to stage
      Call Position_to_bytes(CurrentSpeed)
      databytes = Chr$(iCommand(3)) + Chr$(iCommand(4)) + Chr$(iCommand(5)) + Chr$(iCommand(6))
      ControlPanel.objCommPort.Output = Chr$(0) + Chr$(22) + databytes
    Else
      en_counttime = False
      t_buffer = t_elapse
      ControlPanel.lblCutStatus.Caption = "Status:               Approaching!"
```

```
        t_display = Round(t_elapse, 2)              'Round to 2 digits for display
        ControlPanel.lblCutTime.Caption = "Machining Time:          " & t_display & " secs"
    End If
    ' display current speed
    Select Case CurrentSpeed
        Case 5
            spd_display = 2#
        Case 4
            spd_display = 1.6
        Case 3
            spd_display = 1.1
        Case 2
            spd_display = 0.8
        Case 1
            spd_display = 0.4
        Case 0, -1
            spd_display = 0
        Case -2
            spd_display = -0.4
        Case -3
            spd_display = -0.8
        Case -4
            spd_display = -1.1
        Case -5
            spd_display = -1.6
        Case -6
            spd_display = -2#
        Case Else
            spd_display = "Error!"
    End Select
    ControlPanel.lblCurrentSpeed.Caption = "Current Feed Speed:    " & spd_display & " (um/s)"
End Sub

Public Sub NIDAQStopTask()
    ' Stop the task and unload it
    On Error GoTo ErrorHandler
    If (taskhandle <> 0) Then
        DAQmxErrChk DAQmxStopTask(taskhandle)
        DAQmxErrChk DAQmxClearTask(taskhandle)
        taskhandle = 0
        taskIsRunning = False
    End If
    Exit Sub
ErrorHandler:
    If taskIsRunning = True Then
        DAQmxStopTask taskhandle
        DAQmxClearTask taskhandle
        taskIsRunning = False
    End If
    MsgBox "Error:" & Err.Number & " " & Err.Description, , "Error"
End Sub

Public Sub Delay(d)
    ' wait for d seconds
    t = Timer
    While (Timer - t) < d
```

```
    Wend
End Sub

Public Sub Position_to_bytes(ByVal Position As Double)
    ' convert the user input data into 4 data bytes to send
    If Position < 0 Then
        'negative value entered by user
        Position = 4294967296# + Position
    End If
        iCommand(6) = Int(Position / (256# * 256# * 256#))
        Position = Position - 256# * 256# * 256# * iCommand(6)
        iCommand(5) = Int(Position / (256# * 256#))
        Position = Position - 256# * 256# * iCommand(5)
        iCommand(4) = Int(Position / 256#)
        Position = Position - 256# * iCommand(4)
        iCommand(3) = Int(Position)
End Sub

Public Sub Bytes_to_position()
    ' convert the 4 received data bytes to a single value
    If bReply(6) > 127 Then         ' negative
    dReplyData = -4294967296# + 256# * 256# * 256# * bReply(6) + 256# * 256# * bReply(5) + 256# *
bReply(4) + bReply(3)
    Else
    dReplyData = 256# * 256# * 256# * bReply(6) + 256# * 256# * bReply(5) + 256# * bReply(4) +
bReply(3)
    End If
    ' determine the value in units of um: ReplyData(um)=ReplyData(usteps)*6.35(um/step)/64(usteps/step)
    dReplyDataUm = Round(dReplyData * 6.35 / 64, 2)
End Sub
```

A.1.3 NIDAQmxErrorCheck.bas

```
Public Sub DAQmxErrChk(errorCode As Long)
'   Utility function to handle errors by recording the DAQmx error code and message.
    Dim errorString As String
    Dim bufferSize As Long
    Dim status As Long
    If (errorCode < 0) Then
        ' Find out the error message length.
        bufferSize = DAQmxGetErrorString(errorCode, 0, 0)
        ' Allocate enough space in the string.
        errorString = String$(bufferSize, 0)
        ' Get the actual error message.
        status = DAQmxGetErrorString(errorCode, errorString, bufferSize)
        ' Trim it to the actual length, and display the message
        errorString = Left(errorString, InStr(errorString, Chr$(0)))
        Err.Raise errorCode, , errorString
    End If
End Sub
```

A.2 Advanced Apparatus

A.2.1 AEControlPanel.frm

```
' Micro-USM Process Control Program with Thorlabs stage and AE detection - Visual Basic 6.0
' Written by Tao Li, with help from Saira Shariff and Rachit Gupta
' Last updated May 18, 2008
"""
' Form-wide NI-DAQmx variables
Const MinVoltage = -10#
Const MaxVoltage = 10#
Const SamplingRate = 50000#
Const SamplesPerChanlToAcquire = 1024
Const Channel As String = "Dev1/ai0"

Private Sub Form_Load()
' Set up of Motor.
    ' Set serial number - either here in code OR use properties of control on form
    ' (use number of actual HW unit or simulated unit)
    MG17Motor1.HWSerialNum = ######## 'located at the back of unit, changed to # for publication
    ' Start motor control.
    MG17Motor1.StartCtrl
    MG17Motor1.SetBLashDist CHAN1_ID, 0
' Initialize combo box choices
    ' Setting the Working Distance choices for calibration
    With comboWD
        For i = 25 To 300 Step 25
        .AddItem i
        Next i
    End With
    ' Setting the speed choices for constant machining
    With comboTargetSpd
        .AddItem 0.05
        .AddItem 0.08
        .AddItem 0.1
        .AddItem 0.2
        .AddItem 0.3
        .AddItem 0.5
        .AddItem 0.8
        .AddItem 1#
        .AddItem 1.5
        .AddItem 2#
    End With
    comboTargetSpd.ListIndex = 0
    ' Setting target AE RMS feedback value
    With comboTargetAERMS
        For i = 1# To 8# Step 1
        .AddItem i
        Next i
    End With
' Initialize parameters
    taskIsRunning = False
```

```
    flag_cal = True
    flag_feedback = False
    RMS_Counter = -1
    STD_Counter = -1
    For i = 0 To 512
        FFTImgIn(i) = 0
        DisplayData(i, 1) = (i + 1) / 512 * SamplingRate / 2 / 1000
        RMS_AE(i) = 0
        RMS_AE(i) = 0
    Next
    For i = 513 To 1023
        FFTImgIn(i) = 0
    Next
End Sub

Private Sub cmdInitialization_Click()
    ' Brings the motors to zero position. Always begin with this position.
    MG17Motor1.MoveHome CHAN1_ID, True
    lblAvgLoad.Caption = "Current Average Load:    " & 0 & " (V)"
    lblMaxLoad.Caption = "Current Peak Load:       " & 0 & " (V)"
    lblCutDepth.Caption = "Current Cut Depth:          " & 0 & " (um)"
    lblCutTime.Caption = "Machining Time:              " & 0 & " secs"
End Sub

Private Sub cmdHome_Click()
    ' Home motors
        ' Move the motors to a point slightly higher (0.3mm) than the initialization point
    MG17Motor1.SetPositionOffset CHAN1_ID, 0
    MG17Motor1.SetAbsMovePos CHAN1_ID, 0.1  ' Sets the desired position
    MG17Motor1.SetVelParams CHAN1_ID, 0, 0.1, 0.3  ' Sets the desired velocity
    MG17Motor1.MoveAbsolute CHAN1_ID, True
    cmdPApproachStart.Enabled = True
    cmdNApproachStart.Enabled = True
End Sub

Private Sub optHighSpdApproach_Click()
    ' Setting the velocity at 200um when the option button is selected
    MG17Motor1.SetVelParams CHAN1_ID, 0, 0.1, 0.2
End Sub

Private Sub optLowSpdApproach_Click()
    ' Setting the velocity at 50um when the option button is selected
    MG17Motor1.SetVelParams CHAN1_ID, 0, 0.1, 0.05
End Sub

Private Sub cmdNApproachStart_Click()
    ' Decrementing at two different speeds i.e. 200um and 50um when the desired option is selected
    If (optHighSpdApproach.Value = True) Then
        ' 200um/s
        MG17Motor1.SetVelParams CHAN1_ID, 0, 0.1, 0.2
        MG17Motor1.MoveVelocity CHAN1_ID, MOVE_REV
    ElseIf (optLowSpdApproach.Value = True) Then
        ' 50um/s
        MG17Motor1.SetVelParams CHAN1_ID, 0, 0.1, 0.05
        MG17Motor1.MoveVelocity CHAN1_ID, MOVE_REV
    Else
```

```
      ' If the '-' button is pressed without selecting the speed, message box will pop
      MsgBox "Please select a speed first!"
   End If
   cmdApproachStop.Enabled = True
   cmdCalibrate.Enabled = False
End Sub

Private Sub cmdPApproachStart_Click()
   ' Incrementing at two different speeds i.e. 200um and 50um when the desired option is selected
   If (optHighSpdApproach.Value = True) Then
      ' 200um/s
      MG17Motor1.SetVelParams CHAN1_ID, 0, 0.1, 0.2
      MG17Motor1.MoveVelocity CHAN1_ID, MOVE_FWD
   ElseIf (optLowSpdApproach.Value = True) Then
      ' 50um/s
      MG17Motor1.SetVelParams CHAN1_ID, 0, 0.1, 0.05
      MG17Motor1.MoveVelocity CHAN1_ID, MOVE_FWD
   Else
      ' If the '+' button is pressed without selecting the speed, message box will pop
      MsgBox "Please select a speed first!"
   End If
   cmdApproachStop.Enabled = True
   cmdCalibrate.Enabled = False
End Sub

Private Sub cmdApproachStop_Click()
   ' Stops the movement
   MG17Motor1.StopProfiled CHAN1_ID
   cmdApproachStop.Enabled = False
   cmdCalibrate.Enabled = True
End Sub

Private Sub cmdCalibrate_Click()
   ' the "Calibrate" button was clicked
   On Error GoTo ErrorHandler
   ' if the com port has already been opened, send the instruction
   flag_cal = True
   """"
   'DAQmx Configure Code'
   DAQmxErrChk DAQmxCreateTask("", taskhandle)
   taskIsRunning = True
   DAQmxErrChk DAQmxCreateAIVoltageChan(taskhandle, Channel, "", DAQmx_Val_Cfg_Default,
MinVoltage, MaxVoltage, DAQmx_Val_VoltageUnits2_Volts, "")
   DAQmxErrChk DAQmxCfgSampClkTiming(taskhandle, "", SamplingRate, DAQmx_Val_Rising,
DAQmx_Val_AcquisitionType_ContSamps, 102400)
   DAQmxErrChk DAQmxRegisterEveryNSamplesEvent(taskhandle, 1, SamplesPerChanlToAcquire, 0,
AddressOf EveryNSamplesEventHandler, Nothing)
   DAQmxErrChk DAQmxRegisterDoneEvent(taskhandle, 0, AddressOf TaskDoneEventHandler,_
Nothing)
   ReDim ScaledData(SamplesPerChanlToAcquire)
   """"
   'DAQmx Start Code'
   DAQmxErrChk DAQmxStartTask(taskhandle)
   """"
   'Stage Control Code'
   MG17Motor1.SetJogMode CHAN1_ID, JOG_CONTINUOUS, STOP_PROFILED
```

```
    MG17Motor1.SetJogVelParams CHAN1_ID, 0, 0.1, CalSpeed
    MG17Motor1.MoveJog CHAN1_ID, JOG_FWD
    """
    cmdPApproachStart.Enabled = False
    cmdNApproachStart.Enabled = False
    cmdApproachStop.Enabled = False
    cmdCSpdStart.Enabled = False
    cmdAEFBStart.Enabled = False
    cmdCalibrate.Enabled = False
    cmdCalStop.Enabled = True
    Exit Sub
ErrorHandler:
    If taskIsRunning = True Then
        DAQmxStopTask taskhandle
        DAQmxClearTask taskhandle
        taskIsRunning = False
    End If
    MsgBox "Error:" & Err.Number & " " & Err.Description, , "Error"
End Sub

Private Sub cmdCalStop_Click()
    ' Stops the movement
    MG17Motor1.StopProfiled CHAN1_ID
    cmdPApproachStart.Enabled = True
    cmdNApproachStart.Enabled = True
    cmdCalibrate.Enabled = True
    cmdCalStop.Enabled = False
    ' Call the NIDAQStopTask module to stop the DAQmx task.
    If taskIsRunning = True Then
        NIDAQStopTask
    End If
End Sub

Private Sub cmdCSpdStart_Click()
    ' the "Constant Speed Feed" button was clicked
    On Error GoTo ErrorHandler
    t_elapse = 0
    t_buffer = 0
    en_counttime = False
    CurrentSpeed = Val(comboTargetSpd.Text)
    Timer1.Interval = 40 / CurrentSpeed     '1000ms / (CurrentSpeed / 0.04nm/sec)
    flag_cal = False
    flag_feedback = False
    """
    'DAQmx Configure Code'
    DAQmxErrChk DAQmxCreateTask("", taskhandle)
    taskIsRunning = True
    DAQmxErrChk DAQmxCreateAIVoltageChan(taskhandle, Channel, "", DAQmx_Val_Cfg_Default,
MinVoltage, MaxVoltage, DAQmx_Val_VoltageUnits2_Volts, "")
    DAQmxErrChk DAQmxCfgSampClkTiming(taskhandle, "", SamplingRate, DAQmx_Val_Rising,
DAQmx_Val_AcquisitionType_ContSamps, 102400)
    DAQmxErrChk DAQmxRegisterEveryNSamplesEvent(taskhandle, 1, SamplesPerChanlToAcquire, 0,
AddressOf EveryNSamplesEventHandler, Nothing)
   DAQmxErrChk DAQmxRegisterDoneEvent(taskhandle, 0, AddressOf TaskDoneEventHandler,_
Nothing)
    ReDim ScaledData(SamplesPerChanlToAcquire)
```

```
    """
    'DAQmx Start Code'
    DAQmxErrChk DAQmxStartTask(taskhandle)
    """
    ' Machining with the desired speeds
    StartMicroStepFeed
    """
    cmdPApproachStart.Enabled = False
    cmdNApproachStart.Enabled = False
    cmdCSpdStart.Enabled = False
    cmdAEFBStart.Enabled = False
    cmdCalibrate.Enabled = False
    cmdCSpdStop.Enabled = True
    Exit Sub
ErrorHandler:
    If taskIsRunning = True Then
        DAQmxStopTask taskhandle
        DAQmxClearTask taskhandle
        taskIsRunning = False
    End If
    MsgBox "Error:" & Err.Number & " " & Err.Description, , "Error"
End Sub

Private Sub cmdCSpdPause_Click()
    ' Stops the movement
    StopMicroStepFeed
    cmdCSpdStop.Enabled = False
End Sub

Private Sub cmdCSpdStop_Click()
    ' the "Stop" button for constant speed feeding was clicked, stop the movement
    StopMicroStepFeed
    """
    lblCutStatus.Caption = "Status:                    Idle"
    lblCurrentSpd.Caption = "Current Feed Speed:          0 (um/s)"
    cmdPApproachStart.Enabled = True
    cmdNApproachStart.Enabled = True
    cmdCalibrate.Enabled = True
    cmdAEFBStart.Enabled = True
    cmdCSpdStart.Enabled = True
    cmdAEFBStop.Enabled = False
    cmdCSpdStop.Enabled = False
    """
    flag_cal = True
    flag_feedback = False
    """
    ' Call the NIDAQStopTask module to stop the DAQmx task.
    If taskIsRunning = True Then
        NIDAQStopTask
    End If
End Sub

Private Sub cmdAEFBStart_Click()
    ' the "AE Feedback Feed" button was clicked
    On Error GoTo ErrorHandler
    t_elapse = 0
```

```
    t_buffer = 0
    en_counttime = False
    CurrentSpeed = InitSpeed
    flag_cal = False
    flag_feedback = True
    """
    'DAQmx Configure Code'
    DAQmxErrChk DAQmxCreateTask("", taskhandle)
    taskIsRunning = True
    DAQmxErrChk DAQmxCreateAIVoltageChan(taskhandle, Channel, "", DAQmx_Val_Cfg_Default,
MinVoltage, MaxVoltage, DAQmx_Val_VoltageUnits2_Volts, "")
    DAQmxErrChk DAQmxCfgSampClkTiming(taskhandle, "", SamplingRate, DAQmx_Val_Rising,_
DAQmx_Val_AcquisitionType_ContSamps, 102400)
    DAQmxErrChk DAQmxRegisterEveryNSamplesEvent(taskhandle, 1, SamplesPerChanlToAcquire, 0,
AddressOf EveryNSamplesEventHandler, Nothing)
    DAQmxErrChk DAQmxRegisterDoneEvent(taskhandle, 0, AddressOf TaskDoneEventHandler,_
Nothing)
    ReDim ScaledData(SamplesPerChanlToAcquire)
    """
    'DAQmx Start Code'
    DAQmxErrChk DAQmxStartTask(taskhandle)
    """
    ' Machining with the desired speeds
    StartMicroStepFeed
    """
    cmdPApproachStart.Enabled = False
    cmdNApproachStart.Enabled = False
    cmdCSpdStart.Enabled = False
    cmdAEFBStart.Enabled = False
    cmdCalibrate.Enabled = False
    cmdAEFBStop.Enabled = True
    Exit Sub
ErrorHandler:
    If taskIsRunning = True Then
        DAQmxStopTask taskhandle
        DAQmxClearTask taskhandle
        taskIsRunning = False
    End If
    MsgBox "Error:" & Err.Number & " " & Err.Description, , "Error"
End Sub

Private Sub cmdAEFBPause_Click()
    ' Stops the movement
    StopMicroStepFeed
    cmdCSpdStop.Enabled = False
End Sub

Private Sub cmdAEFBStop_Click()
    ' the "Stop" button for AE feedback feeding was clicked, stop the movement
    StopMicroStepFeed
    """
    lblCutStatus.Caption = "Status:                Idle"
    lblCurrentSpd.Caption = "Current Feed Speed:          0 (um/s)"
    """
    cmdPApproachStart.Enabled = True
    cmdNApproachStart.Enabled = True
```

```
    cmdCSpdStart.Enabled = True
    cmdAEFBStart.Enabled = True
    cmdCalibrate.Enabled = True
    cmdAEFBStop.Enabled = False
    """
    flag_cal = True
    flag_feedback = False
    """
    ' Call the NIDAQStopTask module to stop the DAQmx task.
    If taskIsRunning = True Then
        NIDAQStopTask
    End If
End Sub

Private Sub Form_Unload(Cancel As Integer)
    ' Stop Motor control
    MG17Motor1.StopCtrl
    If taskIsRunning = True Then
        '  Call the NIDAQStopTask module to stop the DAQmx task.
        NIDAQStopTask
    End If
    End
End Sub

Private Sub cmdExit_Click()
    ' Unload form
    Unload Me
    End
End Sub

Private Sub Timer1_Timer()
    MoveRelDist
End Sub
```

A.2.2 EventHandler.bas

```
Public Declare Function GetCurrentThreadId Lib "kernel32" () As Long

'NI-DAQmx variables
Public taskhandle As Long             ' NI DAQ Task Handler
Public taskIsRunning As Boolean       ' NI DAQ Task running flag
Public ScaledData() As Double         ' Scaled Data Array from NI DAQ
' Other Global Variables
Public AvgForce As Double             ' statistic sensor data
Public MaxForce As Double
Public RMS_AE(513) As Double
Public RMS_Counter As Integer
Public MaxAE As Double
Public AvgData As Double
Public SumData As Double
Public SumDataAvg As Double
Public MaxData As Double
Public FFTRealOut(1024) As Double, FFTImgIn(1024) As Double, FFTImgOut(1024) As Double
Public FFTData(513) As Double
```

```
Public Const CalSpeed = 0.005          ' Calibration feeding speed
Public Const InitSpeed = 0.0005            ' initial feeding speed
Public CurrentSpeed As Single            ' current feeding speed
Public Const CuttingThreshold = 0.5    ' threshold value for machining starting point
Public t_start As Double              ' machining starting timer value
Public t_end As Double                ' machining ending timer value
Public t_elapse As Double             ' machining time
Public t_buffer As Double             ' machining time buffer
Public en_counttime                 ' Time counter state control flag
Public flag_cal As Boolean            ' Flag to choose calibration or machining feeding
Public flag_feedback As Boolean       ' Flag to choose force feedback feeding or constant speed feeding
Public zeropos As Single              ' zero position of tool head
Public currentpos As Single           ' current position of tool head
Public currentCutDepth As Double      ' Current cutting depth

Public Function TaskDoneEventHandler(ByVal LocalTaskhandle As Long, ByVal status As Long, ByVal
callbackData As Long) As Long
   MsgBox "Task ended in error! In task done event handler."
   TaskDoneEventHandler = 0
End Function

Public Function EveryNSamplesEventHandler(ByVal LocalTaskhandle As Long, ByVal eventType As
Long, ByVal NumSamples As Long, ByVal callbackData As Long) As Long
   On Error GoTo ErrorHandler
   Dim i
   Dim numRead As Long
   MaxData = 0
   SumData = 0
   SumDataAvg = 0
   ' Read data
   DAQmxErrChk DAQmxReadAnalogF64(LocalTaskhandle, NumSamples, 10,_
DAQmx_Val_GroupByScanNumber, ScaledData(0), NumSamples, numRead, ByVal 0)
   If flag_cal = True Then
      Call CalibrateFeeding(ScaledData)
   Else
      Call MachiningFeeding(ScaledData)
   End If
   EveryNSamplesEventHandler = 0
   Exit Function
ErrorHandler:
   If taskIsRunning = True Then
      DAQmxStopTask LocalTaskhandle
      DAQmxClearTask LocalTaskhandle
      taskIsRunning = False
   End If
   MsgBox "Error:" & Err.Number & " " & Err.Description, , "Error"
End Function

Public Sub CalibrateFeeding(CalData() As Double)
   For i = 0 To 1023
      SumData = SumData + CalData(i) ^ 2
      SumDataAvg = SumDataAvg + CalData(i)
      If Abs(CalData(i)) > MaxData Then
         MaxData = Abs(CalData(i))
      End If
   Next
```

```
    AvgData = SumDataAvg / 1024
    If RMS_Counter < 512 Then
        RMS_Counter = RMS_Counter + 1
        RMS_AE(RMS_Counter) = Sqr(SumData / 1024 - AvgData ^ 2)
    Else
        RMS_Counter = 0
        RMS_AE(RMS_Counter) = Sqr(SumData / 1024 - AvgData ^ 2)
    End If
    AEControlPanel.CWGraph1.PlotY RMS_AE
    If RMS_AE(RMS_Counter) > 0.2 Then
        ' Call the NIDAQStopTask module to stop the DAQmx task.
        NIDAQStopTask
        """"
        AEControlPanel.MG17Motor1.StopProfiled CHAN1_ID
        ' return its current position to record as zero position
        AEControlPanel.MG17Motor1.GetPosition CHAN1_ID, zeropos
        zeropos = Round(zeropos * 1000, 2)
        AEControlPanel.lblZero.Caption = "Zero position: " & zeropos & " (um)"
        AEControlPanel.lblCutDepth.Caption = "Current Cut Depth: " & -
Val(AEControlPanel.comboWD.Text) & " (um)"
        ' move relatively -WD um
        AEControlPanel.MG17Motor1.SetVelParams CHAN1_ID, 0, 0.1, 0.3  ' Sets the desired velocity
        t = CSng(-Val(AEControlPanel.comboWD.Text) / 1000)
        AEControlPanel.MG17Motor1.SetRelMoveDist CHAN1_ID,_
CSng(-Val(AEControlPanel.comboWD.Text) / 1000)
        AEControlPanel.MG17Motor1.MoveRelative CHAN1_ID, False
        """"
        AEControlPanel.cmdPApproachStart.Enabled = True
        AEControlPanel.cmdNApproachStart.Enabled = True
        AEControlPanel.cmdCalibrate.Enabled = True
        AEControlPanel.cmdCSpdStart.Enabled = True
        AEControlPanel.cmdAEFBStart.Enabled = True
        AEControlPanel.cmdCalStop.Enabled = False
    End If
End Sub

Public Sub MachiningFeeding(AEFBData() As Double)
    For i = 0 To 1023
        SumData = SumData + AEFBData(i) ^ 2
        SumDataAvg = SumDataAvg + AEFBData(i)
       If Abs(AEFBData(i)) > MaxData Then
           MaxData = Abs(AEFBData(i))
        End If
    Next
    AvgData = SumDataAvg / 1024
    If RMS_Counter < 512 Then
        RMS_Counter = RMS_Counter + 1
        RMS_AE(RMS_Counter) = Sqr(SumData / 1024 - AvgData ^ 2)
    Else
        RMS_Counter = 0
        RMS_AE(RMS_Counter) = Sqr(SumData / 1024 - AvgData ^ 2)
    End If
    If AEControlPanel.optFFTDisplay.Value = True Then
        Call FFTDouble(1024, False, AEFBData(0), FFTImgIn(0), FFTRealOut(0), FFTImgOut(0))
        For i = 0 To 512
            FFTData(i) = Sqr(FFTRealOut(i) ^ 2 + FFTImgOut(i) ^ 2)
```

```
      Next
      AEControlPanel.CWGraph1.PlotY FFTData
   Else
      AEControlPanel.CWGraph1.PlotY RMS_AE
   End If
   """"
   AEControlPanel.lblAvgLoad.Caption = "Current Average Load:    " &_
Round(RMS_AE(RMS_Counter), 3) & " (V)"
   AEControlPanel.lblMaxLoad.Caption = "Current Peak Load:         " & Round(MaxData - AvgData, 3) &
" (V)"
   AEControlPanel.MG17Motor1.GetPosition CHAN1_ID, currentpos
   If AEControlPanel.optManualZero.Value = True Then
      currentCutDepth = currentpos * 1000 - Val(AEControlPanel.txtManualZero.Text)
   Else
      currentCutDepth = currentpos * 1000 - zeropos
   End If
   AEControlPanel.lblCutDepth.Caption = "Current Cut Depth:              " & Round(currentCutDepth, 2) &
" (um)"
   If RMS_AE(RMS_Counter) >= CuttingThreshold Then
      AEControlPanel.lblCutStatus.Caption = "Status:                    Machining!"
      If en_counttime = False Then
         t_start = Timer
      End If
      en_counttime = True
      t_end = Timer
      t_elapse = t_buffer + t_end - t_start
      t_display = Round(t_elapse, 2)             'Round to 2 digits for display
      AEControlPanel.lblCutTime.Caption = "Machining Time:                 " & t_display & " secs"
      If flag_feedback = True Then
         ' AE feedback feeding mode
         If RMS_AE(RMS_Counter) > (Val(AEControlPanel.comboTargetAERMS.Text) * 1.10) Then
            If CurrentSpeed >= 0.00005 Then
               CurrentSpeed = CurrentSpeed - 0.00005
            End If
         ElseIf RMS_AE(RMS_Counter) < (Val(AEControlPanel.comboTargetAERMS.Text) * 0.90) Then
            If CurrentSpeed <= 0.001 Then
            CurrentSpeed = CurrentSpeed + 0.0001
            End If
         Else
            CurrentSpeed = CurrentSpeed
         End If
         AEControlPanel.Timer1.Interval = 40 / CurrentSpeed     '1000ms / (CurrentSpeed / 0.04nm/sec)
      End If
   Else
      en_counttime = False
      t_buffer = t_elapse
      AEControlPanel.lblCutStatus.Caption = "Status:                    Approaching!"
      t_display = Round(t_elapse, 2)              'Round to 2 digits for display
      AEControlPanel.lblCutTime.Caption = "Machining Time:                 " & t_display & " secs"
   End If
   ' display current speed
   AEControlPanel.lblCurrentSpd.Caption = "Current Feed Speed:           " & Round(CurrentSpeed * 1000,
2) & " (um/s)"
End Sub

Public Sub NIDAQStopTask()
```

```
    ' Stop the task and unload it
    On Error GoTo ErrorHandler
    If (taskhandle <> 0) Then
        DAQmxErrChk DAQmxStopTask(taskhandle)
        DAQmxErrChk DAQmxClearTask(taskhandle)
        taskhandle = 0
        taskIsRunning = False
    End If
    Exit Sub
ErrorHandler:
    If taskIsRunning = True Then
        DAQmxStopTask taskhandle
        DAQmxClearTask taskhandle
        taskIsRunning = False
    End If
    MsgBox "Error:" & Err.Number & " " & Err.Description, , "Error"
End Sub

Public Sub Delay(d)
    ' wait for d seconds
    t = Timer
    While (Timer - t) < d
    Wend
End Sub

Public Sub SetRelDist()
    Dim lRetVal As Long
    Dim lRelDist As Long

    lRelDist = 1
    lRetVal = AEControlPanel.MG17Motor1.LLSetGetMoveRelParams(True, CHAN1_ID, lRelDist)
    If lRetVal <> MG17_OK Then
        MsgBox "LLSetGetMoveRelParams Error Code" & Format$(lRetVal)
    End If
End Sub

Public Sub MoveRelDist()                ' microstep level control of the stage movement using timer
    Dim lRetVal As Long
    MousePointer = 11
    SetRelDist
    lRetVal = AEControlPanel.MG17Motor1.MoveRelative(CHAN1_ID, True)
    If lRetVal <> MG17_OK Then
        MsgBox "MoveRelative Error Code" & Format$(lRetVal)
    End If
    MousePointer = 0
End Sub

Public Sub StartMicroStepFeed()
    AEControlPanel.Timer1.Enabled = True
End Sub

Public Sub StopMicroStepFeed()
    AEControlPanel.Timer1.Enabled = False
End Sub
```

A.2.3 FFTLib.bas

```
'Declaration for FFT.DLL, a dynamic link library for FFT made by Murphy McCauley (08/01/99)

' (RealIn, ImagIn, RealOut, ImagOut) are represented as a single variable, not an array.  Pass the FIRST ELEMENT of the array in the Sub arguments.

 Declare Sub FFTDouble Lib "FFT.dll" Alias "fft_double" _
  (ByVal NumSamples As Long, ByVal InverseTransform As Boolean, _
  RealIn As Double, _
  ImagIn As Double, _
  RealOut As Double, _
  ImagOut As Double)

 Declare Sub FFTSingle Lib "FFT.dll" Alias "fft_float" _
  (ByVal NumSamples As Long, ByVal InverseTransform As Boolean, _
  RealIn As Single, _
  ImagIn As Single, _
  RealOut As Single, _
  ImagOut As Single)

 Declare Function IndexToFrequency Lib "FFT.dll" _
  Alias "Index_to_frequency" _
  (ByVal NumSamples As Long, _
  ByVal Index As Long) As Double
```

A.2.4 NIDAQmxErrorCheck.bas

```
Public Sub DAQmxErrChk(errorCode As Long)
'   Utility function to handle errors by recording the DAQmx error code and message.
    Dim errorString As String
    Dim bufferSize As Long
    Dim status As Long
    If (errorCode < 0) Then
        ' Find out the error message length.
        bufferSize = DAQmxGetErrorString(errorCode, 0, 0)
        ' Allocate enough space in the string.
        errorString = String$(bufferSize, 0)
        ' Get the actual error message.
        status = DAQmxGetErrorString(errorCode, errorString, bufferSize)
        ' Trim it to the actual length, and display the message
        errorString = Left(errorString, InStr(errorString, Chr$(0)))
        Err.Raise errorCode, , errorString
    End If
End Sub
```

APPENDIX B

Fabrication Process Flow of the Tissue Contrast Sensor with Interface Circuit

(Last updated 4/30/2008)

(CMOS portion adapted from UM Active Probe Flow, Rev. 9/16/02)

Table of Mask Layers

#	Layout Name	Full Name	GDS #	Polarity	Aligned to	Alignment Mark #
1	CWP	P Well Implant	41	Dark	Flat	1
2	CAA	Active	43	Clear	CWP	5
3	CFI	Field Implant	11	Dark	CWP/CAA	6
4	CPG	Poly 1	46	Clear	CAA	7
5	CEL	Poly 2	56	Clear	CPG	8
6	CSP/CSN	P/N Select	44/45	Dark	CAA	9
7	CCC	Contact	10	Dark	CAA/CPG	10
8	CMF	Metal	49	Dark	CCC	11
9	CNT	EDP	14	Dark	CCC	4
10	CVA	LTO Patterning	50	Dark	CCC/CNT	15/17
11	CVT	Metal Electrodes	16	Dark	CVA/CNT	16/18
12	CDE	DRIE	15	Dark	CVA/CVT/CNT	12/13/14

---

1. Prepare starting wafers

   - Si wafer, 4" OD, (100), thickness 500 μm, single side polished, N-type, 1.0 – 1.5 [Ω-cm]
   - Scribe wafer IDs
   - Check resistivity of the wafers with 4-point probe
   - Rinse: DI-H_2O, 2 min; spin dry
   - Inspect surface

---

2. Pre-furnace clean

---

3. Grow P-Well implant oxide (B2)

   - Recipe: DWD/TCA; Variable Parameter Table Settings: DWDSKIN
   - Expected Thickness = 7000 Å

UPGAS/A	N2-3	SETTIME	00:15:00	PUL-600	200
TEMP/A	800	DRY1	00:05:00	SETTLE	SPKSET
TEMPRMP	MAX	WET	00:00:00	LOWSET	-2.0
DRY/A	01:00:00	WET/TCA	01:30:00	HIGHSET	+2.0

UPGAS/B	N2-3	DRY2	00:05:00	LON2	30
TEMP/B	1100	N2ANNEAL	00:05:00	RAMPDWN	MAX
		DOWNGAS	N2-3		

4. Mask #1: P-Well (CWP)

   - Drybake, HMDS Prime, Spin, and Prebake: ACS 200 Cluster Tool, SPR220 3µm
   - Expose: AutoStep 200 Stepper, 0.21 sec.
   - Post-Exposure bake: ACS 200 Cluster Tool, 115°C 90 sec.
   - Develop: ACS 200 Cluster Tool, 300DEV 30 sec.
   - Rinse: DI-H_2O, 3 min.; spin dry
   - Postbake: 15 min.@110°C

5. Pattern P-Well masking oxide

   - Descum in March tool
   - Etch: BHF ~7:30 min., to hydrophobic, ~1000Å/min.
   - Rinse: DI-H_2O, 3 min.; spin dry
   - Inspect surface for trace of oxide
   - Postbake PR for implantation: 20 min.@110°C

6. Implant P-Well

   - Boron
   - Dose: $1.5\times10^{13}/cm^2$
   - Energy: 100 KeV
   - Include bare wafer T1 as monitor.

7. Strip photoresist

   - Strip in hot PRS 2000 (non-metal) for 15 min.
   - Rinse: DI-H_2O, 5 min; spin dry
   - Inspect surface for trace of resist.

8. Prefurnace Clean

9. Well drive-in

   - Recipe: DA1; Variable Parameter Table Settings: OXIDIZE
   - Expected Thickness = 3350 / 8000 Å

UPGAS/A	N2-3	SETTIME	00:15:00	PUL-600	200
TEMP/A	1100	DRY1	06:00:00	SETTLE	SPKSET
TEMPRMP	MAX	WET	00:00:00	LOWSET	-5.0
DRY/A	--	WET/TCA	--	HIGHSET	+5.0
UPGAS/B	--	DRY2	00:00:00	LON2	--
TEMP/B	--	N2ANNEAL	10:40:00	RAMPDWN	--
		DOWNGAS	N2-3		

10. Strip oxide

- Etch: BHF, until hydrophobic, ~8-10 min., 1000Å/min.
- Rinse: DI-H_2O, 5 min.; spin dry
- Pull Monitor T1: Junction depth: x_j=6 μm; sheet resistance (4 pt. probe): 1500±500 Ω/□

---

11. Prefurnace Clean

- Add monitor (T2, T3) for B2

---

12. Grow pad oxide (B2)

- Recipe: DWD/TCA; Variable Parameter Table Settings: DWDSKIN
- Expected Thickness = 500 Å
- Measure oxide thickness with T2; T3 goes to C4 with CMOS wafers.

UPGAS/A	O2-3	SETTIME	00:15:00	PUL-600	200
TEMP/A	800	DRY1	00:17:00	SETTLE	SPKSET
TEMPRMP	10	WET	00:00:00	LOWSET	-5.0
DRY/A	01:00:00	WET/TCA	00:11:30	HIGHSET	+5.0
UPGAS/B	N2-3	DRY2	00:05:00	LON2	25
TEMP/B	900	N2ANNEAL	00:05:00	RAMPDWN	MAX
		DOWNGAS	N2-3		

---

13. Deposit LPCVD Nitride (C4)

- Recipe: CVD NITR; Variable Parameter Table Settings: CVD
- Expected Thickness = 1200 Å
- Inspect Monitor

---

14. Mask #2: Active (CAA)

- Include Monitor T3 in this step
- Drybake, HMDS Prime, Spin, and Prebake: ACS 200 Cluster Tool, SPR220 3μm
- Expose: AutoStep 200 Stepper, 0.30 sec.
- Post-Exposure bake: ACS 200 Cluster Tool, 115°C 90 sec.
- Develop: ACS 200 Cluster Tool, 300DEV 35 sec.
- Rinse: DI-H_2O, 2 min.; spin dry
- Postbake: 15 min. @ 110°C

---

15. RIE etch (Plasmatherm)

- Include Monitor T3 in this step
- Check current recipes for etch rates and times

	Etch #1: Descum	Etch #2A: Nitride	Etch #2B: Nitride
Gas/Flow	O_2 50 sccm	CF_4 20 sccm	CF_4 20 sccm
Gas/Flow		O_2 1 sccm	O_2 1 sccm
Pressure	300 mT	100 mT	100 mT
Power	25 W	80 W	80 W
Time	1:00 min.		

- Inspect and measure with Nanospec. Make sure there is no SiN left in trench.

---

16. Hard bake resist

- Bake 180 min. @ 120°C
- DO NOT remove resist from active step.

---

17. Mask #3: P-field implant (CFI)

- Drybake, HMDS Prime, Spin, and Prebake: ACS 200 Cluster Tool, SPR220 2.5µm
- Expose: AutoStep 200 Stepper, 0.41 sec.
- Post-Exposure bake: ACS 200 Cluster Tool, 115°C 90 sec.
- Develop: AZ300 Developer, 60 sec. manually
- Rinse: DI-H_2O, 3 min.; spin dry
- Postbake: 20 min. @ 110°C

---

18. P-Field Implant

- Boron
- Dose: $5\times10^{13}/cm^2$
- Energy: 55 KeV

---

19. Strip Photoresist

- O_2 plasma (O_2: 100 sccm, Pressure: 300 mT, Power: 200 W, 20min.)
- If necessary, clean with H_2SO_4:H_2O 1.2:1, 15 min.;
- Rinse: DI-H_2O, 5 min; spin dry
- Inspect for traces of resist!

---

20. Pre-furnace clean

- Clean monitor wafers (T3, bare-Si T4) for B2

---

21. Grow Field Oxide (B2)

- Recipe: DWD/TCA; Variable Parameter Table Settings: DWDSKIN
- Expected Thickness = 11,000 Å

UPGAS/A	O2-3	SETTIME	00:10:00	PUL-600	200
TEMP/A	800	DRY1	00:05:00	SETTLE	SPKSET
TEMPRMP	10	WET	00:00:00	LOWSET	-5.0
DRY/A	01:00:00	WET/TCA	04:10:00	HIGHSET	+5.0
UPGAS/B	N2-3	DRY2	00:05:00	LON2	30
TEMP/B	1040	N2ANNEAL	00:05:00	RAMPDWN	MAX
		DOWNGAS	N2-3		

---

22. Remove Oxide on Nitride

- On CMOS wafers and monitor T3, measure to make sure no oxide left on nitride
- Set monitor wafers (T4) aside
- BHF Dip, 24 sec., estimated from (thickness SiO_2 on Nitride)/ (1000 Å) min
- Rinse: DI-H2O, 2 min; spin dry

---

23. Strip Nitride

- Make new H_3PO_4

- Heat H_3PO_4 to 160°C
- Run with test monitor T3 to get actual etch rate
- Etch CMOS wafers (~1 hour)
- Rinse: DI-H_2O, 5 min; spin dry
- Check Oxide left in field

---

24. Etch Pad Oxide / Remaining Nitride

- BHF Dip 30 sec
- Rinse: DI-H_2O, 2 min; spin dry

---

25. Pre-furnace clean

- Clean one monitor wafer (T5) for B2, Also clean 3 test wafers for C1 gate oxide test run.
- Also: Run C1 gate oxidation test to get 500Å

---

26. Grow Sacrificial Oxide (B2)

- Recipe: DWD/TCA; Variable Parameter Table Settings: DWDSKIN
- Expected Thickness = 500 Å

UPGAS/A	O2-3	SETTIME	00:10:00	PUL-600	200
TEMP/A	800	DRY1	00:17:00	SETTLE	SPKSET
TEMPRMP	10	WET	00:00:00	LOWSET	-5.0
DRY/A	01:00:00	WET/TCA	00:15:00	HIGHSET	+5.0
UPGAS/B	N2-3	DRY2	00:05:00	LON2	25
TEMP/B	900	N2ANNEAL	00:05:00	RAMPDWN	MAX
		DOWNGAS	N2-3		

---

27. Threshold implant for PMOS

- Boron
- Dose: $6\times10^{11}/cm^2$
- Energy: 35 KeV
- Note: during wait for threshold implant, test C1 gate oxidation + TCA clean

---

28. Strip sacrificial oxide

- Leave 9 wafers behind at this point, just in case something goes wrong in gate oxidation.
- Include SiO_2 monitor T5
- Make sure BHF solution is new!
- BHF Dip: 48 sec. or until backside turn hydrophobic
- Rinse: DI-H_2O, 2 min; spin dry

---

29. Pre-furnace clean

- Clean two monitor wafers (T6, T7) for C1
- Run C3 Poly to check the deposition rate.

---

30. Grow Gate Oxide (C1)

- C1 tube should be cleaned within one day before use.

- Recipe: DA1; Variable Parameter Table Settings: OXIDIZE
- Add two monitor wafers (T6, T7) at the center
- Expected Thickness = 500 Å
- After C1 run, keep one monitor (T7) from this run to Poly1 deposition in C3

UPGAS/A	N2-3	DRY1	01:05:00	PUL-600	200
DOWNGAS	N2-3	WET	00:00:00	SETTLE	SPKSET
TEMP	1000	DRY2	00:00:00	LOWSET	-2.0
TEMPRMP	10	N2ANNEAL	00:25:00	HIGHSET	+2.0
SETTIME	00:10:00				

---

31. Deposit LPCVD Poly1 (C3)

- Recipe: LOW POLY (570ºC LPCVD); Variable Parameter Table Settings: CVD
- Add one of the oxidized monitor wafers (T7) or any 1500Å oxide wafer
- Expected Thickness = 6600 Å

Polysilicon	6600 Å
POLYTIM	(>4 hrs)

---

32. Dope Poly1 (B3)

- Recipe: PHOSDEP2; Variable Parameter Table Settings: POCL DEP

UPGAS	N2-3	DEPTIME	00:15:00	LOWSET	-5.0
DOWNGAS	N2-3	SOAKTIM	00:15:00	HIGHSET	+5.0
TEMP	950	PUL-600	200	O2FLOW	150
TEMPRMP	MAX	SETTLE	SPKSET	LON2FLO	400
SETTIME	00:10:00				

---

33. Deglaze

- Etch: BHF, 12 sec.
- Rinse: DI-H_2O, 2 min; spin dry
- Measure poly sheet resistance with four-point probe @ 1mA (R_s=V/I*4.53) on T7
- Expected sheet resistance ~12 Ω/sq.

---

34. Mask #4: Poly1 Gate (CPG)

- Drybake: 5 min.@110 °C on hotplate
- Spin: HMDS/1813@4K rpm
- Prebake: 1 min.@110°C on hotplate
- Expose: AutoStep 200 Stepper, 0.32 sec.
- Develop: MF 319, 1 min.
- Rinse: DI-H_2O, 3 min.; spin dry

---

35. RIE Pattern Poly1

- Check current recipes for etch rates and times on Trion RIE
- Recipe for poly etching: Si-etch01

	Etch #1: Descum	Etch #2A: Oxide breakthrough	Etch #2B: Poly-Si	Etch #3: Ash
Gas/Flow	O_2 50 sccm	Cl_2 50 sccm	Cl_2 20 sccm	O_2 99 sccm

Gas/Flow			HBr 50 sccm	
Gas/Flow			He 20 sccm	
Pressure	20 mT	35 mT	35 mT	300 mT
ICP Power	100 W (<200 W)	350 W	350 W	400 W
RIE Power	50 W (<100 W)	100 W	100 W	100 W
Time	1 min.	5 sec.	(<2 min.)	1 min.

- Inspect after etch run, probe at test structure to see if there is any short.

---

36. Strip Photoresist

- If necessary, clean with H_2SO_4:H_2O 1.2:1, 15 min.;
- Rinse: DI-H_2O, 5 min; spin dry
- Inspect for traces of resist.

---

37. Pre-furnace clean

- Include T7 monitor (with Poly1 on it) and a bare-Si (T8)

---

38. Grow Capacitor Oxide (B2)

- Recipe: DA1; Variable Parameter Table Settings: OXIDIZE
- Expected Thickness = 750 Å on Poly1 film
- Note: After this run, take one monitor (T7) from this run to measure SiO2 thickness
- Stack from the bottom up: Oxide (50nm) + POLY1 (unknown) + SiO2 (unknown)

UPGAS	O2-3	DRY1	00:45:00	PUL-600	200
DOWNGAS	N2-3	WET	00:00:00	SETTLE	SPKSET
TEMP	1000	DRY2	00:00:00	LOWSET	-5.0
TEMPRMP	MAX	N2ANNEAL	00:10:00	HIGHSET	+5.0
SETTIME	00:10:00				

---

39. Deposit LPCVD Poly2 (C3)

- Recipe: LOW POLY (570ºC LPCVD); Variable Parameter Table Settings: CVD
- Check current deposition rate for LOW POLY
- Add one of the oxidized monitor wafers (T8) or a 1500Å SiO_2 wafer
- Expected Thickness = 5600 Å

Polysilicon	5600 Å
POLYTIM	(3-4:30 hrs)

---

40. Dope Poly2 (B3)

- Recipe: PHOSDEP2; Variable Parameter Table Settings: POCL DEP

UPGAS	N2-3	DEPTIME	00:15:00	LOWSET	-5.0
DOWNGAS	N2-3	SOAKTIM	00:15:00	HIGHSET	+5.0
TEMP	950	PUL-600	200	O2FLOW	150
TEMPRMP	MAX	SETTLE	SPKSET	LON2FLO	400
SETTIME	00:10:00				

---

41. Deglaze

- Etch: BHF, 12 sec.
- Rinse: DI-H_2O, 2 min; spin dry
- Measure poly sheet resistance with four-point probe @ 1mA (R_s=V/I*4.53) on T8
- Expected sheet resistance: ~28 Ω/sq.
- Keep Monitor (T8) for Poly2 oxidation

---

42. Mask #5: Poly2 (CEL)

- Drybake: 5 min.@110 °C on hotplate
- Spin: HMDS/1813@4K rpm
- Prebake: 1 min.@110°C on hotplate
- Expose: AutoStep 200 Stepper, 0.32 sec.
- Develop: MF 319, 1 min.
- Rinse: DI-H_2O, 3 min.; spin dry

---

43. RIE Pattern Poly2

- Check current recipes for etch rates and times on Trion RIE
- Recipe for poly etching: Si-etch01

	Etch #1: Descum	Etch #2A: Oxide breakthrough	Etch #2B: Poly-Si	Etch #3: Ash
Gas/Flow	O_2 50 sccm	Cl_2 50 sccm	Cl_2 20 sccm	O_2 99 sccm
Gas/Flow			HBr 50 sccm	
Gas/Flow			He 20 sccm	
Pressure	20 mT	35 mT	35 mT	300 mT
ICP Power	100 W (<200 W)	350 W	350 W	400 W
RIE Power	50 W (<100 W)	100 W	100 W	100 W
Time	1 min.	5 sec.		1 min.

- Inspect after etch run, probe at test structure to see if there is any short.

---

44. Strip Photoresist

- If necessary, clean with H_2SO_4:H_2O 1.2:1, 15 min.;
- Rinse: DI-H_2O, 5 min; spin dry
- Inspect for traces of resist.

---

45. Pre-furnace clean

- Include monitor wafer (T8) for B2 run

---

46. Poly2 Reoxidation (B2)

- Recipe: DWDA1; Variable Parameter Table Settings: OXIDIZE
- Expected Thickness = 1200 Å
- Note: After measure SiO_2 thickness on Poly2, Strip oxide in BHF and measure poly2 left.

UPGAS	O2-3	DRY1	00:05:00	PUL-600	200
DOWNGAS	N2-3	WET	00:40:00	SETTLE	SPKSET
TEMP	800	DRY2	00:05:00	LOWSET	-5.0
TEMPRMP	MAX	N2ANNEAL	00:05:00	HIGHSET	+5.0
SETTIME	00:10:00				

47. Mask #6: P+ Implant (CSP)

- Include one patterned monitor (T9), and flood exposure on half of the wafer (MA6: 5 sec.)
- Drybake, HMDS Prime, Spin, and Prebake: ACS 200 Cluster Tool, SPR220 3µm
- Expose: AutoStep 200 Stepper, 0.35 sec.
- Post-Exposure bake: ACS 200 Cluster Tool, 115°C 90 sec.
- Develop: ACS 200 Cluster Tool, 300DEV 30 sec.
- Rinse: DI-H_2O, 2 min.; spin dry
- Postbake: 15 min. @ 110°C
- Inspect

---

48. P+ S/D Implant – P Select

- Boron
- Dose: $7\times10^{15}/cm^2$
- Energy: 40 KeV

---

49. Strip Hard Photoresist

- O_2 Plasma:

Etch: O_2 Plasma Ash	
Gas/Flow	O_2 99 sccm
Pressure	300 mT
ICP Power	400 W
RIE Power	100 W
Time	5 min.

- Piranha Clean: H_2SO_4:H_2O 1.2:1, 15 min.
- Rinse: DI-H_2O, 3 min; spin dry
- Inspect for photoresist.

---

50. Mask #6: N+ Implant (CSN)

- Include one patterned monitor (T10), and flood exposure on half of it (MA6: 5 sec.).
- Drybake, HMDS Prime, Spin, and Prebake: ACS 200 Cluster Tool, SPR220 3µm
- Expose: AutoStep 200 Stepper, 0.35 sec.
- Post-Exposure bake: ACS 200 Cluster Tool, 115°C 90 sec.
- Develop: ACS 200 Cluster Tool, 300DEV 30 sec.
- Rinse: DI-H_2O, 2 min.; spin dry
- Postbake: 15 min. @ 110°C
- Inspect

---

51. N+ S/D Implant – N Select

- Phosphorus
- Dose: $8\times10^{15}/cm^2$
- Energy: 70 KeV

---

52. Strip Hard Photoresist

- O_2 Plasma:

Etch: O_2 Plasma Ash	
Gas/Flow	O_2 99 sccm
Pressure	300 mT
ICP Power	400 W
RIE Power	100 W
Time	5 min.

- Piranha Clean: H_2SO_4:H_2O 1.2:1, 15 min.
- Rinse: DI-H_2O, 3 min; spin dry
- Inspect for photoresist!

---

53. Pre-furnace clean

- Include a monitor wafers (T11) for C4 run

---

54. Deposit LPCVD dielectrics (C4)

- Recipe: HTO; Variable Parameter Table Settings: CVD
- Check current deposition rate of nitride and oxide
- Add one bare Si monitor (T11), take it out after this run to measure oxide thickness
- After this run all CMOS wafers go straight to B3
- Expected Thickness = 5000 Å

Oxide	5000 Å
HTOTIM	(~110 min)

---

55. P-Diffusion, Dope CVD Oxide (B3)

- Recipe: PHOSDEP2; Variable Parameter Table Settings: POCL DEP
- Take CMOS wafers out of this run immediately after completion

UPGAS	N2-3	DEPTIME	00:30:00	LOWSET	-5.0
DOWNGAS	N2-3	SOAKTIM	00:00:00	HIGHSET	+5.0
TEMP	900	PUL-600	200	O2FLOW	150
TEMPRMP	MAX	SETTLE	SPKSET	LON2FLO	400
SETTIME	00:10:00				

---

56. Deglaze

- Etch: BHF, 12 sec.
- Rinse: DI-H_2O, 2 min; spin dry
- Measure resistivity
- Comments:

---

57. Mask #7: Contacts (CCC)

- Drybake: 5 min.@110 °C on hotplate
- Spin: HMDS/1813@4K rpm
- Prebake: 1 min.@110°C
- Expose: AutoStep 200 Stepper, 0.32 sec.
- Develop: MF 319, 1.1 min.
- Rinse: DI-H_2O, 3 min.; spin dry
- Inspect to make sure contacts are opened!

58. RIE open contact

- Check current recipes for etch rates and times on Trion RIE
- Recipe for oxide etching: Ox-slow

	Etch #1: Descum	Etch #2: Oxide
Gas/Flow	O_2 50 sccm	He 20 sccm
Gas/Flow		C_4F_8 10 sccm
Pressure	20 mT	10 mT
ICP Power	100 W (<200 W)	200 W
RIE Power	50 W (<100 W)	30 W
Time	1 min.	

- Check on test structure to make sure that contacts are opened.
- Oxide wet etching: BHF dip ~30 sec.
- Rinse: DI-H_2O, 2 min.; spin dry

---

59. Strip Photoresist

- Strip: PRS-2000 @65°C, 10min.
- Rinse: DI-H_2O, 3 min; spin dry
- Piranha Clean in addition if necessary: H_2SO_4:H_2O 1.2:1, 15 min.
- Rinse: DI-H_2O, 3 min; spin dry
- Inspect for photoresist!

---

60. Mask #8: Metal (CMF)

- Drybake: 5 min. @110 °C on hotplate
- Spin: HMDS/1827@4K rpm
- Prebake: 90 sec. @110°C on hotplate
- Expose: AutoStep 200 Stepper, 0.6 sec.
- Chlorobenzene soak, 5 min., N_2 gun blow dry, no DI rinse
- Develop: MF 319, ~3-5 min.
- Rinse: DI-H_2O, 3 min.; spin dry
- Inspect to make sure no residue PR in contact holes.
- Descum in March tool.

---

61. Sputter Ti/TiN/Al (1% Si)/Ti/Al (1% Si)/Ti

- Rinse DI-H_2O, 1 min., dip in BHF immediately
- Etch: BHF, 15 sec.
- Rinse: DI-H_2O, 2 min.; N_2 gun blow dry; load into sputtering chamber immediately
- Pump down to 3×10^{-6} Torr (4 hrs or more)
- Target #1: DC 550 W, 500 Å Ti (10'40")
- Target #1: DC 550 W, 1200 Å TiN (N_2 gas 13.5%) (16'40")
- Target #3: DC 3 Amp, 1000 Å Al (1% Si) (4'20")
- Target #1: DC 550 W, 300 Å Ti (6'40")
- Target #3: DC 3 Amp, 1000 Å Al (1% Si) (4'20")
- Target #1: DC 550 W, 300 Å Ti (6'40")

---

62. Lift off

- Heat up 1112A Remover @50-60°C, ≈10 min.
- Soak wafer in 1112A for 2min.
- Ultrasonic bath, 3min.
- Repeat: Heat up 1112A remover 5min. + 3~5min. in ultrasonic batch
- Rinse: DI-H_2O, 5 min.; spin dry (inspect for flakes)

---

63. Pre-sinter Clean

- Rinse 150 sec. in Rinser/Dryer
- Acetone: 5 min.
- IPA: 5 min.
- DI-H_2O: 5 min., 3 times
- Rinse 150 sec. in Rinser/Dryer

---

64. Sinter Contacts (A1)

- Recipe: ANNEAL-2; Variable Parameter Table Settings: ANNEAL-1

ANL GAS	N2/H2ANL	SETTIME	00:10:00	PUL-600	200
UPGAS	N2-3	STBLTIM	00:01:00	DOWNGAS	N2-4
TEMP	450	ANELTIM	00:30:00	HIGHSET	+15
TEMPRMP	MAX			LOWSET	-15

---

65. Test wafer

- Contact resistance for a string of 100 contacts should be 2.5 kΩ for all areas.
- P-well/N+ diode should turn on at 0.5 – 0.7 V, reverse breakdown ~ 22V.
- P-well/N-epi diode should turn on at 0.7 V, reverse breakdown > 40V.

---

66. PECVD low-stress oxynitride: protect CMOS metal during EDP etching

- GSI PECVD, deposition temperature: 400 °C
- 1.0 μm, deposited in 2 separate steps (0.5 μm each step)

Gases	N_2:SiH_4:NH_3:N_2O
Gas Flow ratios (sscm)	200:45:360:1920
Pressure (Torr)	2.6
HF Power (W)	320
LF Power (W)	38
Temperature (°C)	400
Deposition rate (Å/min)	9700

---

67. Mask #9: EDP (CNT)

- Drybake: 3 min.@110 °C on hotplate
- Spin: HMDS/1827@4K rpm
- Prebake: 1 min.@110°C on hotplate
- Expose: AutoStep 200 Stepper, 0.64 sec.
- Develop: MF 319, 1.5 min.
- Rinse: DI-H_2O, 3 min.; spin dry

---

68. Pattern EDP-mask oxide

- RIE until 1000-2000Å left
- Recipe for oxide etching: Ox-slow (~850-900 Å/min.)

	Etch #1: Oxide	Etch #2: Descum
Gas/Flow	He 20 sccm	O_2 50 sccm
Gas/Flow	C_4F_8 10 sccm	
Pressure	10 mT	20 mT
ICP Power	200 W	100 W (<200 W)
RIE Power	30 W	50 W (<100 W)
Time	(~20-25min.)	1 min.

- Check oxide thickness in patterned area.
- Oxide wet etching: BHF dip, ~1 min.
- Rinse: DI-H_2O, 2 min.; spin dry
- Strip photoresist in hot PRS2000 for 10 min.
- Rinse: DI-H_2O, 3 min.; spin dry
- Measure thickness of oxide layer before EDP

---

69. EDP

- Etch rate at 110°C is 80 μm/hour. Target etch depth: 40 μm. Time: ~30 min.
- Rinse: DI-H_2O, 10 min.

---

70. Post-EDP clean & overhanging oxide etching

- Overnight clean in hot water.
- Rinse: DI-H_2O, 5 min.; spin dry
- Soak: Acetone 5 min.; IPA 5 min.; DI-H_2O rinse 5 min.
- Measure EDP etch depth
- Measure thickness of oxide layer after EDP
- BHF etching 60% of the remaining LTO layer. (Protect circuit area with PR if necessary)
- Rinse: DI-H_2O, 3 min.; spin dry
- Verify under microscope that no overhanging oxide left at the edges of the EDP cavities.

---

71. PECVD low-stress oxynitride: insulating exposed silicon substrate

- GSI PECVD, deposition temperature: 400 °C
- 1.0 μm, deposited in 2 separate steps (0.5 μm each step)

Gases	N_2:SiH_4:NH_3:N_2O
Gas Flow ratios (sscm)	200:45:360:1920
Pressure (Torr)	2.6
HF Power (W)	320
LF Power (W)	38
Temperature (°C)	400
Deposition rate (Å/min)	9700

---

72. Mask #10: Oxynitride patterning (CVA) to reopen CMOS pad areas

- Drybake: 3 min.@110 °C on hotplate
- Spin: HMDS/9260@2K rpm
- Reflow: 5min.
- Prebake: 30 min.@90°C in oven

- Expose: AutoStep 200 Stepper, 5 sec.
- Develop: AZ400K:DI-H_2O (1:3), 3.5 min.
- Rinse: DI-H_2O, 3 min.; spin dry

---

73. Reopen CMOS pad areas by patterning oxynitride

- Recipe for oxide etching: Ox-slow (~850-900 Å/min.)

	Etch #1: Oxide	Etch #2: Ash
Gas/Flow	He 20 sccm	O_2 99 sccm
Gas/Flow	C_4F_8 10 sccm	
Pressure	10 mT	100 mT
ICP Power	200 W	500 W
RIE Power	30 W	0 W
Time	(~25min.)	2 min.

- Exam carefully to prevent damaging the underlying Al layers
- PR strip: PRS 2000 15 min.
- Rinse: DI-H_2O, 3 min.; spin dry

---

74. Mask #11: Metal Electrode (CVT)

- Drybake: 15 min.@110 °C
- Spin: HMDS/9260@2K rpm
- Reflow: 5min.
- Prebake: 30 min.@90°C in oven
- Expose: AutoStep 200 Stepper, 9 sec.
- Develop: AZ400:DI-H_2O (1:3), 8 min.
- Rinse: DI-H_2O, 3 min.; spin dry

---

75. Sputter Ti/Au

- Descum in March tool, probe metal pads to ensure good exposure of metals
- Target #1: DC 600 W, 500 Å Cr (3'45")
- Target #3: DC 0.5 A, 4000 Å Au (15')

---

76. Liftoff

- Liftoff: 1112A Remover @60-70°C, ≈25 min., with ultrasound
- Rinse: DI-H_2O, 5 min.; spin dry (inspect for flakes!)

---

77. Wafer preparation for HF Nitric thin down

- Spin 9260@2K rpm to protect front of wafer and bake 30 min.@90°C in oven.
- Trion etching oxide on backside of wafer, recipe: m-oxide1, 20 min. Use carrier wafer.
- Wafer diced into quarter size.

---

78. Thinning backside with HF: HNO_3

- One quarter wafer each time to get better uniformity across the wafer quarter.
- Thin down to 100 μm! Monitor closely, note uniformity.
- HNO_3: HF: CH3COOH = 900ml: 95 ml: 5 ml

- Time: ~35 min., etch rate: 11.5 μm/min.
- Measure thickness before and after thinning.

---

79. Mask #12: DRIE (CDE)

- Use acetone/xylene to clean residue wax from bonding for HF-Nitric etching
- Rinse: DI-H_2O, 2 min.
- Spin: HMDS/1827@1K rpm, mount one wafer quarter backside up.
- Spin: HMDS/1827@2K rpm
- Prebake: 90"@110°C
- Expose: MA-6 aligner, ~16 sec. soft contact, 20mW/cm^2, backside alignment
- Develop: MF319, 1.1 min.
- Rinse: DI-H_2O, 2 min.; spin dry

---

80. Backside DRIE

- Target etch depth: ~40-50 μm to get a diaphragm thickness of 10-20 μm
- Process recipe: (GC). Process time: ~4 μm/min.
- Measure etch depth.

---

81. Sensor dies release

- PR strip: acetone 10 mins.
- Gently knock the wafer quarter, push with tweezer tip if necessary to release sensor dies.
- Acetone, IPA, DI H_2O, 5 min. each in ultrasound cleaner.

---

82. PZT disc mounting

- Apply a small amount of silver epoxy at the bottom of cavity.
- With a stereoscope, manually place the PZT disc batch-fabricated by μUSM into cavity.
- PZT disc is self-centered with the cavity due to the slope of cavity sidewall.
- Bake: 20 min. @ 80°C in oven.

---

83. PZT disc insulating

- With a stereoscope, after silver epoxy has cured, apply a small amount of nonconductive epoxy at the edge of PZT disc and let it flow to fill the gap around the disc, and secure the disc in the cavity.

---

84. Top electrode connection

- With a stereoscope, after nonconductive epoxy has cured, apply a small amount of silver epoxy to electrically connect the top electrode to the large metal pad beside the cavity.
- Check the resistance between the two metal pads beside the cavity using a probe station and multimeter. If no short circuit occurs during integration of the PZT disc, the resistance should be >500 KΩ.

---

85. Device encapsulation

- Wire bonding to metal pads if necessary.
- Parylene deposition for encapsulation: 3 μm thick.

APPENDIX C

An *In Vivo* Blood Sampling Microsystem for Pharmacokinetic Applications

This appendix describes a microsystem for automated blood sampling from laboratory mice used in pharmacokinetic (PK) studies[1]. The work was performed in collaboration with Pfizer, Inc. as a side project during the main dissertation work. Intended to be mounted as a "backpack" on a mouse, the system uses a microneedle, reservoir, and an actuator to instantaneously prick the animal for a time-point sample, eliminating the need for a tethered catheter with large dead volume. The blood is collected by capillary effect through a 31-33 gauge microneedle (250-210 μm OD) into a ≈1 μL micromachined steel reservoir. The voice coil actuator provides a peak force of ≈300 mN, which amply exceeds the measured piercing force of mouse skin (*i.e.*, 60-85 mN for a 31-gauge needle with 12° bevel). The sampling system was tested *in vitro* using a mock vessel with adjustable pressure; the reservoir was filled in <0.15 sec by a combination of the capillary effect and blood pressure. The system may also be used to sample interstitial fluid, but the absence of blood pressure makes it necessary to enhance the capillary effect of the needle. This is accomplished by either electropolishing on the inner surface to make it more hydrophilic or using a polymer wire insert to increase the surface area. The steel surface of the reservoir is also coated with PECVD silicon oxynitride to improve its hydrophilicity. Blood from fresh bovine tissue was collected into the reservoir to simulate interstitial fluid sampling. *In vivo* tests on live, anesthetized

[1] Part of this work was done with help from Adam Barnett as an undergraduate research project.

mice resulted in successful collection of blood into the reservoir. The possible integration of the device in microanalytical systems and the device scalability for multisampling are discussed.

C.1 Introduction

Pharmacokinetics (PK) is the study of how a living organism transports and eliminates drugs, and is essential to pharmaceutical research. PK studies involve administering a drug to a lab animal and withdrawing a series of blood samples over time. The samples are then analyzed to quantify the drug and metabolite concentration as a function of time.

The sample collections and transfers in a typical PK study can use either manual or automated approaches. The manual approaches involve repetitive procedures that are tedious and time consuming, making them impractical for the time-resolved studies. Commercially-available automated sampling systems (*e.g.* DiLab AccuSampler®) use surgically-implanted catheters to obtain blood samples from a lab animal. The catheter is connected to a processing system that automatically withdraws blood at set time points. However, such systems require the animal to be anesthetized for catheter insertion and tethered for the whole duration of multi-point blood collection, and are known to cause stress-related endocrine changes which can potentially affect the result of the study [Roy04]. More importantly, the need for sample transfers and tube flushing set a lower limit of ≈100 μL on the sample size that must be withdrawn. This relatively large minimum sample size substantially increases the number of mice that must be sacrificed during a PK study. A 20 g transgenic mouse has a total blood volume of only 1.7 mL. A

single 100 μL sample is nearly 6% of the total blood volume, making such a sample very detrimental to the mouse. For a study that requires multiple samples, it becomes necessary to use more than one mouse. This has a multiplicative effect: at least 3 mice are sacrificed for each time sample to account for variability between specimens. Thus, an eight time-point study typically consumes 24 mice. A technology that provides isolated 1-10 μL samples at each time point would enable obtaining a full PK profile from a single mouse, which is desirable scientifically and saves animal resources. The recently introduced DiLab AccuSampler® μ is intended for 5-50 μl blood sampling [Dil09], but it still requires animal tethering and surgery for catheter insertion. Moreover, it is not compatible with microfluidic technologies to form a microanalytical (lab-on-a-chip) system that would permit the *in vivo* microsampling, sample preparation, and analysis, all to be integrated.

This paper proposes a system that can sample blood from lab mouse in the ≈1 μL range [Li07a], eliminating the large dead volume of conventional approaches. The system is designed to be worn as a "backpack" that suddenly pricks the animal with a microneedle. Since the animal does not have to be tethered, the sample may be less affected by endocrine changes. The blood sample is drawn through the needle and into a biocompatible steel reservoir that could be interchanged for a microanalytical chip. A voice coil actuator is triggered to provide the piercing action of the microneedle into the skin at each sampling time point.

Microneedles have been previously fabricated from silicon [Gar03, Gri03, Muk04, Sto05], polymer [Aoy06], and stainless steel [Oki03] for use in drug delivery and transdermal fluid sampling. For fluid sampling, the needle must at least penetrate

through the stratum corneum layer of the skin into the dermis layer, which contains blood vessels and nerves. Sampling can then be accomplished using an integrated micropump or the capillary effect. Capillary effect sampling using a hydrophilic microcapillary is a simple, reliable and cost-effective alternative to micropump sampling. This approach has been demonstrated for body fluid sampling with an array of silicon microneedles [Muk04] and biodegradable polymer needles [Aoy06]. Although these materials can be easily micromachined to form the needle shape and surface treated to provide high capillary effect, their brittleness makes them susceptible to fracture during skin insertion. Biocompatible stainless steels are more ductile and make better candidates for the application. However, untreated stainless steel is only slightly hydrophilic, and additional measures are necessary to support sampling by the capillary effect.

The system design and fabrication are described in Section C.2. The experimentally measured piercing force required for the mice and rats, and the available force from the actuator are described in Section C.3.1. Fabricated microsystems were tested both *in vitro* and *in vivo*. The *in vitro* tests included blood vessel sampling using a mock vessel with adjustable internal pressure, and interstitial fluid sampling from bovine tissue. The *in vivo* tests were performed to collect whole blood from live mice. The *in vitro* and *in vivo* experimental results are discussed in Sections C.3.2 and C.3.3 respectively, and are followed by discussions in Section C.4.

C.2 Device Design and Fabrication

In this section, the overall architecture of the sampling microsystem is discussed, as well as the design detail of each component in the system.

C.2.1 System Architecture

The scheme for *in vivo* microsampling of mouse blood is shown in Figure C.1. A miniaturized "backpack" positions the sampling microsystem at a target spot on a lab mouse. To make this backpack, a commercial mouse jacket (Lomir Biomedical, Inc.) can be modified with Velcro tape. The sampling system consists of a microneedle, reservoir, and an actuator. The actuator can be triggered to suddenly prick the animal with the microneedle for a single time-point sample. Fluid is collected through the needle into the reservoir by the capillary effect, and the actuator is then triggered in the reverse direction to retract the needle from the animal body.

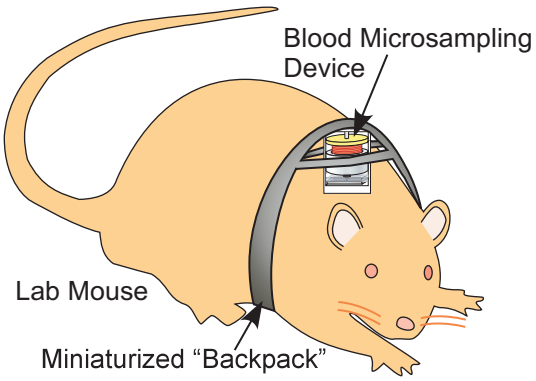

Figure C.1: Diagram showing application scheme of the blood sampling microsystem for pharmacokinetic studies.

The structure of the prototype system is shown in Figure C.2. A microneedle is mounted on a miniature blood reservoir with a target volume of 1-10 μL. The reservoir is covered with a glass lid that enables visual observation of the sample without opening the reservoir. An actuator, which provides the insertion and retraction movement of the needle and reservoir assembly, is integrated in a custom-designed Macor® ceramic housing. The top of the actuator is attached by an adjustable screw to the housing as

shown in Figure C.2(a). With the proper needle and housing dimensions, a 2 mm deflection of the actuator can drive the needle 1 mm into the mouse through a hole in the ceramic housing. This depth can reach the mouse jugular in certain locations for vessel blood sampling [Hof00]. Other insertion depth can be achieved by simply modifying the needle length and position of the adjustment screw for different sampling targets. The design considerations for each component in the system are provided in the following subsections.

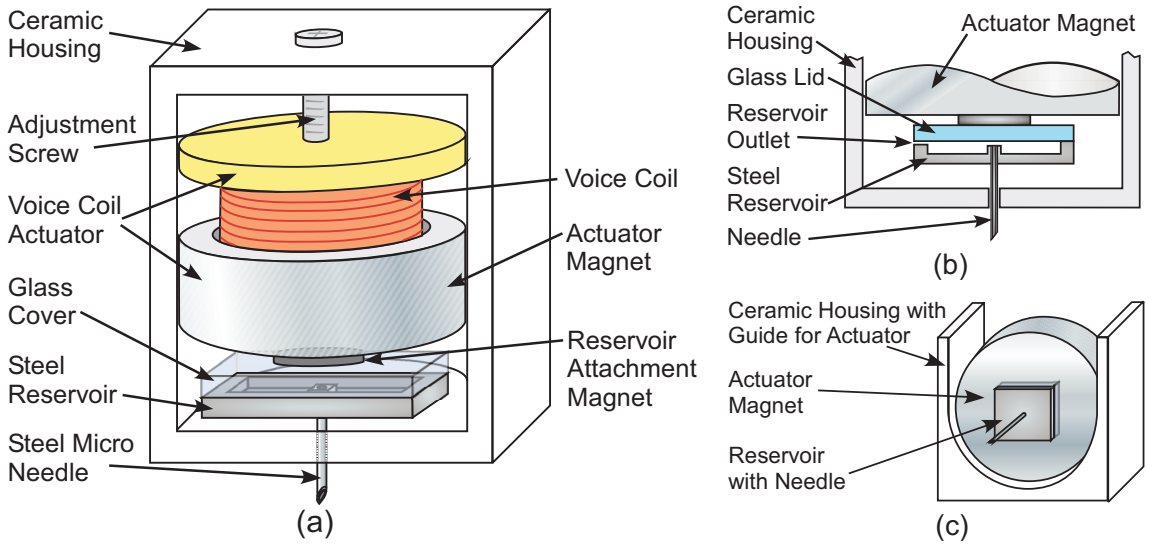

Figure C.2: Schematic diagram of the proposed system: (a) in front view; and in cross-sectional view (b) showing the reservoir; (c) showing the actuator and its guide on the Macor ceramic housing.

C.2.2 Needle and reservoir

Capillary draw is possible when adhesive forces between a solid surface and a liquid surface are stronger than the cohesive forces between the liquid molecules. For a cylindrical channel, the surface tension force that tends to draw liquid into the channel is [Coh04]:

$$F_t = 2\pi r \gamma_{\mathrm{lg}} \cos\theta_c \tag{C.1}$$

where γ_{lg} is the surface tension at the liquid-air interface and r is the radius of the channel. θ_c is the contact angle between the liquid and the channel material. Its nominal value at equilibrium for a certain solid-liquid-gas interface is given by Young's equation

$$\cos\theta_c = \frac{\gamma_{sg} - \gamma_{sl}}{\gamma_{\mathrm{lg}}} \tag{C.2}$$

where γ_{sg} and γ_{sl} are surface tensions at the solid-air and solid-liquid interfaces, respectively. As can be seen from Equation C.2, $\theta_c \leq 90°$ suggests that $\gamma_{sg} > \gamma_{sl}$. This causes the solid-liquid interface area to increase and results in a positive F_t which drives the flow in the channel [Man98]. When the channel is held horizontally, this force alone can drive the liquid to fill up the channel. When the channel is held vertically, the height h of the liquid column entering the channel is limited by the force of gravity, and is given by

$$F_t = G = \rho g h(\pi r^2) \Rightarrow h = \frac{2\gamma_{\mathrm{lg}} \cos\theta_c}{\rho g r} \tag{C.3}$$

where G is the force of gravity on the liquid, ρ is the density of the liquid, and g is the acceleration due to gravity. As is clear from Equation C.3, small θ_c and r are both desirable in order to enhance the capillary effect in the channel and increase the capillary height h. These terms can serve as guidelines for the selection of the material and the dimensions of the microneedle.

Among the materials that have been used to form microneedles, silicon and polymeric materials can be easily surface treated to achieve a small θ_c for superior wettability, thus providing a strong capillary effect. These materials are also compatible with standard microfabrication technology and can be easily integrated with other micromachined devices for on-chip sample processing and analysis. However, these

materials have relatively low strength and ductility, resulting in a high risk of fracture during skin insertion [Dav04]. The structure of these needles must be carefully designed to withstand the skin piercing force [Sto05]. Microneedle arrays can increase overall mechanical strength and fluid flow rate. However, arrays take up more space on the device and can push the skin down uniformly without penetrating it if the spacing between needles is too small.

Stainless steel has higher strength and is more ductile than silicon and polymeric materials, making steel needles safer and less prone to fracture during insertion. However, untreated stainless steel has only weak hydrophilicity, making it difficult to sample using the capillary effect. The contact angle θ_c of water on stainless steel depends on surface properties and the type of alloy [Aga95, Bou06, Man94]. Stainless steel 304 and 316L, which are the most commonly used alloys for hypodermic needles, are slightly hydrophilic and have a water contact angle of 50-70°. Needles made from these materials are used in this effort. However, surface treatments and other measures are employed to facilitate capillary draw. Note that while the contact angle of water is used to discuss the wettability of steels, the contact angle of whole blood has been shown to be similar [Aga95].

Various treatments have been proposed to improve the wettability of stainless steel by modifying the surface roughness, oxygen content, or organic contamination layer of the surface [Bou06, Jen05, Man94, San04]. However, most treatments are either not permanent or are impractical to perform on the inner surface of a 31 or 33 gauge needle. Electropolishing is commonly used to clean stainless steel surfaces [Bhu05] and can be performed on the inner surface of a needle. This procedure decreases the roughness of

the surface and removes any existing organic contamination layer, which has been shown to improve wettability [Man94]. A second approach to obtain a stronger capillary effect is to insert a hydrophilic wire into the needle. This wire serves as a "wick" by increasing the liquid-solid interface area. This additional surface area adds a second term to Equation C.1:

$$F_t = 2\pi r_1 \gamma_{lg} \cos\theta_{c1} + 2\pi r_2 \gamma_{lg} \cos\theta_{c2} \qquad \text{(C.4)}$$

where r_1 and r_2 are the radii of the channel and the wick insert, respectively; θ_{c1} and θ_{c2} are the contact angles between the liquid and the channel material and between the liquid and wick insert material, respectively. As shown in Figure C.3, a polymer wire can be inserted into the needle for this purpose. The polymer is hydrophilic, with a copper core that can be reshaped so that the wire can stay inside the needle lumen after deployment. The top end of the wire touches the overhead glass lid, traversing a 50-100 μm gap.

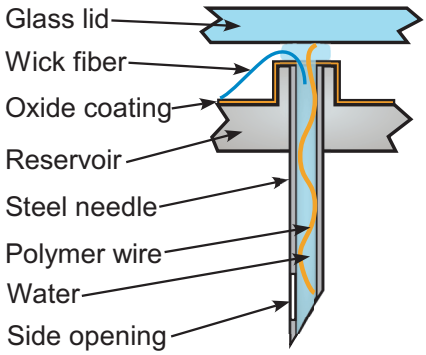

Figure C.3: Design variations used to improve capillary effect and *in vivo* sampling. A polymer wire is used as insert in the needle tube to increase surface area; a wick fiber is used to guide liquid from the needle exit into the reservoir; an opening is formed on the sidewall of the needle near the tip to prevent the needle lumen from being clogged by tissue during insertion.

Also shown in Figure C.3, an opening can be formed on the sidewall of the microneedle near the tip. This feature is helpful during *in vivo* experiments by providing

a second path for blood flow into the needle, especially if the needle tip is clogged by tissue during insertion.

The liquid entering the needle encounters a barrier at the joint of the needle and reservoir due to the discontinuity of the capillary surface. In the absence of an external pump, this barrier prevents the liquid from flowing into the reservoir cavity because of the liquid surface tension. As shown in Figure C.3, a simple solution is used for the prototype system by using wick fibers to guide the liquid from the needle exit into the reservoir and continue the capillary effect. Once the liquid from the needle tube reaches the highly hydrophilic surface of the glass lid and the reservoir, it is quickly drawn into and fills the reservoir. An alternative approach is to make a slanted wall forming a wedge angle at the needle exit to the reservoir. A properly designed wedge will cause the liquid to form a convex meniscus at the entry into the reservoir as discussed in [Man98]. The top of this meniscus would contact the hydrophilic glass lid surface 50-100 μm above the needle exit, continuing the capillary effect to drive the liquid into the reservoir. However, this approach requires a more complex microfabrication procedure especially due to the requirement of 3D micromachining of steels.

The volume of the reservoir can be designed to suit the requirements of different applications. A volume of 1 μL is demonstrated in this prototype. As shown in Figure C.2(b), the reservoir features a microchannel on one wall that permits air to leave the cavity during sampling. A side port can also be formed at the exit of the microchannel to allow the device to interface with additional components for *in situ* sample preparation and analysis. The reservoir is made from stainless steel to maintain consistency with the needle material, and can be replaced by others such as glass and polymer if needed for

integration with other microfluidic devices to form a microanalytical system for an all-in-one solution for PK studies, as will be discussed in Section C.4. The inner surface of the steel reservoir is made highly wettable with a hydrophilic coating such as silicon oxide or oxynitride.

C.2.3 Actuator

The actuator is triggered to insert the needle through the animal skin to a certain depth depending on the requirement of different sampling targets such as blood from vessels or interstitial fluid from the dermis layer.

During needle insertion, the outer epidermis layer of the skin poses the largest resistance force. The force on the needle increases with displacement of the needle as the skin is stretched, reaches a maximum, and then sharply decreases as the epidermis is pierced. The actuator must be able to supply at least this piercing force, which depends on the type of the skin and the needle tip diameter. Previous studies have measured the piercing force of human skin with surgical needles and microfabricated silicon needles to be <100 mN for a tip cross sectional area of <3000 μm^2 [Bre97, Dav04]. The force required to puncture a blood vessel in a rabbit ear with a 400 μm diameter hypodermic needle was measured to be 151 mN [Sai06]. The piercing force of mouse skin is difficult to estimate from these results due to the differences in thickness and elasticity. However, it is expected to be less than that of human skin because the mouse epidermis is only 9.1-13.7 μm thick, while the human epidermis is 60-130 μm [Azz05]. Experiments were conducted to measure the piercing force of the stainless steel needle into mouse and rat skin to examine the feasibility of the actuator selection.

The rough upper bound of 100 mN for the piercing force is one guideline for the actuator selection, and the other requirement is that the actuator must provide a stroke >3 mm. The travel distance of the actuator determines the insertion depth of the needle, and a stroke of this magnitude is necessary to reach the dermis layer of mouse skin or deeper for different sampling targets. For practical use, needle insertion depth should also be adjustable so that the microsystem can be used for different targets. Voice coil electromagnetic actuators are chosen for the prototype to meet both requirements. Compared with piezoelectric and electrostatic actuators, these magnetic actuators can easily provide the desired force and stroke with a compact size and low driving voltage.

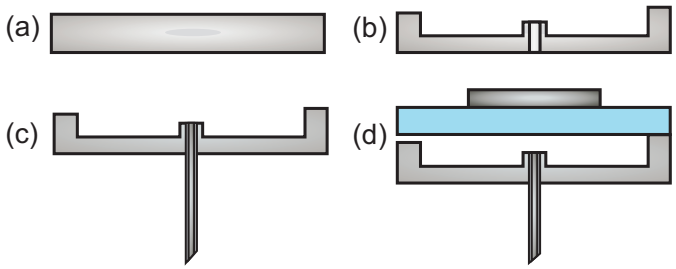

Figure C.4: Fabrication process for the reservoir: (a) the process starts with a biocompatible stainless steel 304 plate; (b) reservoir features are fabricated on the plate by μEDM; (c) the microneedle with μEDM'ed side opening is attached to the reservoir using polymer; (d) the glass lid and the magnet for actuator attachment is mounted using polymer after any wire insert and wick fiber are deployed.

As shown in Figure C.2, a commercial voice coil actuator (H2W Technologies, Inc., USA) is selected for the system and integrated into the Macor ceramic housing, which also guides the motion of the actuator magnet. A separate rare earth magnet is used to bond the glass cover of a sampling reservoir to the actuator magnet for easy attachment or removal of the reservoir. The actuator has a nominal peak force of 300 mN and a stroke of 3.2 mm, meeting requirements of the actuator for both the force and insertion depth. The magnet for reservoir attachment also enhances the actuator

performance by increasing the strength of its magnetic field, and will be verified with experiments in Section C.3.1.

C.2.4 Reservoir Fabrication

The fabrication steps for the sampling system are shown in Figure C.4. The reservoir is made from a 500 μm-thick, biocompatible stainless steel 304 plate using micro electro-discharge machining (μEDM). The SEM image of a fabricated 1 μL reservoir is shown in Figure C.5(a). The cavity is 300 μm deep with a 2.3 mm square interior footprint, and features a 600 μm-square, 200 μm-tall protruding inlet at the center for needle attachment. An optional side port, which can be used for interfacing to external sample processing components, is also shown in the figure. The reservoir is then coated with silicon oxide or oxynitride using plasma-enhanced chemical vapor deposition (PECVD) to obtain a hydrophilic surface. The steel microneedle is formed by using μEDM to re-work either of two types of commercial needles: 33-gauge needle (210 μm OD, 115 μm ID) from World Precision Instruments (WPI), Inc. (Figure C.5b), and 31 gauge needle (250 μm OD, ≈130 μm ID) from Becton Dickinson (BD). The capillary draw of the needle is enhanced by either electropolishing or inserting a polymer wire as discussed in Section C.2.2. For electropolishing, a method discussed in [Bhu05] is used to enhance the hydrophilic property of the inner surface of the needle, with the outer surface protected from the solution by a polymer coating. This method utilizes commercially-available EPS4000, which is a mixture of phosphoric and sulfuric acid. The needle is then attached to the reservoir using curable polymer. The 500 μm-thick glass lid and 3 mm-diameter rare earth magnet are then mounted onto the reservoir

(Figure C.6a), leaving a 50-100 µm gap between the top end of the needle and the glass lid for blood inflow. The assembled reservoir is then attached to the actuator magnet and mounted in the custom-machined Macor® ceramic housing. The housing has dimensions of 23.9 mm (L) × 15.2 mm (W) × 13.7 mm (H), and has a 250 µm-diameter hole on the bottom sidewall for the needle. The assembled system is shown in Figure C.6(b).

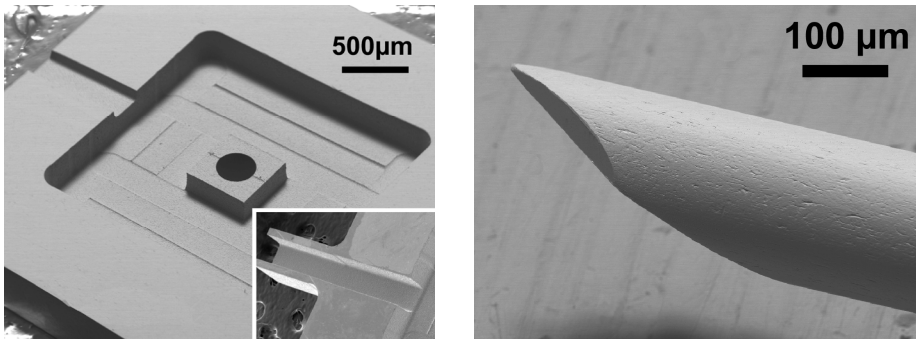

(a) (b)

Figure C.5: SEM images of: (a) the µEDM'ed reservoir showing a shallow channel on the wall for air exit, and an optional exit connector with deeper channel for external devices for sample processing. Cavity volume: ≈1.0 µL. (b) the tip of the 33-gauge needle. Outer diameter: 210 µm; Inner diameter: 115 µm.

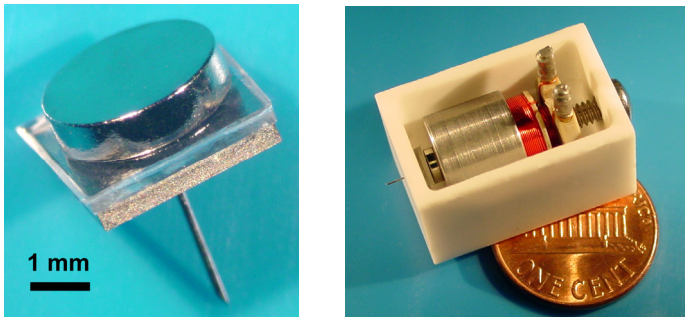

(a) (b)

Figure C.6: Photos of: (a) the assembled reservoir with glass lid and attached magnet; (b) the full sampling microsystem. A glass cover can be used to seal the ceramic housing.

C.3 Experimental Results

C.3.1 Actuator Evaluation

The piercing force of mouse skin depends heavily on the needle tip size and bevel shape, and experiments were carried out to characterize the piercing force of the BD 31-gauge microneedle with regular 12° bevel into fresh mouse carcasses. The carcasses were located on a motorized stage and fed toward a testing needle. The needle was mounted on a force gauge and measured force data were recorded into a computer.

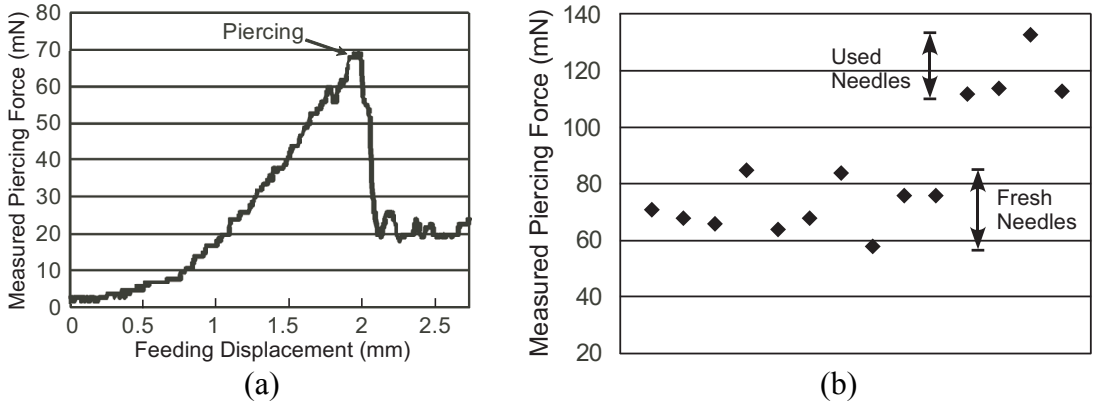

Figure C.7: Measurement results of the piercing force of BD 31-gauge needles into mouse skin: (a) force data recorded during a single insertion showing the peaking force at piercing; (b) distribution of multiple measurement results using either fresh needles or needles that have been used.

The recorded force data during a single insertion into the skin of a laboratory mouse is shown in Figure C.7(a). As expected, the force increases in the beginning as the skin deflects, reaches a maximum when the skin is pierced, and then sharply decreases to a lower stable value which corresponds to the friction force between the needle shank and the tissue. The measurement was repeated at different locations of the mouse body including back, side and abdomen, at varying feeding speeds ranging from 50 μm/sec to 750 μm/sec, using either fresh or used needle. Tests were also repeated on a second

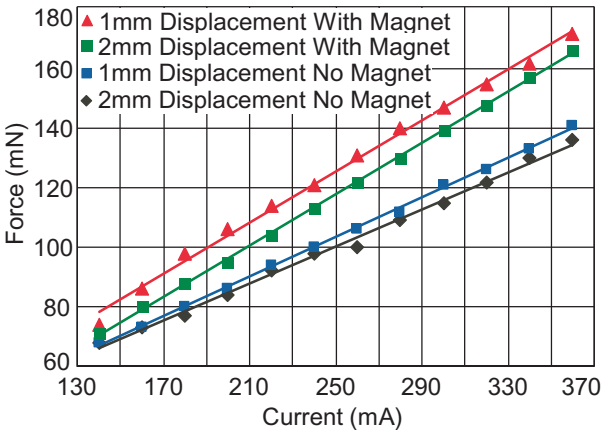

(a)

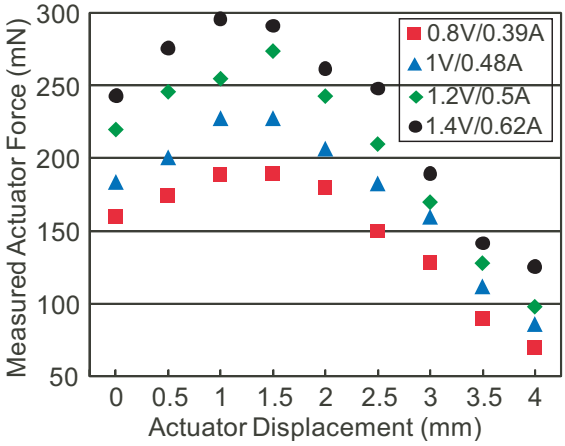

(b)

Figure C.8: Measurement results of the supplied force from the voice coil actuator. (a) Measured force *vs.* supplied current at certain displacement. The actuator force is enhanced by ≈30% with the presence of the magnet for reservoir attachment. (b) Measured force *vs.* actuator displacement at certain supplied current.

mouse carcass to account for variability. As shown in Figure C.7(b), the piecing force with a fresh needle varies between 60-85 mN, while with a used needle it rises to 110-130 mN. This force does not vary much with different feeding speed, or at the three locations on mouse body. The measured piercing force is much larger than is estimated using empirical equations for silicon microneedles from [Dav04], or experiments on silicon rubber, which is an artificial skin material with mechanical properties similar to human skin [Li07a, She05]. The testing results were used as a design guideline for

actuator selection. Piercing force of rat skin was also tested, and was found to be 170-190 mN with a fresh needle and 260-300 mN with a used needle.

The force supplied by the commercial voice coil actuator is also measured using the force gauge. The results shown in Figure C.8 indicate that the actuator amply exceeds the piercing force requirement for mouse skin when supplied current is more than ≈200 mA (≈0.4 V). The additional reservoir attachment magnet provides a ≈30% enhancement, reaching ≈170 mN with 360 mA applied at a displacement of ≈1 mm. A maximum force of ≈300 mN can be obtained at about ≈1 mm displacement with ≈620 mA (≈1.4 V) supplied, and quickly drops when the displacement becomes larger. The generated force over the entire stroke of the actuator remains greater than ≈85 mN when the supplied current is more than ≈480 mA (1 V).

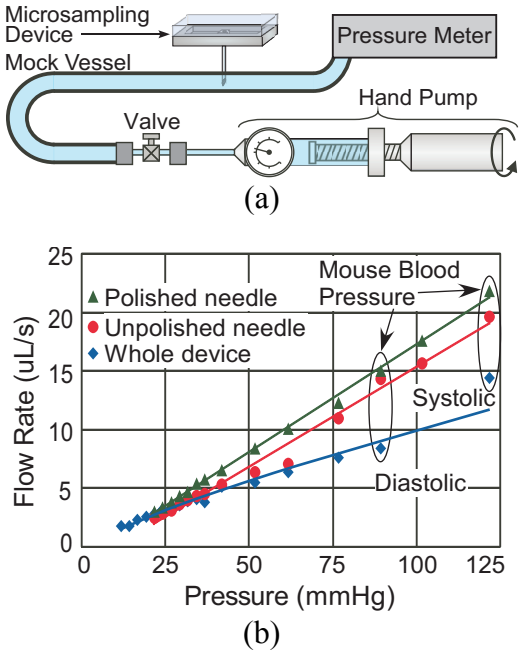

Figure C.9: (a) Schematic of testing setup for blood sampling from mock vessel. (b) Results showing measured flow rate *vs.* applied pressure through the whole device, a polished and an unpolished needle.

C.3.2 *In Vitro* Experiments

The assembled system was first tested *in vitro*: (*i*) using pressure-driven flow, with presence of unenhanced capillary forces; (*ii*) using capillary-driven flow, unassisted by a pressure differential along the needle. The first test was designed to study the fluidic characteristics of the system when sampling from a blood vessel, while the second test was performed to evaluate the sampling system before and after the modifications to enhance capillary effect, and the feasibility of using the system for interstitial fluid sampling.

(i) Pressure-Driven Flow

The experimental setup shown in Figure C.9(a) is built to evaluate the capability of the system to sample blood from a vessel, *e.g.* the jugular vein. A 4 mm-long needle (WPI 33-gauge) that has not been enhanced for capillary draw is inserted into the mock vessel. The mock vessel contains water instead of blood, and can be pressurized by a hand pump. This substitution is further discussed in Section C.4. Due to the weakly hydrophilic nature of the inner surface of the needle, the capillary effect does not, by itself, draw liquid into the needle. A pressure threshold of ≈29.0 mmHg is necessary to permit water flow through the needle. Once the water reaches the highly hydrophilic glass lid, the reservoir quickly fills by a combination of pressure-driven flow and the capillary effect. This pressure threshold is much smaller than mouse blood pressure (125 mmHg systolic, 90 mmHg diastolic), so additional surface treatment to enhance the capillary effect is unnecessary for vessel sampling. At either pressure, systolic or diastolic, it takes <0.15 sec to fill the reservoir.

The flow rate through the needle, reservoir, and a pipe of 600 μm ID attached at the reservoir outlet was measured to study the capability of the device to deliver liquid to microfluidic components for *in-situ* sample analysis. Figure C.9(b) shows this flow rate through the whole device as a function of "vascular" pressure in the mock vessel. The resulting flow rate is adequate for many microfluidic applications.

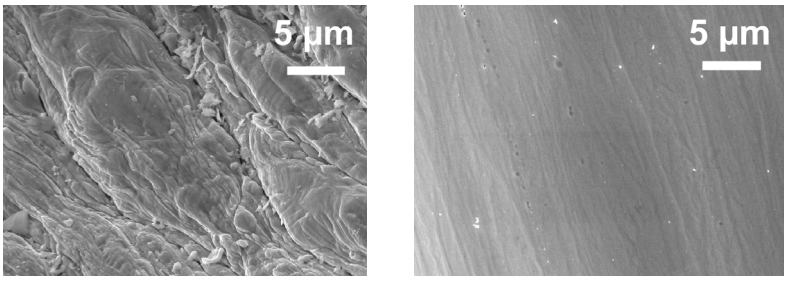

(a) (b)

Figure C.10: SEM images of the needle inner surface: (a) before electropolishing; (b) after electropolishing using EPS4000. A slot opening was cut in the needle tube using μEDM before taking the SEM images.

Table C.1: Capillary effect of the 33-guage needle.

	Unpolished	Polished
Water height in vertical needle	≈0	≈4 mm
Time to fill a 10 mm-long horizontal needle	>3 sec	≈1 sec

(ii) Capillary Flow

Two approaches, as discussed in Section C.2, were used to enhance capillary flow, as would be required to sample interstitial fluids. The first approach, electropolishing with the EPS4000 solution, was first tested on a bare stainless steel 304 sample. The water contact angle improved from ≈94° before polishing and cleaning to ≈34° after polishing, indicating the improved wettability of the electropolished surface. The inner surface of the WPI 33-gauge microneedles were then electropolished by EPS4000. A typical polished surface is shown in the SEM images in Figure C.10. The

capillary effect was tested and is compared in Table C.1. After polishing, the capillary effect raises the water level in a vertical needle by ≈4 mm and fills a 10 mm horizontal needle in ≈1 second, the difference being caused by gravity. The 4 mm height is sufficient to fill the needle in the present design.

To evaluate the effect of polishing on flow rate at a given pressure differential, a 25 mm-long needle was tested with the setup in Figure C.9(a) before and after electropolishing. The results shown in Figure C.9(b) have been scaled to match the 4 mm length of the needle in the sampling system, and indicate a clear increase in flow rate with the polished inner surface and increased inner diameter of the needle.

Although the eletropolishing approach effectively improves the capillary effect, there are a few challenges in polishing the inner surface of needles. These include limited polishing efficiency and uniformity due to higher current density at the two opening ends of the needle compared with the inner surface towards the center.

The second approach, as discussed in Section C.2, uses a 50 μm-diameter polymer wire inserted into the needle tube to increase surface area for capillary effect. Experiments showed that this scheme can easily raise the water level to fill a 25 mm-long needle tube that is positioned vertically.

To compare different PECVD silicon oxide and oxynitride layers as the hydrophilic coating on the inner surface of the reservoir, water contact angles on stainless steel 304 surface with different coatings were measured and results are shown in Table C.2. According to the measurement, the cleaned bare stainless steel 304 surface has a fairly large water contact angle of 64-68°. After coating with oxide or oxynitride layers, the measured contact angles dropped, and the low-stress oxynitride coating provided the

lowest contact angle (15-21°). This coating material has an index of refraction of 1.5, suggesting its structural, optical and thermal characteristics are closer to those of oxide than to nitride [Aga05]. The coating is called low stress because of its zero residue stress on silicon substrate after deposition. It stays well on the substrate without peeling off, and is selected to coat the reservoirs.

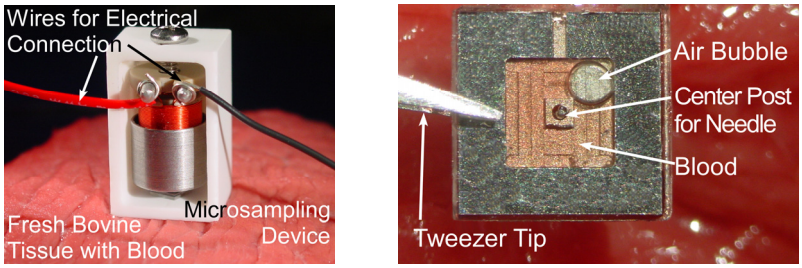

(a) (b)

Figure C.11: Experiments with bovine tissue to explore the possibility of sampling interstitial fluid. (a) Photo of the system placed on the tissue sample for experiment. (b) Photo of the obtained blood sample in the reservoir with a small air bubble.

To explore the possibility of sampling interstitial fluid rather than blood from vasculature, the sampling system with modified needle and reservoir were tested with bovine tissue samples. Figure C.11 shows the reservoir is almost completely flooded, leaving a small bubble of air.

Table C.2: Results on contact angle measurement for different stainless steel 304 (SS304) surfaces with and without oxide or oxynitride PECVD coatings.

Surface Type	Deposition Temperature (˚C)	Coating Thickness (μm)	Measured Contact Angle (˚)
Cleaned bare SS304	-	-	64-68
Low-stress oxynitride	400	5	15-21
Oxynitride	400	5	26-28
Oxide	200	2	25-31
Oxide	380	2	50-53

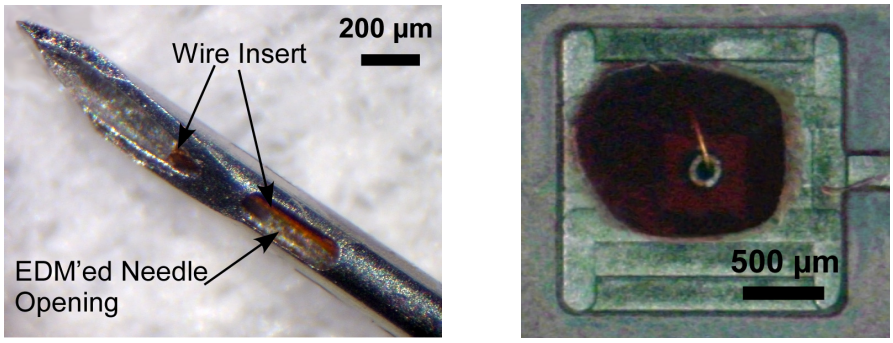

(a) (b)

Figure C.12: Photos of: (a) µEDM'ed BD 31-gauge needle with a side opening and a polymer wire insert; (b) blood collected into the reservoir from live mouse body using a sampling system with a modified needle.

C.3.3 *In Vivo* Experiments

In vivo tests were performed on the microsystem using laboratory mice for blood sampling. The BD 31-gauge needles with polymer wire insert and side opening near the tip (Figure C.12a) were used for these tests. The reservoirs were coated with PECVD oxynitride, and wick fibers were used to guide fluid from the needle exit into the reservoir. The animals were anesthetized for easier device mounting and testing operation, but this is not required for the normal operation of the automated sampling system. Tested sampling locations include mouse back, abdomen, thigh, and neck regions, and target skin spots were shaved and cleaned with antiseptic and alcohol. For testing convenience at multiple sampling locations, the system with ceramic housing is manually held against the shaved skin of the anesthetized mouse. The actuator drove the needle into the mouse body when operated with >400 mA (0.8V) current, and after a sampling time of 1-2 seconds which was empirically determined, it was triggered in the opposite direction to retract the needle from the mouse body. Blood was collected into

the reservoir from all sampling sites, and a reservoir with collected blood is shown in Figure C.12(b).

C.4 Discussion

It is worthwhile to consider system integration and scalability. As noted in Section C.2, the present version of the microsampling reservoir has a side port for convenient sample transfer to microanalytical modules such as microfluidic components for sample concentration, separation and analysis. The external components can also be fabricated on the same substrate as the sampling reservoir, further reducing dead sample volumes caused by large interconnection distances between devices. Stainless steel is a promising substrate material for microfluidic devices, especially for reactors and mixers [Yos08]. With the lithographic pattern transfer capability provided by batch mode μEDM [Tak02], implementation of microfluidic devices with complex patterns on this type of substrate is feasible. However, the more commonly used materials for microfluidic devices, such as glass and polymers, can also be used to fabricate sampling reservoir for ease of integration. In the long term, it is possible to envision a system that provides complete *in situ* blood sampling and analysis for a PK profile.

As discussed in Section C.1, a complete PK study involves multisampling from the animals to monitor the change in its concentration over time. As the microsystem size is scaled down in the future, a method must be devised to array the sampling needles and reservoirs, to accommodate multiple time-point samples to be taken by a single assembly. An assembly of this type may require several microactuators, or a single

actuator that is repositionable. For use with animals other than mice, the actuator would also have to provide the necessary force and displacement.

During the *in vitro* testing of the sampling system, water was used instead of blood. As mentioned in Section C.2, the contact angles of water and whole blood are similar, and thus the results are reflective of the qualitative behavior that is expected with blood. The fluidic properties of blood plasma, which is mostly composed of water, are also comparable to those of water. However, the blood cells, which make up almost half of the whole blood by volume, are expected to result in a higher viscosity and thus slower flow rate through the sampling components than does the water. Further investigations would be necessary if the system is to be used for blood vessel sampling and driving additional fluidic components.

C.5 Conclusions

A microsystem for automated sampling of blood is fabricated and evaluated using *in vitro* studies and *in vivo* studies with anesthetized mice. The system uses a 31-33 gauge needle and a reservoir with ≈1 μL volume, reducing the minimum sample size. It can help to substantially reduce the number of animals sacrificed in an extended time point study. The research effort highlights system-level considerations, identifying challenges in actuator force and displacement, needle and reservoir hydrophilicity, and system integration, and presents potential solutions for each of these challenges.

APPENDIX D

List of Publications Related to This Dissertation

D.1 Journals

T. Li, R. Y. Gianchandani, and Y. B. Gianchandani, "Micromachined bulk PZT tissue contrast sensor for fine needle aspiration biopsy," *Lab on a Chip,* vol. 7, no. 2, pp. 179-185, Feb. 2007.

T. Li and Y. B. Gianchandani, "A micromachining process for die-scale pattern transfer in ceramics and its application to bulk piezoelectric actuators," *IEEE/ASME J. Micromechanical Systems,* vol. 15, no. 3, pp. 605-612, Jun. 2006.

T. Li, A. Barnett, K. L. Rogers, and Y. B. Gianchandani, "A blood sampling microsystem for pharmacokinetic applications: design, fabrication, *in vitro* and *in vivo* results," (to be submitted).

T. Li, R. Y. Gianchandani, and Y. B. Gianchandani, "Micromachined bulk-PZT differential sensor with integrated interface circuit for tissue contrast detection in fine needle aspiration biopsy," (in preparation).

D.2 Conference Proceedings

T. Li, A. Barnett, D. Xiao, M. Zhong, and Y. B. Gianchandani, "An *in vivo* blood microsampling device for pharmacokinetic applications," in *Proc. 14th Int. Conf. Solid-State Sensors, Actuators and Microsystems (Transducers 2007)*, Lyon, France, Jun. 2007, pp. 225-228.

T. Li and Y. B. Gianchandani, "An empirical model for a piezoelectric tissue contrast sensor embedded in a biopsy tool," in *Proc. 10th Int. Conf. Miniaturized Systems for Chemistry and Life Sciences (μTAS 2006)*, Tokyo, Japan, Nov. 2006, pp. 837-839.

T. Li, R. Y. Gianchandani, and Y. B. Gianchandani, "A bulk PZT microsensor for *in-situ* tissue contrast detection during fine needle aspiration biopsy of thyroid nodules," in *Proc. IEEE Int. Conf. Micro Electro Mechanical Systems (MEMS 2006)*, Istanbul, Turkey, Jan. 2006, pp. 12-15.

T. Li and Y. B. Gianchandani, "A die-scale micromachining process for bulk PZT and its application to in-plane actuators," in *Proc. IEEE Int. Conf. Micro Electro Mechanical Systems (MEMS 2005)*, Miami Beach, FL, Jan. 2005, pp. 387-390.

T. Li and Y. B. Gianchandani, "LEEDUS: A micromachining process for die-scale pattern transfer in ceramics with high resolution and throughput," in *Tech. Digest Solid State Sensor, Actuator and Microsystems Workshop (Hilton Head 2004)*, Hilton Head Island, SC, Jun. 2004, pp. 324-327.

D.3 Pending Patents

Y.B. Gianchandani, T. Li, and R.Y. Gianchandani, "*In situ* tissue analysis device and method," US Patent Application No. 20070191733, filed in Jan. 2007.

BIBLIOGRAPHY

[Axi08] *Axiom Co. Ltd. Website*, http://www.axiom-j.co.jp.

[Aga05] M. Agah and K. D. Wise, "A fully-dry PECVD-oxynitride process for microGC column fabrication," in *Proc. IEEE Int. Conf. Micro Electro Mechanical Systems (MEMS 2005)*, Miami Beach, FL, Jan. 2005, pp. 774-777.

[Aga95] S. Agathopoulos and P. Nikolopoulos, "Wettability and interfacial interactions in bioceramic-body-liquid systems," *J. Biomedical Materials Research,* vol. 29, no. 4, pp. 421-429, Apr. 1995.

[All87] P. E. Allen and D. R. Holberg, *CMOS Analog Circuit Design*. New York: Holt, Rinehart and Winston, 1987.

[Ang02] Z. Anguelov, "Fine-needle aspiration biopsy," in *Currents: Physician-To-Physician Clinical Resource*. vol. 3, no. 2, Iowa City, IA: University of Iowa Hospitals and Clinics, Spring 2002, http://www.uihealthcare.com/news/currents/index.html

[Aoy06] S. Aoyagi, H. Izumi, Y. Isono, K. Makihira, and M. Fukuda, "Biodegradable polymer needle having a trench for collecting blood by capillary force," in *Proc. IEEE Int. Conf. Micro Electro Mechanical Systems (MEMS 2006)*, Istanbul, Turkey, Jan. 2006, pp. 450-453.

[Ayr98] J. W. Ayres, F. Lalande, Z. Chaudhry, and C. A. Rogers, "Qualitative impedance-based health monitoring of civil infrastructures," *Smart Mater. Struct.,* vol. 7, no. 5, pp. 599-605, Oct. 1998.

[Azz05] L. Azzi, M. El-Alfy, C. Martel, and F. Labrie, "Gender differences in mouse skin morphology and specific effects of sex steroids and dehydroepiandrosterone," *J. Investigative Dermatology,* vol. 124, no. 1, pp. 22-27, Jan. 2005.

[Ban98] A. Bandyopadhyay, R. K. Panda, T. F. McNulty, F. Mohammadi, S. C. Danforth, and A. Safari, "Piezoelectric ceramics and composites via rapid prototyping techniques," *Rapid Prototyping Journal,* vol. 4, no. 1, pp. 37-49, 1998.

[Baz02] M. Bazzocchi, G. E. Francescutti, C. Zuiani, C. Del Frate, and V. Londero, "Breast pseudoaneurysm in a woman after core biopsy: percutaneous treatment with alcohol," *Am. J. Roentgenol.,* vol. 179, no. 3, pp. 696-698, Sept. 2002.

[Bhu05] A. Bhuyan, B. Gregory, H. Lei, S. Y. Yee, and Y. B. Gianchandani, "Pulse and DC electropolishing of stainless steel for stents and other devices," in *Proc. Fourth IEEE Conf. Sensors (IEEE Sensors 2005)*, Irvine, CA, Oct. 2005, pp. 314-317.

[Bou06] L. Boulange-Petermann, C. Gabet, and B. Baroux, "On the respective effect of the surface energy and micro-geometry in the cleaning ability of bare and coated steels," *Colloids Surfaces A: Physicochem. Eng. Aspects,* vol. 272, no. 1-2, pp. 56-62, Jan. 2006.

[Bre97] P. N. Brett, T. J. Parker, A. J. Harrison, T. A. Thomas, and A. Carr, "Simulation of resistance forces acting on surgical needles," *Proc. Inst. Mech. Eng., Part H: J. Eng. Med.,* vol. 211, no. 4, pp. 335-347, 1997.

[Bro99] W. D. Brown, Ed., *Advanced Electronic Packaging : With Emphasis on Multichip Modules*. New York: Wiley-IEEE Press, 1999.

[Buc86] R. C. Buchanan, Ed., *Ceramic Materials for Electronics: Processing, Properties, and Applications*. New York: Marcel Dekker, Inc., 1986.

[Bul09] *Bullen Ultrasonics, Inc. Website*, http://www.bullen-ultrasonics.com.

[Cap03] S. Caplet, N. Sillon, M.-T. Delaye, and P. Berruyer, "Vacuum wafer-level packaging for MEMS applications," in *Proc. SPIE - Micromachining and Microfabrication Process Technology VIII*, vol. 4979, San Jose, CA, Jan. 2003, pp. 271-278.

[Cha03] Z. Chang, S. Sherrit, X. Bao, and Y. Bar-Cohen, "*In situ* rock probing using the ultrasonic/sonic driller/corer (USDC)," in *Proc. SPIE - Smart Structures and Materials Conference*, vol. 5056, San Diego, 2003, pp. 567-573.

[Cho92] S. T. Cho and J. Ji, *University of Michigan Technologies for CMOS Integrated Circuits and Silicon Micromachining*, University of Michigan, Ann Arbor, Technical Report No. 203, Feb. 1992.

[Cho03] H.-Z. Choi, S.-W. Lee, and B.-G. Lee, "Micro-hole machining using ultrasonic vibration," *Key Engineering Materials,* vol. 238-239, pp. 29-34, 2003.

[Coh04] I. M. Cohen and P. K. Kundu, *Fluid Mechanics*, 3rd ed. Boston: Elsevier Academic Press, 2004.

[Dav04] S. P. Davis, B. J. Landis, Z. H. Adams, M. G. Allen, and M. R. Prausnitz, "Insertion of microneedles into skin: measurement and prediction of insertion force and needle fracture force," *J. Biomechanics,* vol. 37, no. 8, pp. 1155-1163, Aug. 2004.

[Dil09] *DiLab Website*, http://www.dilab.com.

[Dow98] D. J. Dowsett, P. A. Kenny, and R. E. Johnston, *The Physics of Diagnostic Imaging*. London, U.K.: Chapman & Hall Medical, 1998.

[Ega99] K. Egashira and T. Masuzawa, "Microultrasonic machining by the application of workpiece vibration," *CIRP Annals - Manufacturing Technology,* vol. 48, no. 1, pp. 131-134, 1999.

[Eng99] J. M. English and M. G. Allen, "Wireless micromachined ceramic pressure sensors," in *Proc. IEEE Int. Conf. Micro Electro Mechanical Systems (MEMS 1999)*, Orlando, FL, Jan. 1999, pp. 511-516.

[Fen03] Z. C. Feng and C. Chicone, "A delay differential equation model for surface acoustic wave sensors," *Sensors Actuators A (Phys.),* vol. 104, no. 2, pp. 171-178, Apr. 2003.

[Fer97] V. Ferrari, D. Marioli, and A. Taroni, "Thick-film resonant piezo-layers as new gravimetric sensors," *Measurement Science & Technology,* vol. 8, no. 1, pp. 42-48, Jan. 1997.

[Fis01] K. Fischer, B. Chaudhuri, S. McNamara, H. Guckel, Y. Gianchandani, and D. Novotny, "A latching, bistable optical fiber switch combining LIGA technology with micromachined permanent magnets," in *Proc. 11th Int. Conf. Solid-State Sensors and Actuators (Transducers 2001)*, vol. 2, Munich, Germany, Jun. 2001, pp. 1340-3.

[Fis09] *Fischione Instruments, Inc. Website*, http://www.fischione.com.

[Gar03] H. J. G. E. Gardeniers, R. Luttge, E. J. W. Berenschot, M. J. de Boer, S. Y. Yeshurun, M. Hefetz, R. van't Oever, and A. van den Berg, "Silicon micromachined hollow microneedles for transdermal liquid transport," *IEEE/ASME J. Micromechanical Systems,* vol. 12, no. 6, pp. 855-862, Dec. 2003.

[Gau02] G. H. Gautschi, *Piezoelectric Sensorics: Force, Strain, Pressure, Acceleration and Acoustic Emission Sensors, Materials and Amplifiers*. New York: Springer, 2002.

[Ger09] G. Germani, M. Pleguezuelo, R. Stigliano, and A. K. Burroughs, "Risk of seeding is reduced by associating diagnostic biopsy with percutaneous ablation for hepatocellular carcinoma," *Gut,* vol. 58, no. 5, pp. 734-735, May 1, 2009.

[Gha93] H. Gharib and J. R. Goellner, "Fine-needle aspiration biopsy of the thyroid: an appraisal," *Ann. Intern. Med.,* vol. 118, no. 4, pp. 282-289, Feb. 1993.

[Gin02] M. D. Gingerich, *Multi-Dimensional Microelectrode Arrays with On-Chip CMOS Circuitry for Neural Stimulation and Recording*, Ph.D. Thesis. University of Michigan, Ann Arbor, 2002.

[Göp92] W. Göpel, J. Hesse, and J. N. Zemel, Eds., *Sensors: a Comprehensive Survey*, vol. 3. New York: F.R.G. Weinheim, 1992.

[Gre97] J. F. Greenleaf, R. Muthupillai, P. J. Rossman, D. J. Lomas, S. J. Riederer, and R. L. Ehman, "Measurement of tissue elasticity using magnetic resonance elastography," in *Review of Progress in Quantitative Nondestructive Evaluation*, vol. 1, Brunswick, ME, Jul. 1997, pp. 19-26.

[Gri01] C. A. Grimes, M. K. Jain, R. S. Singh, Q. Cai, A. Mason, K. Takahata, and Y. Gianchandani, "Magnetoelastic microsensors for environmental monitoring," in *Proc. IEEE Int. Conf. Micro Electro Mechanical Systems (MEMS 2001)*, Interlaken, Switzerland, Jan. 2001, pp. 278-281.

[Gri03] P. Griss and G. Stemme, "Side-opened out-of-plane microneedles for microfluidic transdermal liquid transfer," *IEEE/ASME J. Micromechanical Systems,* vol. 12, no. 3, pp. 296-301, Jun. 2003.

[Guc98] H. Guckel, "High-aspect-ratio micromachining via deep X-ray lithography," in *Proc. IEEE*, vol. 86, no. 8, Aug. 1998, pp. 1586-1593.

[Hof00] J. Hoff, "Methods of blood collection in the mouse," *Lab Animal,* vol. 29, no. 10, pp. 47-53, Nov. 2000.

[Hon98] Y. Honma, K. Takahashi, and M. Muro, "Micro-machining of magnetic metal film using electro-discharge technique," in *Proc. Int. Conf. Micromechatronics for Information and Precision Equipment (MIPE 1997)*, vol. 2, Tokyo, Japan, Jul. 1997, pp. 383-399.

[How95] W. Y. Howng, "Ceramic technologies for portable radio applications," in *Materials and Processes for Wireless Communications*, T. Negas and H. C. Ling, Eds. Westerville, OH: American Ceramic Society, 1995.

[IEC76] *Guide to Dynamic Measurements of Piezoelectric Ceramics with High Electromechanical Coupling*, IEC Standard Publication 60483, 1976

[IEE88] *IEEE Standard on Piezoelectricity*, ANSI/IEEE Std 176-1987, New York: IEEE Inc., 1988, withdrawn in 2000.

[Ike90] T. Ikeda, *Fundamentals of Piezoelectricity*. New York: Oxford University Press, 1990.

[Jen05] H. P. Jennissen, "Ultra-hydrophilic transition metals as histophilic biomaterials," *Macromolecular Symposia,* vol. 225, pp. 43-69, May 2005.

[Joh08] J. T. Johnson and L. Zimmer, *Fine-Needle Aspiration of Neck Masses*, eMedicine World Medical Library from WebMD, 2005, http://www.emedicine.com/ent/topic561.htm.

[Kal03] S. Kalpakjian and S. R. Schmid, *Manufacturing Processes for Engineering Materials*, 4th ed. Upper Saddle River, NJ: Prentice Hall, 2003.

[Kan01] V. V. Kancharla, K. K. Hendricks, and S. Chen, "Micromachining of packaging materials for MEMS using lasers," in *Proc. SPIE - Micromachining and Microfabrication Process Technology VII*, vol. 4557, San Francisco, CA, Oct. 2001, pp. 220-224.

[Kol84] H. H. Kolm and E. A. Kolm, *Spiral Piezoelectric Rotary Actuator*, U.S. Patent no. 4,435,667. 1984.

[Kom93] M. Komaraiah and P. N. Reddy, "A study on the influence of workpiece properties in ultrasonic machining," *Int. J. Machine Tools & Manufacture,* vol. 33, no. 3, pp. 495-505, 1993.

[Kum96] P. N. Kumta, G. S. Rohrer, and U. Balachandran, Eds., *Role of Ceramics in Advanced Electrochemical Systems*. Westerville, OH: American Ceramic Society, 1996.

[Lav74] V. V. Lavrinenko, A. P. Miroshnichenko, and V. A. Khraschevsky, *Method of Making a Piezoelectric Element*, U.S. Patent no. 3,781,955. 1974.

[Li04] T. Li and Y. B. Gianchandani, "LEEDUS: A micromachining process for die-scale pattern transfer in ceramics with high resolution and throughput," in *Tech. Digest Solid State Sensor, Actuator and Microsystems Workshop (Hilton Head 2004)*, Hilton Head Island, SC, Jun. 2004, pp. 324-327.

[Li05] T. Li and Y. B. Gianchandani, "A die-scale micromachining process for bulk PZT and its application to in-plane actuators," in *Proc. IEEE Int. Conf. Micro Electro Mechanical Systems (MEMS 2005)*, Miami Beach, FL, Jan. 2005, pp. 387-390.

[Li06] T. Li and Y. B. Gianchandani, "A micromachining process for die-scale pattern transfer in ceramics and its application to bulk piezoelectric actuators," *IEEE/ASME J. Micromechanical Systems,* vol. 15, no. 3, pp. 605-612, Jun. 2006.

[Li06a] T. Li, R. Y. Gianchandani, and Y. B. Gianchandani, "A bulk PZT microsensor for *in-situ* tissue contrast detection during fine needle aspiration biopsy of thyroid nodules," in *Proc. IEEE Int. Conf. Micro Electro Mechanical Systems (MEMS 2006)*, Istanbul, Turkey, Jan. 2006, pp. 12-15.

[Li06b] T. Li and Y. B. Gianchandani, "An empirical model for a piezoelectric tissue contrast sensor embedded in a biopsy tool," in *Proc. 10th Int. Conf. Miniaturized Systems for Chemistry and Life Sciences (μTAS 2006)*, Tokyo, Japan, Nov. 2006, pp. 837-839.

[Li07] T. Li, R. Y. Gianchandani, and Y. B. Gianchandani, "Micromachined bulk PZT tissue contrast sensor for fine needle aspiration biopsy," *Lab on a Chip,* vol. 7, no. 2, pp. 179-185, Feb. 2007.

[Li07a] T. Li, A. Barnett, D. Xiao, M. Zhong, and Y. B. Gianchandani, "An *in vivo* blood microsampling device for pharmacokinetic applications," in *Proc. 14th Int. Conf. Solid-State Sensors, Actuators and Microsystems (Transducers 2007)*, Lyon, France, Jun. 2007, pp. 225-228.

[Mac04] E. J. Mackenzie and R. H. Mortimer, "6: Thyroid nodules and thyroid cancer," *The Medical Journal of Australia,* vol. 180, no. 5, pp. 242-247, Mar. 1, 2004.

[Mad02] M. J. Madou, *Fundamentals of Microfabrication: The Science of Miniaturization*, 2nd ed. Boca Raton, FL: CRC Press, 2002.

[Mak99] E. Makino, T. Shibata, and Y. Yamada, "Micromachining of fine ceramics by photolithography," *Sensors Actuators A (Phys.),* vol. 75, no. 3, pp. 278-288, Jun. 1999.

[Mam02] A. G. Mamalis, J. Kundrak, K. Gyani, and M. Horvath, "On the precision grinding of advanced ceramics," *Int. J. Advanced Manufacturing Technology,* vol. 20, no. 4, pp. 255-258, Aug. 2002.

[Man98] P. F. Man, C. H. Mastrangelo, M. A. Burns, and D. T. Burke, "Microfabricated capillarity-driven stop valve and sample injector," in *Proc. IEEE Int. Conf. Micro Electro Mechanical Systems (MEMS 1998)*, Heidelberg, Germany, Jan. 1998, pp. 45-50.

[Man94] M. Mantel and J. P. Wightman, "Influence of the surface chemistry on the wettability of stainless steel," *Surface Interface Analysis,* vol. 21, no. 9, pp. 595-605, Sep. 1994.

[Mar91] S. J. Martin, V. E. Granstaff, and G. C. Frye, "Characterization of a quartz crystal microbalance with simultaneous mass and liquid loading," *Anal. Chem.,* vol. 63, no. 20, pp. 2272-2281, Oct 1991.

[Mas90] T. Masaki, K. Kawata, and T. Masuzawa, "Micro electro-discharge machining and its applications," in *Proc. IEEE Int. Conf. Micro Electro Mechanical Systems: An Investigation of Micro Structures, Sensors, Actuators, Machines and Robots*, Napa Valley, CA, Feb. 1990, pp. 21-26.

[Mas85] T. Masuzawa, M. Fujino, K. Kobayashi, T. Suzuki, and N. Kinoshita, "Wire electro-discharge grinding for micro-machining," *CIRP Annals - Manufacturing Technology,* vol. 34, no. 1, pp. 431-434, 1985.

[Mck98] R. E. McKeighen, "Design guidelines for medical ultrasonic arrays," in *Proc. SPIE - Medical Imaging Conf.*, vol. 3341, San Diego, CA, Feb. 1998, pp. 2-18.

[Moh99] F. Mohammadi, A. L. Kholkin, B. Jadidian, and A. Safari, "High-displacement spiral piezoelectric actuators," *Appl. Phys. Lett.,* vol. 75, no. 16, pp. 2488-90, Oct. 1999.

[Moh00] F. Mohammadi, B. Jadidian, A. L. Kholkin, S. C. Danforth, and A. Safari, "Electromechanical properties of piezoelectric spiral actuators," in *Proc. 12th IEEE Int. Symp. Applications of Ferroelectrics (ISAF 2000)*, Honolulu, HI, 2000, pp. 101-104.

[Mom96] A. Momose, T. Takeda, Y. Itai, and K. Hirano, "Tomographic image reconstruction using x-ray phase information," in *Proc. SPIE - Medical Imaging Conf.*, vol. 2708, Newport Beach, CA, Feb. 1996, pp. 674-684.

[Mor92] M. A. Moreland, "Ultrasonic machining," in *Engineered Materials Handbook*, S. J. Schneider, Ed. Metals Park, OH: ASM International, 1992, pp. 359-362.

[Mor02] N. Moronuki and E. Brinksmeier, "Micromachining of brittle materials by ultrasonic lapping with tool wear compensation," in *Proc. 3rd euspen Int. Conf.*, vol. 2, Eindhoven, Netherlands, May 2002, pp. 399-402.

[Muk04] E. V. Mukerjee, S. D. Collins, R. R. Isseroff, and R. L. Smith, "Microneedle array for transdermal biological fluid extraction and *in situ* analysis," *Sensors and Actuators A: Physical,* vol. 114, no. 2-3, pp. 267-275, Sep. 2004.

[Mur04] T. E. Murphy, S. Walavalkar, and J. D. Phillips, "Epitaxial growth and surface modeling of ZnO on c-plane Al_2O_3," *Appl. Phys. Lett.,* vol. 85, no. 26, pp. 6338-6340, Dec. 2004.

[Net03] F. H. Netter, *Atlas of Human Anatomy*, 3rd ed. Teterboro, NJ: Icon Learning Systems, 2003.

[Oki03] A. Oki, M. Takai, H. Ogawa, Y. Takamura, T. Fukasawa, J. Kikuchi, Y. Ito, T. Ichiki, and Y. Horiike, "Healthcare chip for checking health condition from analysis of trace blood collected by painless needle," *Japan. J. Applied Physics,* vol. 42, no. 6A, pp. 3722-3727, Jun. 2003.

[Oma92] S. Omata and Y. Terunuma, "New tactile sensor like the human hand and its applications," *Sensors Actuators A (Phys.),* vol. 35, no. 1, pp. 9-15, Oct. 1992.

[Ots93] K. Otsuka, *Multilayer Ceramic Substrate-Technology for VLSI Package/Multichip Module*. London, U.K.: Elsevier Applied Science, 1993.

[Pac96] F. Pacini and L. J. De Groot, "Thyroid neoplasia," in *The Thyroid and its Diseases*, 6th ed. New York: W.B. Saunders Company, 1996, updated online at http://www.thyroidmanager.org, Feb. 2006.

[Pal99] D. W. Palmer, "High-temperature electronics packaging," in *High Temperature Electronics*, R. Kirschman, Ed. New York: IEEE Press, 1999.

[Pan06] W. Pan, P. Soussan, B. Nauwelaers, and H. A. C. Tilmans, "A surface micromachined electrostatically tunable film bulk acoustic resonator," *Sensors Actuators A (Phys.),* vol. 126, no. 2, pp. 436-446, Feb. 2006.

[Pan00] *Operating Instructions for Panasonic MG-ED72W Micro EDM Machine*, Panasonic, Inc.

[Pcb03] *PCB Piezotronics, Inc. Website*, http://www.pcb.com.

[Pol96] D. L. Polla and L. F. Francis, "Ferroelectric thin films in micro-electromechanical systems applications," *MRS Bulletin,* vol. 21, no. 7, pp. 59-65, Jul. 1996.

[Poz05] D. M. Pozar, *Microwave Engineering*, 3rd ed. Hoboken, NJ: John Wiley & Sons, Inc., 2005.

[Rey00] D. Reynaerts, W. Meeusen, X. Song, H. Van Brussel, S. Reyntjens, D. De Bruyker, and R. Puers, "Integrating electro-discharge machining and photolithography: work in progress," *J. Micromechanics and Microengineering,* vol. 10, no. 2, pp. 189-195, Jun. 2000.

[Ric05] M. T. Richardson and Y. B. Gianchandani, "A passivated electrode batch μEDM technology for bulk metal transducers and packages," in *Proc. 4th IEEE Conf. Sensors*, Irvine, CA, Nov. 2005, pp. 219-222.

[Ric06] M. T. Richardson, Y. B. Gianchandani, and D. S. Skala, "A parametric study of dimensional tolerance and hydrodynamic debris removal in micro-electro-discharge machining," in *Proc. IEEE Int. Conf. Micro Electro Mechanical Systems (MEMS 2006)*, Istanbul, Turkey, Jan. 2006, pp. 314-317.

[Roy04] F. Royo, N. Bjork, H.-E. Carlsson, S. Mayo, and J. Hau, "Impact of chronic catheterization and automated blood sampling (Accusampler) on serum corticosterone and fecal immunoreactive corticosterone metabolites and immunoglobulin A in male rats," *J. Endocrinology,* vol. 180, no. 1, pp. 145-153, Jan. 2004.

[Sai06] H. Saito, K. Mitsubayashi, and T. Togawa, "Detection of needle puncture to blood vessel by using electric conductivity of blood for automatic blood sampling," *Sensors Actuators A (Phys.),* vol. 125, no. 2, pp. 446-450, Jan. 2006.

[San04] O. Santos, T. Nylander, R. Rosmaninho, G. Rizzo, S. Yiantsios, N. Andritsos, A. Karabelas, H. Muller-Steinhagen, L. Melo, L. Boulange-Petermann, C. Gabet, A. Braem, C. Tragardh, and M. Paulsson, "Modified stainless steel

surfaces targeted to reduce fouling - surface characterization," *J. Food Engineering,* vol. 64, no. 1, pp. 63-79, Sep. 2004.

[Sed04] A. S. Sedra and K. C. Smith, *Microelectronic Circuits*, 5th ed. New York: Oxford University Press, 2004.

[She02] J. A. Shepherd, K. M. Kerlikowske, R. Smith-Bindman, H. K. Genant, and S. R. Cummings, "Measurement of breast density with dual X-ray absorptiometry: feasibility," *Radiology,* vol. 223, no. 2, pp. 554-557, May 2002.

[She05] O. A. Shergold and N. A. Fleck, "Experimental investigation into the deep penetration of soft solids by sharp and blunt punches, with application to the piercing of skin," *J. Biomech. Eng.,* vol. 127, no. 5, pp. 838-848, Oct. 2005.

[Son09] *Sonic-Mill Website*, http://www.sonicmill.com/machine.html.

[Son00] *Models H520 and H540 Hand Held Welders Instruction Manual*, Sonics & Materials, Inc.

[Sto05] B. Stoeber and D. Liepmann, "Arrays of hollow out-of-plane microneedles for drug delivery," *IEEE/ASME J. Micromechanical Systems,* vol. 14, no. 3, pp. 472-479, Jun. 2005.

[Su01] Q.-X. Su, P. Kirby, E. Komuro, M. Imura, Q. Zhang, and R. Whatmore, "Thin-film bulk acoustic resonators and filters using ZnO and lead-zirconium-titanate thin films," *IEEE Trans. Microwave Theory Tech.,* vol. 49, no. 4, pp. 769-778, Apr. 2001.

[Sun96] X.-Q. Sun, T. Masuzawa, and M. Fujino, "Micro ultrasonic machining and its applications in MEMS," *Sensors Actuators A (Phys.),* vol. 57, no. 2, pp. 159-164, Nov. 1996.

[Tak99] K. Takahata, N. Shibaike, and H. Guckel, "A novel micro electro-discharge machining method using electrodes fabricated by the LIGA process," in *Proc. IEEE Int. Conf. Micro Electro Mechanical Systems (MEMS 1999)*, Orlando, FL, Jan. 1999, pp. 238-243.

[Tak00] K. Takahata, N. Shibaike, and H. Guckel, "High-aspect-ratio WC-Co microstructure produced by the combination of LIGA and micro-EDM," *Microsystem Technologies,* vol. 6, no. 5, pp. 175-178, 2000.

[Tak01] K. Takahata and Y. B. Gianchandani, "Batch mode micro-EDM for high-density and high-throughput micromachining," in *Proc. IEEE Int. Conf. Micro Electro Mechanical Systems (MEMS 2001)*, Interlaken, Switzerland, Jan. 2001, pp. 72-75.

[Tak02] K. Takahata and Y. B. Gianchandani, "Batch mode micro-electro-discharge machining," *IEEE/ASME J. Micromechanical Systems,* vol. 11, no. 2, pp. 102-110, Apr. 2002.

[Tak05] K. Takahata, *Batch Manufacturing Technology based on Micro-Electro-Discharge Machining and Application to Cardiovascular Stents*, Ph.D. Thesis. University of Michigan, Ann Arbor, MI, 2005.

[Tak94] S. Takashima, H. Fukuda, and T. Kobayashi, "Thyroid nodules: clinical effect of ultrasound-guided fine-needle aspiration biopsy," *J. Clinical Ultrasound,* vol. 22, no. 9, pp. 535-542, Nov.-Dec. 1994.

[Tho98] T. B. Thoe, D. K. Aspinwall, and M. L. H. Wise, "Review on ultrasonic machining," *Int. J. Machine Tools & Manufacture,* vol. 38, no. 4, pp. 239-255, Apr. 1998.

[Tho03] *Thorlabs, Inc. Website*, http://www.thorlabs.com.

[Tro04] S. Trolier-Mckinstry and P. Muralt, "Thin film piezoelectrics for MEMS," *J. Electroceramics,* vol. 12, no. 1-2, pp. 7-17, Jan. 2004.

[Tse05] K. K. Tseng and L. Wang, "Impedance-based method for nondestructive damage identification," *J. Engineering Mechanics,* vol. 131, no. 1, pp. 58-64, Jan. 2005.

[Uch97] K. Uchino, *Piezoelectric Actuators and Ultrasonic Motors*. Boston, MA: Kluwer Academic, 1997.

[Ude06] K. J. Udeshi, *On-Chip High Voltage Generation Using Mechanical Oscillators*, Ph.D. Thesis. University of Michigan, Ann Arbor, MI, 2006.

[Ult08] *Ultra Sonic Seal Website*, http://www.ultrasonicseal.com/upa.html.

[Wak03] M. Wakuda, Y. Yamauchi, and S. Kanzaki, "Material response to particle impact during abrasive jet machining of alumina ceramics," *J. Materials Processing Technology,* vol. 132, no. 1-3, pp. 177-183, Jan. 2003.

[Wan00] L. P. Wang, R. Wolf, Q. Zhou, S. Trolier-McKinstry, and R. J. Davis, "Wet-etch patterning of lead zirconate titanate (PZT) thick films for microelectromechanical systems (MEMS) applications," in *Proc. Materials Science of Microelectromechanical Systems (MEMS) Devices III. Symp.*, no. Copyright 2002, IEE, Boston, MA, 2000, pp. EE5.39.1-EE5.39.6.

[Wan99] S. Wang, X. Li, K. Wakabayashi, and M. Esashi, "Deep reactive ion etching of lead zirconate titanate using sulfur hexafluoride gas," *J. American Ceramic Society,* vol. 82, no. 5, pp. 1339-1341, May 1999.

[Wen00] H. Wensink, J. W. Berenschot, H. V. Jansen, and M. C. Elwenspoek, "High resolution powder blast micromachining," in *Proc. IEEE Int. Conf. Micro Electro Mechanical Systems (MEMS 2000)*, Miyazaki, Japan, 2000, pp. 769-774.

[Wen02] H. Wensink and M. C. Elwenspoek, "Reduction of sidewall inclination and blast lag of powder blasted channels," *Sensors Actuators A (Phys.),* vol. 102, no. 1-2, pp. 157-164, Dec. 2002.

[Yan87] M. F. Yan, K. Niwa, H. M. O'Bryan, and W. S. Young, Eds., *Ceramic Substrates and Packages for Electronic Applications*. Westerville, OH: American Ceramic Society, 1987.

[Yos08] J. Yoshida, *Flash Chemistry: Fast Organic Synthesis in Microsystems*. Hoboken, N.J.: Wiley, 2008.

[Zab03] *Zaber Technologies, Inc. Website*, http://www.zaber.com.

[Zha04] H. Zhang, M. S. Marma, E. S. Kim, C. E. McKenna, and M. E. Thompson, "Implantable resonant mass sensor for liquid biochemical sensing," in *Proc. IEEE Int. Conf. Micro Electro Mechanical Systems (MEMS 2004)*, Maastricht, Netherlands, Jan. 2004, pp. 347-350.

[Zha05] H. Zhang and E. S. Kim, "Micromachined acoustic resonant mass sensor," *IEEE/ASME J. Micromechanical Systems,* vol. 14, no. 4, pp. 699-706, Aug. 2005.